

SERPENTINIZATION AND CARBONATIZATION OF  
TECTONIC MÉLANGES IN THE COY POND COMPLEX,  
CENTRAL NEWFOUNDLAND

CENTRE FOR NEWFOUNDLAND STUDIES

**TOTAL OF 10 PAGES ONLY  
MAY BE XEROXED**

(Without Author's Permission)

NICOLAI ADRIAN TIMBAL





National Library  
of Canada

Acquisitions and  
Bibliographic Services Branch

395 Wellington Street  
Ottawa, Ontario  
K1A 0N4

Bibliothèque nationale  
du Canada

Direction des acquisitions et  
des services bibliographiques

395, rue Wellington  
Ottawa (Ontario)  
K1A 0N4

*Your file - Votre référence*

*Our file - Notre référence*

## NOTICE

The quality of this microform is heavily dependent upon the quality of the original thesis submitted for microfilming. Every effort has been made to ensure the highest quality of reproduction possible.

If pages are missing, contact the university which granted the degree.

Some pages may have indistinct print especially if the original pages were typed with a poor typewriter ribbon or if the university sent us an inferior photocopy.

Reproduction in full or in part of this microform is governed by the Canadian Copyright Act, R.S.C. 1970, c. C-30, and subsequent amendments.

## AVIS

La qualité de cette microforme dépend grandement de la qualité de la thèse soumise au microfilmage. Nous avons tout fait pour assurer une qualité supérieure de reproduction.

S'il manque des pages, veuillez communiquer avec l'université qui a conféré le grade.

La qualité d'impression de certaines pages peut laisser à désirer, surtout si les pages originales ont été dactylographiées à l'aide d'un ruban usé ou si l'université nous a fait parvenir une photocopie de qualité inférieure.

La reproduction, même partielle, de cette microforme est soumise à la Loi canadienne sur le droit d'auteur, SRC 1970, c. C-30, et ses amendements subséquents.

Canada



**SERPENTINIZATION AND CARBONATIZATION  
OF TECTONIC MÉLANGES IN THE  
COY POND COMPLEX, CENTRAL NEWFOUNDLAND**

by

• Nicolai Adrian Timbal, Licenciante

A Thesis submitted in partial fulfillment  
of the requirements for the degree of  
Master of Science

Department of Earth Sciences  
Memorial University of Newfoundland





National Library  
of Canada

Acquisitions and  
Bibliographic Services Branch

395 Wellington Street  
Ottawa, Ontario  
K1A 0N4

Bibliothèque nationale  
du Canada

Direction des acquisitions et  
des services bibliographiques

395, rue Wellington  
Ottawa (Ontario)  
K1A 0N4

*Your file - Votre référence*

*Our file - Notre référence*

The author has granted an irrevocable non-exclusive licence allowing the National Library of Canada to reproduce, loan, distribute or sell copies of his/her thesis by any means and in any form or format, making this thesis available to interested persons.

L'auteur a accordé une licence irrévocable et non exclusive permettant à la Bibliothèque nationale du Canada de reproduire, prêter, distribuer ou vendre des copies de sa thèse de quelque manière et sous quelque forme que ce soit pour mettre des exemplaires de cette thèse à la disposition des personnes intéressées.

The author retains ownership of the copyright in his/her thesis. Neither the thesis nor substantial extracts from it may be printed or otherwise reproduced without his/her permission.

L'auteur conserve la propriété du droit d'auteur qui protège sa thèse. Ni la thèse ni des extraits substantiels de celle-ci ne doivent être imprimés ou autrement reproduits sans son autorisation.

ISBN 0-315-82636-3

Canada

## A B S T R A C T

Mount Cormack Terrane, an elliptical tectonic window in the Dunnage Zone of central Newfoundland, is a structural dome comprising a central zone of variably metamorphosed metasediments surrounded by remnants of several ophiolitic complexes including the Coy Pond Complex, the subject of this study. The ophiolite complexes have been interpreted to represent remnants of the early Paleozoic Iapetus ocean floor, which was obducted onto the continental margin of Gondwana.

The Coy Pond Complex, is an imbricated, but complete ophiolite which is oriented subvertically and dips and youngs outward from the tectonic window.

Analyses of relict olivines, pyroxenes and spinels in the Coy Pond Complex indicate that it has an arc-related petrogenesis.

The Coy Pond Complex is composed of two structural slices separated by two tectonic mélanges. From west to east the principal structural elements are: (i) basal structural slice composed of harzburgite and dunite; (ii) western tectonic mélange; (iii) central structural slice comprising pyroxenite, gabbro-diabase, pillow lava and sedimentary rocks; (iv) the eastern tectonic mélange.

Locally the basal structural slice is missing and its

place is taken by the mixed lithology slice, which is composed of exotic (i.e. non-ophiolitic) lithologies that were probably derived from the tectonically overlying and underlying units.

The tectonic mélanges, are composed of ultramafic fragments up to 2 m in longest diameter enveloped in an ultramafic matrix. They display evidence of brittle (fragments) and ductile (matrix) deformation and are interpreted to have formed during fault movement and emplacement of the ophiolite. On the basis of the lithologies of the fragments, the tectonic mélanges are interpreted to have formed from the transition zone (dunite) and upper part of the mantle tectonite (harzburgite).

Both fragments and matrix in the tectonic mélanges are extensively serpentized and variably carbonatized. Petrographic evidence indicates that serpentization initially involved hydration of the peridotite and formation of a pseudomorphic assemblage of lizardite ± brucite. Subsequently most of the original lizardite recrystallized to antigorite and to schistose serpentinite in the matrix. Veins of chrysotile are rare.

Carbonatization resulted in replacement firstly of brucite by magnesite, and subsequently of the serpentine assemblages (lizardite and/or antigorite) by magnesite ± talc. Later, quartz-magnesite formed by replacement of talc or by



breakdown of remaining lizardite. These assemblages indicate a progressive increase in  $\text{XCO}_2$  in the fluid phase during formation of the metamorphic assemblages with temperatures  $<300^\circ\text{C}$  for quartz-magnesite and  $>300^\circ\text{C}$  for talc-magnesite assemblages.

Carbon and oxygen isotopic compositions of magnesite coexisting with lizardite, antigorite, talc and quartz were measured from the eastern and western tectonic mélanges.  $\delta^{18}\text{O}$  values of magnesite vary only slightly, from 12.3 to 17.5, with higher values occurring in the quartz-magnesite assemblages.  $\delta^{13}\text{C}$  values show considerable variation in isotopic composition from -4.2 to -9.1 for magnesite associated with lizardite and talc, from -10.8 to -13.6 for magnesite associated with antigorite, and from -11.9 to -20.4 for magnesite associated with quartz (in the western tectonic mélange). These data are interpreted to indicate that the different magnesite assemblages formed from different carbon reservoirs, with magnesite associated with lizardite and talc having an oceanic and/or average crustal carbon isotopic signature, whereas magnesite associated with antigorite and quartz shows a progressively more organic (continental) carbon isotopic signature.

Structural, metamorphic and isotopic information have been used to construct a tectonic model for the formation and

evolution of the tectonic mélanges, which involves several stages.

(a) Early serpentinization of dunites during detachment of the ophiolitic nappe.

(b) Initiation of the formation of the tectonic mélanges during imbrication? and obduction of the ophiolite nappe onto the continental margin, together with partial carbonatization. At this stage magnesite associated with lizardite and with talc was formed.

(c) Emplacement of Coy Pond ophiolite on top of the continental margin, consisting of Spruce Brook Formation.

(d) Extension of the continental margin induced heat transfer into the tectonically underlying sediments (Spruce Brook Formation) which were affected by a low-P metamorphism.

(e) This induced isostatic instability in the lower crust, with mechanical and thermal doming of the Mount Cormack Terrane, followed by renewed imbrication and final emplacement of the Coy Pond Complex, by extensional faulting, into its present subvertical orientation. It is assumed that the formation of the tectonic mélanges was concluded during the extensional faulting, when magnesite associated with antigorite and with quartz assemblages was formed in equilibrium with fluids carrying carbon of organic origin.

## ACKNOWLEDGEMENTS

I would like to acknowledge the guidance of several people, without whose help and support this project could not have been completed.

It is a great pleasure to thank my supervisors, Toby Rivers and Mark Wilson. With great courage they accepted me as a graduate student and offered guidance throughout this study. During these years I have greatly benefitted from their knowledge, hospitality and financial generosity. With sympathy and humour I was introduced to mysteries of Newfoundland geology, isotopes and the English language.

Steve Colman-Sadd generously suggested that a study of the Coy Pond Complex would be fruitful and made freely available his report (which was indispensable) maps, equipment and advice.

John Tuach, who had previously given a financial boost to my Canadian life through employment, helped me again with his drafting facilities.

Thanks to the School of Graduate Studies, Memorial University of Newfoundland for its generous graduate fellowship, and also to Faculty and Staff at the Department of Earth Sciences at the Memorial University for help in important aspects of this study.

Thanks to David O'Hanley who during a chance meeting



greatly encouraged me, and to all my colleagues who have helped me in learning computer skills: Adrian O., Dennis B., Don F., Flemming M., Jim C., Dave E., Jim W., Jahan R., Adam S., Jeroen G., and Sung.

A special thanks to Jeana and Monica who were neglected, but fully supported me for all these years.

## TABLE OF CONTENTS

ABSTRACT.....	ii
ACKNOWLEDGEMENTS.....	vi
LIST OF TABLES.....	xii
LIST OF FIGURES.....	xiii

### Chapter 1 INTRODUCTION

1.1 Subject and scope of the thesis.....	1
1.2 Ophiolites in Newfoundland and regional setting.....	7
1.3 Location, access, description of the study area.....	8
1.4 Previous work.....	9
1.5 Present investigation.....	11

### Chapter 2 REGIONAL GEOLOGY

2.1 Mount Cormack Terrane.....	12
2.2 Pipestone Pond Complex.....	13
2.3 Coy Pond Complex.....	14
2.4 Great Bend Complex .....	17
2.5 Baie d'Espoir Group.....	18
2.6 Partridgeberry Hills Granite.....	18
2.7 Age constraints.....	18

### Chapter 3 STRUCTURAL FRAMEWORK

3.1 Imbricated structure of the Coy Pond Complex.....	21
3.1.1 Basal slice.....	26
3.1.1.1 Asthenospheric structures.....	26
3.1.1.2 Lithospheric structures.....	28
3.1.2 Mixed lithology slice.....	30
3.1.3 Central slice.....	31
3.1.4 Tectonic mélanges.....	32
3.1.4.1 General statement.....	32
3.1.4.2 Composition and characteristics of the Coy Pond tectonic mélanges.....	34
3.2 Serpentinite deformation - experimental data.....	38
3.3 Summary .....	40

## Chapter 4 THE MANTLE TECTONITES

4.1. Introduction.....	43
4.2. Rock classification and textures.....	43
4.3. Distribution and contacts.....	46
4.4. Harzburgite.....	47
4.4.1. Petrography and microstructures.....	48
4.4.2. Discussion and conclusions.....	56
4.5. Dunite.....	59
4.5.1. Petrography and microstructures.....	60
4.5.2. Discussion and conclusions.....	63
4.6. Pyroxenite dikes.....	64
4.7. Discussion and conclusions.....	65

## Chapter 5 THE TRANSITION ZONE

5.1. Introduction.....	67
5.2. Composition.....	67
5.3. Distribution and contacts .....	70
5.4. Petrography .....	72
5.4.1. Dunite.....	72
5.4.2. Clinopyroxenite.....	72
5.4.3. Rodingite.....	78
5.5. Conclusions.....	78

## Chapter 6 THE TECTONIC MÉLANGES

6.1. Introduction.....	83
6.2. MÉLANGE FRAGMENTS.....	84
6.2.1 Serpentinite fragments with pseudomorphic textures.....	85
6.2.2 Serpentinite fragments with non-pseudomorphic textures.....	108
6.2.3 Talc-magnesite fragments.....	114
6.3. MATRIX OF TECTONIC MÉLANGES.....	120
6.3.1 Schistose serpentinite matrix.....	125
6.3.2 Brecciated serpentinite matrix.....	134
6.3.3 Talc-magnesite matrix.....	137
6.3.4 Chlorite blackwall rocks.....	146
6.4. QUARTZ-MAGNESITE ASSEMBLAGE	
6.4.1 Introduction.....	147
6.4.2 Petrographic description.....	152
6.4.3 Conclusions on matrix and quartz-magnesite rocks.....	162



6.5 MÉLANGE BLOCKS.....	165
6.5.1 Pyroxenite blocks.....	166
6.5.2 Clastic metasedimentary blocks.....	166
6.5.3 Volcanogenic metasedimentary blocks.....	166

#### Chapter 7

##### MIXED LITHOLOGY SLICE

7.1 Introduction.....	172
7.2 Metabasic and intermediate volcanic/ hypabyssal ? rocks.....	172
7.3 Pyroclastic rocks.....	177
7.4 Actinolite epidote schist.....	180
7.5 Metasedimentary schist.....	183
7.6 Origin of rocks in Mixed Lithology Slice.....	188

#### Chapter 8

##### MINERAL CHEMISTRY

8.1 Introduction.....	189
8.2 Primary minerals.....	190
8.2.1 Olivine.....	190
8.2.2 Orthopyroxene.....	193
8.2.3 Clinopyroxene.....	196
8.2.4 Spinel.....	197
8.2.5 Conclusions.....	204
8.3 Secondary minerals .....	205
8.3.1 Serpentine minerals.....	209
8.3.2 Brucite.....	211
8.3.3 Talc.....	212
8.3.4 Magnesite.....	212
8.3.5 Opaque phases.....	219
8.3.6 Conclusions.....	219

#### Chapter 9

##### PHASE EQUILIBRIA AND METAMORPHISM OF THE TECTONIC MÉLANGE

9.1 Introduction.....	221
9.2 Serpentinization of peridotites.....	222
9.3 Carbonatization of serpentinite.....	231
9.4 Recrystallization of serpentine.....	235
9.5 Conclusions.....	239

Chapter 10  
CARBON ISOTOPE GEOCHEMISTRY OF MAGNESITE  
IN THE TECTONIC MÉLANGE

10.1	Purpose and theoretical considerations.....	242
10.2	Carbonate and graphite-bearing lithologies.....	248
10.3	Previous isotopic studies on magnesite.....	250
10.4	Analytical techniques.....	253
10.5	Results, interpretation and discussion.....	254
10.5.1	Temperature constraints .....	261
10.5.2	Constraints on fluid composition.....	269
10.5.3	Differences between the eastern and the western tectonic mélanges.....	278
10.5.4	Other carbonates.....	280
10.6	Conclusions.....	281

Chapter 11  
GEOTECTONIC MODEL FOR THE FORMATION  
OF THE COY POND TECTONIC MÉLANGES

.....286

REFERENCES

.....302

APPENDICES

Appendix 1	Serpentine pseudomorphic textures.....	315
Appendix 2(A)	Microanalyser characteristics.....	317
Appendix 2(B)	Correction for magnesite analyses containing serpentine inclusions.....	317
Appendix 2(C)	X-ray powder diffraction procedure.....	319
Appendix 3	Microprobe analyses of olivine (4p).....	320
Appendix 4	Microprobe analyses of pyroxenes (5p)....	324
Appendix 5	Microprobe analyses of Cr-spinel in harzburgite (3p).....	329
Appendix 6	Microprobe analyses of Cr-spinel in dunite (3p).....	332
Appendix 7	Microprobe analyses of Cr-spinel in pyroxenite (2p).....	335
Appendix 8	Microprobe analyses of Cr-spinel in mélange assemblages (3p).....	337
Appendix 9	Microprobe analyses of serpentine (7p)...	340
Appendix 10	Microprobe analyses of magnesite in serpentine (4p).....	347
Appendix 11	Microprobe analyses of magnesite in talc-magnesite (2p).....	351
Appendix 12	Microprobe analyses of magnesite in quartz-magnesite (4p).....	353

## LIST OF TABLES

Table 8.1	Electron microprobe analyses of olivines ...	191
Table 8.2	Electron microprobe analyses of pyroxenes...	194
Table 8.3	Calculated compositions of Cr-spinels.....	198
Table 8.4	Electron microprobe analyses of serpentines.	206
Table 8.5	Average magnesite analyses in different assemblages and calculated oxides (in text).	214
Table 8.6	Electron microprobe analyses of magnesite...	215
Table 10.1	Fractionation factors between alkali-earth carbonates and water (in text).....	247
Table 10.2	Isotopic composition of magnesite from Coy Pond mélanges.....	255
Table 10.3	Isotopic composition of carbonates other than magnesite.....	256
Table 10.4	Oxygen isotopic composition of waters calculated to be in equilibrium with magnesite.....	270



## LIST OF FIGURES

Fig 1.1	Simplified tectonic map of Newfoundland.....	3
Fig 1.2	Geologic map of Mount Cormack Terrane .....	5
Fig 2.1	Geological map and cross-section of the Coy Pond Complex.....	16
Fig 3.1	Geological map of the western tectonic mélange.	23
Fig 3.2	Geological map of the eastern tectonic mélange.	25
Fig 3.3	Block diagram of the tectonic mélange.....	36
Fig 4.1	IUGS nomenclature for ultramafic rocks.....	45
Fig 4.2	Representative view of harzburgite and dunite..	45
Fig 4.3	Harzburgite with porphyroclastic texture.....	51
Fig 4.4	Harzburgite with porphyroclastic and neoblastic texture.....	51
Fig 4.5	Harzburgite with porphyroclastic texture.....	53
Fig 4.6	Harzburgite with porphyroclastic texture.....	53
Fig 4.7	Detail of harzburgite with porphyroclastic texture.....	55
Fig 4.8	Harzburgite with porphyroclastic to protomylonitic texture.....	55
Fig 4.9	Harzburgite with mylonitic texture.....	58
Fig 4.10	Harzburgite with protomylonitic texture.....	58
Fig 4.11	Field photograph of dunite in harzburgite.....	62
Fig 4.12	Field photograph foliated dunite .....	62
Fig 5.1	Field photograph of pyroxenite layering .....	69
Fig 5.2	Photomicrograph of coarse grained pyroxenite...	69
Fig 5.3	Photomicrograph of adcumulus texture in clinopyroxene.....	75
Fig 5.4	Photomicrograph showing low grade metamorphism in pyroxenite .....	75
Fig 5.5	Photomicrograph of serpentized olivine in clinopyroxenite .....	77
Fig 5.6	Photomicrograph of partial rodingitization of clinopyroxenite.....	77
Fig 5.7	Photomicrograph of completely rodingitized rock.....	80
Fig 6.1	Schematic representation of lizardite pseudomorphic textures after olivine and orthopyroxene .....	88
Fig 6.2	Serpentinized dunite fragment in mélange .....	91
Fig 6.3	Serpentinized dunite fragment in tectonic mélange with pseudomorphic $\gamma$ -mesh texture....	91

Fig 6.4	Photomicrograph representing banded growth or curtain-like texture.....	94
Fig 6.5	Photomicrograph of pure hourglass texture.....	94
Fig 6.6	Detail of 6.5.....	97
Fig 6.7	Serpentinized dunite fragment in mélange with hourglass texture.....	97
Fig 6.8	Serpentinite fragment with hourglass texture..	99
Fig 6.9	Same as 6.8; plane polarized light.....	99
Fig 6.10	Photomicrograph of partially serpentinized harzburgite fragment .....	102
Fig 6.11	Incompletely serpentinized harzburgite fragment in tectonic mélange.....	102
Fig 6.12	Photomicrograph of serpentinized harzburgite fragment and bastite types.....	104
Fig 6.13	Same as Fig 6.12 with gypsum plate .....	104
Fig 6.14	Completely serpentinized harzburgite .....	106
Fig 6.15	Photomicrograph of carbonatized serpentinized dunite.....	106
Fig 6.16	Photomicrograph of serpentinite with non-pseudomorphic texture.....	110
Fig 6.17	Photomicrograph of serpentinite fragment with pseudomorphic and non-pseudomorphic texture..	110
Fig 6.18	Partially carbonatized serpentinite with interpenetrating texture.....	112
Fig 6.19	Photomicrograph of serpentinite with interlocking texture.....	112
Fig 6.20	Photograph of talc-magnesite fragments .....	116
Fig 6.21	Photomicrograph of talc-magnesite and relict antigorite.....	116
Fig 6.22	Photomicrograph of talc-magnesite .....	119
Fig 6.23	Talc-magnesite fragment in tectonic mélange..	119
Fig 6.24	Field photograph of talc-magnesite matrix ...	122
Fig 6.25	Field view of tectonic mélange with sheared serpentinite matrix and elongated serpentinite fragment .....	122
Fig 6.26	Field photograph showing chaotically distributed fragments in matrix.....	124
Fig 6.27	Photograph of schistose serpentinite matrix .	124
Fig 6.28	Photomicrograph of schistose serpentinite....	128
Fig 6.29	Photomicrograph of schistose serpentinite....	128
Fig 6.30	Photomicrograph showing matrix foliation ....	130
Fig 6.31	Partially recrystallized serpentinite.....	130
Fig 6.32	Photomicrograph of schistose serpentinite and antigorite .....	132
Fig 6.33	Photomicrograph of mélange matrix illustrating shear sense indicators.....	132
Fig 6.34	Photograph of slab of tectonic mélange with small serpentinite fragments .....	136

Fig 6.35	Field photograph showing talc-magnesite matrix .....	136
Fig 6.36	Talc-magnesite matrix of the mélange .....	139
Fig 6.37	Photograph of slab of talc-magnesite matrix .....	139
Fig 6.38	Photomicrograph of talc-magnesite matrix ....	142
Fig 6.39	Photomicrograph showing large skeletal cryptocrystalline magnesite .....	142
Fig 6.40	Detail of talc-magnesite matrix in tectonic mélange.....	144
Fig 6.41	Photomicrograph of chloritic blackwall .....	144
Fig 6.42	Photograph of quartz-magnesite outcrop .....	149
Fig 6.43	Photograph of quartz-magnesite matrix .....	149
Fig 6.44	Photograph of quartz-magnesite outcrop .....	151
Fig 6.45	Photograph of quartz-magnesite .....	151
Fig 6.46	Quartz-magnesite matrix with foliation .....	155
Fig 6.47	Photomicrograph of quartz-magnesite .....	155
Fig 6.48	Detail of quartz-magnesite .....	157
Fig 6.49	General view of quartz-magnesite .....	157
Fig 6.50	Photomicrograph showing interstitial quartz and xenoblastic cryptocrystalline magnesite.....	159
Fig 6.51	Foliated quartz-magnesite matrix .....	159
Fig 6.52	Field photograph of a massive coarse-grained clinopyroxenite block.....	168
Fig 6.53	Photomicrograph showing metasandstone .....	168
Fig 6.54	Photomicrograph showing fine grained volcanogenic metasediment .....	171
Fig 6.55	Detail of figure 6.54 .....	171
Fig 7.1	Photomicrograph of low grade intermediate volcanic rock .....	174
Fig 7.2	Low grade, fine-grained basic volcanic .....	174
Fig 7.3	Metamorphosed basic or intermediate rock ....	176
Fig 7.4	Photomicrograph of weakly metamorphosed basic volcanic rock.....	176
Fig 7.5	Photomicrograph showing lapilli in microcrystalline groundmass.....	179
Fig 7.6	Photomicrograph representing shards .....	179
Fig 7.7	Strongly foliated actinolite-epidose schist with granonematoblastic texture.....	182
Fig 7.8	Detail of 7.7. ....	182
Fig 7.9	Fine grained metasedimentary rock with granolepidoblastic texture.....	185
Fig 7.10	Photomicrograph of strongly foliated and retrograde metamorphic garnetiferous schist.....	187
Fig 7.11	Same as 7.10; crossed polars.....	187
Fig 8.1	Compositions of Cr-spinel from Coy Pond .....	202

Fig 9.1	Equilibrium curves for reaction (1) .....	224
Figs 9.2	Schematic T-XCO <sub>2</sub> diagram .....	227
Fig 10.1	Graph showing the variation of the equilibrium fractionation factor with ionic radius of alkali-earth carbonates at various temperatures.....	245
Fig 10.2	Isotopic fractionation curve for magnesite-water constructed from Fig 10.1...	245
Fig 10.3	$\delta^{18}\text{O}$ vs $\delta^{13}\text{C}$ of magnesite in different mineral assemblages in tectonic mélanges ...	259
Figs 10.4	Phase diagram showing the isobaric equilibrium curves in the model system MgO-SiO <sub>2</sub> -H <sub>2</sub> O-CO <sub>2</sub> .....	262
Fig 10.5	$\delta^{18}\text{O}$ vs $\delta^{13}\text{C}$ diagram showing fields of magnesite compositions in mélanges, and the $\delta^{13}\text{C}$ ranges of possible carbon sources.....	272
Fig 10.6	Isotope distribution of oxygen and carbon in magnesite from principal mineral assemblages .....	283
Fig 10.7	Chart representing evolution of $\delta^{13}\text{C}$ in magnesite in different mineral assemblages in tectonic mélanges .....	284
Fig 11.1	Reconstructed stratigraphic column of the Coy Pond Ophiolite complex and evolution model for the tectonic mélanges ..	290
Fig 11.2	Schematic diagram showing the formation and obduction of the Coy Pond Complex onto the Gander Zone continental margin.....	294
Fig 11.3	The evolution of the Mount Cormack Terrane and the Coy Pond Complex after obduction of ophiolite nappe onto the continental margin.....	297
Sample location map - western tectonic mélange (in pocket)		
Sample location map - eastern tectonic mélange (in pocket)		

## Chapter 1

### INTRODUCTION

#### 1.1 Subject and purpose of the thesis

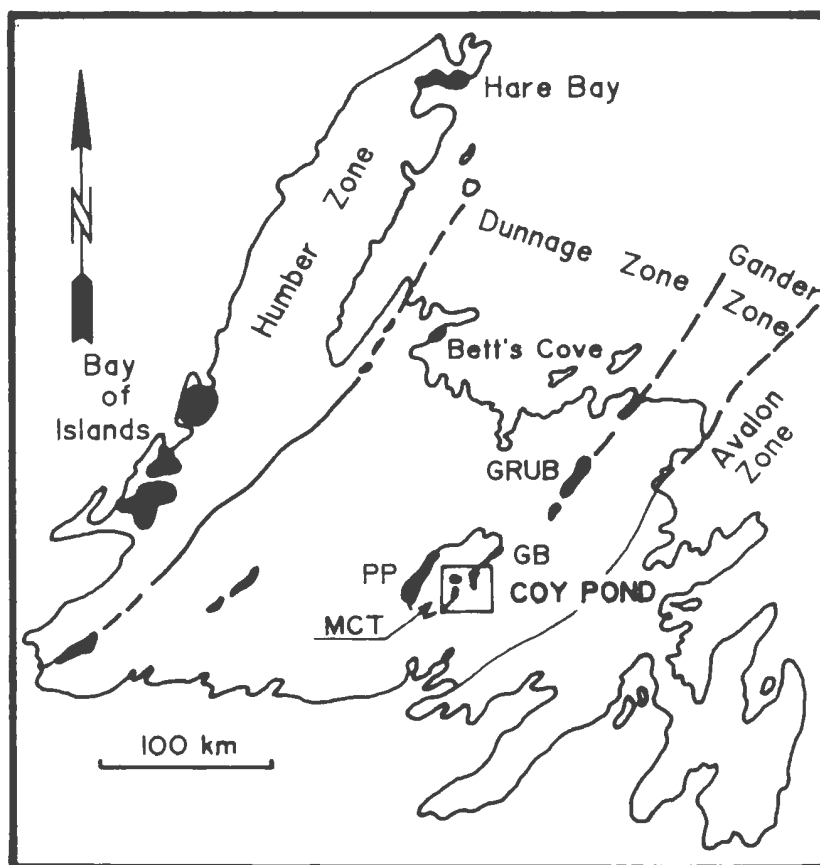
This thesis is concerned with the deformation and associated low grade metamorphism of the ultramafic section of an obducted ophiolite. This aspect of the evolution of ophiolite complexes has attracted much less attention than for example the study of asthenospheric flow in the mantle tectonite sections of ophiolites, or studies of the high grade metamorphism of the crustal sections of ophiolite complexes. The area chosen for this study is the Coy Pond Ophiolite Complex in Central Newfoundland (Fig 1.1), a little known body (Fig 1.2) that tectonically overlies the metasedimentary Spruce Brook Formation (Colman-Sadd, 1985).

During the 1988 field season, two formerly unrecognized tectonic mélanges were mapped in the Coy Pond Ophiolite Complex, which are inferred to have formed during transport and/or emplacement of the ophiolite onto the Palaeozoic continental margin. The tectonic mélanges are interpreted to mark the sites of major faults, where components of the ophiolite with and without the underlying sedimentary substrate and overlying sedimentary cover were intimately mixed.

This study focuses on the tectonic mélanges for two

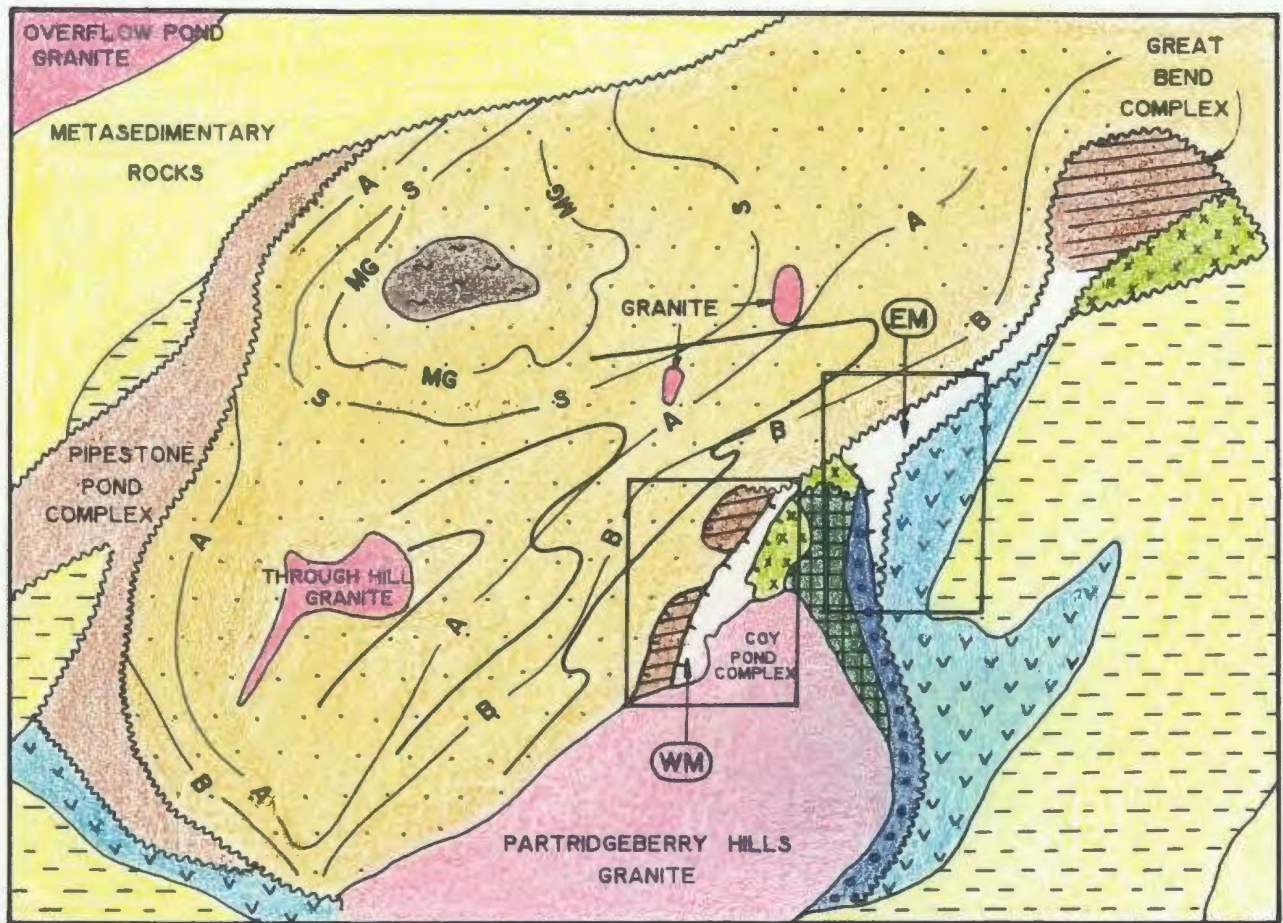
**Fig 1.1** Simplified tectonic map of Newfoundland showing the four tectonic zones (after Williams, 1984), and the location of the main ophiolite complexes. Box represents the Coy Pond area. Abbreviations:

GRUB = Gander River Ultramafic Belt;  
PP = Pipestone Pond ophiolite complex;  
MCT = Mount Cormack Terrane;  
GB = Great Bend ophiolite complex;



**Fig 1.2 Geological map of Mount Cormack Terrane**  
(modified after Colman-Sadd, 1985). Boxes represent the  
locations of maps of the western tectonic mélange (WM) and  
the eastern tectonic mélange (EM). Abbreviations:  
A = andalusite isograd;  
B = biotite isograd;  
S = sillimanite isograd;  
MG = beginning of migmatization;  
No lithologies are indicated for EM and WM; see text for  
discussion





#### OPHIOLITE COMPLEXES

- Pillow lava and sedimentary rocks
- Gabbro and diabase
- Pyroxenite
- Harzburgite and dunite
- Volcanics
- Sediments

#### MOUNT CORMACK TERRANE

- Spruce Brook Formation
- Amphibolite
- High angle fault
- Fault
- Form lines of major folds

reasons; firstly because similar feature have not been widely recorded and interpreted in other ophiolite complexes, and secondly because metamorphic and deformational effects are particularly well displayed in these units.

Detailed petrographic and mineral chemical studies were conducted on both tectonic *mélange* units, and on the mantle tectonite and the pyroxenite of the transition zone, both of which supplied material that was incorporated in the tectonic *mélanges*. Other units of the ophiolite complex have been studied in less detail.

The purpose of the study is to obtain information on the metamorphism and deformation of the ophiolite complex during and after its formation and subsequent obduction and emplacement onto the continental margin. To this end, the structure and microstructure of the tectonic *mélanges* have been utilized as a framework for detailed studies of the mineralogy, petrography and petrology of their constituent fragments and matrix, which have yielded a rich history concerning the evolution of the complex. The petrological data were subsequently used as the foundation for a stable isotope (C,O) study of fluids involved in the metamorphic reactions.

## 1.2 Ophiolites in Newfoundland and the regional setting

The closure of the Iapetus Ocean (Harland and Gayer, 1972) occurred during the early Palaeozoic, at which time numerous ophiolites were emplaced within the Appalachian/Caledonian orogen (Williams, 1964; Wilson, 1966; Dewey and Bird, 1970). The island of Newfoundland, situated in the northeastern part of the Appalachian orogen, is well known for the occurrence of several complete ophiolite suites (Fig 1.1), the better known of which are located in the western part of the island (Stevens, 1970). These slices of oceanic lithosphere were detached from the ocean floor, and obducted both westwards and eastwards. The former were obducted onto the Humber Zone (Fig 1.1) with its Grenvillian basement, together composing the Palaeozoic eastern margin of North America (Stevens, 1970). The latter were obducted onto the eastern margin of Iapetus, which was the continent of Gondwanaland, represented locally by the Avalon Zone, and its miogeoclinal prism of turbidites to the west known as the Gander Zone.

Between the two Palaeozoic continental margins, remnants of which are currently situated at the eastern and western extremities of Newfoundland, is the Dunnage Zone (Fig 1.1). The Dunnage Zone comprises remnants of Iapetan oceanic crust and associated arc volcanic sequences, which during ocean

closure were thrust both westward on top of Humber Zone (e.g. Bay of Islands Complex) and eastward on top of Gander Zone (eg. Coy Pond complex). Gander Zone, which is composed of remnants of a continentally-derived Paleozoic sedimentary wedge (Colman-Sadd et al., 1991), is predominantly situated to the east of the Dunnage Zone, but also crops out as several autochthonous tectonic windows through the Dunnage Zone.

One of these tectonic windows is the Mount Cormack Terrane, which is surrounded by several little known ophiolite bodies. On its western side is located the Pipestone Pond Ophiolite Complex, on its eastern side the Coy Pond Complex and its northeasterly prolongation, the Great Bend Complex (Figs 1.1 and 1.2).

### 1.3 Location, access, description of the study area

The Coy Pond Ophiolite Complex is located in central Newfoundland about half way between Grand Falls and Milltown. The lines of longitude of 55°40'W and latitude of 48°25'N intersect in the central part of the ophiolite body. The power transmission line between Baie d'Espoir and Grand Falls is situated about 2 to 4 km to the west of the ophiolite complex, and the Bishop Falls-Baie d'Espoir highway is situated about 10 km to the east of it.

Access into the western part of the ophiolite body during the summer of 1989 was by helicopter from Milltown, with exit from the eastern part of the area by car, using a recently cut woods road. Apart from this woods road (which in the summer of 1991 was only partially usable) there are no other roads in the area. The main drainage system in the area is the Northwest Gander River, which flows approximately northward along the strike of the ultramafic units of the ophiolite, then turns northeastward along the faulted contact between the Spruce Brook Formation and the Coy Pond and Great Bend Complexes. Coy Pond and Huxter Pond are the biggest ponds in the area.

The topography of the area has an average elevation between 550 to 600 m for the ophiolite units, higher for the pyroxenite (650 m) and lower for the eastern tectonic mélanges (about 500 m). In the northern part of the area, in the tectonically underlying Spruce Brook Formation, the relief is about 400 m.

#### 1.4 Previous work

According to Colman-Sadd (1985), the first recorded geological observations on ultramafic rocks in the area were made by Cormack in 1823, who noted the presence of ultramafic rocks at Pipestone Pond. The Coy Pond Complex was

discovered by Howley in 1876. In the first half of this century, both the Pipestone Pond and Coy Pond complexes were explored for chromite occurrences described by Snelgrove in 1934. The ultramafic part of the Coy Pond Complex was mapped by Grady in 1953 (cited by Colman-Sadd, 1985), as part of a search by Newfoundland and Labrador Corporation for asbestos. Asbestos Mines Co. (1963) drilled six holes in the western tectonic mélangé with poor results, and H. Tibo and Tasu Resources prospected for chromite in 1981. The granites in the area were examined by Elias (1981) and Elias and Strong (1982). Detailed mapping in the Coy Pond Ophiolite Complex and surroundings was conducted by Colman-Sadd (1985) who described the units of the Coy Pond Ophiolite Complex. The two tectonic mélanges in the ophiolitic complex were appropriately described as "shear zones". The tectonics of the Coy Pond Ophiolite and its relation to the Gander Zone were discussed by Colman-Sadd and Swinden (1985), who were the first to propose the existence of a tectonic window through the Dunnage Zone, exposing rocks of the underlying Gander Zone. Analysis and age determination of a single zircon fraction from the Coy Pond Complex was conducted by Dunning and Krogh (1985).

### 1.5 Present investigation

This thesis is based on field work conducted during the summer of 1989 and subsequent examination of the sampled material. During the field work, about six weeks were spent mapping the western tectonic mélangé and the ultramafic units of the Coy Pond Complex and about two weeks mapping the eastern tectonic mélangé. In total about 470 stations were established and about 350 samples collected. Petrographic examination of about 160 thin sections was carried out in order to establish stable mineral assemblages, and the various paragenetic sequences in ultramafic rocks throughout the area. Microprobe analyses of the principal minerals were conducted on about 40 polished thin sections at the microprobe facility at Memorial University. After X-ray analyses of mineral separates to confirm sample purity, carbon and oxygen isotope compositions of magnesite and other carbonates were determined in the stable isotope lab at Memorial University.

## Chapter 2

### REGIONAL GEOLOGY

#### 2.1 Mount Cormack Terrane

The Mount Cormack Terrane is an elliptical tectonic window about 60x25 km surrounded by three ophiolite complexes, the Pipestone Pond, Coy Pond and Great Bend Complexes (Figs 1.1 and 1.2). Mount Cormack Terrane is underlain by metasediments of the Spruce Brook Formation, which range in metamorphic grade from greenschist facies near the margin of the terrane to upper amphibolitic facies in two locations near the center, where they are intruded by the Through Hill Granite (Colman-Sadd, 1985). The Spruce Brook Formation comprises metamorphosed interbanded quartz-rich psammitic and pelitic rocks that have been correlated with similar rocks in the Gander Group occurring in the eastern Gander Zone (Colman-Sadd et al., 1992). Because of the gradational nature of the contacts between pelitic and psammitic layers and the general uniformity of rock composition, clastic input into the unit is considered to have been derived from a single continental source (Colman-Sadd, 1985). The age of the Spruce Brook Formation has recently been discussed by Colman-Sadd et al. (1992), who concluded on the basis of fossil and radiometric ages of detrital grains that it was deposited between Late



Precambrian and Late Arenig time.

The top of the Spruce Brook Formation cannot be defined in the study area, as all contacts with the overlying ultramafic units are faulted. The Spruce Brook Formation has been folded into a dome exposing rocks of low metamorphic grade at the margins (chlorite zone) and high metamorphic grade at the center (sillimanite-K feldspar zone), where migmatization is common.

The Through Hill Granite intrusions occur in Through Hill and in several other places around the metamorphic core of the Mount Cormack Terrane. Through Hill Granite is an aluminous S-type granite that was probably produced by anatexis of metasediments of Spruce Brook Formation at the peak of metamorphism (Colman-Sadd et al., 1992).

## 2.2 Pipestone Pond Complex

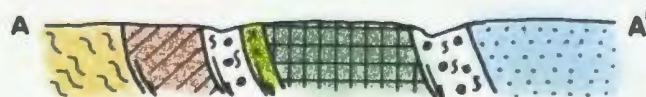
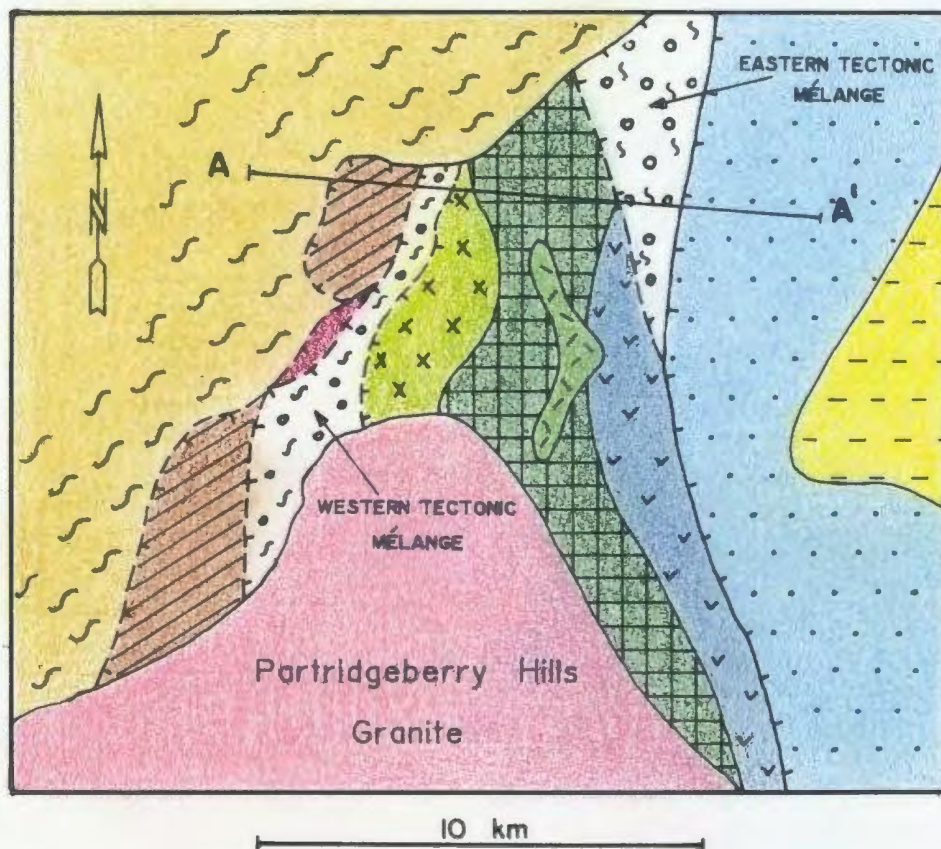
Pipestone Pond Complex, situated on the western side of Mount Cormack Terrane (Figs 1.1 and 1.2), is a complete but disrupted ophiolite, consisting of westward facing sequence of mafic and ultramafic rocks (Swinden, 1988). In an east-west cross-section, the following sequence occurs: metasediments of Spruce Brook Formation tectonically overlain by harzburgite and minor dunite that pass westward into pyroxenite, gabbro with diabase and plagiogranite and

rocks of the Baie d'Espoir Group. The ophiolite is in tectonic contact with the underlying Spruce Brook Formation and with the overlying Baie d'Espoir Group. The ophiolite sequence is disrupted by internal faulting and no section contains the complete ophiolitic stratigraphy (Swinden, 1988).


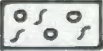
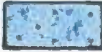










### 2.3 Coy Pond Complex

Situated on the eastern site of the Mount Cormack Terrane (Figs 1.2 and 2.1), the Coy Pond Ophiolite Complex is about 7x7 km in size with a roughly rectangular shape, and lies in tectonic contact with all the surrounding units except for an inferred intrusive contact (Colman-Sadd 1985; Colman-Sadd et al., 1992) with the Partridgeberry Hills Granite in the south (Fig 2.1). To the west and north, it tectonically overlies metasediments of the Spruce Brook Formation, and to the east it is in tectonic contact with Baie d'Espoir Group. It comprises an imbricated but complete ophiolite stratigraphy in a subvertical orientation that faces outwards, with the ultramafic unit at the base (similar to the Pipestone Pond Complex). In a west-east cross-section (Fig 2.2) the following units occur: (i) harzburgite and dunite tectonite, (ii) western tectonic mélange, (iii) layered pyroxenite, dunite and rodingite of the transition

**Fig 2.1** Geological map and cross-section A-A' of the Coy  
Pond Complex (partly after Colman-Sadd, 1985).



## LEGEND

 Davidsville Group	 Ophiolitic tectonic mélange
 Baie D'Espoir Group	 Harzburgite and dunite
 Pillow lava	 Spruce Brook : metasedimentary rocks
 Gabbro and diabase	 Fault (inferred)
 Trondhjemite	 High angle fault
 Pyroxenite	 Geologic boundary
 Mixed lithologies slice	

zone, (iv) gabbro and diabase, (v) trondhjemite and keratophyre, (vi) pillow lavas, (vii) eastern tectonic mélange, and (viii) Baie d'Espoir Group.

#### 2.4 Great Bend Complex

The Great Bend ophiolite (Fig 1.1 and 1.2) is an ultramafic body about 8-10 km in diameter situated on the Northwest Gander River just upstream of its confluence with Great Gull River, near the Bay d'Espoir Highway. It is composed of ultramafic lithologies such as dunite, harzburgite and pyroxenite together with gabbroic rocks (Zwicker and Strong, 1986). On account of its roughly circular shape, lithological zonation and inferred intrusive contacts, the Great Bend Complex was previously considered to be a classic example of an intrusive mantle diapir (Stevens and Strong, 1974; Malpas and Strong, 1974). However, recent mapping in the area has shown the existence of a basal dynamothermal aureole, composed of mylonitic gabbro and amphibolite schist (Dickson, 1992), implying that, as with Coy Pond and Pipestone Pond Complexes, it is part of an ophiolite complex.

The Great Bend and Coy Pond Complexes, are linked along the Northwest Gander river by a narrow strip of intensely tectonized and carbonatized ultramafic rocks similar in many

respects to the eastern tectonic mélange of the Coy Pond Complex.

## 2.5 Baie d'Espoir Group

At its eastern boundary, the Coy Pond Complex is in fault contact with volcano-sedimentary rocks of the Baie d'Espoir Group (Fig 2.1). The unit, which is widely exposed in south-central Newfoundland, is dominated by sandstone, siltstone and phyllite, but east of Coy Pond it comprises principally metavolcanics of intermediate to felsic composition (Colman-Sadd, 1985).

## 2.6 Partridgeberry Hills Granite

Situated to the south of the Coy Pond Complex (Fig 2.1), the Partridgeberry Hills Granite underlies an area of about 270 square kilometers. It is a biotite and biotite-muscovite granite that is widely chloritized. A silica-rich phase crops out near Burnt Hill and in the Partridgeberry Hills (Colman-Sadd, 1985).

## 2.7 Age constraints

The following age constraints have recently been

established.

(i) The Spruce Brook Formation is older than Llanvirn-Llandeilo, on the basis of a late Arenig age determination from fossils in an unconformably overlying limestone conglomerate and it is probably younger than latest Precambrian (Colman-Sadd et al., 1992).

(ii) The Through Hills Granite, which intrudes the Spruce Brook Formation in the south-central part of Mount Cormack Terrane, is considered to have formed by anatexis during the regional metamorphism. Its crystallization age was determined to be  $464 \pm 4/-3$  Ma by U/Pb (zircon) geochronology (Colman-Sadd et al., 1992).

(iii) The Mount Cormack Migmatite Complex is situated in north-central part of the Mount Cormack Terrane, where partial melting of the Spruce Brook Formation occurred during the peak of the regional metamorphism. U/Pb age determinations on monazite fractions from leucosomes have yielded an age of  $465 \pm 2$  Ma (Colman-Sadd et al., 1992), which overlap with the age of the Through Hill Granite.

(iv) The Coy Pond Complex has a minimum age of 489 Ma (Pb/Pb age) based on one single zircon fraction from trondhjemite (Dunning and Krogh, 1985).

(v) The Pipestone Pond Complex formed  $494 \pm 3/-2$  Ma ago based on a U/Pb (zircon) age of the intruding trondhjemite (Dunning and Krogh, 1985).

(vi) Two zircon fractions from a distinctive quartz-plagioclase porphyry unit known as the Twillick Group Member of the Baie d'Espoir Group (Colman-Sadd et al., 1992), have yielded an age of  $468 \pm 2$  Ma. This unit, which crops out as a narrow strip about 70 km long, is mostly enclosed in the Baie d'Espoir Group, but its northwestern end is considered concordant with the Gander Group (Blackwood, 1983).

(vii) Coarse-grained and unfoliated microcline porphyritic biotite granite representing the Partridgeberry Hills Granite, has been dated of  $474 \pm 6/-3$  by the U/Pb zircon method (Colman-Sadd et al., 1992).



## Chapter 3

### STRUCTURAL FRAMEWORK

#### 3.1 Imbricate structure of the Coy Pond Complex

In spite of the imbrication process which occurred during the transport and emplacement of the ophiolite nappe, the Coy Pond Complex, which is composed of two tectonic slices and two tectonic mélanges, preserves a complete ophiolite stratigraphy. The tectonic units and their petrologic components strike about north-south ( $010$  to  $030^\circ$ ) and dip  $70-80^\circ\text{E}$  (Fig 2.1). From west to the east, the Coy Pond Complex comprises four principal tectonic units, which are informally referred to as: (i) the basal slice, (ii) the western tectonic mélange, (iii) the central slice and (iv), the eastern tectonic mélange (Figs 2.1, 3.1 and 3.2). Near Chrome Brook, between the Spruce Brook Formation and the western tectonic mélange, another tectonic unit, informally referred to as the Mixed Lithology Slice also occurs (Fig 3.1 and Chapter 7). The general nature of the three tectonic slices is presented first, followed by a more detailed discussion of the tectonic mélanges, which form the subject of investigation of this thesis.

**Fig 3.1** Simplified geological map of the western tectonic  
mélange of the Coy Pond Complex. Abbreviations:

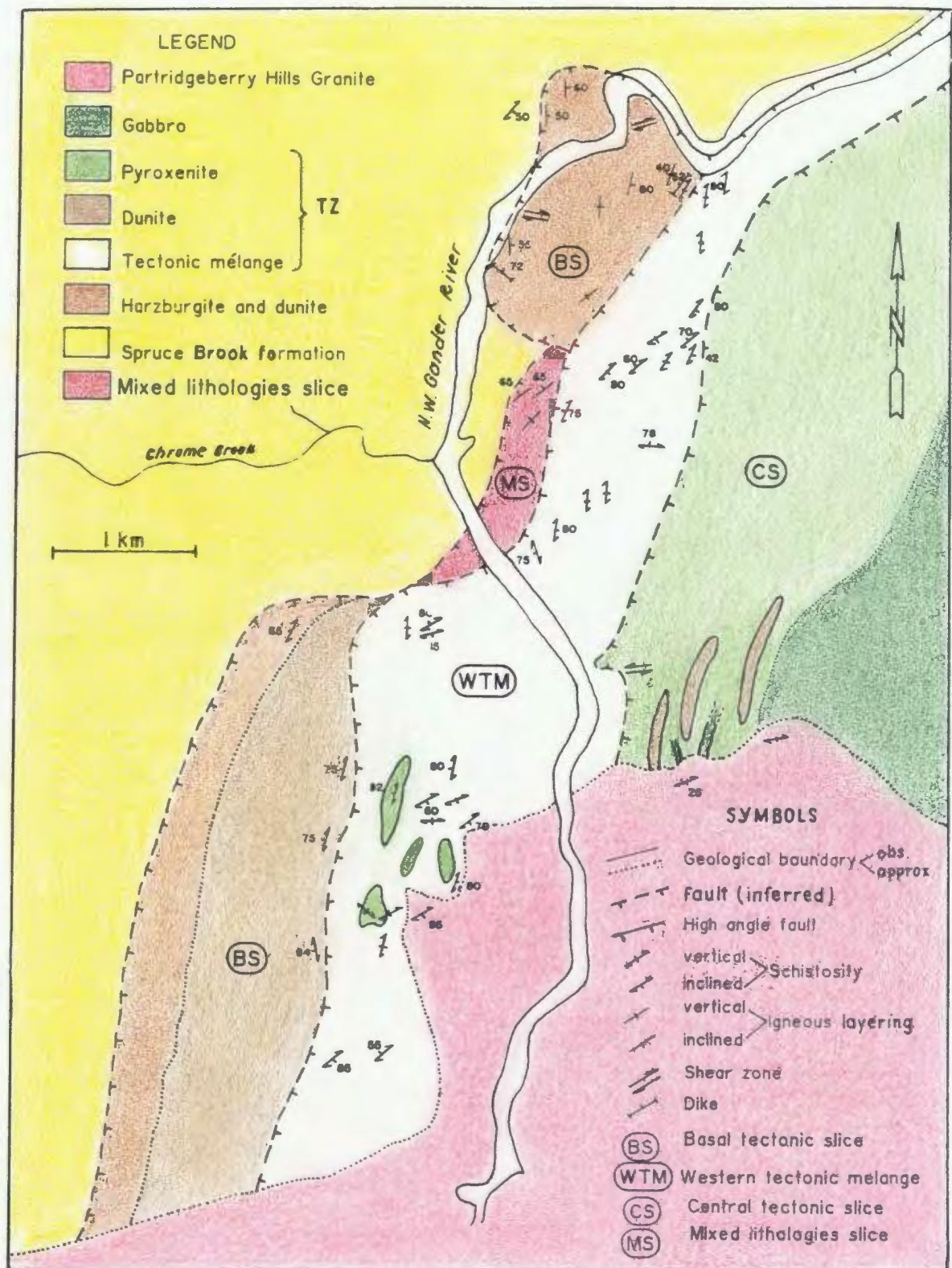
BS = basal structural slice

WTM = western tectonic mélange

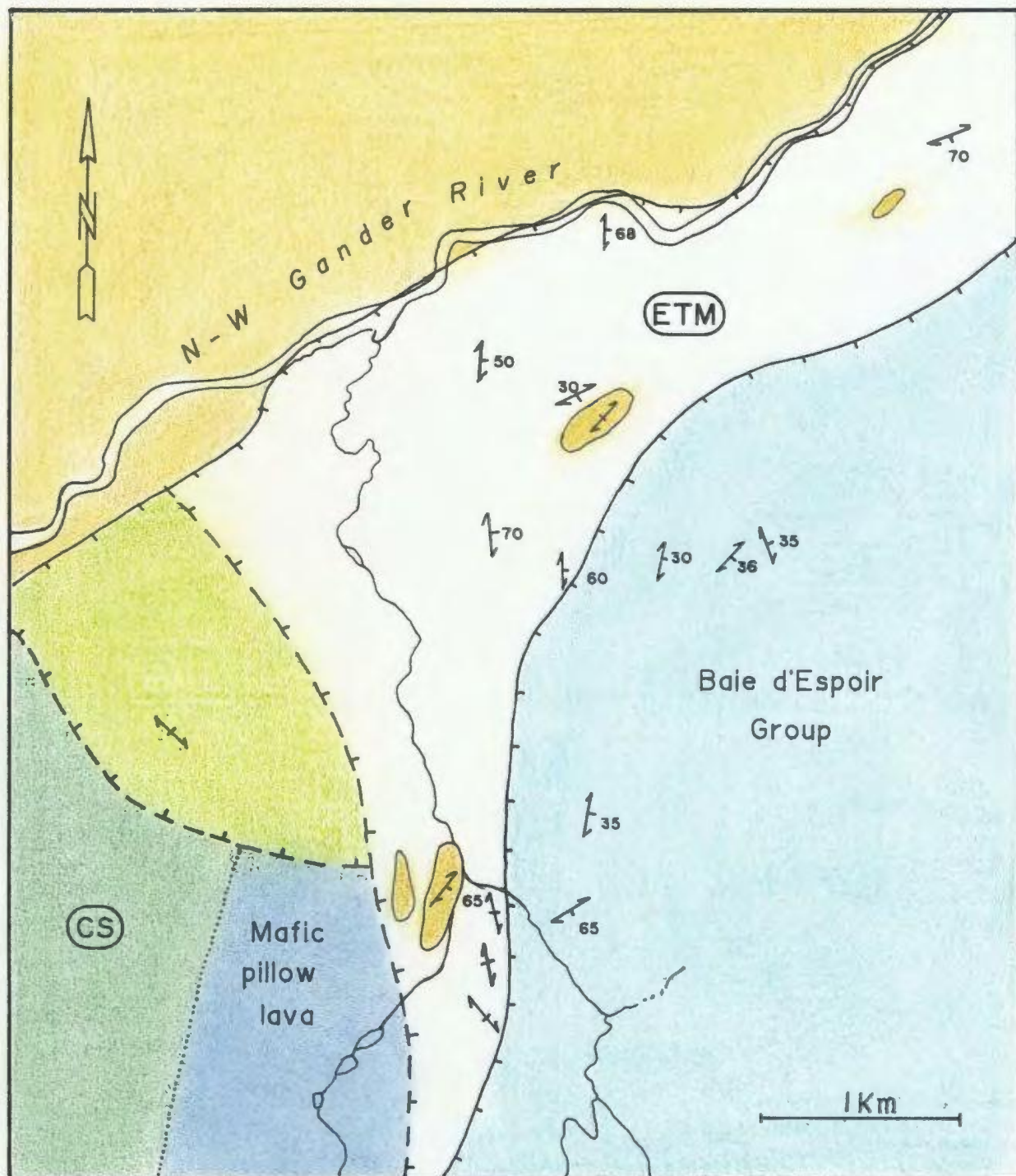
CS = central structural slice

MS = mixed lithology slice

TZ = former transition zone, largely replaced  
by WTM (see text for discussion)



**Fig 3.2** Simplified geological map of the eastern tectonic mélange of Coy Pond Complex. Legend as in Fig 3.1, except for mafic pillow lava and Baie d'Espoir Group, which are indicated. Abbreviations:  
CS = central structural slice  
ETM = eastern tectonic mélange.



### 3.1.1 Basal slice

The basal slice is situated between the Spruce Brook Formation at the west and north, the western tectonic mélange at the east, and the Partridgeberry Hills Granite at the south. It is about 1 km wide and is exposed for about 9 km along strike. In the area near the confluence of Chrome Brook and Northwest Gander River, the basal slice is missing from the tectonic stratigraphy for a distance of about 2.5 km.

North of Chrome Brook, the basal slice comprises upper mantle tectonites, harzburgite and dunite; south of Chrome Brook, it comprises mantle tectonites (poorly exposed) and dunite of the transition zone (Figs 2.1 and 3.1).

Two main groups of structural features are distinguished in the mantle tectonite unit: primary mantle flow structures and secondary structures of shallow lithospheric origin. These are discussed below.

#### 3.1.1.1 Asthenospheric structures

Asthenospheric (primary) structures include layering and foliation. The compositional layering is defined by variations in olivine to pyroxene ratios and consists of rhythmically alternating layers 1 to 5 cm in width of



pyroxene-rich and pyroxene-poor harzburgite. This feature is very common in the northwestern part of the Coy Pond mantle tectonite unit, where orthopyroxene layers may form up to 50 percent of the outcrops.

Possible mechanisms for the origin of this layering have been widely discussed in the literature and include magmatic differentiation by gravitational settling (Coombs et al., 1976), tectonically induced mechanical segregation processes of two phases under shear gradients (Dick and Sinton, 1979), and metamorphic differentiation accompanying deformation, pressure solution creep and anatexis of the peridotite (Dick and Sinton, 1979). The latter, deformation-related processes appear more likely in the Coy Pond Complex because the mantle tectonites, especially the harzburgites, show a penetrative foliation which can be seen on outcrop and microscopic scales. The foliation is a result of the flattening of enstatite and chrome-spinel grains in the foliation plane, and is interpreted to have been acquired in the mantle during plastic flow. Mantle foliations in the harzburgite dip 50 to 60° to the east and strike approximately 330-350° throughout most of the unit (Fig 3.1).

The southern part of the basal slice, situated south of Chrome Brook, comprises harzburgite with overlying residual dunite, which according to Nicolas and Prinzhofer (1982)

occur in the lower part of the transition zone. In dunite, the mantle foliation is defined by deformed Cr-spinel strings and lenses which strike about north-south and dip 75 to 85° east (Fig 3.1).

#### 3.1.1.2 Lithospheric structures

Lithospheric structures of shallow origin such as faults, cleavage, shear zones and also the tectonic mélanges, were produced during the transport and emplacement of the ophiolite in the brittle or brittle/ductile domain.

Major faults are confined to the margins of the basal slice. Along the western margin, the basal slice is in tectonic contact with the autochthonous Spruce Brook Formation along a cryptic northeast-striking fault that is inferred to be vertical to steeply east dipping (Fig 2.1). This fault is interpreted to have had initially a thrust sense of displacement (during the emplacement of the ophiolite), and was subsequently rotated towards the vertical during doming, and may also have been reactivated during late extensional faulting.

To the east, the basal slice is in tectonic contact with the western tectonic mélange along another northeast-trending subvertical fault. The origin of this fault is not certain, but it, and the western tectonic mélange may have



developed during obduction and thrust emplacement of the ophiolite nappe onto the continental margin, or they may have developed during post emplacement extensional faulting. This is discussed more fully in Chapter 11. Along its northern margin, the basal slice is cut by late high angle normal faults which place it against the Spruce Brook Formation along the Northwest Gander River (Fig 3.1). Fault breccia composed of ultramafic and sedimentary fragments can be seen in the river bed. To the south, the Partridgeberry Hills Granite is considered to be in intrusive contact with the tectonite unit (Colman-Sadd, 1985; Colman-Sadd et al., 1992) as well with the other ophiolite units.

Three sets of fracture cleavages are well-developed in the tectonite unit. The two main ones have orientations of  $340/80^{\circ}$  E and  $260/90^{\circ}$  with the third set being subhorizontal. These three fracture cleavages sets are roughly perpendicular to each other and bound quasi-cubic rock volumes. They form the basic framework of the serpentinite mesh structure on olivine down to the microscopic scale (see Chapter 6).

Brittle shear zones occur in the tectonite as rather poorly defined zones of intensely brecciated harzburgite and dunite. They are best exposed in the northern part of the unit where the North West Gander River produces large exposures. Here, they are a few m in width, several tens of

m in length and commonly show subvertical dips (Fig 3.1).

Tectonic mélanges, which contain abundant evidence of the brittle/ductile response of the ophiolite complex during the lithospheric deformation, are discussed in detail in section 3.1.4.

### 3.1.2 Mixed lithology slice

At the base of Coy Pond Complex and situated in an area where the basal ultramafic slice is missing (east of Chrome Brook near its confluence with the Northwest Gander River), there is a small tectonic slice composed of imbricated exotic (i.e. non-ophiolitic) rocks of a variety of compositions (including pelitic schist and various types of metavolcanic rocks) informally referred to as the mixed lithology slice (Fig 3.1). This slice, which is about 2 km long and 500 m wide, is situated between the western tectonic mélange to the east and the Spruce Brook Formation to the west. To the north and south it is inferred to be in fault contact with the mantle tectonite unit. The component lithologies form small hills tens to hundreds of meters in size which are characteristically covered by thick vegetation in sharp contrast to the denuded ultramafic surroundings.

Petrographic characteristics of the component lithologies

are described in Chapter 7 and their origin is discussed in Chapter 11.

### 3.1.3 Central slice

The central slice, situated between the western and eastern tectonic mélanges, comprises most of the units of the Coy Pond Complex: pyroxenite of the transition zone, gabbro and diabase, trondhjemite and keratophyre, pillow lava and locally overlying metasedimentary rocks. It is between 5 to 6 km in width (Figs 2.1 and 3.1).

To the west, the central slice is in fault contact with the western tectonic mélange, and to the east the boundary with the eastern tectonic mélange is also a fault. The northern contact with the Spruce Brook Formation is interpreted to be a high angle normal fault, and in the south the central slice is intruded by the Partridgeberry Hills Granite. A minor ductile shear zone about 10 m wide and more than hundred m long occurs about 500 m north of the granite, cutting the layered pyroxenite on a west-east direction (Fig 3.1).

The ultramafic portion of the central slice comprises layered pyroxenite of the transition zone and concordant dunite bands and lenses. The best exposures occur near the southern contact of the unit with the Partridgeberry Hills

Granite (Fig 3.1). Generally these formations strike north-south to 030°, and dip subvertically. Two dikes containing rodingite, (initially probably of gabbroic origin), are apparently concordant with pyroxenite layers and are visible near the contact zone with the granite.

#### 3.1.4 Tectonic mélanges

##### 3.1.4.1 General statement

The term *mélange* (French = mixture) was introduced into the geologic literature by Greenly (1919; cited by Williams, 1977) to describe "a chaotic mixture of unsorted blocks in a much finer, commonly sheared matrix". *Mélanges* are classified according to their process of formation: sedimentary, diapiric, tectonic or a combination of such processes.

Two main processes contribute to the genesis of any *mélange*: (i) the rock fragmentation (resulting from different mechanical behaviour of lithologies during deformation), and (ii) the mixing (Hsü, 1968).

The intimate relationship between *mélanges* and ophiolites was first recognized by Gansser (1974) who also proposed the term of ophiolitic *mélange* in order to distinguish it from those of purely tectonic or purely sedimentary (olistostromal) origin. However I prefer not to use this

term, as it does not distinguish ophiolitic mélanges of sedimentary origin (normally composed of ultramafic blocks in a black shale matrix) from those of tectonic origin that are composed of ultramafic blocks in an ultramafic matrix.

In the Coy Pond mélanges, both fragments and matrix are predominantly of ultramafic composition; sedimentary blocks occur only rarely and are restricted to the eastern tectonic mélange. So the Coy Pond mélanges can reasonably be considered tectonic mélanges. Moreover, the few sedimentary blocks that are present (only in the eastern tectonic mélange) were not incorporated within the mélange through a sedimentary process (as in the case of an olistostrome); they were incorporated into the deforming ophiolite nappe during displacement and were subsequently mechanically mixed with fragments of ultramafic origin.

In the text which follows two similar terms, namely fragments and blocks, are both used to refer to undeformed or little deformed bodies situated in a much finer schistose matrix. Fragments are elliptical bodies of invariably ultramafic origin, (of dunitic and harzburgitic protoliths) that are commonly less than 1 to 2 m in size, whereas blocks are much larger, tens to hundreds of m in size, and are composed of sedimentary rocks (eastern tectonic mélange) and pyroxenite (western tectonic mélange).

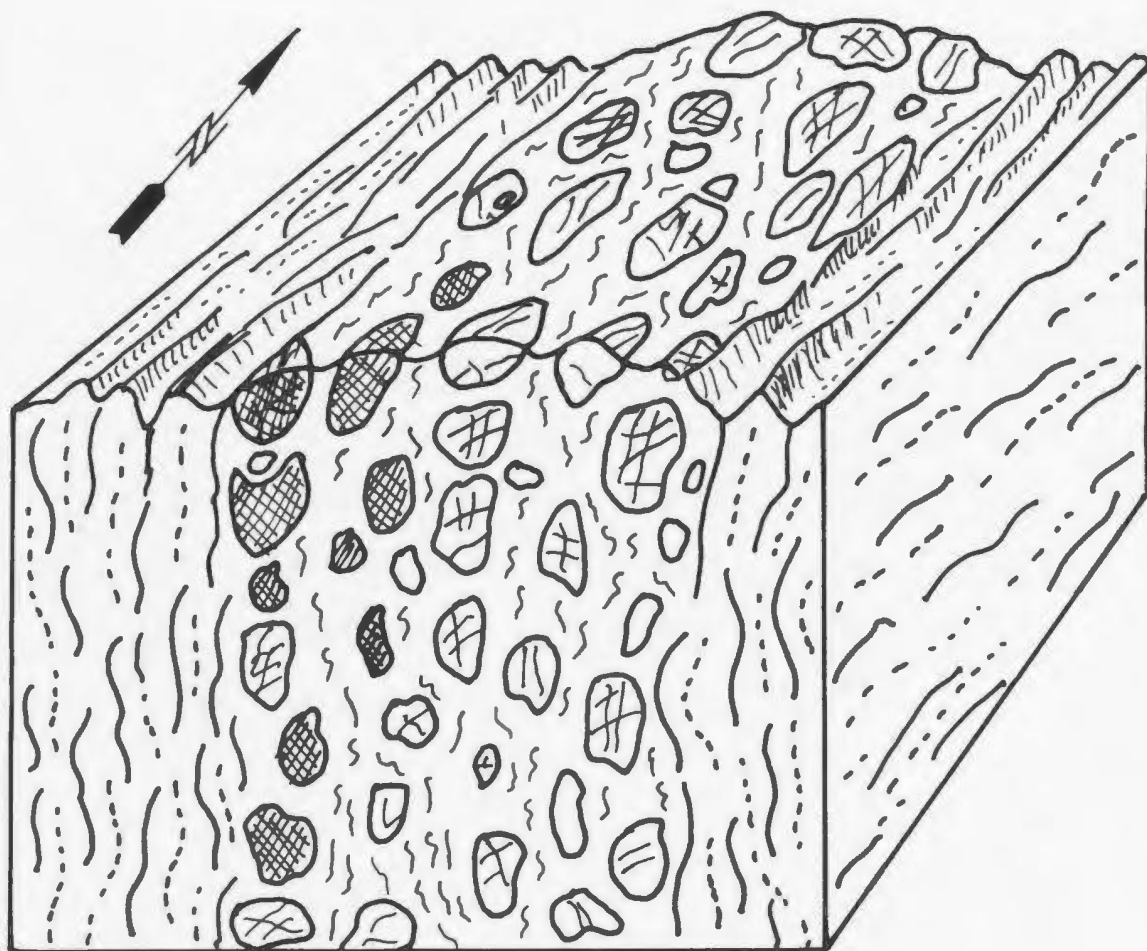
#### 3.1.4.2 Composition and characteristics of the Coy Pond tectonic mélanges

General characteristics of the tectonic mélanges include the following:

- (i) Fragments and matrix in both western and eastern tectonic mélanges have a common protolith of ultramafic (dunitic-harzburgitic) origin.
- (ii) Both tectonic mélanges are composed of sub-rounded fragments enclosed in a strongly sheared matrix (Fig 3.3).
- (iii) The fragment size ranges from several cm to a few m, with an average of about 1 m (Fig 3.3).
- (iv) Although on a small scale the schistose matrix can be seen to wrap around the mélange fragments, at a larger outcrop scale the matrix schistosity is consistently subparallel to the boundaries of the tectonic mélange unit;
- (v) Many individual fragments show evidence around their margins of in situ comminution to matrix through progressive shearing and recrystallization.
- (vi) The ultramafic protoliths underwent a retrograde metamorphism: both fragments and matrix were completely serpentized and later recrystallized and carbonatized to a variable degree.


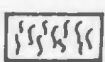
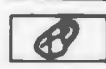
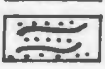
Particular characteristics of the two tectonic mélanges are discussed below:

**Fig 3.3** Simplified block diagram showing typical shape and spatial arrangement of the fragments and matrix in tectonic mélange.



5 m

# LEGEND

	Lizardite		Schistose serpentinite matrix
	Antigorite		Talc - magnesite matrix



**The western tectonic mélange (Figs 2.1; 3.1 and 3.3):**

(i) Is composed exclusively of fragments and matrix of ultramafic origin principally dunite and harzburgite, and in its southern part also contains several large (hundreds of m) pyroxenite blocks.

(ii) Both the serpentinite fragments and the matrix are partially carbonatized to talc-magnesite assemblages, with the matrix typically more carbonatized than the fragments.

(iii) The assemblage quartz-magnesite is not widespread, occurring only in a strip about 1 km long and several hundreds of m wide in the central part of the tectonic mélange, at the contact with the central thrust slice.

**The eastern tectonic mélange (Figs 2.1 and 3.2):**

(i) Is extensively carbonatized and only few relics of serpentinite occur between widespread (and commonly mingled) talc-magnesite and quartz-magnesite assemblages.

(ii) On account of the high degree of carbonatization, the original nature of the ultramafic protolith cannot be determined.

(iii) Several large (tens to hundreds of m) exotic blocks, of sedimentary and volcanosedimentary origin occur in the eastern tectonic mélange.

### 3.2 Serpentinite deformation

Experimental data on sealed serpentinite specimens at low temperatures show that the lithology has considerable strength in comparison to that of granite, but exhibits a marked weakening with increasing temperatures. For example, mesh textured lizardite deforms little below 300-350°C, above which its strength decreases dramatically (Raleigh and Paterson, 1965). Deformation is by brittle fracture at confining pressures <2 kbars, and by ductile mechanisms above 2 kbars (Raleigh and Paterson, 1965). The weakening of serpentinite with increasing temperature is related to the dehydration of both lizardite and antigorite to form forsterite and talc as the pore pressure of the released water reduces the effective confining pressure (Raleigh and Paterson, 1965). Dehydration of brucite-bearing serpentinite (at 3 kbars confining pressure) occurs at even lower temperatures of about 300°C (Scarfe and Wyllie, 1967).

Experiments on the strength and fracture behaviour of rocks having strong planar anisotropy have shown that the strength is orientation dependent, and that the orientation of the fractures is largely controlled by the orientation of the pre-existing structural anisotropies (Donath, 1970). This is particularly of interest for serpentinite, for which measured data on samples with a strong shear fabric yield

extremely low shear strengths of between 1 and 5 bars (Cowan and Mansfield, 1970). These data may help to explain the mechanism of displacement of dismembered ophiolite complexes as a whole and as individual tectonic slices bound by the tectonic *mélange* units.

On the basis of the protoliths of the fragments and the blocks in the western tectonic *mélange*, the tectonic *mélanges* units appear to have formed at about the level of the transition zone in the Coy Pond ophiolite. It can be imagined that several factors probably contributed to the development of the tectonic *mélange* within the transition zone rather than elsewhere.

(1) The existence of inherited weak, sheared (serpentinite) zones above the mantle sequence at this level (see also Fig 11 A and B), which can accommodate large crustal rotations (up to 45°) between the mantle sequence and rotated crustal blocks, as recognized empirically in the Josephine and Troodos ophiolites (Allerton and Vine, 1987; Norrel and Harper, 1988).

(2) The presence of sharp compositional and structural anisotropies between the harzburgite tectonite and the residual dunite at the base of the transition zone. The harzburgite tectonite, with a mechanically strong foliation (defined by pyroxenite layers) oriented at a high angle to the shear or *mélange* zone boundary, has a higher shear

strength than the underlying dunite with its mechanically weaker foliation defined by chromite seams and layers oriented subparallel to the shear direction (Donath, 1961). Similarly, the upper contact of the dunite at the dunite-pyroxenite boundary was also a zone of weakness.

(3) Serpentinization of the dunitic layer at the base of the transition zone (the locus of the *mélange* formation), which may have occurred in the ocean realm predated *mélange* formation, would have produced the well-known sub-cubic fracture pattern in serpentinite as a result of the large volume increase (up to 48% in serpentitized dunite; Hostetler, 1966).

### 3.3 Summary

(i) The Coy Pond Complex is in a subvertical orientation and faces outwards from the core of the Mount Cormack Terrane.

(ii) The Coy Pond Complex is in fault contact with all adjacent units except the intrusive Partridgeberry Hills Granite (Colman-Sadd and Swinden, 1984). Most of the faults are not exposed; some of the faults are interpreted to have had an initial thrust sense of moving (e.g. the contact between the Spruce brook Formation and the basal slice), but there is also considerable circumstantial evidence for extensional faulting.

(iii) The Coy Pond Complex is an imbricated, but complete, ophiolite body comprising two tectonic slices (basal and central slice) separated by two tectonic mélanges (western and eastern mélanges).

(iv) Stratigraphic and tectonic units (slices and mélanges) strike about north-south and dip vertically to 70-80° east;

(v) The basal tectonic slice is missing for a distance of 2 km, and its place is taken by the Mixed Lithology Slice, a tectonic sliver composed of miscellaneous blocks which were derived from both ophiolite slab and underneath metasedimentary rocks.

(vi) The basal tectonic slice, composed mainly of harzburgite and dunite tectonite, exhibits asthenospheric structures (layering and foliation), and lithospheric structures (faults, fracture cleavage and shear zones).

(vii) The two tectonic mélanges, which are composed of meter-sized elliptical fragments (formed in the brittle domain) enclosed in a schistose serpentinite matrix (formed in ductile domain), were formed by fragmentation and shearing of harzburgite and dunite during the detachment/transport and/or emplacement of the ophiolite nappe.

(viii) Most likely, the formation of the tectonic mélanges started in the brittle domain with mechanical fragmentation

of the dunite layer situated between harzburgite and pyroxenite, which was already weakened because of serpentinization and transport. The brittle comminution of serpentinite fragments was followed by the in situ formation of the serpentinite matrix (recrystallized lizardite) in the ductile domain.

## Chapter 4

### THE MANTLE TECTONITES

#### 4.1 Introduction

It is widely accepted that peridotites, which constitute the basal part of most ophiolites, represent depleted oceanic upper mantle (Coleman, 1977; Nicolas et al., 1980). The predominant fabric of peridotites in most ophiolites reflects the solid state flow deformations produced in the upper mantle during the process of sea-floor spreading. Superimposed shear fabrics, typically concentrated near the base of ophiolite sections, reflect high strain associated with the formation and obduction of ophiolite slices. On account of their typically high state of strain, these rocks are generally referred as tectonized peridotites or more simply as mantle tectonites (Turner and Weiss, 1963 p.39).

#### 4.2 Rock classification and textures

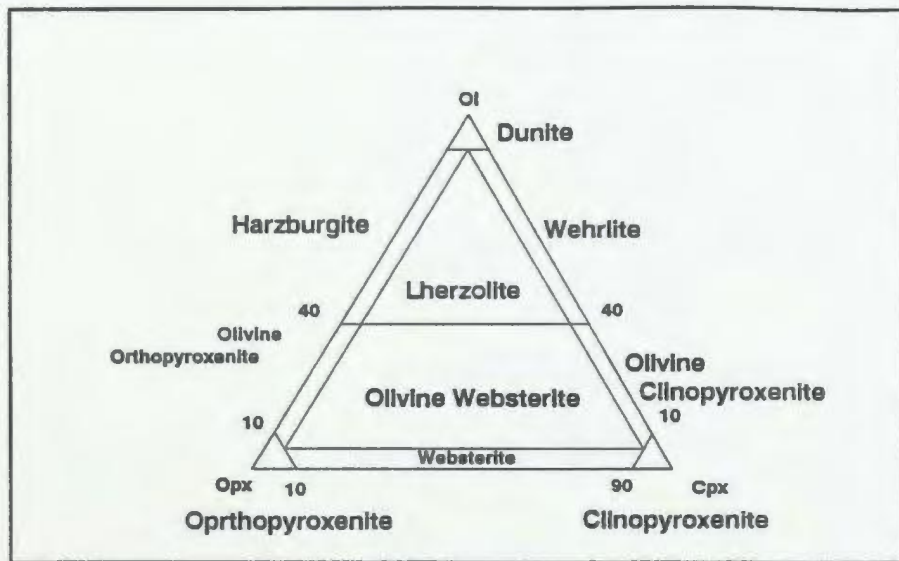
The rock classification scheme of Streckeisen (1976) and the nomenclature of the I.U.G.S. have been used in this study (Fig 4.1).

Modal compositions have been qualitatively assessed with the optical microscope. Where serpentinization was minimal this can be achieved without difficulty. In cases of

**Fig 4.1** IUGS nomenclature (based on modal mineral proportions) for ultramafic rocks with <5% spinel and lacking plagioclase, hornblende and garnet (Streckeisen, 1976).

**Fig 4.2** Representative view of harzburgite and dunite of tectonite unit. Brownish weathering harzburgite with 2 cm wide dunite layer (horizontal layer across central part of the figure) cross-cut by a network of serpentinized (white) fractures. Harzburgite exhibits a rough weathering surface, with pyroxene and chromite grains standing out in relief, in contrast to dunite which weathers to a smooth surface. Outcrop located in northwestern corner of tectonites, 100 m east of Northwest Gander River.





advanced or complete serpentization the least deformed specimens, having pseudomorphic textures which preserve all the main characteristics of the protolith minerals, have been used.

Tectonite textures have been classified using the scheme for textures of ultramafic xenoliths in basalts (Mercier and Nicolas, 1975; Pike and Schwarzman, 1977; Harte, 1977) and the classification for peridotite textures (Nicolas, 1978; Nicolas et al., 1980; Nicolas, 1986).

#### 4.3 Distribution and contacts

The mantle tectonites in the Coy Pond ophiolite, which constitute only a small (<5%) part of the entire ophiolite complex, occur in two separate slices in the extreme west of the ophiolite, adjacent to the underlying Spruce Brook Formation (Fig 3.1). The more northerly slice, situated between Chrome Brook and the broad bend in the Northwest Gander River, is a well exposed body about (2 km x 1 km) consisting of harzburgite and dunite. The southern slice situated south of Chrome Brook is in a poorly exposed area and consists of several showings of very altered, mylonitized harzburgite.

In terms of its structural position, the tectonite unit forms the structurally lowest basal thrust slice in this

part of the Dunnage Zone, directly overlying the Spruce Brook Formation and underlying the ophiolitic tectonic mélange.

The tectonized peridotites in the Coy Pond ophiolites are composed of two main lithologies, harzburgite and dunite and subsidiary rare pyroxenite dikes.

#### 4.4 Harzburgite

In outcrop, harzburgite exhibits a yellowish-brown weathering rind (Fig 4.2) that may be up to 1 cm thick. On fresh surfaces the rock is dark greenish to black and has a hackly conchoidal fracture. The unaltered pyroxene imparts a greyish-green colour to the rock, but with serpentinization the rock becomes darker. Completely serpentinized harzburgite and dunite have a greyish-black coloration. Serpentinized harzburgite weathers to a rough surface, produced by differential weathering which leaves resistant pyroxene "hobnails" and smaller chromite grains (Fig 4.2). Pyroxene grains are up to 1 cm in size and have a bronze-like metallic lustre (schiller). Bands and clusters of pyroxene in some sites impart a good foliation to the rock.

Chrome spinel grains are black and up to several mm in diameter. They commonly occur in trails and fine pods defining a compositional banding. Where flattened and

elongated, spinel grains also define a tectonic foliation in the rock.

#### 4.4.1 Petrography and microstructures

The primary mineral assemblage of the harzburgite is difficult to assess because of subsequent serpentinization. Commonly the harzburgite tectonites are about 30 to 50 per cent by volume altered to serpentine minerals. Harzburgite specimens collected near the western boundary of the unit, near the base of the tectonite slice are up to 80 percent serpentinized. The average original modal composition of harzburgite is estimated to have been: olivine 70-80 %; orthopyroxene 20-30 %; chrome spinel 1-2 %; clinopyroxene <1 %.

Olivine and pyroxene are commonly segregated in olivine-rich and pyroxene-rich bands which confer a foliation to the rock. Where this occurs, it is a conspicuous feature on both mesoscopic and microscopic scales. Two main textures occur in harzburgite:

- (i) coarse porphyroclastic textures
- (ii) protomylonitic textures

The coarse porphyroclastic textures (Mercier and Nicolas, 1975; Harte, 1977) are the more primitive and are produced by asthenospheric flow (Nicolas, 1986). Such textures,

implying an asthenospheric signature with little or no overprinting by lithospheric deformation, are restricted to harzburgite situated in the northwestern part of the tectonite unit. They are characterized by large olivine grains (up to 10 mm) which have tabular shapes and straight boundaries. Kink banding and undulose extinction are common (Fig.4.3). Well-recovered substructures also occur. The large composite olivine porphyroclasts may be composed of small (<0.5 mm) idioblastic olivine grains (neoblasts) produced by subgrain formation. Large porphyroclasts form more than 50 per cent of the rock and indicate the low degree of recrystallization of the olivine. The neoblasts of olivine form a mosaic texture with common 120° triple point junctions due to annealing processes (Fig 4.4).

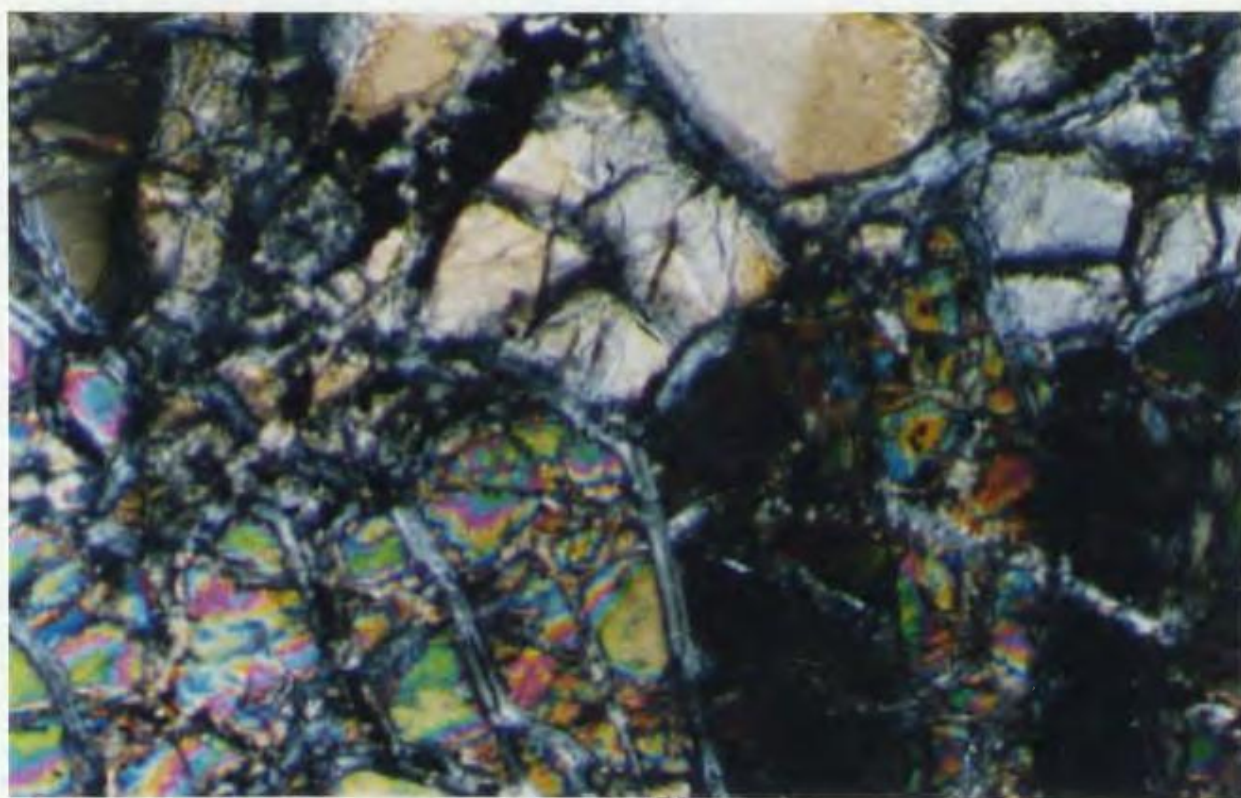
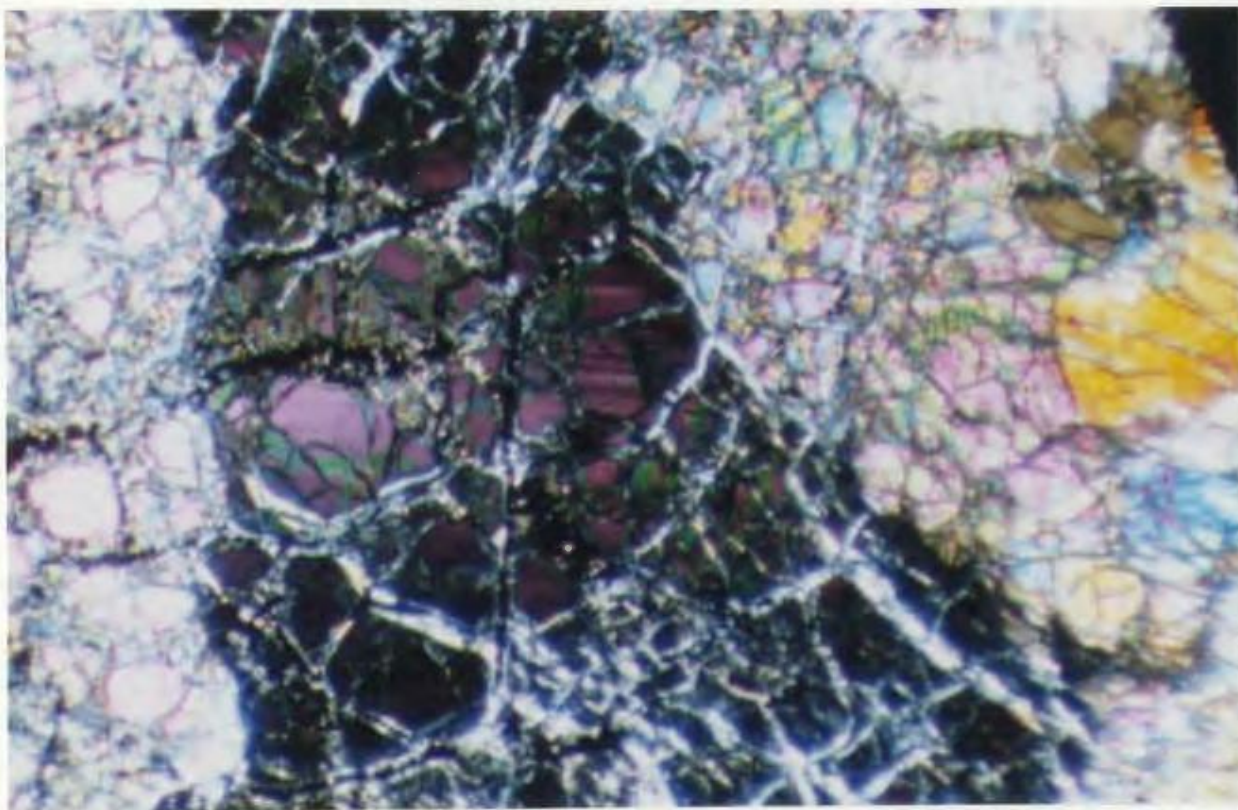
Orthopyroxene (enstatite) up to 5 mm in size generally forms clusters of irregularly shaped grains giving a weak foliation to the rock. Commonly these grains have olivine inclusions and large embayments filled with olivine (Figs 4.5 and 4.6), and many show evidence of brittle or brittle-plastic deformation (Figs 4.5).

Spinel typically occurs as small blebs enclosed in olivine and orthopyroxene porphyroclasts (Fig 4.7) and rarely occurs as interstitial grains with a weakly-developed holly-leaf shape between olivine grains, and an idioblastic shape where in contact with pyroxene.

**Fig 4.3** Harzburgite with porphyroclastic texture. 3 large olivine porphyroclasts (high order pink to green birefringence colors) with subsidiary orthopyroxene (yellow) on the right hand side. The central olivine grain shows undulose extinction (from black to purple) and fine deformation lamellae. The olivine grains are fractured and partially replaced by mesh textured lizardite (white). Specimen 175; X 3.2; crossed polars; bar represents 0.5 mm.

**Fig 4.4** Harzburgite with porphyroclastic and neoblastic texture. An example of the recrystallization of olivine by grain boundary migration toward a state of minimum interfacial energy. In the lower right hand corner three olivine bands or subgrains (the middle one showing high order birefringence colors between two grains at extinction) in contact with unstrained olivine neoblasts (upper half of the figure). The  $120^\circ$  triple point junctions are between differently oriented bands which act as separate grains. Sample 175; X 3.2; crossed polars; bar represents 0.5 mm.

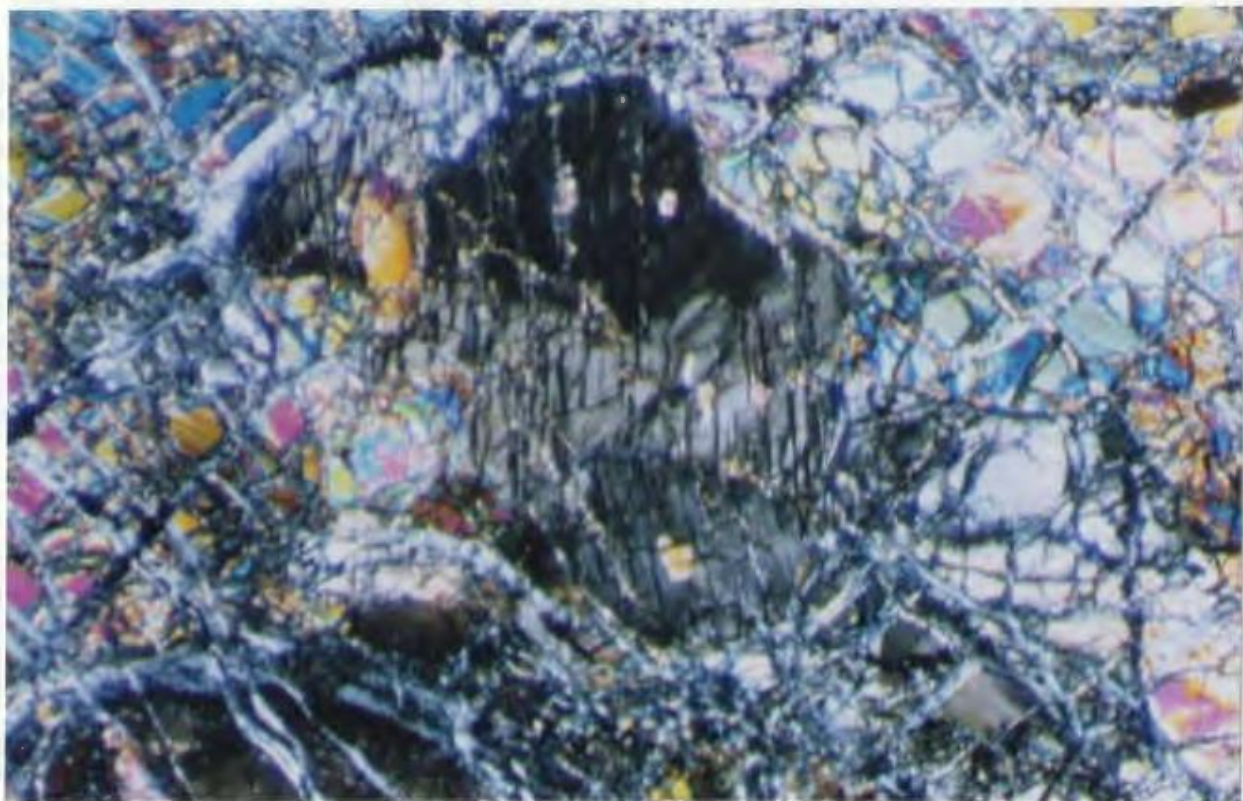




**Fig 4.5** Harzburgite with porphyroclastic texture. Highly strained and fractured orthopyroxene porphyroclast (grey) in the central part of the figure in a groundmass of recrystallized olivine grains. The orthopyroxene grain contains olivine in inclusions and embayments, and narrow clinopyroxene exsolution lamellae. Sample 175; X 3.2; crossed polars; bar represents 0.5 mm.

**Fig 4.6** Detail of harzburgite with porphyroclastic texture. Cusped, fractured orthopyroxene grain (yellow) showing several stages of partial melting and replacement by olivine (grey, purple and blue). Black is serpentine and magnetite. Specimen 184; X 10; crossed polars; bar represents 0.2 mm.





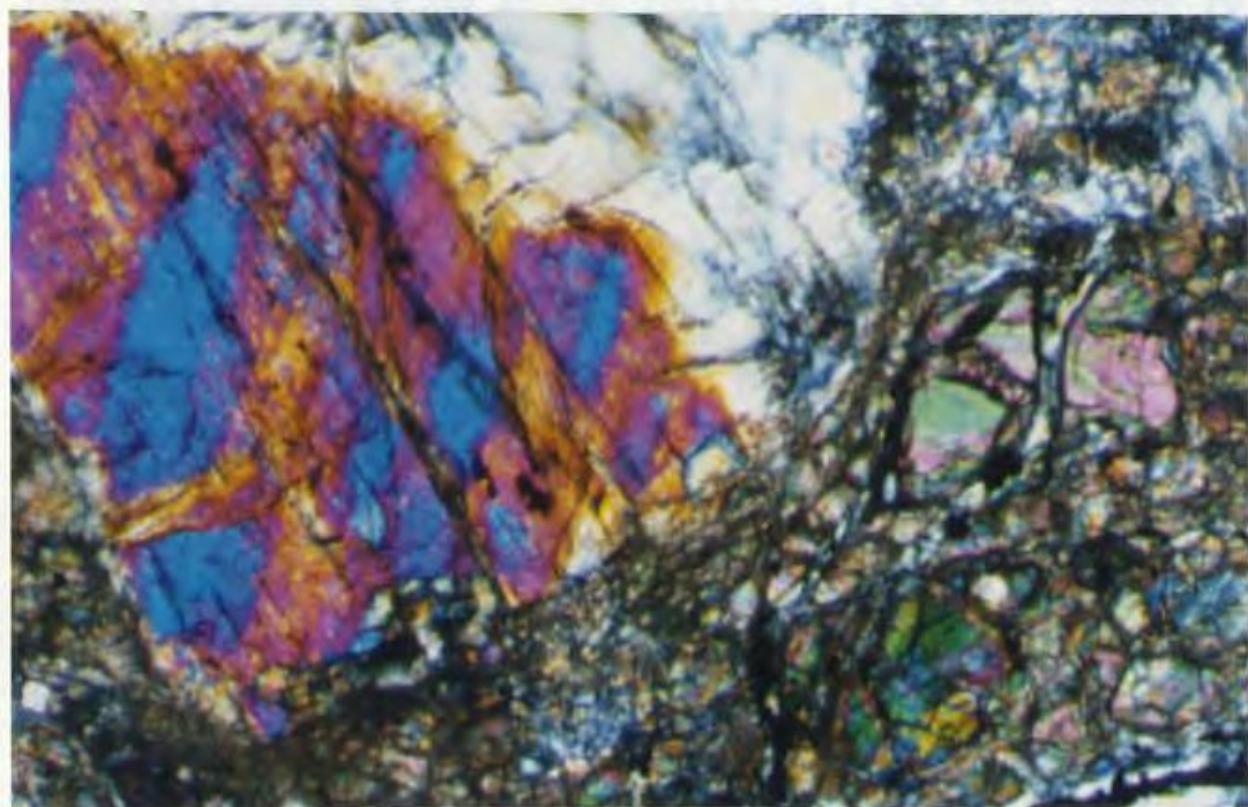
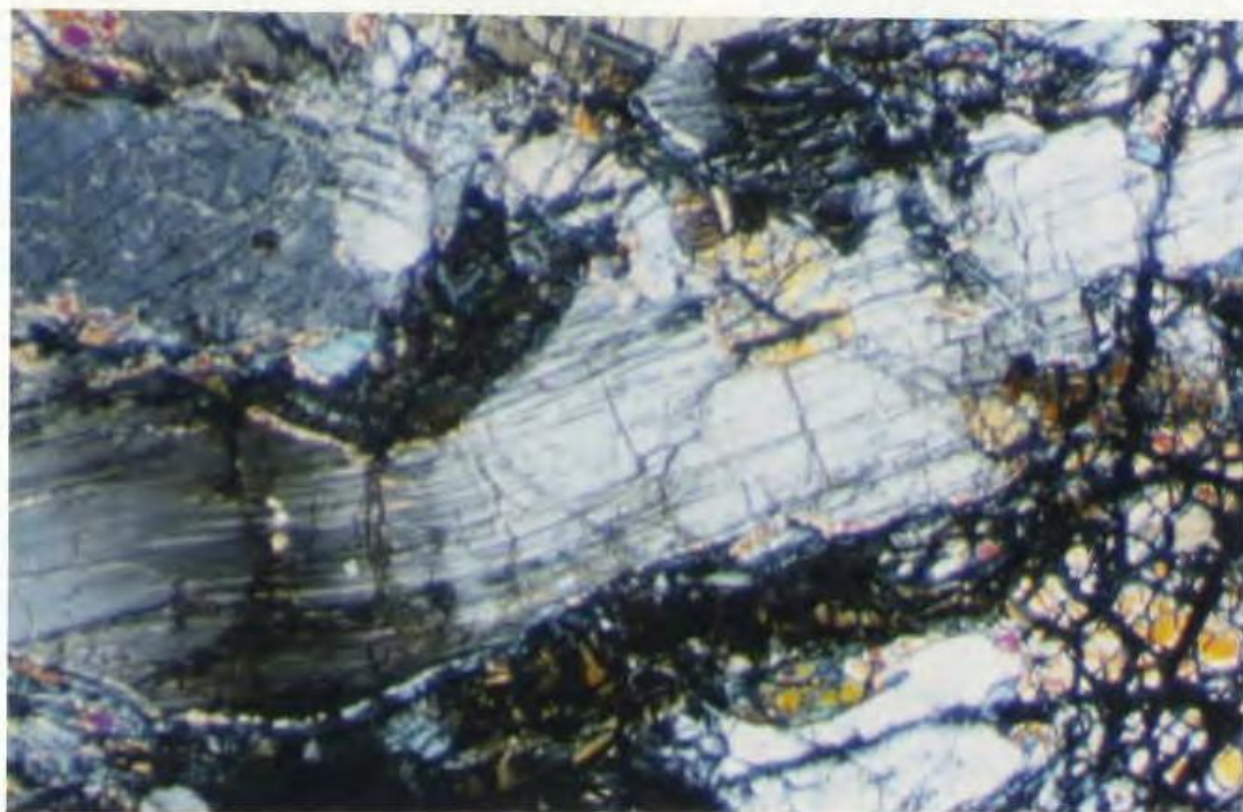
**Fig 4.7** Detail of harzburgite with porphyroclastic texture. Elongate, stretched and bent enstatite grain in foliation plane. The grain shows undulose extinction, clinopyroxene exsolution lamellae, and olivine in inclusions (yellow) and embayments. Fractures are developed perpendicular to the maximum dimension indicating that the enstatite crystal has been stretched in the plane of foliation. In the upper left part of the figure there is another orthopyroxene grain (grey) with a small spinel inclusion (brown). Olivine grains are yellow and reddish, serpentine and magnetite are black. Sample 50; X 3.2; crossed polars; bar represents 0.5 mm.

**Fig 4.8** Harzburgite with porphyroclastic to protomylonitic texture.

Detail showing a mylonitic layer band between a highly strained and fractured pyroxene grain (blue and purple to orange birefringence in the left hand side of the figure) and relict olivine porphyroclast (pink and green in the bottom right corner). The pyroxene is partially altered to lizardite-bastite (white). Between the olivine and pyroxene there is a narrow mylonite zone composed of small olivine grains and iron oxides.

Specimen 79-A; X 10; crossed polars; bar represents 0.2 mm.





Protomylonitic textures (Nicolas, Boudier and Bouchez, 1980) are common in the harzburgite tectonite of the Coy Pond ophiolite (Figs 4.8 to 4.10). This texture is a result of advanced recrystallization, the olivine neoblasts comprising dynamically recrystallized small grains ( $<0.1$  mm) with a mosaic texture (Figs 4.8 and 4.9). Rare larger ( $<5$  mm in size) relict olivine porphyroclasts (Fig 4.8) are still present and exhibit strongly undulose extinction. Orthopyroxenes are variable in size, from porphyroclasts up to 8 mm in length, to small grains about 0.5 mm in size. All orthopyroxene grains are highly strained, and clinopyroxene exsolution lamellae and bent crystals are common. Elongate and stretched grains in the foliation plane also occur (Fig 4.10). Small spinel grains are commonly flattened and are oriented with their long axes in the foliation plane (Fig.4.10).

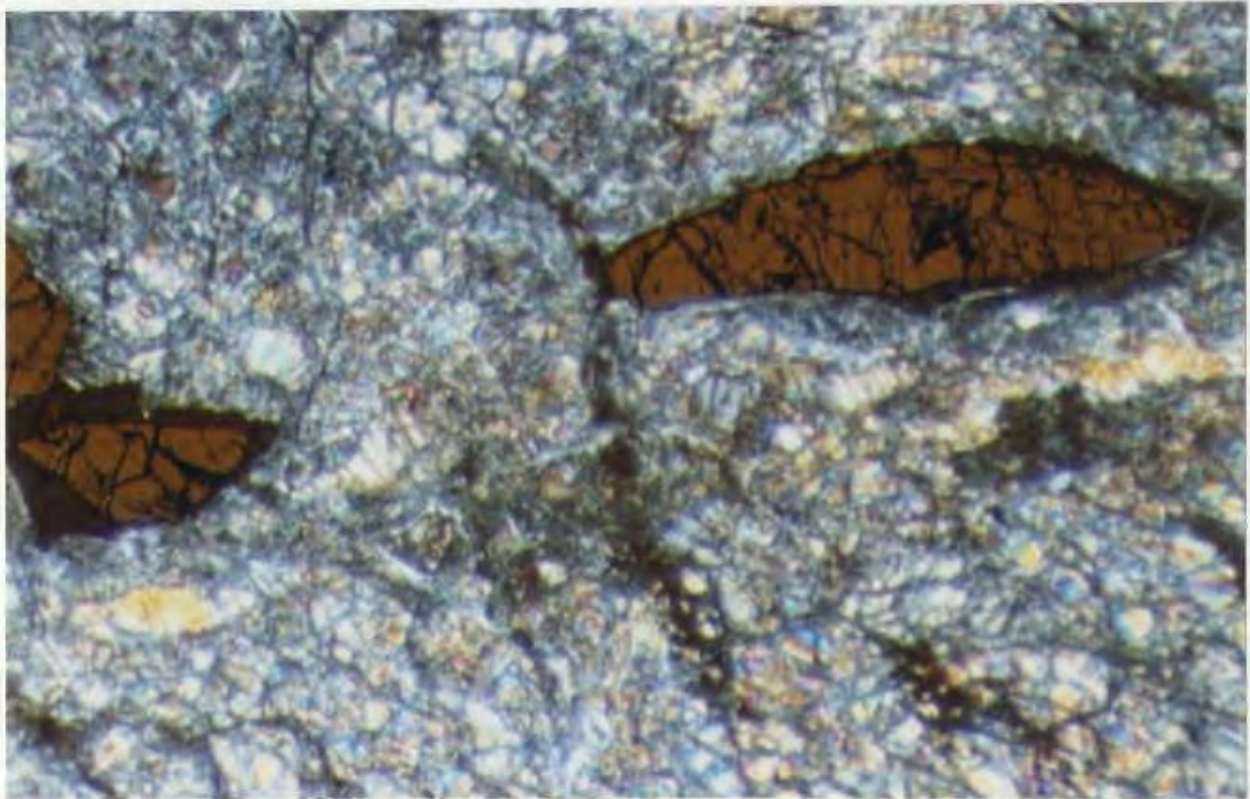
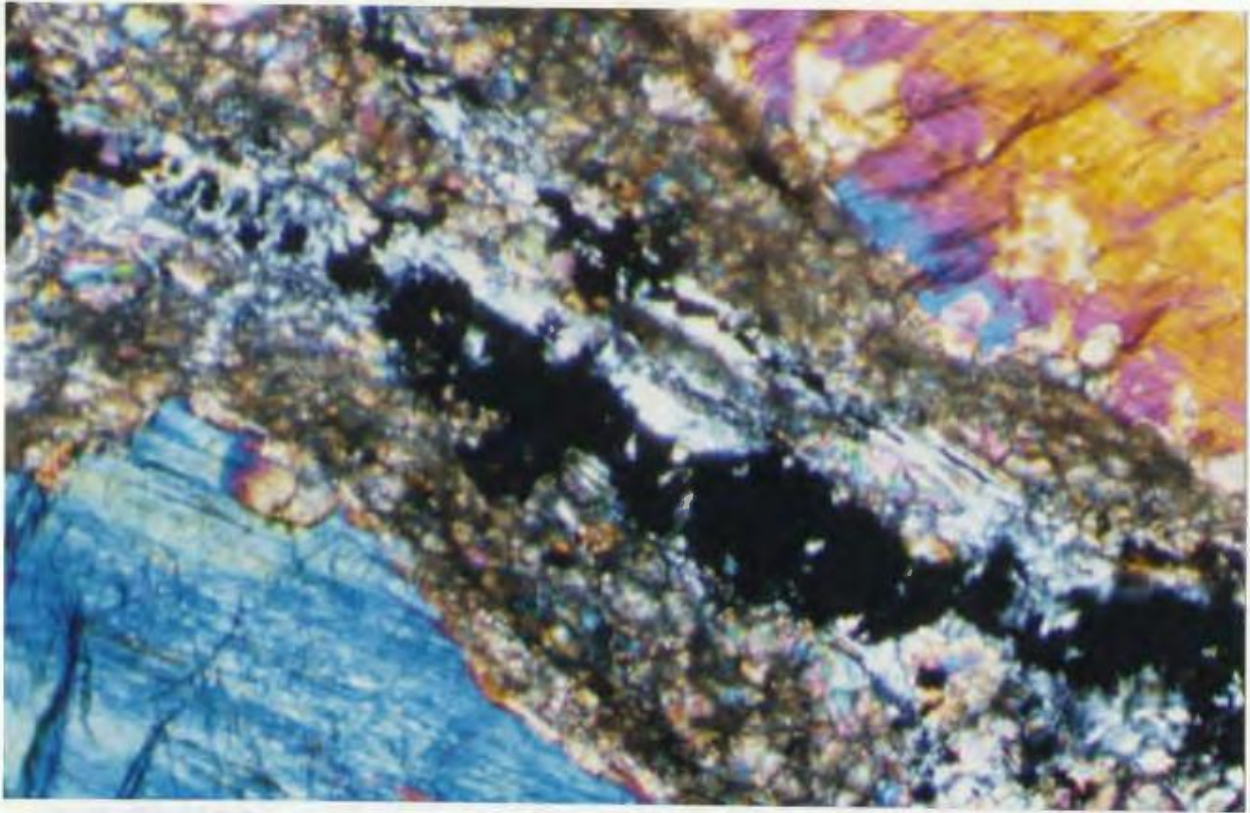
#### 4.4.2 Discussion and conclusions

According to Nicolas (1978; 1986) the coarse-porphyroclastic textures are achieved by asthenospheric deformation at temperatures around 1000-1200 °C, and under low deviatoric stresses. The strong recovery is due to very active grain boundary migration. A characteristic of porphyroclastic textures is the resorption of pyroxene and

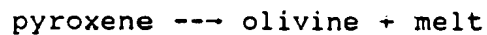
**Fig 4.9.** Harzburgite with mylonitic texture.  
Detail showing mylonitization of olivine between two large orthopyroxene grains. The fragmented material in the mylonite zone consists of olivine (brownish), chrome spinel and magnetite (black), and serpentine (white).  
Specimen 79-A; X 10; crossed polars; bar represents 0.2 mm.

**Fig 4.10** Harzburgite with protomylonitic texture.  
Spinel (brown) and orthopyroxene (yellow) form a train of elongate small grains in a groundmass of mylonitized olivine. Spinel grains show fractures approximately perpendicular to maximum stretching direction which are filled with secondary magnetite (black).  
Section perpendicular to foliation and parallel to lineation.  
Specimen 156; X 3.2; crossed polars and partially reflected light; bar represents 0.5 mm.





replacement "in situ" by olivine (Fig 4.6). This feature occurs during partial melting of peridotite and is attributed to a reaction such as:



(Dick and Sinton, 1978; Quick, 1981), with the melt phase subsequently being removed.

Protomylonitic textures are generally more common within the harzburgite tectonite where they show low-temperature (around 800° C), high-stress microstructures and fabrics typical of lithospheric deformation at the base of tectonite (Nicolas, 1986; Nicolas et al., 1980).

#### 4.5 Dunite

About 20% of the mantle tectonites consists of dunite bodies. They are irregularly distributed within harzburgite and occur in the following forms:

(i) broad tabular bodies (Fig 4.2) a few cm to a few m in width and several hundreds of m in length;

(ii) smaller irregularly shaped patches, commonly interfingering with the harzburgitic host, and having decimeter to meter size (Fig 4.11);

(iii) small tabular bodies (as dunitic walls) between clinopyroxene-rich dikes and harzburgitic host.

Dunite exhibits similar features to the harzburgite in the

field, except that it has a smooth weathering surface due to the lack of pyroxenes (Figs 4.2, 4.11 and 4.12). In the serpentized samples, the dunite has a black coloration and a homogeneous aspect. Locally, layering is defined by the relative abundance of chrome spinel (Figs 4.11 and 4.12). Layers of chrome spinel up to 2 cm thick and few meters in length are not uncommon.

#### 4.5.1 Petrography and microstructures

The modal composition of the serpentized dunite is typically: serpentine 70-80 %, brucite 10-30 %, orthopyroxene 0-2 %, magnetite 1-5 %, chrome spinel 1-5 %. The original modal composition of dunite is estimated to have been: olivine 95-99 %; chrome spinel 1-5 %; orthopyroxene 0-2 %. Relict olivine grains, comprising about 2 to 3 percent of the serpentized dunite, were found in only one specimen (collected from a dunite band). Typically the olivine is altered to lizardite + brucite in mesh textures or poorly developed hourglass textures, and the relict olivine occurs as mesh centers in lizardite mesh texture.

Because of the large degree of alteration, the original dunite texture was inferred mainly from serpentine pseudomorphs after olivine, in which the original olivine



**Fig 4.11** Field photograph of harzburgite enclosing an irregularly shaped, decimetric-sized patch of dunite (central part of figure). Dunite, showing brown-yellow weathering color and smooth surface is cut by Cr-spinel pods and veinlets (black). Outcrop location: in the northern part of tectonite unit, in the river bed about 500 m south of the large bend of the Northwest Gander River.

**Fig 4.12** Field photograph showing dunite with foliation defined by layers of Cr-spinel grains. Location: about 150 m north of Fig 4.11.



texture is commonly undisturbed. Detailed petrographic observations on lizardite pseudomorphic textures indicate a granuloblastic texture for the olivine protolith. The rare relict olivine grains noted above (less than 0.3 mm in diameter) were part of originally larger grains (5 to 10 mm in size) which show vague undulose extinction indicative of relatively low strain.

Chrome spinel grains (<3 mm in size) may form up to 5 percent of the dunites. They are scattered throughout the rock and also occur in layers where they confer a weak compositional banding to the rock (Fig 4.11).

#### 4.5.2 Discussion and conclusions

Dunite bodies, with granuloblastic texture and evidence of weak strain, probably postdated the plastic deformation of the harzburgite and may have formed in the crustal environment under subsolidus conditions.

The formation of these late bodies has been attributed to replacement of pyroxene by olivine as fluids percolated through the harzburgite protolith (Irvine, 1974; Quick, 1981), or to feeder dikes transporting olivine-rich picritic melts from depths (Hopson et al., 1981; Boudier and Coleman, 1981). Alternatively, since olivine is considered to be the most refractory residue produced by partial melting in the

mantle, dunite units may represent zones in which partial melting was more extensive and removal of the melt more complete (Dick and Sinton, 1979).

#### 4.6 Pyroxenite dikes

Two pyroxenite dikes within harzburgite occur in the northern part of the tectonite unit. One dike is 30 cm in width, the other is about 3-3.5 m. Both dikes cut harzburgite and are largely (60-70%) altered to talc and lizardite bastite. Most of the rock is crossed by narrow (1-3 mm) serpentine veins.

The orthopyroxenite is a coarse-grained, dark-green rock in which the individual crystals can be seen in hand specimen. Enstatite comprises roughly 90 per cent of the dikes, occurring in a hypidiomorphic granular intergrowth. The remaining 10 per cent of the rock consists mainly of interstitial olivine (now altered to serpentine), about 1% clinopyroxene and rare Cr-spinel.

The contacts between grains are interlocking, locally irregular. The grain size is rather large, 1 to 15 mm with an average of 4-5 mm. Deformation of the pyroxenes has produced undulose extinction. Clinopyroxene occurs as rare small (<0.5 mm) ragged interstitial grains, and as exsolution lamellae within orthopyroxene. The spinel occurs

as minute blebs within pyroxene and as anhedral interstitial grains <1 mm in size. Late serpentization reactions have resulted in the complete replacement of interstitial olivine by mesh-textured lizardite. The large olivine grains (up to 5 mm diameter) forming the dike walls are also replaced by mesh-textured lizardite, but fresh olivine may still be found in some of the larger mesh centers. Orthopyroxene is largely replaced by talc and in lesser amounts by lizardite-bastite. The clinopyroxene grains are also partially altered to lizardite-bastite.

The relatively irregular contacts with the host rock and the presence of dunite on dike walls suggest an indigenous origin. Comparison with similar dikes reported in the literature suggests that the dikes may have formed by precipitation of pyroxene from a water-rich solution which leached the wall rocks, or from a residual magma which reacted with solidified peridotite (wall rock reaction) (Green and Ringwood, 1967; Nicolas, 1986).

#### 4.7 Discussion and conclusions

The Coy Pond complex shows evidence of three types of structure and associated metamorphism that have been acquired in three different tectonic environments.

- (1) Primary or asthenospheric structures were acquired in

the mantle during high-temperature, low-stress ductile deformation. Compositional layering and foliations defined by elongate olivine and pyroxenes such as are seen in the Coy Pond complex, are indicative of crystal-plastic flow deformation at temperatures higher than 1000°C (Mercier and Nicolas, 1975; Nicolas et al. 1980).

(2) The mylonitic textures involving ductile deformations of olivine and pyroxene, and recrystallization of olivine neoblasts imply somewhat lower temperatures (800-700°C) and can be attributed to oceanic detachment and obduction of the ophiolite (Boudier and Coleman 1981; Nicolas and Le Pichon 1980).

(3) Structures of shallow origin, including fractures, faults and cleavages, originated in the upper crustal environment and are associated with serpentinization. They affect all the earlier structures. The Coy Pond tectonite is quite strongly fractured, the degree generally increasing toward the margins of the body. Some fractures may have been associated with obduction, but it is also likely that many faults and cleavages were related to post-obduction processes.

## Chapter 5

### THE TRANSITION ZONE

#### 5.1. Introduction

The transition zone in an ophiolite complex is defined as the zone situated between the ultramafic and mafic units, and it has characteristics in common with both of them (Coleman, 1977). The boundary with the underlying tectonite unit is defined by the disappearance of orthopyroxene from harzburgite, and the boundary with the overlying gabbro is marked by the disappearance of peridotites (Nicolas and Prinzhofer, 1982). In well-studied ophiolites, the transition zone has been shown to be composed of interlayered ultramafic (dunite, wehrlite, pyroxenite) and mafic rocks, and its thickness may vary from several meters up to 3000 m (Girardeau and Nicolas, 1981).

#### 5.2. Composition

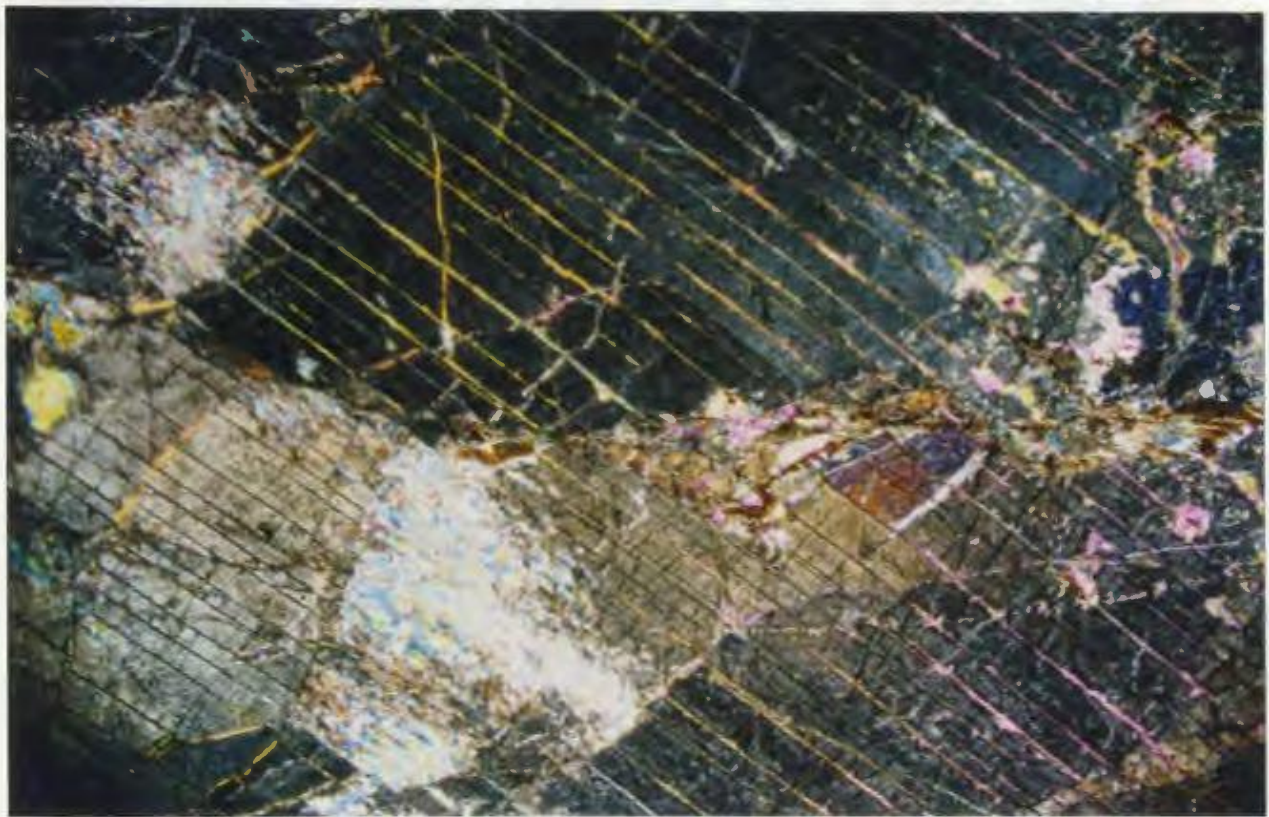
The rocks of the transition zone of the Coy Pond ophiolite complex are represented mainly by alternations of olivine-clinopyroxenite, subordinate dunite and minor gabbro dikes. The main characteristics of this unit are the regularity of the mineralogic layering (Fig 5.1), the gradational nature of the contacts between adjacent layers, and the marked

**Fig 5.1** Field photograph showing pyroxenite layering in transition zone. Medium grained olivine-clinopyroxenite layer about 50 cm thick (under compass) and fine-grained clinopyroxenite layer to the left. The fabric variation over short distances is notable.

Location: about 200 m north of Partridgeberry Hills Granite on the western margin of western dunite lens.

**Fig 5.2** Photomicrograph of coarse-grained pyroxenite, in which the entire field of view is occupied by a large fractured diopside grain at or near extinction. Clinopyroxene has narrow orthopyroxene exsolution lamellae. Patches with high birefringence colors (white, blue and pink) are tremolite-actinolite alteration. Specimen 289-A; X1.5; crossed polars; bar represents 1 mm.





variation in strain between adjacent layers. In a west-east cross-section in the central part of the ophiolite complex, where the transition zone is best exposed, three components can be distinguished.

(i) The base of the transition zone comprises a subzone about 1 km thick of dunite overlying the residual mantle harzburgite.

(ii) The central part of the transition zone (also about 1 km thick) is composed of olivine and clinopyroxene with a continuous variation in the proportions between the two minerals. The cyclic character of the interlayered olivine clinopyroxenite and dunite, occurring as bands and lenses with thickness scales that range from several tens of centimeters up to hundreds of meters, is very characteristic of this subzone.

(iii) The upper part of the transition zone is distinguished by the disappearance of dunite and the appearance of gabbro.

### 5.3. Distribution and contacts

The present distribution of the transition zone in the Coy Pond Ophiolite (partially visible in Fig 3.1) reflects the fragmentation and mechanical mixing that occurred during ophiolite obduction and emplacement.

Most of the lower dunitic part of the transition zone (entirely in the northern half of the western tectonic *mélange* and partially in the southern half of the western tectonic *mélange*), and part of the central pyroxenite unit (in the southern half of the western tectonic *mélange*), were completely separated from the unit, and were recycled to form the western tectonic *mélange*. The remainder is best exposed north of the Partridgeberry Hills Granite (Fig 3.1) which truncates the transition zone. Farther north, rocks of the transition zone outcrop only rarely.

A dismembered section of the transition zone, represented by olivine clinopyroxenite, occurs as a tectonic block (2.5x1 km) in the northeastern part of the ophiolite complex.

Cumulate pyroxenite is easily distinguished from the associated dunite due to the presence of layering and its grey to brown weathering color (Fig 5.1). The rocks are dark green colored when fresh. Commonly they are medium-grained, but in the central subzone of the transition zone and also in the dismembered tectonic block, the pyroxenites are coarse-grained and massive. Cumulate dunite, on the other hand, is red brick in color on weathered surfaces, and black where fresh. Rodingites, which occur locally, are generally grey-white mottled with green.

## 5.4. Petrography

### 5.4.1 Dunite

The dunites are adcumulates composed almost entirely of cumulus olivines which were enlarged by adcumulus growth. Chromite-rich ribbons are common. The composition of the olivine is not known because it has been completely replaced by serpentine, commonly in very fine interpenetrating (about 0.05 mm) or interlocking (<0.01 mm) textures. Serpentinized dunite cumulates are identical to the serpentinite fragments in the tectonic mélange in all respects, and detailed petrographic descriptions of dunite have been given given in the Chapter 4 and are not repeated here.

### 5.4.2. Clinopyroxenite

The modal composition of clinopyroxenite is: clinopyroxene 65-95%, olivine 0-30%, orthopyroxene 0-5%, and chrome spinel < 1%. The exact proportions of olivine and orthopyroxene are difficult to assess because of subsequent serpentinization. The clinopyroxene is an augitic diopside and shows a remarkably uniform chemical composition (see Chapter 8) across the entire transition zone.

Two main types of clinopyroxenite occur: coarse and banded.

**Coarse clinopyroxenite** (Fig 5.2) is massive with idiomorphic to hypidiomorphic clinopyroxene grains up to several tens of mm in an adcumulus interlocking texture. These clinopyroxene grains commonly show strain features such as bending, crystal fracturing or local shearing (Fig 5.2) and are locally uralitized. Olivine, which comprises less than 10% of the rock volume as an intercumulus phase, is invariably replaced by lizardite and magnetite.

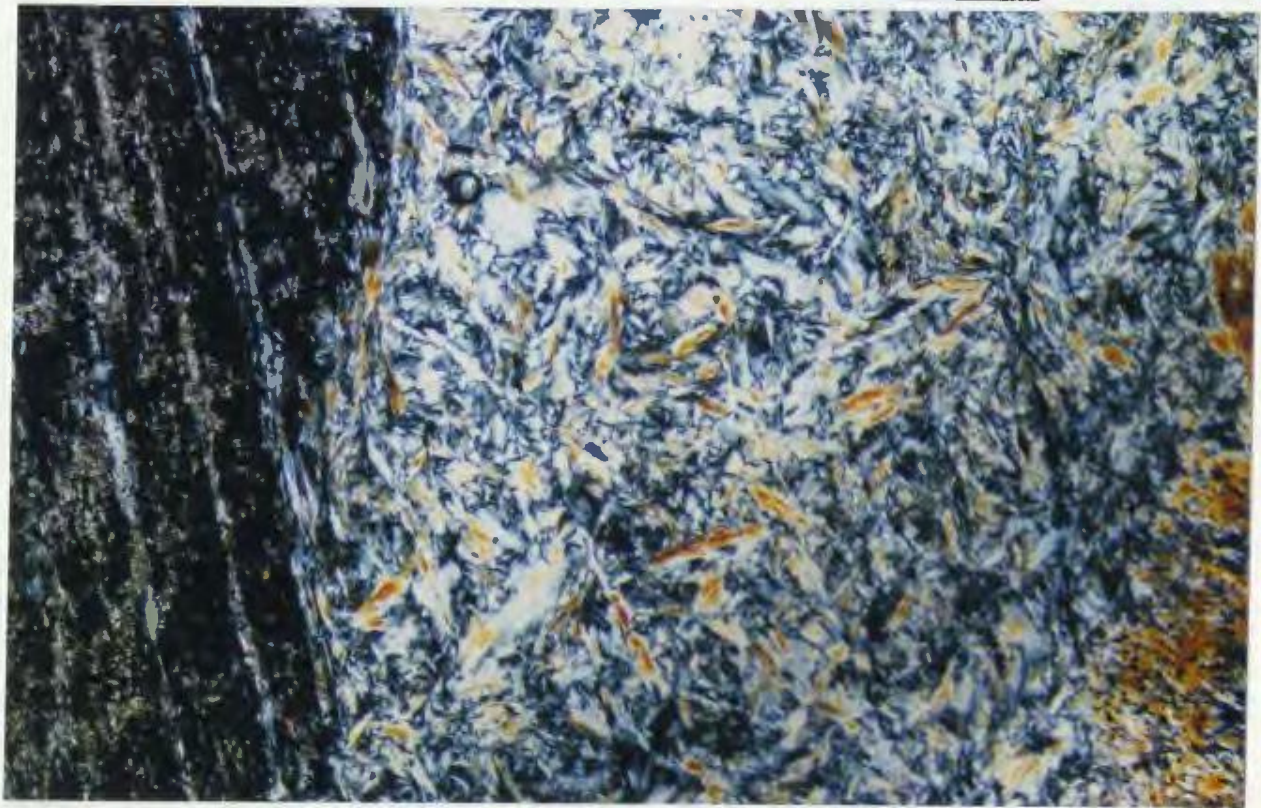
**Banded clinopyroxenite** is composed of adcumulus clinopyroxene and intercumulus olivine and clinopyroxene in proportions between 65-90% and 10-30% respectively. Commonly the clinopyroxene grains occur as crystals 2 to 4 mm in size surrounded by 0.1 to 0.3 mm clinopyroxene neoblasts (Fig 5.3). The larger crystals commonly have undulose extinction and show strain features such as bending and microfractures. Orthopyroxene exsolution lamellae in clinopyroxene are widespread. The neoblasts, which have similar chemical composition, are undeformed and do not show any of the above strain features.

Hydration is commonly quite advanced in these rocks. Orthopyroxene is uralitized and replaced by dense green mats of Ca-amphibole (Fig 5.4). Olivine was initially serpentized to lizardite mesh or banded growth textures (Fig 5.5), which were commonly recrystallized to interpenetrating or interlocking textures.

Fig 5.3 Photomicrograph showing adcumulus texture of clinopyroxene in a banded clinopyroxenite. Diopside (which comprises about 90% by volume of the rock) appears in this illustration as large black porphyroblasts (at extinction) with orthopyroxene exsolution lamellae (white) and undulose extinction (not visible), surrounded by smaller diopside neoblasts. In the center of the figure, between the two porphyroblasts, a small elongate orthopyroxene grain (pale brown) is visible. Specimen 257-B; X 1.5; crossed polars; bar represents 1 mm.

Fig 5.4 Photomicrograph showing advanced low grade metamorphism in pyroxenite. In the central part of the figure tremolite-actinolite and chlorite aggregates occur between two large clinopyroxene grains. At the left margin, a clinopyroxene grain at maximum extinction (black) with exsolution lamellae of orthopyroxene replaced by bastite (white to grey) and minute talc flakes (pale brown). On the right margin of the figure, a tremolite-actinolite aggregate (brown) pseudomorphically replaces clinopyroxene. Specimen 402; X 10; crossed polars; bar represents 0.2 mm.

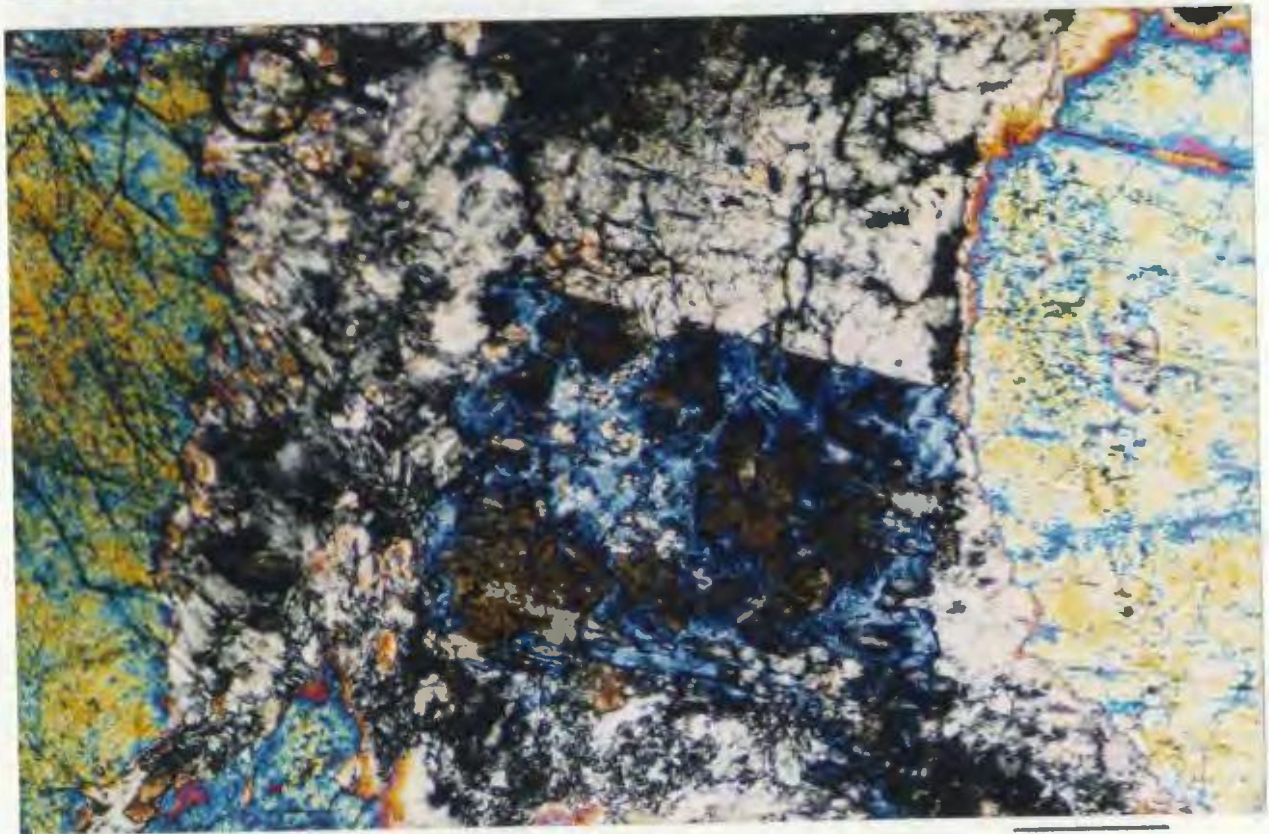
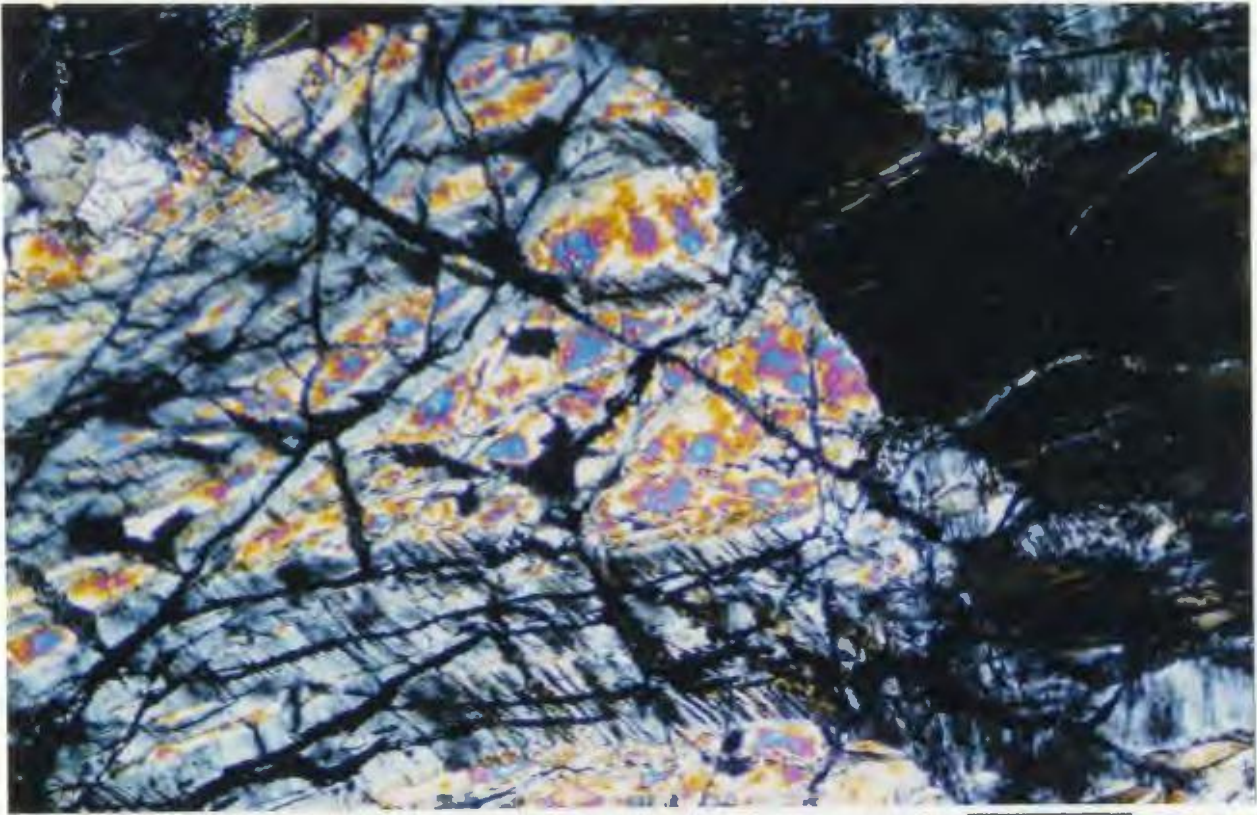




**Fig 5.5** Photomicrograph of serpentized olivine in an olivine clinopyroxenite band in clinopyroxenite cumulate. Fractured olivine (high birefringence colors), is partially replaced by lizardite with banded growth texture (grey) and magnetite (black). At the right hand side of the figure is a clinopyroxene grain at maximum extinction (black) with lizardite (grey) in fractures. Specimen 257-A; X10; crossed polars; bar represents 0.2 mm.

**Fig 5.6** Photomicrograph showing the partial rodingitization of clinopyroxenite. In the central part of the figure is a sharp contact between two xonotlite grains (or possibly a single twinned grain), showing anomalous brown and blue birefringence colors (upper part), the other with grey birefringence colors (the lower part). At the left and right margins of the figure are clinopyroxene grains with bright birefringence colors. Specimen 379; X 10; crossed polars; bar represents 0.2 mm.





The clinopyroxenites are the freshest and most resistant to hydration among all the phases. However under high strain conditions in shear zones and faults, the clinopyroxenites were completely replaced by chlorite, tremolite and talc.

#### 5.4.3. Rodingite

At the top of the transition zone, north of the Partridgeberry Hills Granite, there occurs one relatively large (about a hundred meters long and tens of meters wide) and several smaller, rodingite layers with medium- to coarse-grained granoblastic texture, that are interbedded with the clinopyroxenite. These rocks are composed mainly of mixtures of diopside and xonotlite [ $\text{Ca}_6\text{Si}_6\text{O}_{17}(\text{OH})_2$ ] (X-ray determination) with minor actinolite, and prehnite (Figs 5.6 and 5.7). Carbonates such as calcite and dolomite occur locally.

#### 5.5. Conclusions

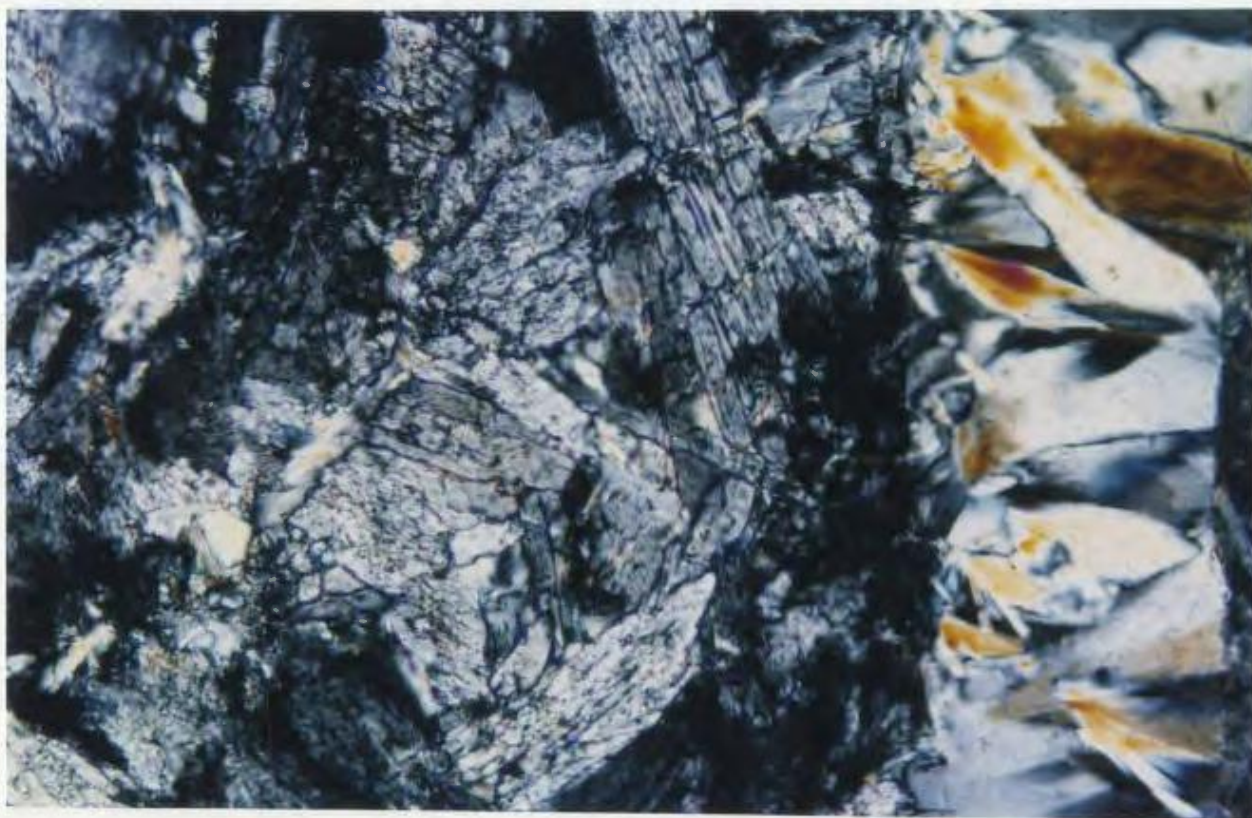
Several conclusions can be drawn from the examination of the transition zone in the Coy Pond Complex.

(i) As implied in the name, the transition zone links the ultrabasic harzburgite unit with the overlying basic rocks.

Fig 5.7 Photomicrograph showing a completely rodingitized rock. The left margin of the figure is occupied by a prehnite (birefringent yellow-orange) vein with the grains perpendicular to the walls. The rest of the figure is formed of columnar xenotlite (grey) with good cleavage and high relief.

Specimen 396; X 10; crossed polars; bar represents 0.2 mm.





(ii) From bottom to top, three main lithologic subunits parts are distinguished, comprising: dunitic, pyroxenitic-dunitic and pyroxenitic-gabbroic compositions respectively

(iii) The lower boundary with the underlying tectonite harzburgite was obliterated as a result of formation of the tectonic mélanges; the upper boundary with the gabbros unit is only partially exposed in the area near the Partridgeberry Hills Granite.

(iv) The thickness of the transition zone is assumed to have been between 2 and 2.5 km, comparable to that exposed at Blow-Me-Down Mountain (3000 m), the thickest among all studied ophiolite complexes (Girardeau and Nicolas, 1981). The possibility that the transition zone in the Coy Pond Complex was thickened by imbrication during transport is not ruled out, but no clear evidence of this was found during the mapping.

(v) The principal characteristic feature of the transition zone is its regular layering produced by oscillations in bulk-rock chemistry, and expressed mineralogically as alternations between clinopyroxene-rich and olivine-rich layers and lenses in the lower part of the transition zone, and lithologically as alternations between clinopyroxenite and gabbro in the upper part of the transition zone. These layers commonly pinch and swell and do not show chilled margins. Dunites, the most depleted rocks, are considered

residues of partial melting, with the pyroxenite and gabbro representing the products of melt accumulation and impregnation processes (Nicolas and Prinzhofer, 1982).

(vi) Rodingites occurring in the upper sections of the transition zone represent highly metasomatized pyroxenite and gabbro layers which formed in the presence of calcium-rich waters.

(vii) Much of the transition zone (mainly the lower dunitic part) was transformed into the western tectonic mélange, which is discussed in detail in the next chapter.

## Chapter 6

### THE TECTONIC MÉLANGES

#### 6.1. Introduction

In the two tectonic mélanges of the Coy Pond Complex, with few exceptions, both fragments and matrix are composed of completely serpentized and variably carbonatized ultramafic rocks of ophiolitic-harzburgitic origin. On the basis of arguments presented in an earlier chapter, it is believed that the fragments and matrix in the tectonic mélanges were derived principally from the transition zone of the Coy Pond ophiolite, with subordinate input from the upper mantle tectonites.

There are some compositional differences between the two tectonic mélanges, which are interpreted to be largely a function of the later metamorphism, which has resulted in the eastern tectonic mélange consisting principally of quartz-magnesite and talc-magnesite assemblages, whereas the western tectonic mélange consists predominantly of serpentinite and is less, but variably carbonatized.

In the description of the tectonic mélanges which follows, the matrix and the fragments are discussed separately (with one exception - see below) as they exhibit different mineralogical and textural features and appear to have behaved to some degree independently from both metamorphic

and rheological perspectives. Emphasis in this chapter is placed on the mineralogical and textural features of the tectonic mélanges in order to trace their mineralogical development, which will be utilized in interpretation of the metamorphic evolution (Chapter 9), and in order to constrain petrographically the choice of samples for stable isotope work (Chapter 10). The exception noted above is for the case of quartz-magnesite assemblages, in which fragments and matrix are treated together because in this lithology there are only minor differences (mainly in grain size, the matrix being coarser grained) between fragments and matrix (see section 6.4 this chapter).

Background information on the nomenclature and interpretation of serpentine textures is given in Appendices 1 and 2 (C), to which the reader is referred for discussion of terminology used in this study.

## 6.2 MÉLANGE FRAGMENTS

Dunite of the transition zone and subordinate harzburgite of the mantle tectonites form the bulk of the material that was reworked into fragments and matrix in both western and eastern tectonic mélanges. Although harzburgite and dunite, both underwent brittle deformation, to form the fragments up to 1-2 m in size, matrix in both tectonic mélanges shows



abundant evidence of ductile deformation features, implying that the tectonic mélange had strongly inhomogeneous rheological properties.

The different rheological behaviour of the fragments and matrix is also reflected in the metamorphic mineral assemblages. Serpentinite fragments are less recrystallized and carbonatized than serpentinite in the matrix, and thus a range of textures and mineral assemblages is commonly present in a single hand specimen and thin section.

Serpentinite fragments have been subdivided petrographically into those that have pseudomorphic and those that have non-pseudomorphic textures, and are discussed bellow.

#### 6.2.1 Serpentinite fragments with pseudomorphic textures

Included in the following descriptions of serpentine textures in the fragments is microstructural information for associated phases such as brucite, magnesite, talc, opaques (Cr-spinel, magnetite) and chlorite, which all form important phases in serpentine-bearing assemblages. Other opaque minerals, such as pentlandite, heaslewoodite, linneaite and awaruite, although occurring only in trace amounts in serpentinite, talc-magnesite or quartz-magnesite assemblages, are also mentioned because they are indicators

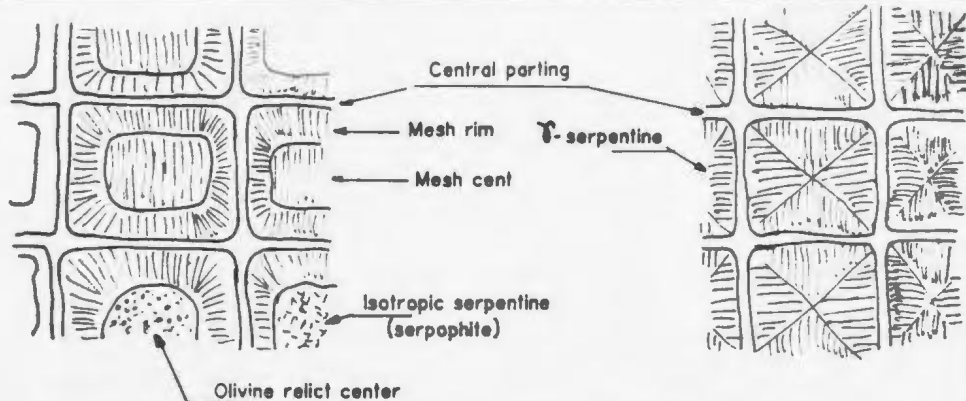
of oxygen fugacity.

Approximately one quarter of the fragments in the western Coy Pond tectonic mélange exhibit good pseudomorphic textures (Figs 6.1 to 6.9) after olivine and pyroxene. Of these fragments, about 80% were derived from dunites, with the remaining 20% having a harzburgitic protolith. Serpentine pseudomorphs show that the dunites generally contained <5% orthopyroxene, whereas the harzburgites contained up to 20-30% orthopyroxene and traces of clinopyroxene (<1%).

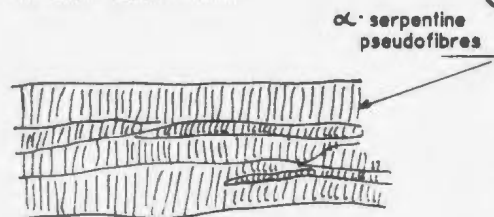
The pseudomorphic hydration of olivine to serpentine along grain boundaries and fractures has produced a tessellation of polygonal cells resulting in mesh texture (Fig 6.1.a), hourglass texture (Fig 6.1.b) and less commonly, a banded growth texture (Fig 6.1.c). The alteration of pyroxenes to serpentine (bastite) was also grain boundary and fracture controlled, and resulted in the formation of orthopyroxene-bastite (Fig 6.1.e and Appendix 1) and less common clinopyroxene-bastite.

Mesh texture is invariably fine-grained and composed of a quasi-cubic arrangement of cross-fibre veinlets (Figs 6.1.a and 6.2) or mesh rims which enclose mesh centers. Each mesh center and its surrounding mesh rim constitutes a mesh cell, which is surrounded by very narrow strip of serpentine (the central parting) which separates each mesh cell from its

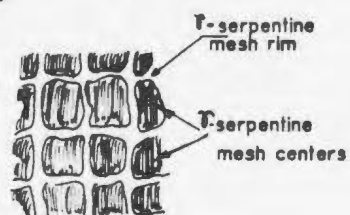
**Fig 6.1** Schematic representation of serpentine pseudomorphic textures after olivine (A,B,C and D) and after pyroxene (bastite) E. (Modified after Francis, 1956).



(A) MESH TEXTURE

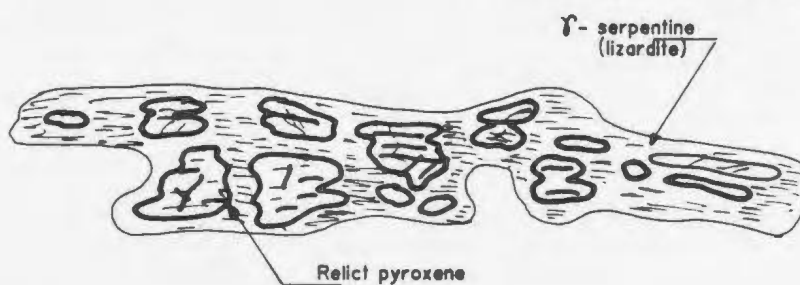


(B) HOURGLASS TEXTURE



(C) BANDED GROWTH TEXTURE

(D)  $\gamma$ -SERPENTINE MESH TEXTURE



(E) PARTIALLY SERPENTINIZED ENSTATITE GRAIN

neighbours. Mesh centers (with sizes from 0.05 to 0.7mm, average 0.2mm) display variable shapes from symmetrical to highly asymmetrical, and are composed of various types of material. Relict olivine mesh centers (Figs 6.1.a and 6.2) have been found only rarely. Most commonly mesh centers are filled with fibrous felted mats of either  $\alpha$ - or both  $\alpha$ - and  $\gamma$ -serpentine or are occupied by isotropic or nearly isotropic lizardite (serpophite). Commonly mesh centers are colorless and show lower birefringence than the mesh rims. Minute grains of disseminated magnetite dust are common throughout the mesh centers in some samples, whereas in others magnetite concentrated at the mesh rim boundaries.

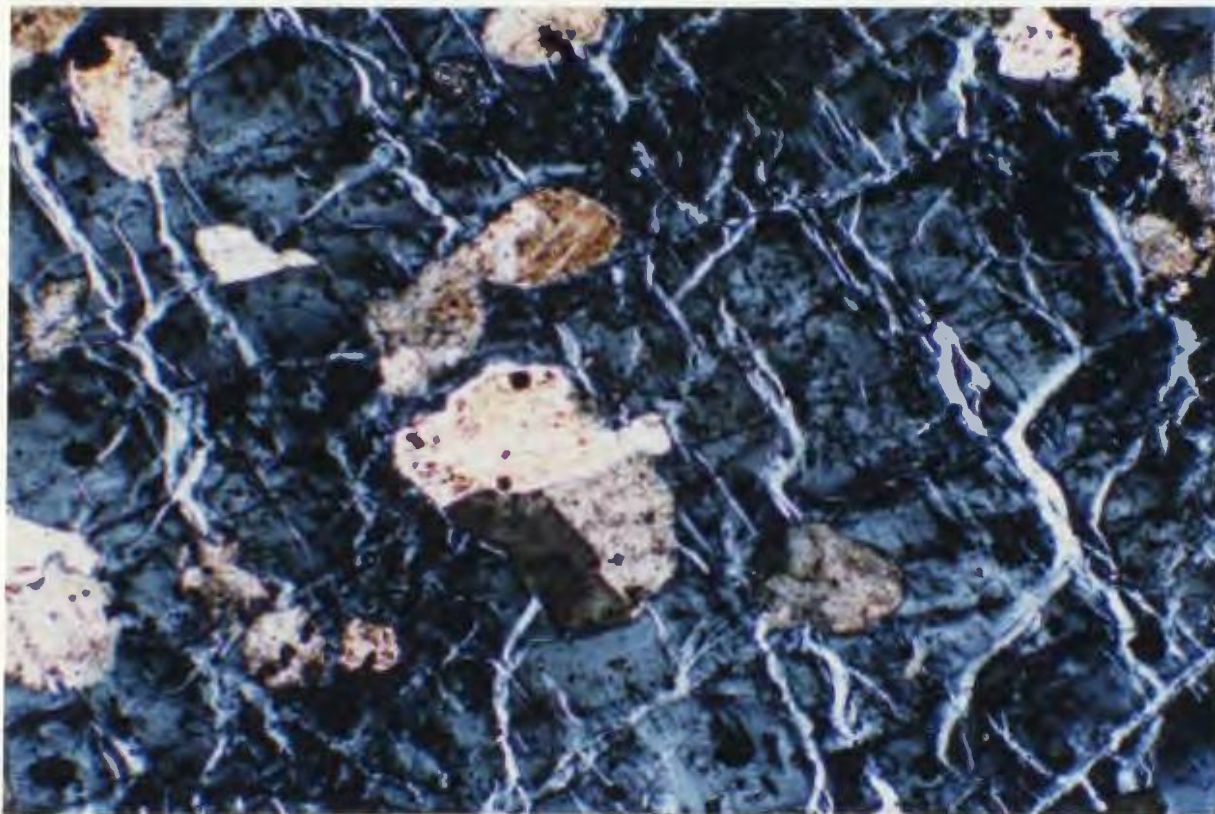
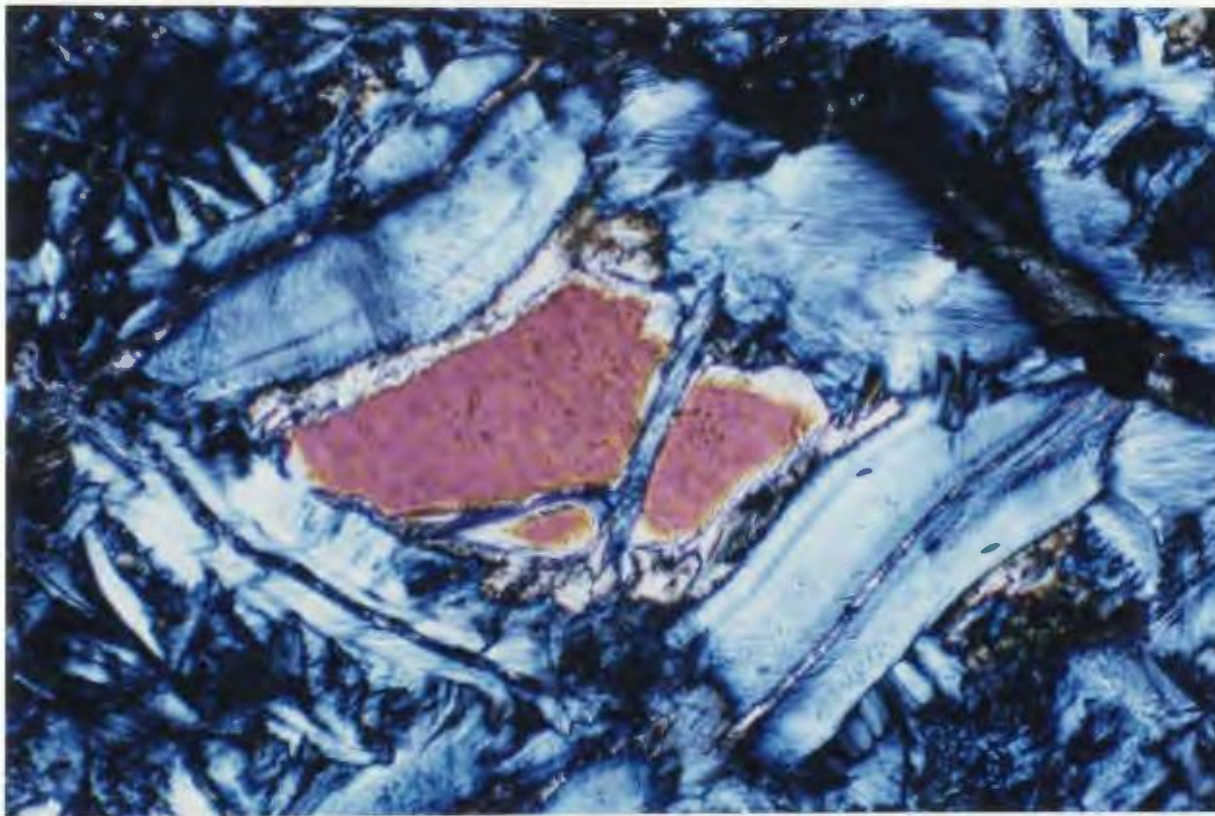
Mesh rims are bands (0.05 mm wide on average) composed of  $\alpha$ -serpentine which under high magnification is seen to be composed of "apparent fibres" lying at high angle (commonly varying within the same thin section from 45° to 90°) to the rim walls (Figs 6.1.a and 6.2). Compared to the mesh centers, the mesh rims exhibit a pale yellow-green color in plane polarized light, extinguish with an undulatory pattern (suggesting that they consist of fine fibres) and typically show higher relief and higher birefringence than the mesh centers. Rarely the mesh rims may contain minute magnetite grains.

The central parting of the mesh rims is a very narrow (0.005 to 0.02 mm) strip, most commonly composed of  $\gamma$ -

**Fig 6.2** Serpentinized dunite fragment in mélange with pseudomorphic  $\alpha$ -mesh texture. Photomicrograph shows a large mesh cell with a relict olivine mesh center (purple) surrounded by a colorless lizardite + brucite corona (cream and brownish) enclosed in lizardite mesh rim (blue). The lizardite mesh rim is composed of  $\alpha$ -serpentine pseudofibres inclined to the walls. Also visible is the very narrow central parting separating the mesh cells. In the lower right hand corner, a mesh cell with a lizardite + brucite mesh center is visible. Specimen 103; X 20; crossed polars; bar represents 0.1 mm.

**Fig 6.3** Serpentinized dunite fragment in tectonic mélange with pseudomorphic  $\gamma$ -mesh texture.  $\gamma$ -serpentine lizardite composes the mesh rims (white) and also the nearly isotropic (blue) mesh centers. Large brucite grains (buff) contain numerous magnetite inclusions (black). Specimen 205-B; X 10; crossed polars; bar represents 0.2 mm.





serpentine having high birefringence (Fig 6.2), but in some cases of unidentified isotropic material.

$\gamma$ -serpentine mesh texture (Figs 6.1.d and 6.3) is a less common mesh texture having mesh rims of positive elongation. Much of the difference between the ordinary ( $\alpha$ - mesh) and  $\gamma$ -serpentine mesh textures occurs in the mesh rim. The  $\gamma$ -serpentine mesh rim is commonly a very narrow band with high birefringence, positive elongation and higher relief than the mesh center. Mesh rims have sharp contacts with the mesh centers and do not display the obvious pseudofibrous character of  $\alpha$ -serpentine mesh rims. Where the serpentine elongation can be determined, the mesh centers have been found to have the same positive elongation as the mesh rim, but more commonly they are composed of isotropic or nearly isotropic serpentine with very low birefringence.

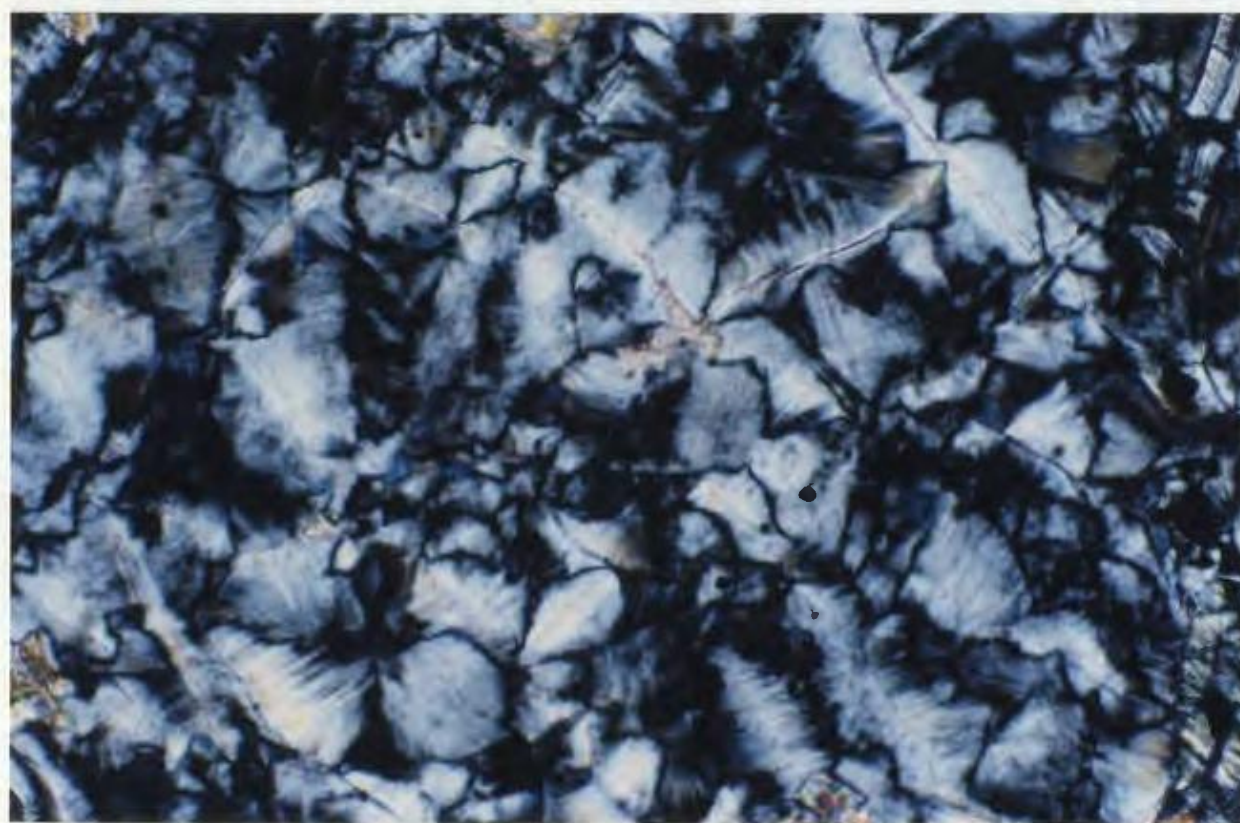
Banded growth or curtain-like texture occurs rarely in fragments of Coy Pond tectonic mélanges. Such a texture is similar to regular mesh textures except that one set of subparallel mesh rims is developed at the expense of the adjacent mesh rims at right angles (Figs 6.1.c and 6.4). All serpentinite specimens with banded growth texture are composed of rows of  $\alpha$ -serpentine.

Hourglass texture (Figs 6.1.b and 6.5 to 6.9) occurs quite commonly in tectonic mélange fragments, all of them being composed of  $\gamma$ -serpentine. Mesh cells are on average 0.2 mm



**Fig 6.4** Photomicrograph representing banded growth or curtain-like texture. Oriented vertically are bands of  $\alpha$ -serpentine lizardite (at extinction). Vertical bands are separated by narrow isotropic (black) central partings consisting of isotropic serpentine. Small magnetite grains are in black.  
Specimen 203-B; X 10; crossed polars; bar represents 0.2 mm.

**Fig 6.5** Photomicrograph showing representative general view of pure hourglass texture. Pseudofibrous  $\gamma$ -serpentine lizardite comprises the cells, which are bordered by very narrow central partings. A few small magnesite grains are distinguished by their high birefringence colors.  
Specimen 79-C; X 40; crossed polars; bar represents 0.04 mm.



in diameter (range 0.05 to 0.5 mm) having polygonal or oval shapes. The very narrow ( $<0.01$  mm) central parting is invariably composed of a high birefringent serpentine strip (Figs 6.6 and 6.7) commonly outlined by minute magnetite grains (Figs 6.8 and 6.9). The hourglass texture varies from pure (Figs 6.5 and 6.6) to incomplete (Figs 6.7 to 6.9). In the case of pure hourglass textures, the recrystallization of serpentine was uninterrupted from the central parting to the cell center and is common in smaller cells. Large cells have either a core of isotropic serpentine (composed of a very fine  $\alpha$ - and  $\gamma$ -serpentine intergrowth) as in Fig 6.7, or consist of a brucite-lizardite intergrowth (Figs 6.8 and 6.9). Brucite intimately intergrown with lizardite has been found in the centres of hourglass textures where it shows a fibrous habit, lower relief than lizardite and exhibits anomalous honey-yellow birefringence colors (Figs 6.8 and 6.9).

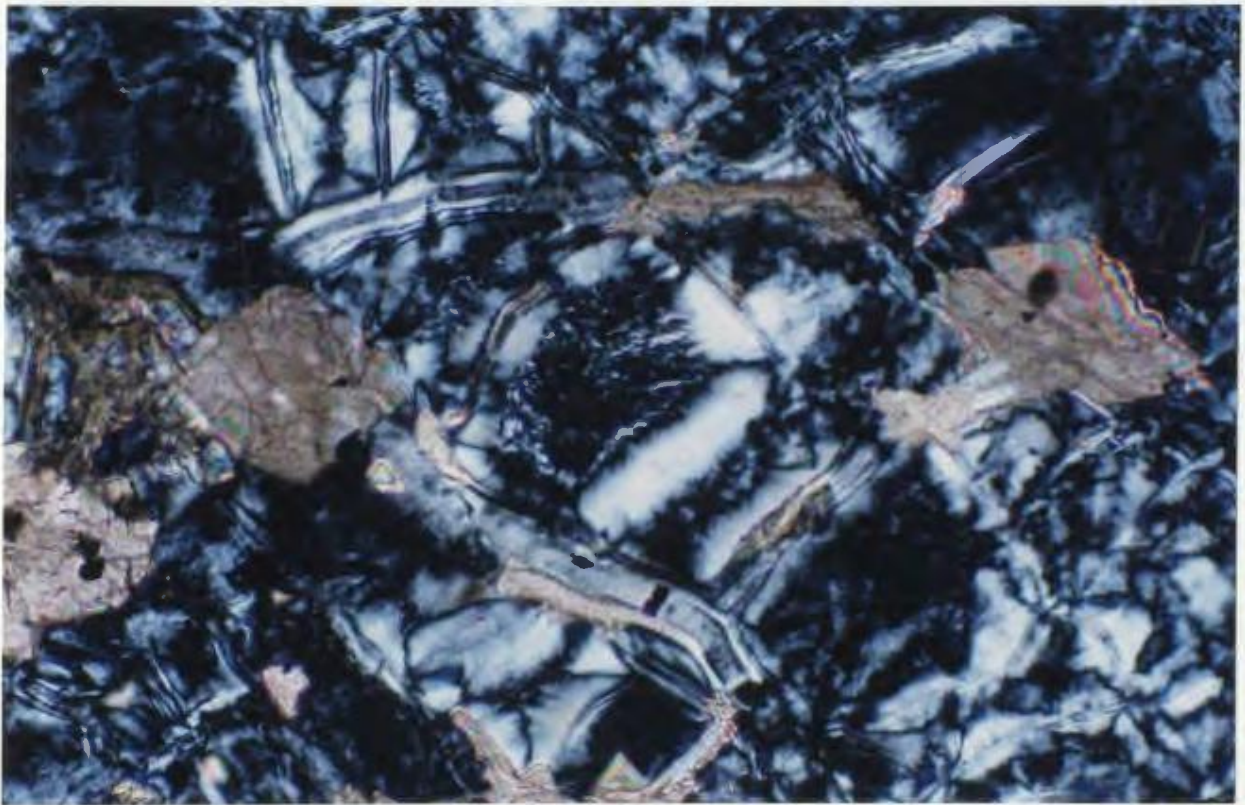
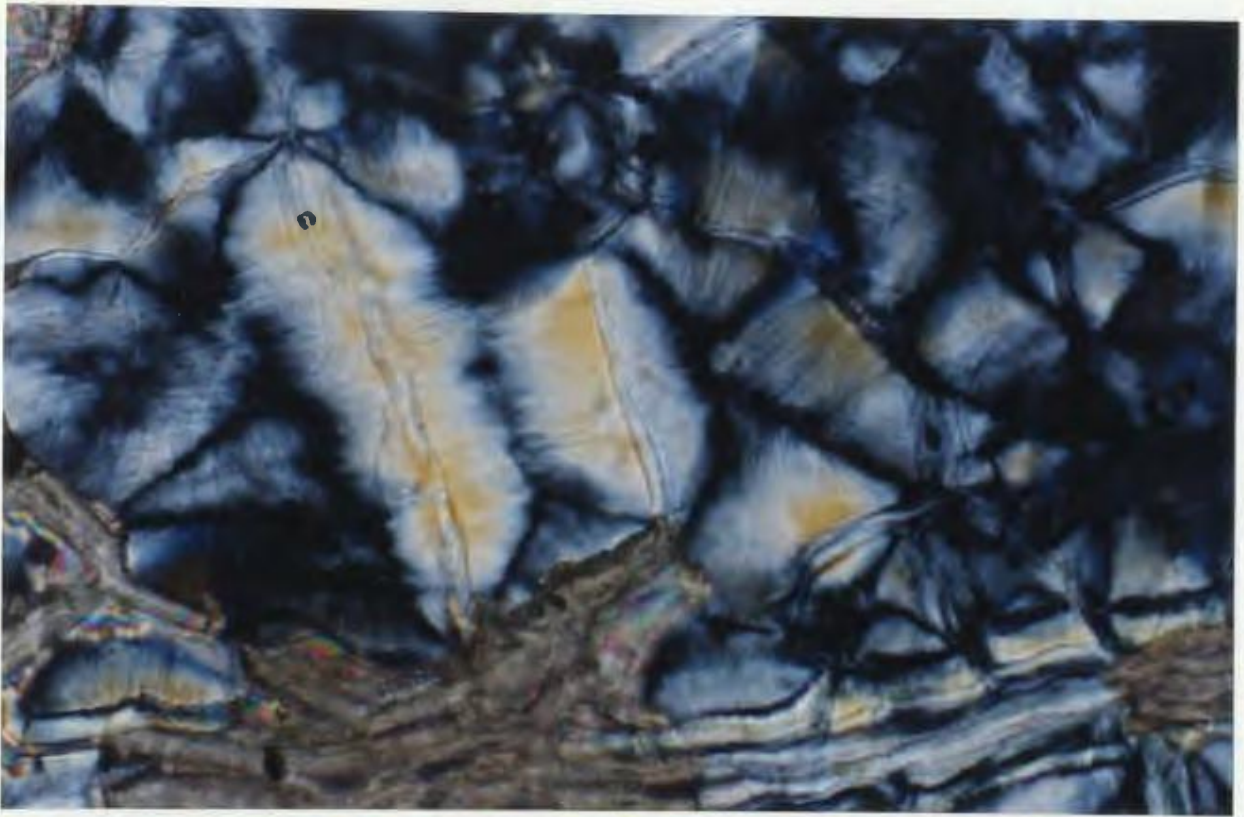
The presence in brucite-bearing samples of opaque minerals such as awaruite ( $\text{Ni}_3\text{Fe}$ ) and heazlewoodite ( $\text{Ni}_3\text{S}_2$ ) provides evidence of the extremely oxygen-deficient environment during serpentinization (see also Moody, 1976).

**Bastite**, the serpentine texture after pyroxenes, is very common in serpentinite mélange fragments. Orthopyroxene-bastite, the most common form of bastite,

**Fig 6.6** Detail of 6.5. In the central part of the photomicrograph, a pure hourglass cell of pseudofibrous  $\gamma$ -serpentine lizardite. Central partings appear as two parallel lines. High relief brownish material in the left and bottom parts of the figure is skeletal magnesite, preferentially replacing the central partings. Specimen 79-C; X 40; crossed polars; bar represents 0.04 mm.

**Fig 6.7** Serpentinized dunite fragment in mélange with hourglass texture. In center, incomplete hourglass texture with isotropic (deep blue) mesh center is developed. In the upper left hand corner, is a small pure hourglass cell (rectangular shape) with  $\gamma$ -serpentine pseudofibrous lizardite developed in the centers between two narrow central partings (vertical). Small pure hourglass cells are also visible in the lower right hand corner of the microphotograph. Several grains of magnesite (pale brown) occur in the figure. Specimen 79-C; X 20; crossed polars; bar represent 0.1 mm.

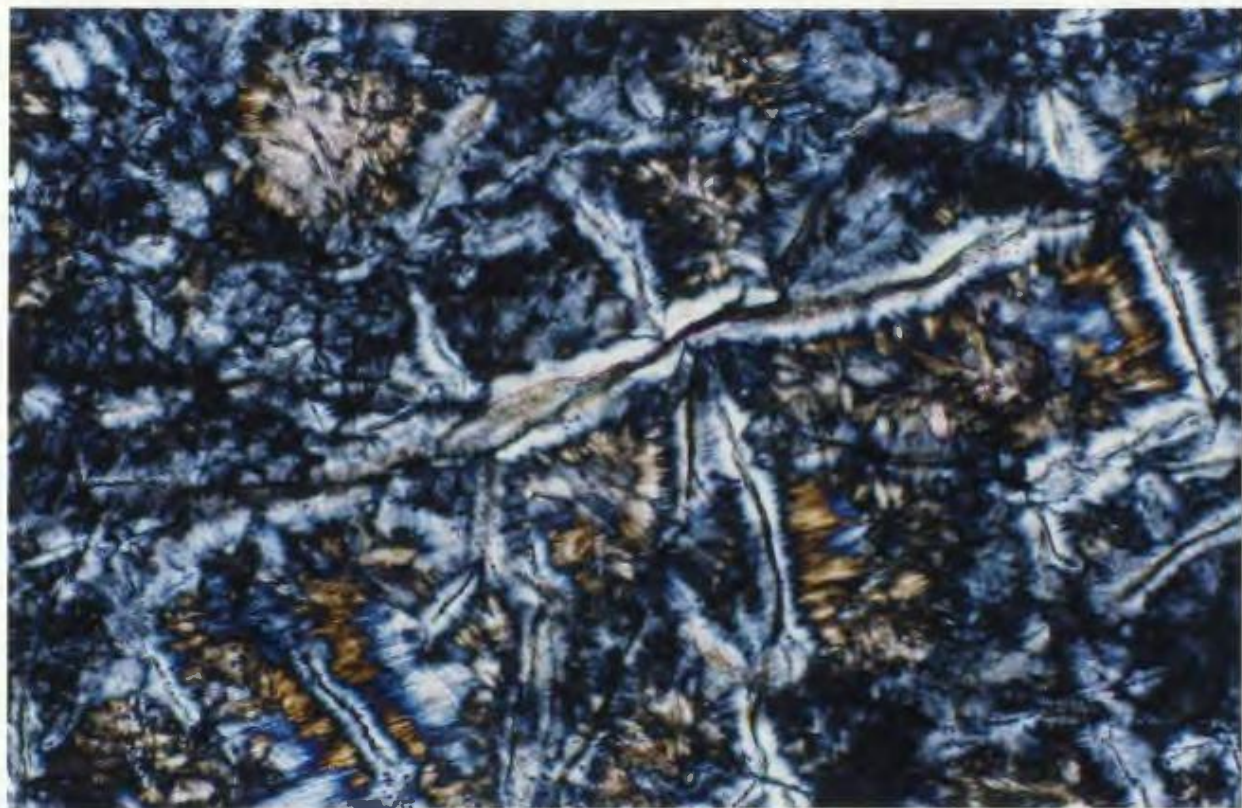




**Fig 6.8** Serpentinite fragment in tectonic mélange with hourglass texture. Bluish is  $\gamma$ -serpentine lizardite, yellowish to brown is brucite-lizardite intergrowth. Specimen 196; X 20; crossed polars; bar represents 0.1 mm.

**Fig 6.9** Same as 6.8; plane polarized light. Hourglass cells are outlined by trains of magnetite grains located in central partings. Also visible is brucite-lizardite intergrowth (brownish) developed towards the centers of the cells conferring a fibrous appearance. Specimen 196; X 20; bar represents 0.1 mm.





occurs as a minor phase, <5% in serpentized dunite fragments and up to 20-30% in serpentized harzburgite fragments. Clinopyroxene-bastite is rare (<1 %) and occurs only in serpentized harzburgite fragments.

The dominant feature of the orthopyroxene-bastite is the uniform replacement of the parent pyroxene by  $\gamma$ -serpentine. The bastite may appear to be either pseudofibrous (Figs 6.1.e; 6.10; 6.12 and 6.13) with the fibres parallel to the length of the pyroxene prism, or smooth featureless plates (Figs 6.11 to 6.14). Clinopyroxene-bastite occurs mainly as serpentized clinopyroxene exsolution lamellae in orthopyroxene (Figs 6.12 to 6.14), and rarely as replacements of clinopyroxene grains, where it characteristically develops in an intergrowth of  $\alpha$ - and  $\gamma$ -serpentine fibres (visible in Fig 6.13). Such intergrowths have a yellow to green color, low birefringence and are commonly isotropic.

Magnesite is an ubiquitous phase in *mélange* fragments with pseudomorphic texture. All *mélange* fragments containing lizardite in mesh and banded growth textures are affected by carbonatization in variable proportions between 10 and 50%. Magnesite does not occur in fragments which contain the assemblage lizardite-brucite.

Magnesite replaces mesh textured lizardite pseudomorphically in tectonic *mélange* fragments.



**Fig 6.10** Photomicrograph of partially serpentized harzburgite fragment in tectonic mélange. Central part of the photomicrograph is a large orthopyroxene grain (cream) with an embayed outline due to partial replacement by olivine (high birefringence colors). Orthopyroxene has olivine inclusions, shows good cleavage and numerous fractures. The large orthopyroxene is surrounded by smaller fragments produced by fragmentation and pulling-apart during crustal deformation. The upper half of the crystal has been replaced by pseudofibrous  $\alpha$ -lizardite bastite (white), which preserves the original cleavage and fractures. The blue-black material in the middle of the bastite is a relict olivine grain serpentized to mesh texture with visible rims and mesh centers. Specimen 175; X 2,5; crossed polars; bar represents 0.5 mm.

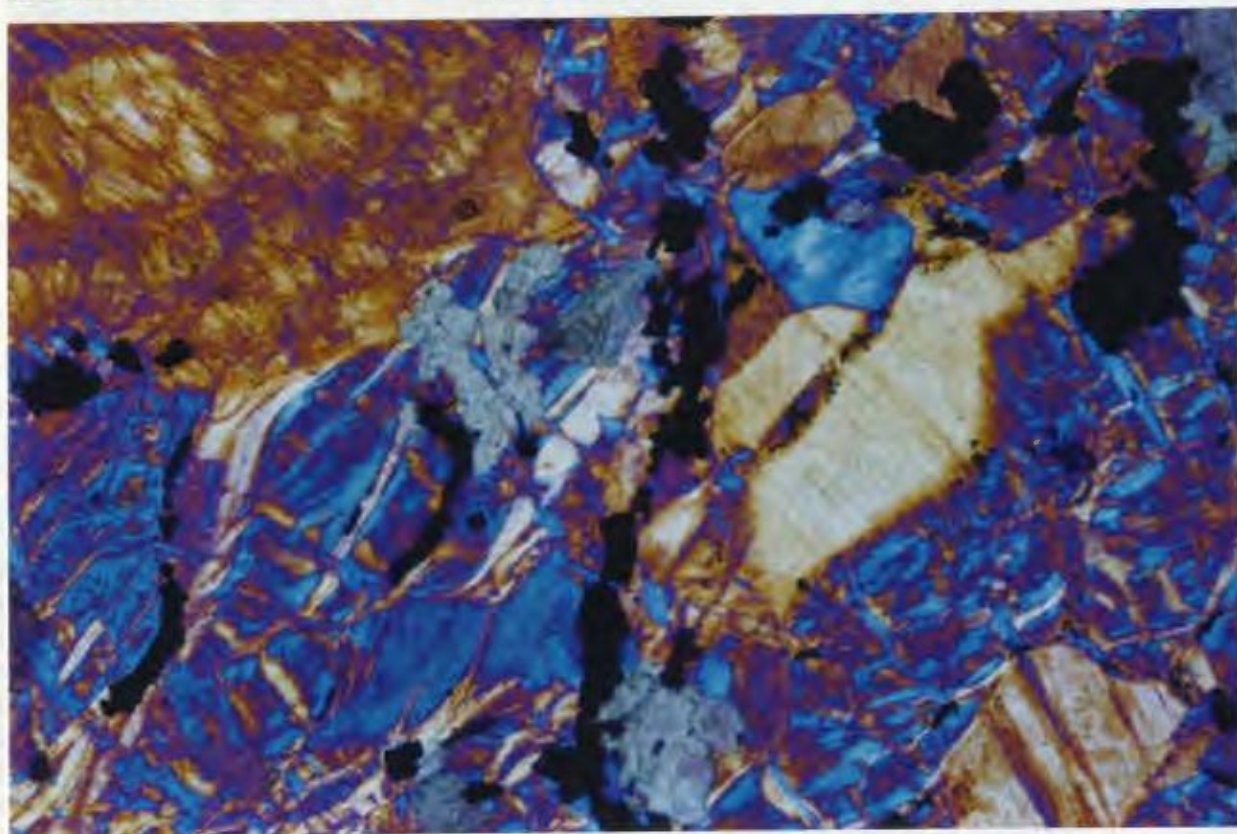
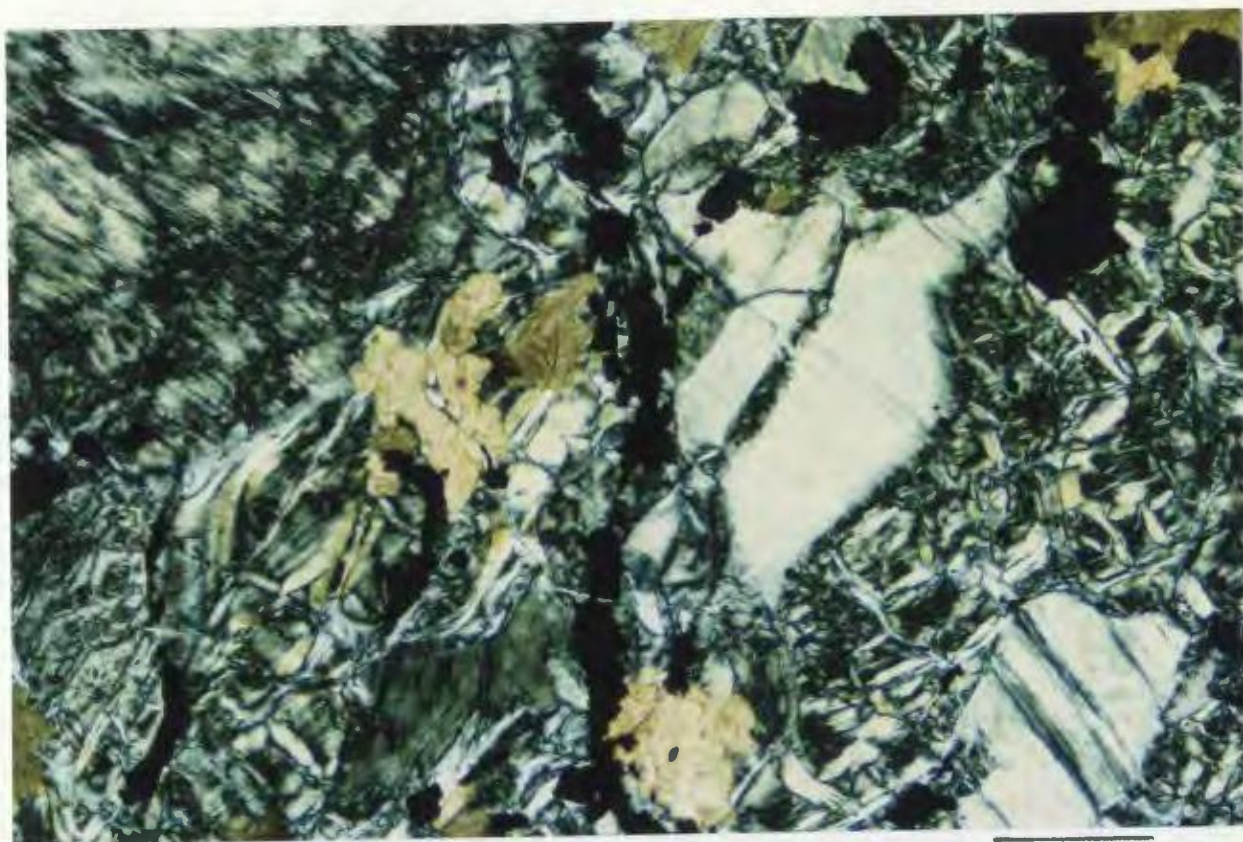
**Fig 6.11** Incompletely serpentized harzburgite fragment in tectonic mélange. Relict elongate and stretched orthopyroxene grain (yellow), partially replaced by platy lizardite-bastite (white). Blue-black is isotropic serpentine intergrown with fine-grained brucite inclusions (yellow). Specimen 175; X 10; crossed polars; bar represents 0.2 mm.



**Fig 6.12** Photomicrograph of serpentized harzburgite fragment in *mélange* showing bastite types. In the upper left hand corner is a large clinopyroxene-bastite with serpentine intergrowth. In the right of centre and in the lower right hand corner there are several platy orthopyroxene-bastites (white) with bastitized clinopyroxene exsolution lamellae. Serpentine mesh texture after olivine (with isotropic mesh centers and colorless mesh rims) occurs between bastite grains. In pale brown are magnesite grains, and in black are aggregates of magnetite grains. Specimen 450-C; X 10; crossed polars; bar represents 0.2 mm.

**Fig 6.13** Same as Fig 6.12 with gypsum plate inserted (orientation shown at edge of photomicrograph) to show constitution of bastite grains.  $\alpha$ - and  $\gamma$ -serpentine intergrowth in clinopyroxene-bastite grain in upper left hand corner;  $\alpha$ -serpentine of orthopyroxene-bastite in the right half of the figure. The mesh rims of the mesh texture ( $\alpha$ -serpentine) are represented by short strips colored in blue and orange color dependent on the orientation of the lizardite pseudofibres with respect to the gypsum plate. Specimen 450-C; X 10; crossed polars; 6.14 crossed polars and gypsum plate; bar represents 0.2 mm.

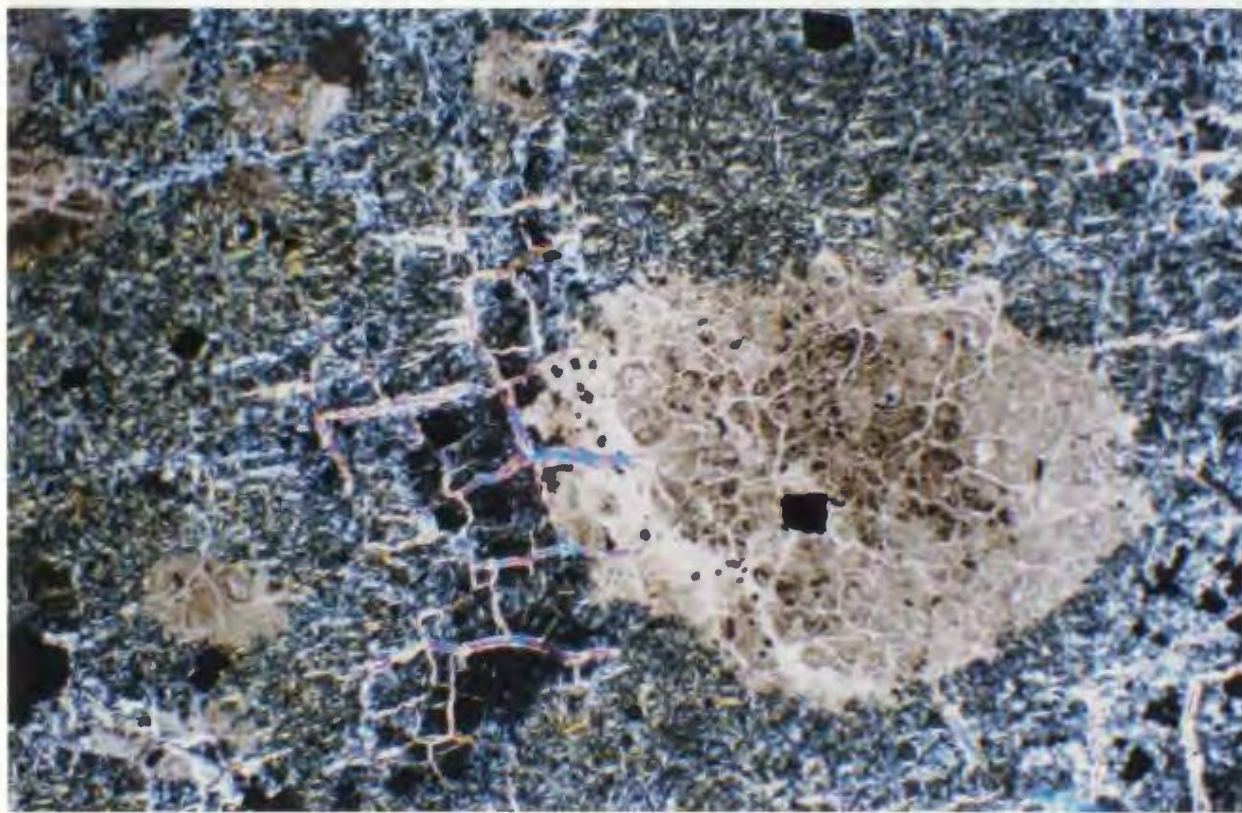
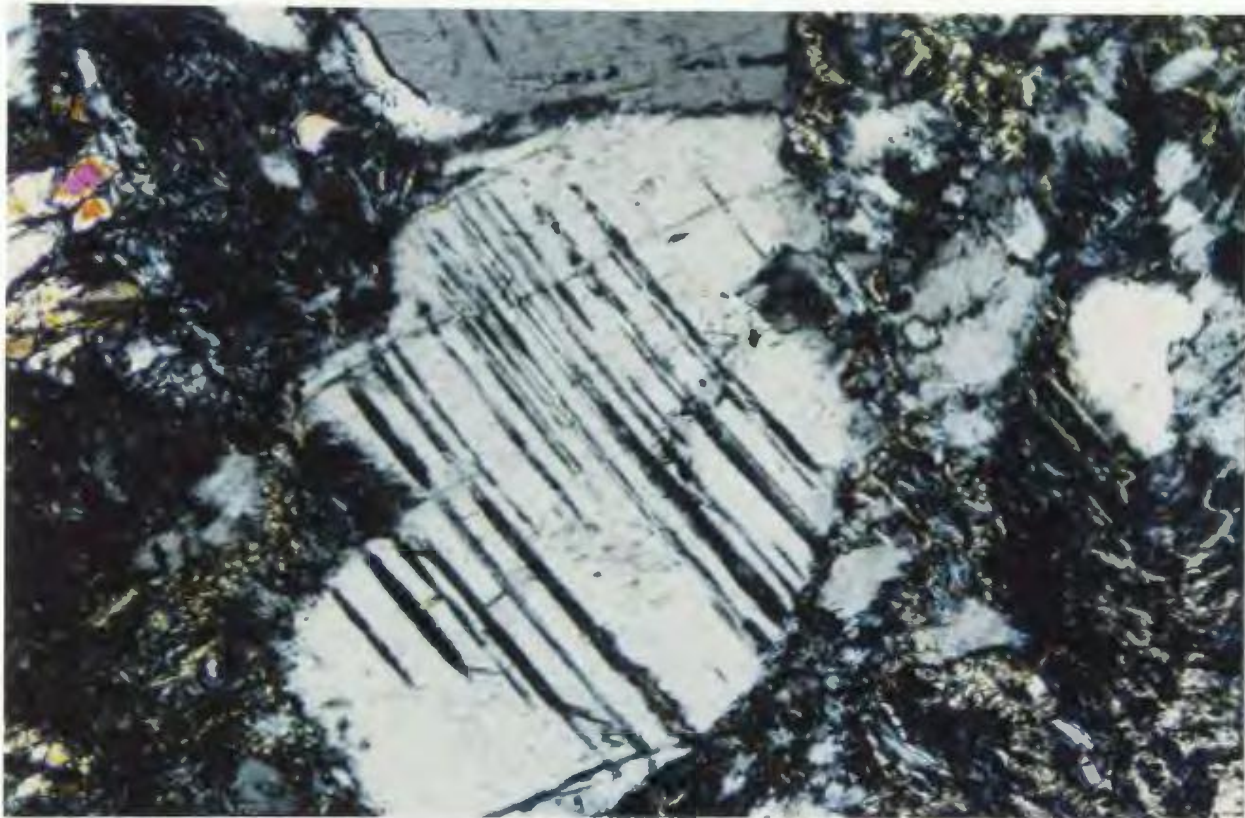




**Fig 6.14** Completely serpentized harzburgite fragment in mélange. In central part of the figure large, an orthopyroxene grain is broken into two fragments, one being slightly rotated with respect to the other (mantle deformation). The grains are replaced by platy orthopyroxene-bastite with clinopyroxene-bastite in exsolution lamellae. The surrounding olivine has been replaced by isotropic serpentine, but a few relict grains (reddish) are preserved near the upper left margin of the figure. Brucite occurs as small flakes (yellow) within isotropic lizardite (black). Brucite occurrences in harzburgites have not been previously mentioned in the literature.  
Specimen 313; X 10; crossed polars; bar represents 0.2 mm.

**Fig 6.15** Photomicrograph of a serpentized dunite fragment in mélange showing carbonate pseudomorph after mesh textured lizardite. Lizardite (green to bluish) occurring as  $\alpha$ -serpentine mesh texture, is partially replaced by magnesite (light brown). The central parting and the mesh rim are replaced by clear, light brown magnesite, whereas the impurities are concentrated in the mesh centers (dark brown). To the left of the large magnesite is an isotropic serpentine vein (bluish and black) cut by short chrysotile gash veins (high birefringent colors). Chrysotile veinlets with a rectangular pattern formed as a result of volume increase during serpentization.  
Specimen 432-C; X 2.5; crossed polars; bar represents 0.5 mm.





Details of the original lizardite mesh texture are easily recognizable where large composite magnesite grains replace several lizardite mesh cells (Fig 6.15). Mesh centers are typically replaced by cryptocrystalline magnesite and mesh rims by spathic magnesite.

A large part of the magnesite is found as isolated cryptocrystalline patches or aggregates chaotically distributed throughout the rock. These patches may be rounded or irregular in form, up to 3 mm in diameter (Fig 6.15), contain many minute inclusions, and are not apparently connected to each other in the plane of the section. Locally parts of the carbonate aggregates have recrystallized into carbonate grains with crystallographic faces, good cleavages and few impurities (spathic magnesite).

In serpentized harzburgite fragments, the lizardite-bastite seems to be unaffected by carbonatization.

#### Conclusions on pseudomorphic textures

Pseudomorphic textures of serpentine after olivine and pyroxene outline the grain shapes of the original minerals and provide information about the primary texture of the ultramafic protolith. The abundance of small (<2 mm) individual mesh cells unrelated to each other, and the scarcity of regions with a regular rectangular mesh texture



imply that the dunite protolith had a granoblastic texture. The original cumulate fabric of these dunites was probably obliterated during shearing and production of the tectonic mélanges. Several serpentinitized harzburgite fragments show tectonite fabrics, including orthopyroxene porphyroclasts (Figs 6.10 and 6.11) that resulted from extensive plastic deformation and recrystallization under mantle conditions. In serpentinitized samples, these now appear as orthopyroxene-bastite pseudomorphs (which preserve the elongate, stretched and commonly pulled-apart porphyroclastic texture) in a mosaic of individual serpentine mesh cells. Kink bands and exsolution lamellae (Figs 6.12 to 6.14) are also recorded by the bastites. Petrographic details show that the porphyroclastic texture of serpentinitized harzburgite fragments in the tectonic mélanges is similar to that in the unserpentinitized harzburgite tectonite.

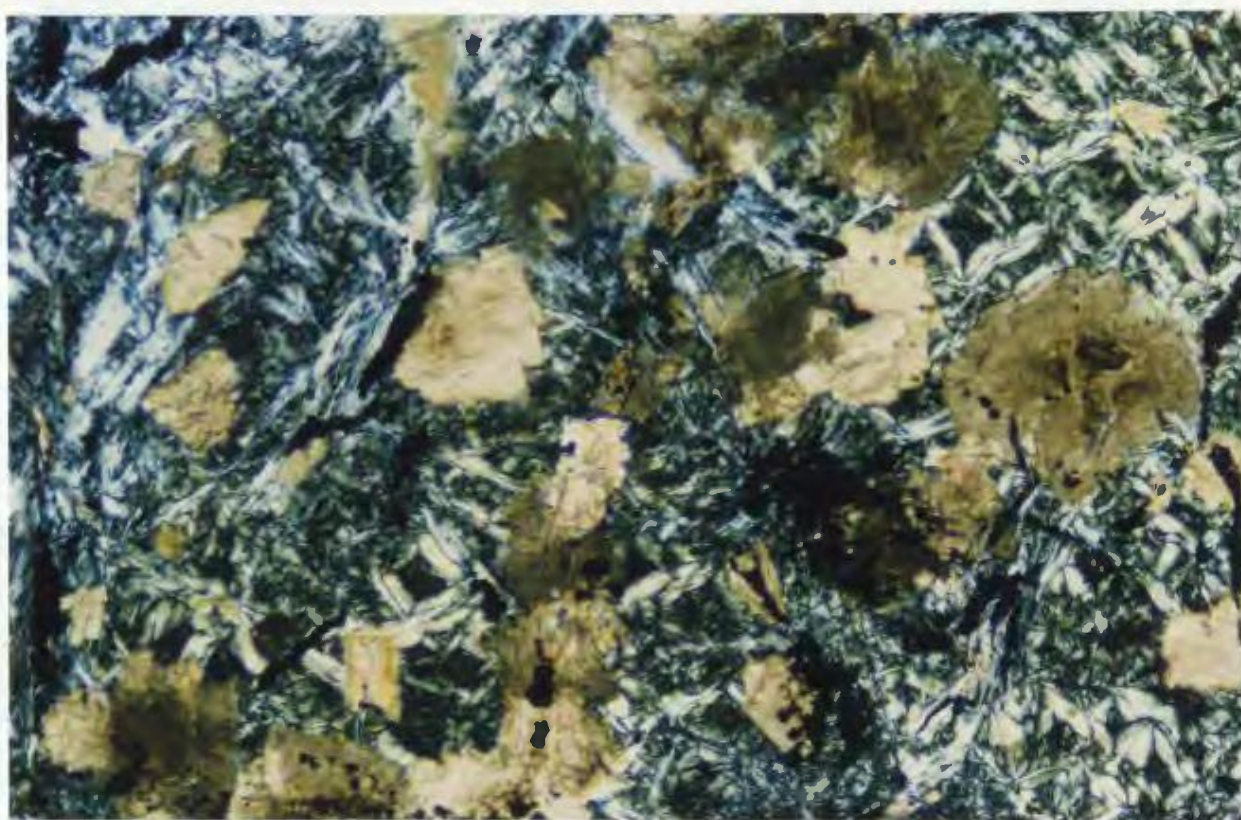
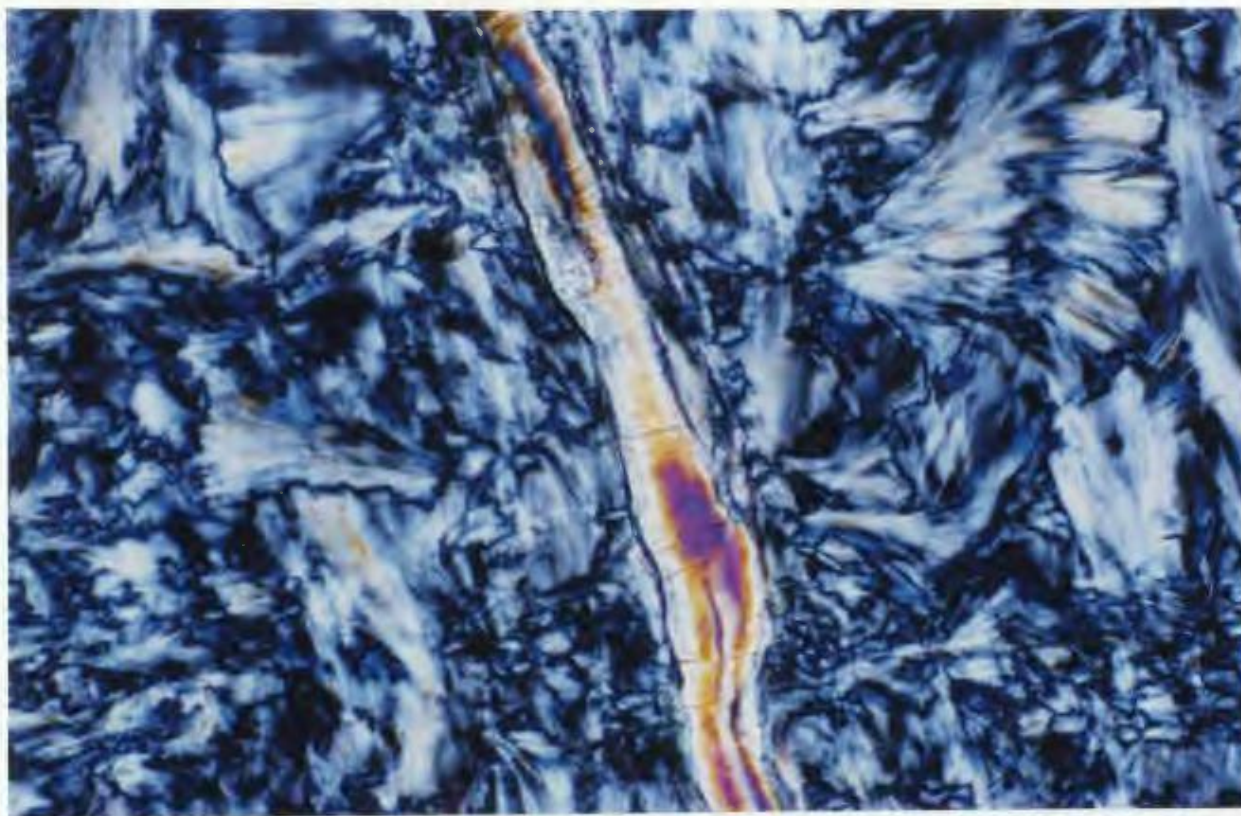
#### 6.2.2 Serpentinite fragments with non-pseudomorphic textures

Approximately 75% of Coy Pond serpentinite fragments display non-pseudomorphic textures which may be subdivided into interpenetrating and interlocking types.

Interpenetrating texture is the most common non-pseudomorphic texture in tectonic mélange fragments (Figs 6.16 to 6.18). X-ray powder diffraction analyses have shown

**Fig 6.16** Photomicrograph showing serpentinite fragment in tectonic mélange with non-pseudomorphic texture. Antigorite blades with ragged margins are arranged in an interpenetrating texture. Some of the blades are fan-shaped, others are in radiating arrangement. The veinlet with high birefringence colors is chrysotile composed of cross-fibres normal to the walls. Specimen 160-B; X 20; crossed polars; bar represents 0.1 mm.

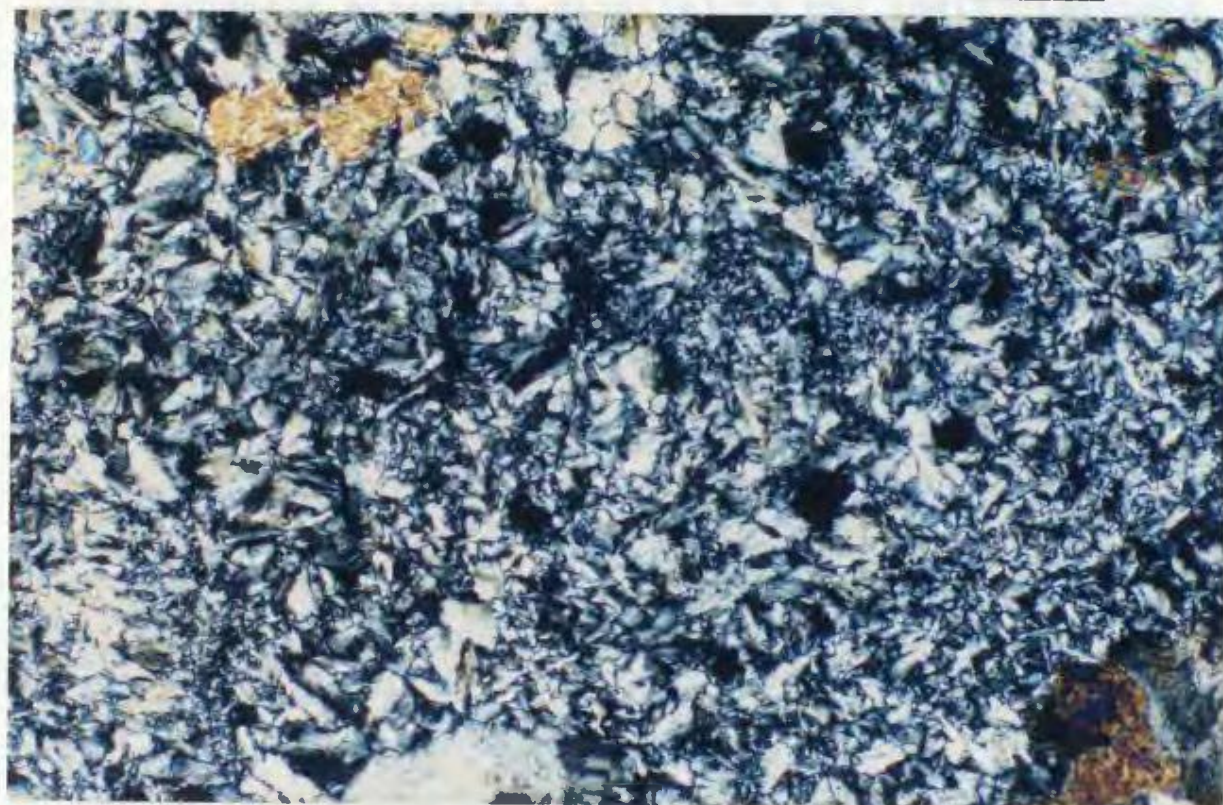
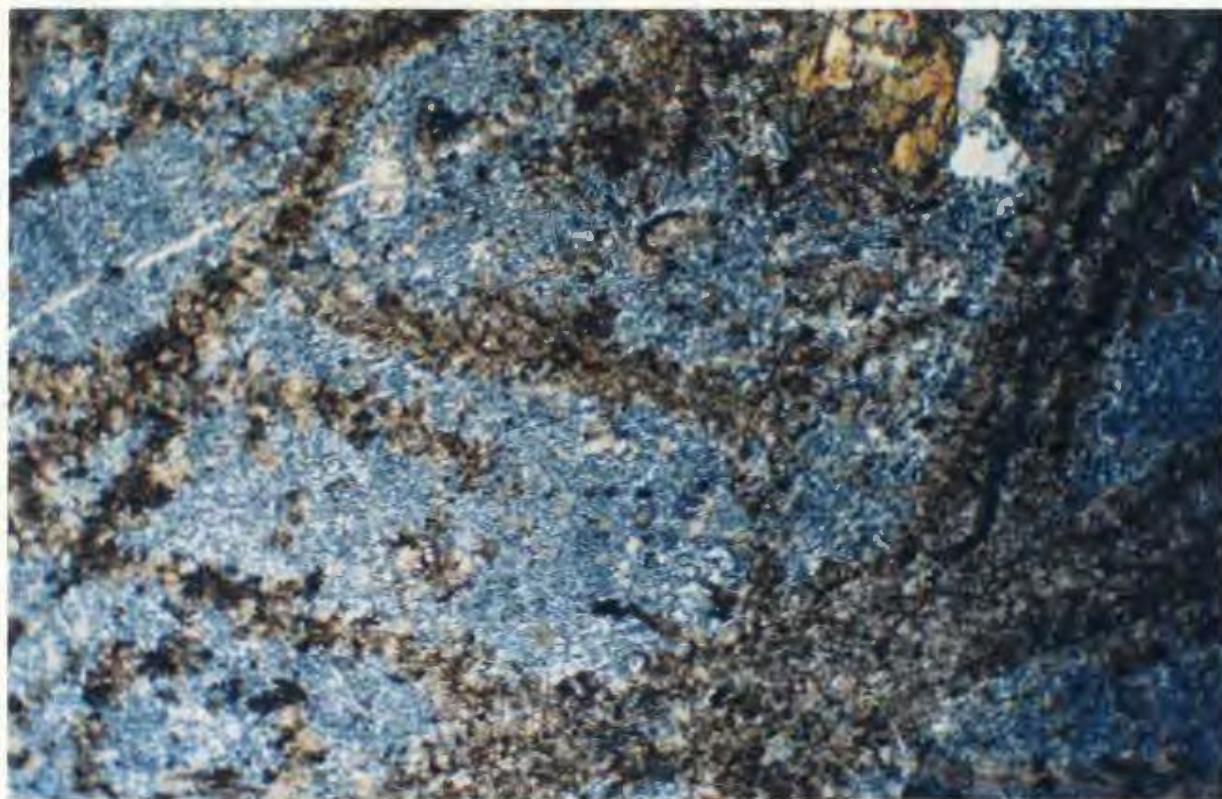
**Fig 6.17** Photomicrograph of serpentinitized fragment in mélange showing the transition from pseudomorphic to non-pseudomorphic texture. The left two thirds of the figure shows mesh-textured lizardite with cells having isotropic centers (dark green to black) and wide mesh rims (white and pale yellow). Most of the mesh cells are undisturbed and have regular rectangular or square shapes. In the lower right hand corner, antigorite blades (bluish) in interpenetrating texture have replaced lizardite. Anhedral brownish grains are magnesite. Dark brown and cloudy material is cryptocrystalline magnesite which preferentially replaces mesh-textured lizardite; pale brown, clear material is crystalline magnesite which replaces antigorite. Aggregates of secondary magnetite are black. Specimen 450-C; X10 ; crossed polars; bar represents 0.2 mm.



**Fig 6.18** Partially carbonatized serpentinite fragment with interpenetrating texture. Antigorite blades (blue) in fine interpenetrating texture are replaced by magnesite (brown) along fractures. In the upper right hand corner is a talc-carbonate aggregate (orange) on relict bastite (white). White veinlet in the upper left part of the figure is a relict chrysotile vein. Specimen 343-D; X 1.5; crossed polars; bar represents 1 mm.

**Fig 6.19** Photomicrograph of serpentinite fragment in mélange with interlocking texture. In the upper left and lower right hand corners, small magnesite grains with high birefringence colors are replacing antigorite. Specimen 252-E; X 40; crossed polars; bar represents 0.04 mm.





that these textures consist mainly of antigorite.

Interpenetrating texture begins to develop as isolated blades or flakes or fan-shaped bundles of blades of  $\gamma$ -serpentine antigorite (Fig 6.17) associated with all types of pseudomorphic textures. Usually the recrystallization starts at mesh centers and progresses until the blades begin to interfere with one another in an interpenetrating fabric. The radiating antigorite blades commonly do not exceed 0.5 mm in length (Fig 6.16). Specimens completely transformed to interpenetrating textured antigorite are common, but many still contain relict mesh textures (Fig 6.17). Optically the antigorite has a fibrolamellar to platy form (Fig 6.16) with crystals elongated parallel to the (001) cleavages. Most have feathery, ragged terminations. Under plane light the antigorite is colorless and has higher relief than lizardite. Under crossed polars antigorite exhibits wavy extinction, positive elongation and commonly anomalous bluish birefringence colors.

Interlocking texture occurs in several of the Coy Pond mélange fragments, all of them being composed of antigorite (X-ray powder diffraction determinations). Under high power it can be seen that the texture is composed of very small (<0.05 mm), equant and irregular antigorite flakes that form a tight interlocking fabric (Fig 6.19).

Magnesite is a major component of mélange fragments with

non-pseudomorphic textures, comprising amounts from several percent to more than 50 % of the rock volume. Magnesite occurs in both microcrystalline and spathic (crystalline) varieties in both lizardite and antigorite serpentinite. Spathic magnesite occurs as disseminated grains (Fig 6.17) or forms a sub-rectangular, locally anastomosing network of grains enclosing relict antigorite patches (Fig 6.18). Commonly the grains contain a core of brownish cryptocrystalline magnesite surrounded by a clear crystalline magnesite rim. Cryptocrystalline magnesite occurs on antigorite in trace amounts as minute rhombohedral grains.

#### 6.2.3 Talc-magnesite fragments

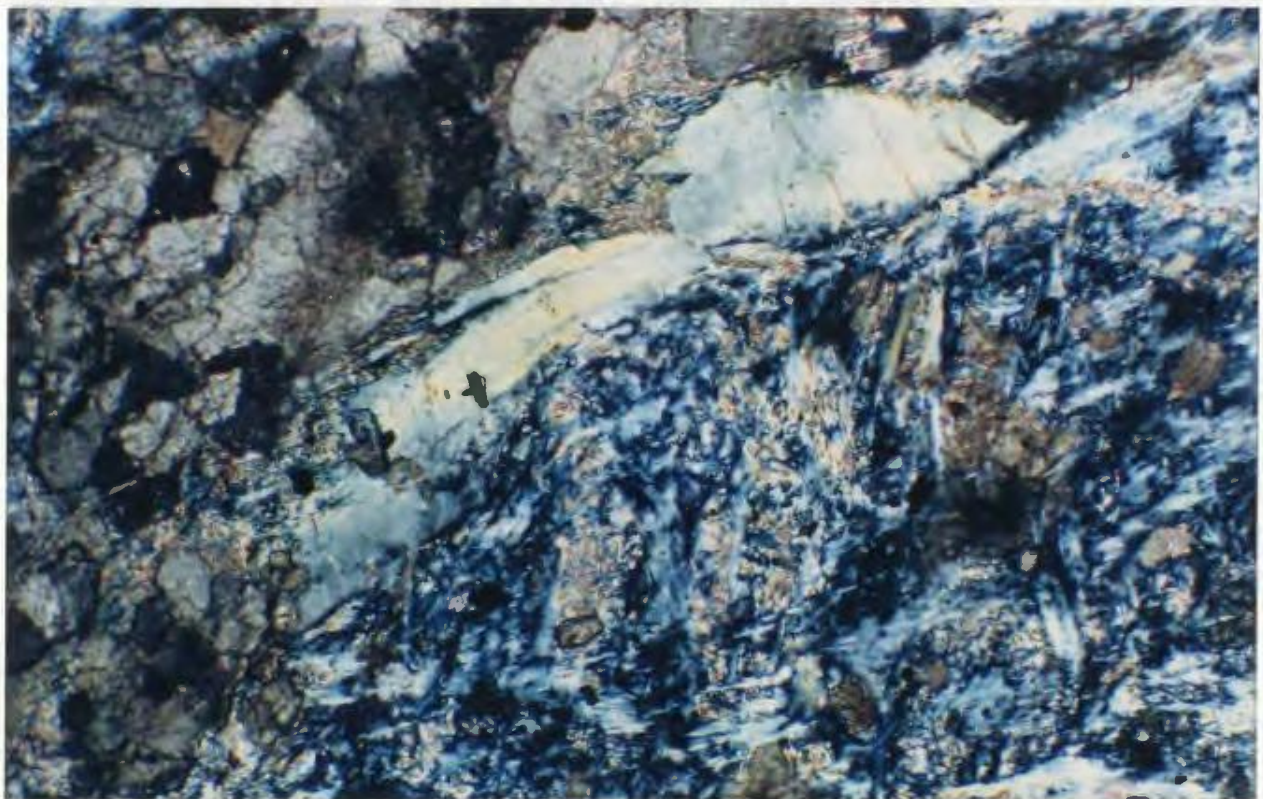
The assemblage talc-magnesite occurs in fragments in the tectonic mélanges in which >50% of the serpentine has been replaced; relict serpentine, where present is commonly antigorite. In the western tectonic mélange, about 20% of the fragments and most of the matrix are composed of talc-magnesite, whereas in the eastern tectonic mélange talc-magnesite forms less than half of the total material.

In talc-magnesite bearing fragments (Fig 6.20), talc replaces antigorite in interpenetrating or interlocking textures. Talc begins to form on serpentine minerals as



**Fig 6.20** Photograph of representative specimens of talc-magnesite fragments in mélange. Specimen 270 (black) is composed largely of magnesite (80 to 90%) and talc, and contains very finely disseminated magnetite (3-5%) which confers the black color to the rock. Specimens 272 (central upper part of the figure) and 252-E are examples in which there was segregation of magnetite (black) in veins during the carbonatization of the serpentinites. Brownish material is talc-magnesite. Specimen 252-E shows an alteration rind (brick red color, 1 cm thick composed of magnesium hydrocarbonates (hydromagnesite) and iron oxides) which is very characteristic of most of the tectonic mélange rocks.

**Fig 6.21** Photomicrograph of talc-magnesite fragment in mélange. Relict antigorite (blue) with interpenetrating texture replaced by magnesite grains (brown) in left part of the figure. Small patches with high birefringence replacing antigorite and surrounding magnesite grains are aggregates of talc flakes. Talc is also visible as inclusions in some of the magnesite grains. The yellow-greenish elongated platy mineral in the center of the figure is chlorite. Specimen 432; X 10; crossed polars; bar represents 0.2 mm.



patches of minute flakes (Fig 6.21) which grow until, in completely reacted specimens, talc is a major component constituting between 40 and 70% of the rock volume. At this stage, talc constitutes the matrix phase enclosing carbonate grains or occurs as pockets among carbonate masses (Figs 6.22 to 6.24). The texture of talc-magnesite mélange fragments is commonly massive and granoblastic (Fig 6.23) or poorly granolepidoblastic depending upon the size and arrangement of the mineral grains.

Magnesite in talc-magnesite fragments is a major phase forming between 30 and 60% of the rock volume. As in serpentine-bearing assemblages, it occurs in both microcrystalline and crystalline varieties. Microcrystalline magnesite forms isolated crystals and aggregates of pale-brown grains with serpentine and magnetite inclusions, whereas crystalline (spathic) magnesite, which may form as much as half of the total magnesite, is commonly found as rims around microcrystalline grains (Fig 6.23), but also occurs as individual crystals. Spathic grains are typically less than 1 mm in size, with an elongate subhedral shape. Generally the grains show a preferred dimensional orientation which confers a crude foliation to the rock. Curved laths and fragmentation into subgrains are common.

Chlorite occurs in talc-carbonate fragments in amounts <10 % of the rock volume (Figs 6.21 and 6.23). In less

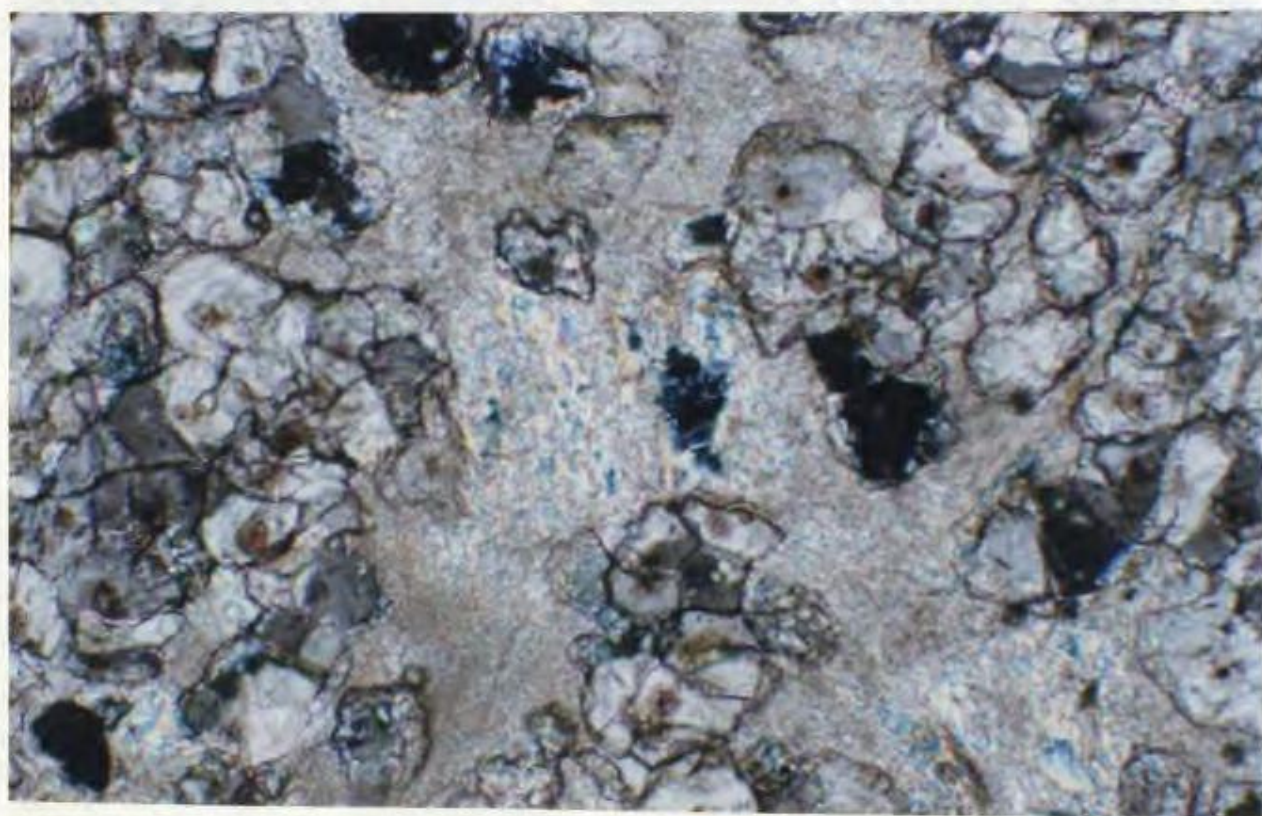
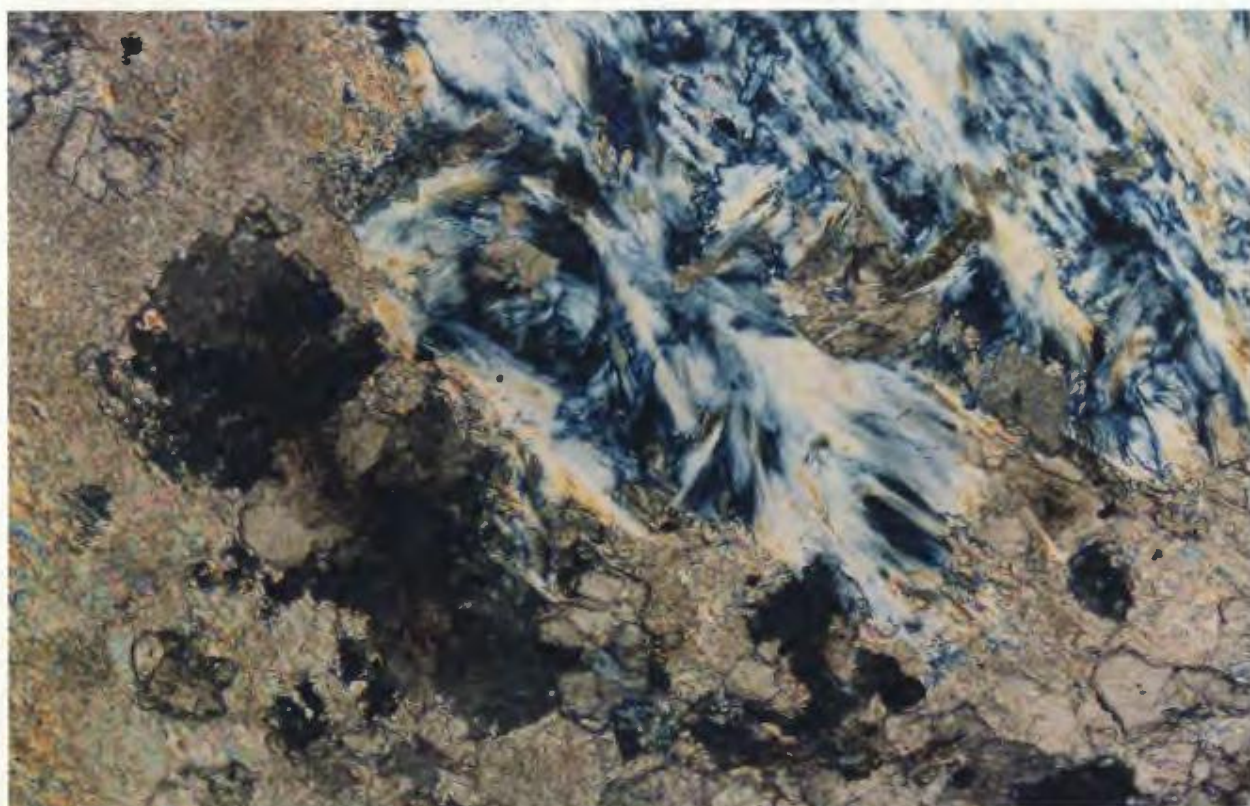
**Fig 6.22** Photomicrograph of talc-magnesite fragment in tectonic *mélange*. Centre and upper right hand corner show relict antigorite with interpenetrating texture overgrown by talc flakes (yellow-orange) and small magnesite grains (brown). In the rest of the figure, small talc grains (brown-red birefringence colors) with interlocking texture coexist with large magnesite grains (high relief). Minute talc inclusions are visible in the large magnesite grains at maximum extinction.

Specimen 432-C; X 10; crossed polars; bar represents 0.2 mm.

**Fig 6.23** Talc-magnesite fragment in tectonic *mélange*. Aggregate of magnesite grains with high relief is set in scaly talc groundmass. Magnesite grains are xenoblastic with microcrystalline centers and spathic rims. In the center of the figure, relict chlorite (deep blue) is partially replaced by talc.

Specimen 272; X 10; crossed polars; bar represents 0.2 mm.





carbonatized specimens chlorite occurs as plates (Fig 6.21) and aggregates of fine grains, whereas in talc-magnesite assemblages the chlorite occurs as diffuse relict patches in talc masses (Fig 6.23) or bordering magnesite grains.

Magnetite is commonly concentrated in veinlets (Fig 6.20) up to several mm in width and as a result the rock takes on a lighter color, typically pale green to yellow-green. During the carbonatization, larger Cr-spinel grains seem to become more fractured and pulled apart than in serpentinite fragments, although the smaller grains seem to be unaffected. Minute grains of high-sulfur minerals such as pentlandite  $(\text{Fe,Ni})_9\text{S}_8$  and linnaeite  $(\text{Co,Ni})_3\text{S}_4$  present in talc-magnesite fragments, indicate a relatively higher  $f_{\text{O}_2}$  (and also  $f_{\text{S}_2}$ ) during carbonatization compared to that during serpentinization (Ekstrand, 1975; Moody, 1976).

### 6.3. MATRIX OF TECTONIC MÉLANGES

The matrix forms between 10 to 25 per cent of most outcrops of the tectonic mélanges and typically weathers low compared to the fragments. The main structural feature of the matrix is the foliation, which at map scale is parallel to the boundaries of the unit. On outcrop scale, however, the foliation may be straight (Fig 6.24), anastomosing



**Fig 6.24** Field view of talc-magnesite matrix with subvertical foliation. In this example the talc-magnesite matrix constitutes a rectiplanar layer oriented parallel to the tectonic mélange boundaries. Location: outcrop 343 (see sample map).

**Fig 6.25** Field view of tectonic mélange with sheared serpentinite matrix and elongated serpentinite fragment in center of the figure. The sheared serpentinite matrix is strongly foliated and the central serpentinite fragment is oriented with its long axis in the plane of the foliation. Note minor brittle fractures in the fragment which extend beyond the margins into the matrix, indicating in situ conversion of fragment to matrix. Note also the evidence of sinistral shear of fragment causing extension parallel to foliation (as viewed in present position). Location: outcrop 343.



**Fig 6.26** Field photograph showing chaotically distributed serpentinite fragments (brick red) of various sizes in an anastomosing foliated matrix (black). Location: outcrop 343 (see sample map).

**Fig 6.27** Schistose serpentinite matrix slab cut normal to the foliation surface. The slab has a typical phacoidal shape (and is breaking down to smaller phacoids) produced by the shearing process. Black is schistose serpentinite (the S planes are visible only in thin section), and light colored veinlets are carbonate, mostly cryptocrystalline magnesite, developed along C planes. Specimen 255-C; scale in cm.





around large blocks (Fig 6.25), or irregular (Fig 6.26), reflecting the inhomogeneous nature of the shearing in the tectonic mélange unit. In general, areas of straight foliation correlate with a lower proportion of fragments and are interpreted to be loci of higher strain in which former fragments are comminuted and obliterated.

As can be readily seen in Fig 6.26 the first stage of matrix formation involved fragmentation and comminution of ultramafic blocks and fragments in the tectonic mélanges, resulting in the formation of sheared schistose serpentinite, coupled with progressive obliteration of all original structures. Subsequent stages of development of the mélange matrix involved more pervasive shearing (with a major component of simple shear) and pervasive to partial carbonatization (Figs 6.24 and 6.27 respectively).

In this study, the matrix of the tectonic mélange has been classified into four categories with respect to lithology and texture:

1. Schistose serpentinite matrix
2. Brecciated serpentinite matrix
3. Talc-magnesite matrix
4. Chlorite blackwall matrix

#### 6.3.1. Schistose serpentinite matrix

In contrast to massive serpentinite in the fragments which

characteristically weathers to a brick-red to orange-red colour, schistose serpentinite is brownish in outcrop (Fig 6.25) and grey on fresh surfaces (Fig 6.27). Schistose serpentinite is made up of slip-fibre serpentinite, which developed at the expense of massive serpentinite during shearing along planes of weakness, together with minor carbonate and oxide phases. The slip-fibre serpentine, which has been identified as lizardite with minor antigorite on the basis of XRD patterns, forms flattened phacoidal flakes which self-replicate at progressively finer scales with increasing degrees of shearing (Fig 6.27). Each flake has smooth polished surfaces, but a lineation is not present.

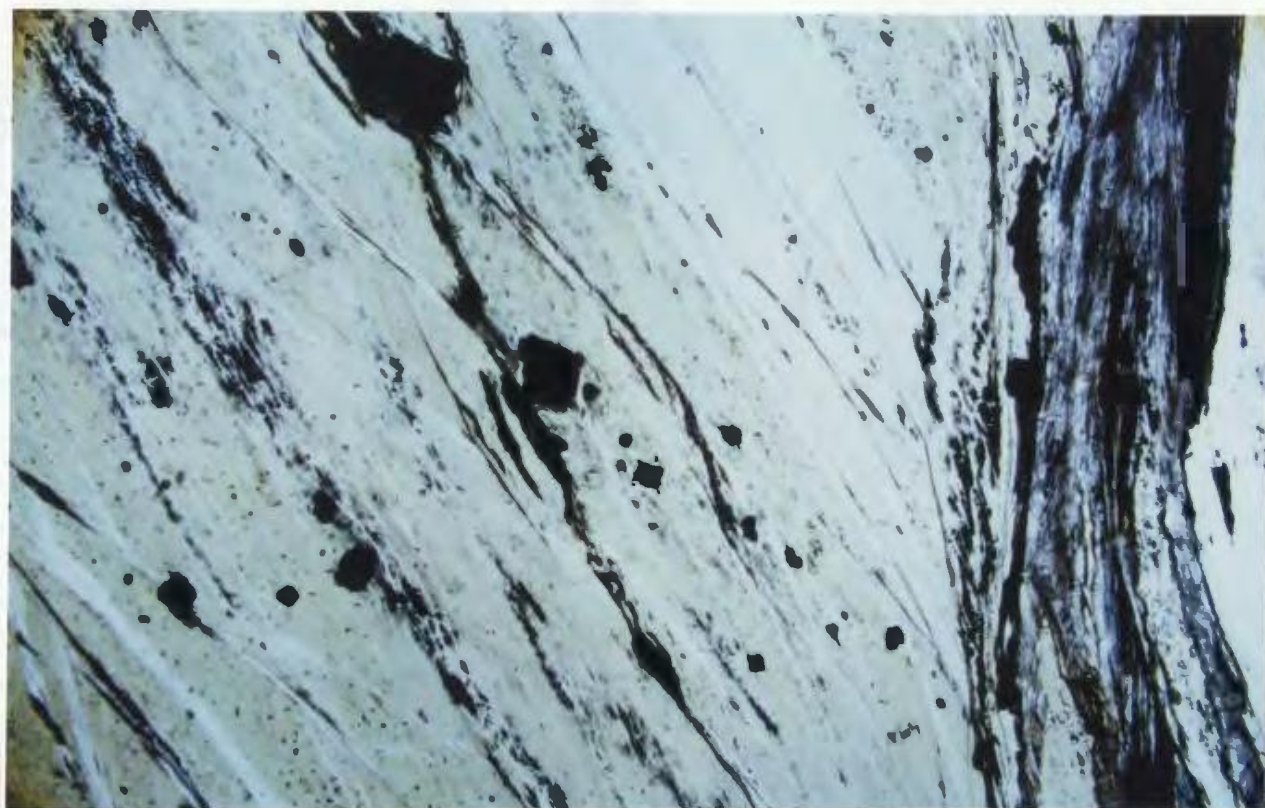
Lizardite in schistose serpentinite occurs in two forms, recrystallized and relict. In thin section, the recrystallized platy lizardite has a pale green color (Figs 6.28 and 6.29) and slightly higher relief than relict lizardite. Recrystallized lizardite, commonly forms platy grains < 5 mm in length that define the schistosity (S) planes (Figs 6.28 to 6.32), or more rarely occurs as longer grains defining microshear sets (C planes). In both cases lizardite is colorless and shows a sweeping extinction.

Relict lizardite on the other hand, displays disturbed mesh or banded growth textures (Fig 6.30 and 6.31). It commonly occurs in elongate bands or lenses that lie in the foliation planes and are truncated by microshear sets. The



**Fig 6.28** Photomicrograph of schistose serpentinite matrix. Elongate lizardite plates (pale green) in parallel arrangement define the schistosity (S) (from upper left to lower right corner) which is also outlined by angular Cr-spinel fragments and magnetite grains and films (black). Schistosity is truncated by the C planes, in a vertical orientation at the right margin of the figure, which are defined by magnetite (black) and cryptocrystalline magnesite (greyish). Specimen 255-B; X 1.5; plane polarized light; bar represents 1 mm.

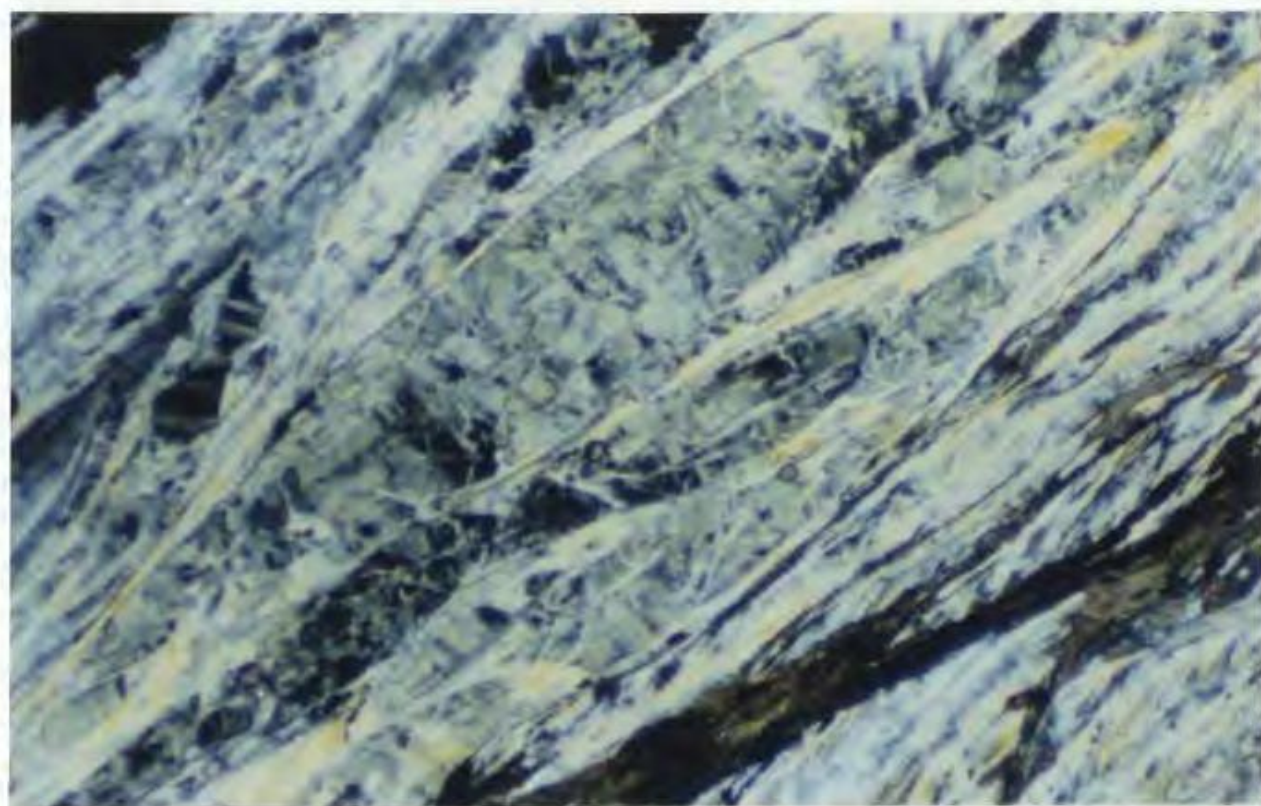
**Fig 6.29** General view of schistose serpentinite matrix. C planes are oriented horizontally and defined by magnesite with magnetite inclusions (grey). Schistosity trends from upper left to lower right. In this figure the recrystallized lizardite is pale brownish and the relict lizardite pale green (lensoid shaped). Specimen 250-D; X 1.5; plane polarized light; bar represents 1 mm.



**Fig 6.30** Photomicrograph showing matrix foliation (S) defined by the parallel arrangement of elongate recrystallized lizardite (pale green and yellow) and lenses of relict mesh-textured lizardite (dark green), which because of the low magnification is not obvious. In the lower right hand corner are magnesite veins with brownish birefringence colors and magnetite (black). Specimen 252-C; X 3.2; crossed polars; bar represents 0.5 mm.

**Fig 6.31** Partially recrystallized schistose serpentinite with relict elongate "boudin" of mesh textured lizardite situated in foliation plane (central lower part of the figure). Beneath the boudin is a small deformed Cr-spinel grain (black) also oriented with its long axis parallel to foliation plane. Magnesite veinlets are brown, magnetite is black. Specimen 250-D; X 1.5; crossed polars; bar represents 1 mm.

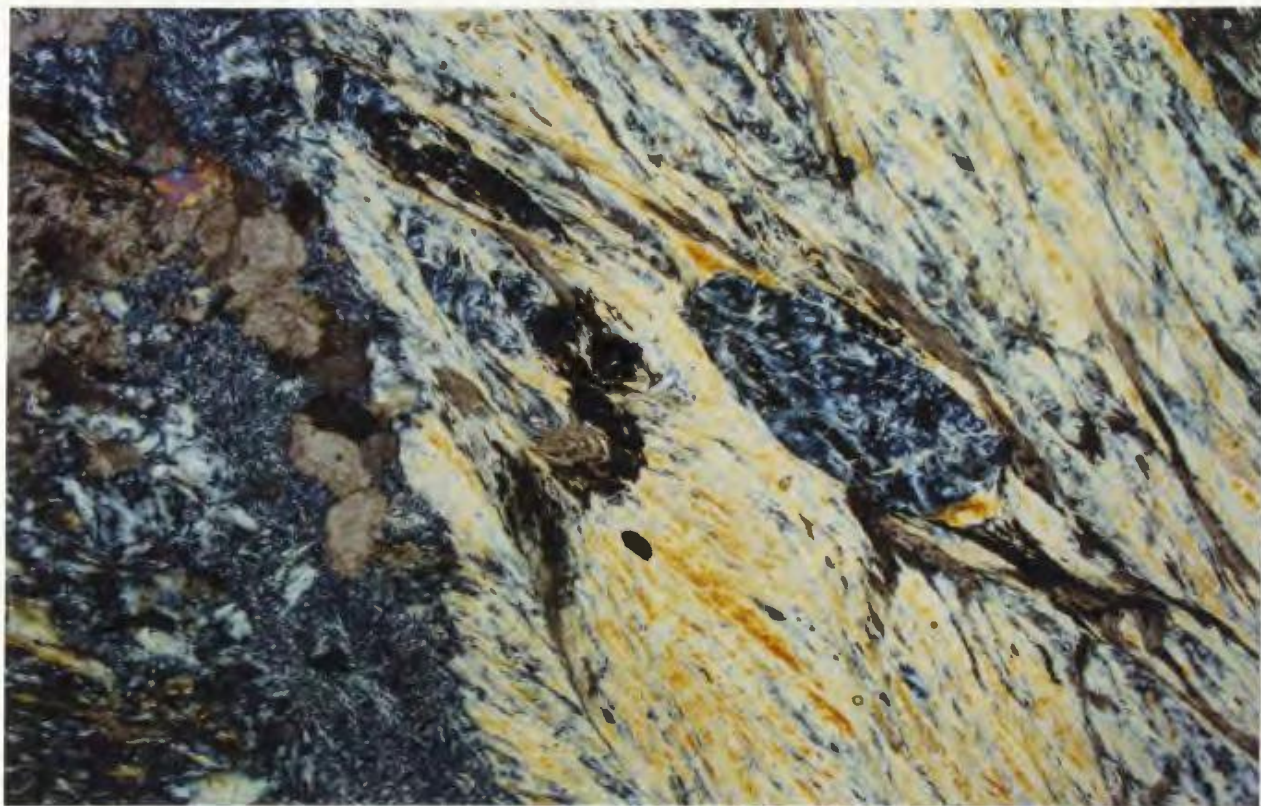




**Fig 6.32** Photomicrograph of schistose serpentinite and antigorite. Along the left margin, in a vertical orientation is a band of interlocking-textured antigorite (blue) and spathic magnesite grains (brown and black). Elongate recrystallized lizardite grains (yellowish) define the foliation in the matrix trending from the upper left to lower right. To the right of centre is an ellipsoidal "boudin" of antigorite with interpenetrating texture. Pseudofibrous magnesite (brown) and magnetite (black) also define the matrix foliation. The coexistence of both serpentine types in this matrix sample is probably due to the in situ transformation of a fragment, initially containing both lizardite and antigorite, to matrix. Specimen 450-D; X 2.5; crossed polars; bar represents 0.5 mm.

**Fig 6.33** Photomicrograph of mélange matrix illustrating a shear sense indicator. In the central part of the figure a deformed Cr-spinel grain shows apparent sinistral sense of displacement. To the left of the Cr-spinel is part of a relict lizardite lens with abundant magnetite (black). Lighter colored material is recrystallized lizardite. Grey material in subvertical orientation at the both right and left margins of the figure is pseudofibrous magnesite defining C planes and containing magnetite dust. Specimen 250-D; X 1.5; plane polarized light; bar represents 1 mm.







relics vary in length from several mm to several cm and also contain lizardite-bastite after orthopyroxene, and Cr-spinel and magnetite. Lizardite-bastite appears to be resistant to recrystallization to platy lizardite and commonly forms small relics (augen) surrounded by platy lizardite.

Relict antigorite, which is colourless with higher relief and lower order birefringence colours (commonly blue) than lizardite, accounts for <10% by volume of the schistose serpentinite, and occurs in two characteristic textures, interpenetrating and interlocking. Interpenetrating-textured antigorite (Fig 6.32) is invariably found in small lenses (1 to 5 mm in size) with their long axes oriented parallel to foliation planes and enveloped in platy lizardite. Where in interlocking textures, antigorite occurs as larger patches oriented parallel to the foliation and composed of very fine (<0.05 mm) equant grains (Fig 6.32).

Carbonates, which occur as minor phases (<15% by volume) in schistose serpentinite matrix, are predominantly magnesite, rarely dolomite. Magnesite commonly occurs in microshear (C) planes as layers up to 5 mm in width (Figs 6.27 to 6.33). Elsewhere magnesite forms solitary crystals, commonly strain free, up to several mm in length demonstrating syn- or post-tectonic growth. Larger layers, with several generations of carbonate grains, are characterized by the presence of very elongate

cryptocrystalline magnesite aggregates which may be distinguished by their pseudofibrous habit (Fig 6.27). These features, and the common presence of serpentine inclusions in magnesite grains, imply that carbonatization occurred during and after the event which produced the foliation and the recrystallization of the lizardite.

Opaque phases comprise <5% by volume of schistose serpentinite. Magnetite is widespread, occurring as fine dust or disseminated grains and grain aggregates that confer the dark colour to the rock (Fig 6.27). With an increase of shearing, magnetite becomes more concentrated in foliation and microshear planes (Fig 6.28 and 6.29) and locally forms veinlets following carbonate.

Relict euhedral or subhedral Cr-spinel grains exhibit evidence of progressive deformation in the schistose serpentine matrix with fractured and pulled apart grains (Fig 6.33), evidence of grain size reduction and augen-like shapes (Fig 6.28).

#### 6.3.2. Brecciated serpentinite matrix

Brecciated serpentinite is a relatively minor component of the matrix that occurs as material between serpentinite fragments. It is composed of randomly oriented fragments of serpentinite in a carbonate and/or serpentine matrix (Fig

**Fig 6.34** Photograph of slab of tectonic mélange with several small serpentinite fragments (black) enclosed in a matrix of brecciated serpentine (grey) and carbonate (medium brown).  
Scale is in cm. Sample 343 (see sample map).

**Fig 6.35** Field photograph showing talc-magnesite matrix (purple) enclosing elongate serpentinite fragments (rusty brown) that are oriented with their long axes parallel to the foliation.  
Scale is in cm. Location: outcrop 343.



6.34), but in contrast to typical *mélange* fragments, these fragments do not show preferred orientation, are smaller in size (<10 cm) and have angular shapes. These fragments are commonly composed of antigorite serpentinite with interpenetrating or highly disturbed mesh textures. In some sites the rock may be highly carbonatized and invaded by chlorite. The brecciated serpentinite matrix is interpreted to form in areas of relatively low strain, but in other respects seems to be comparable to schistose serpentinite.

#### 6.3.3. Talc-magnesite matrix

Talc-magnesite schist is the dominant component among matrix lithologies. It occurs as foliated layers up to several meters thick (Fig 6.24) along shear zones which anastomose around hard kernels of less deformed and carbonatized serpentinite fragments (Fig 6.35). The rock is soft and readily eroded, and is commonly exposed in locations where it is shielded by more resistant lithologies. It is inferred that talc-magnesite schist forms the bulk of the *mélange* unit, but is largely unexposed.

The rock has a distinctive brown to purple weathering color (Fig 6.35) and is pale brown to black when fresh (Fig 6.36 and 6.37). The content of talc is variable. The rock is characteristically layered, with talc-rich and magnesite-

**Fig 6.36** Talc-magnesite matrix of the *mélange* exhibiting the phacoidal shape typical for sheared matrix rocks. Buff colored material is talc, brownish augen and veins are magnesite, black is Cr-spinel and magnetite. Visible fabric is C planes that are outlined by thin films of magnetite. Wavy pattern of foliation is due to incipient shear band formation. Schistosity (S) surface defined by talc is visible in thin section. Scale is in cm.

**Fig 6.37** Photograph of slab of talc-magnesite matrix showing magnetite-rich magnesite (black) lenses with their long axes parallel to the foliation plane (horizontal), separated by bands of talc (light greenish). Scale is in cm.





rich layers. Magnesite rich varieties are commonly also rich in magnetite which gives a darker color to the rock (Fig 6.37). Such specimens are harder and exhibit a weaker foliation than talc-rich specimens. Talc-rich varieties are greasy and crumbly, and easily split along cleavage surfaces.

Talc-carbonate rocks have a simple mineralogy, being composed mainly of talc and magnesite in variable proportions, with minor amounts of accessory opaque minerals. Relict serpentine is very rare.

The granolepidoblastic texture is conferred by the medium-grained magnesite set in a finer grained talc matrix. Talc typically defines the foliation (S) which is characteristically cut at low angles by shear planes (C) outlined by fine magnetite films (Figs 6.36 and 6.38). Fracturing along shear planes produces so called "phacoids" (Figs 6.27, 6.36 and 6.37) resembling the shape of the strain ellipsoid.

Magnesite is present in both cryptocrystalline and crystalline varieties. Cryptocrystalline magnesite (Fig 6.39 and 6.40) forms less than half of the total magnesite and has similar features to that already described. However, the grain shapes tend to be more elongate, and exhibit a dimensional preferred orientation. Rarely cryptocrystalline magnesite still preserves the outline of the original mesh

**Fig 6.38** Photomicrograph of talc-magnesite matrix of tectonic mélange showing cryptocrystalline magnesite grains (brownish) and colorless spathic magnesite forming grain aggregates parallel to the foliation plane (left side of figure). Talc is colorless with low relief and forms bands oriented parallel to the foliation (S) which is vertical. In the right hand side of the figure, shear planes (C) outlined by magnetite cut the foliation at low angles. In black, and commonly concentrated along C planes, are Cr-spinel and magnetite.  
Specimen 177-C; X 1.5; plane polarized light; bar represents 1 mm.

**Fig 6.39** Photomicrograph showing large skeletal dusty cryptocrystalline magnesite (brownish) which still preserves the outline (cells and rims) of the original lizardite mesh texture (left margin, centre and right margin of the figure). The mesh centers are occupied by talc or chlorite (platy irregular grain in the lower right hand corner beneath the dark magnesite). To the left of centre is a vertical vein with a fine-grained talc core (high birefringence colors) and a margin composed of spathic subidioblastic magnesite grains (colorless) growing perpendicular to the walls.  
Specimen 177-D; X 10; crossed polars; bar represents 0.2 mm.



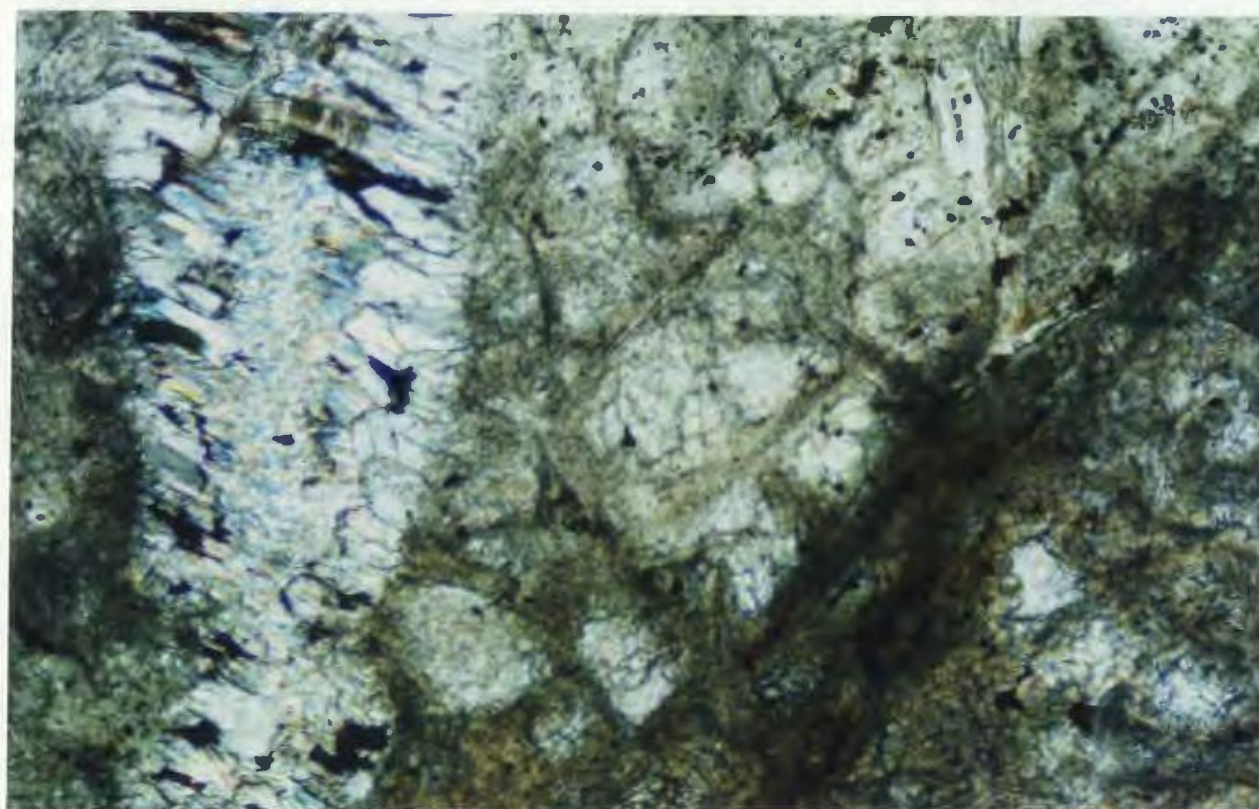
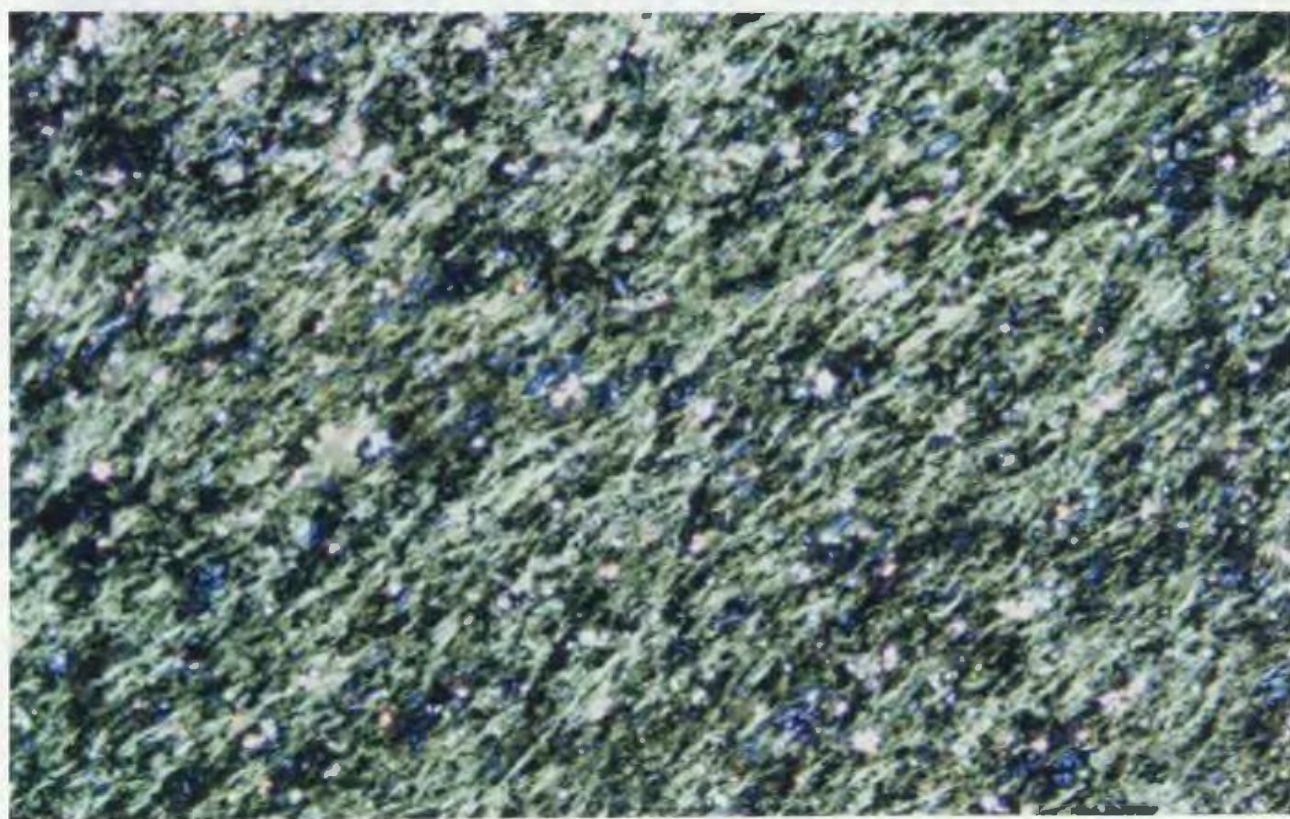
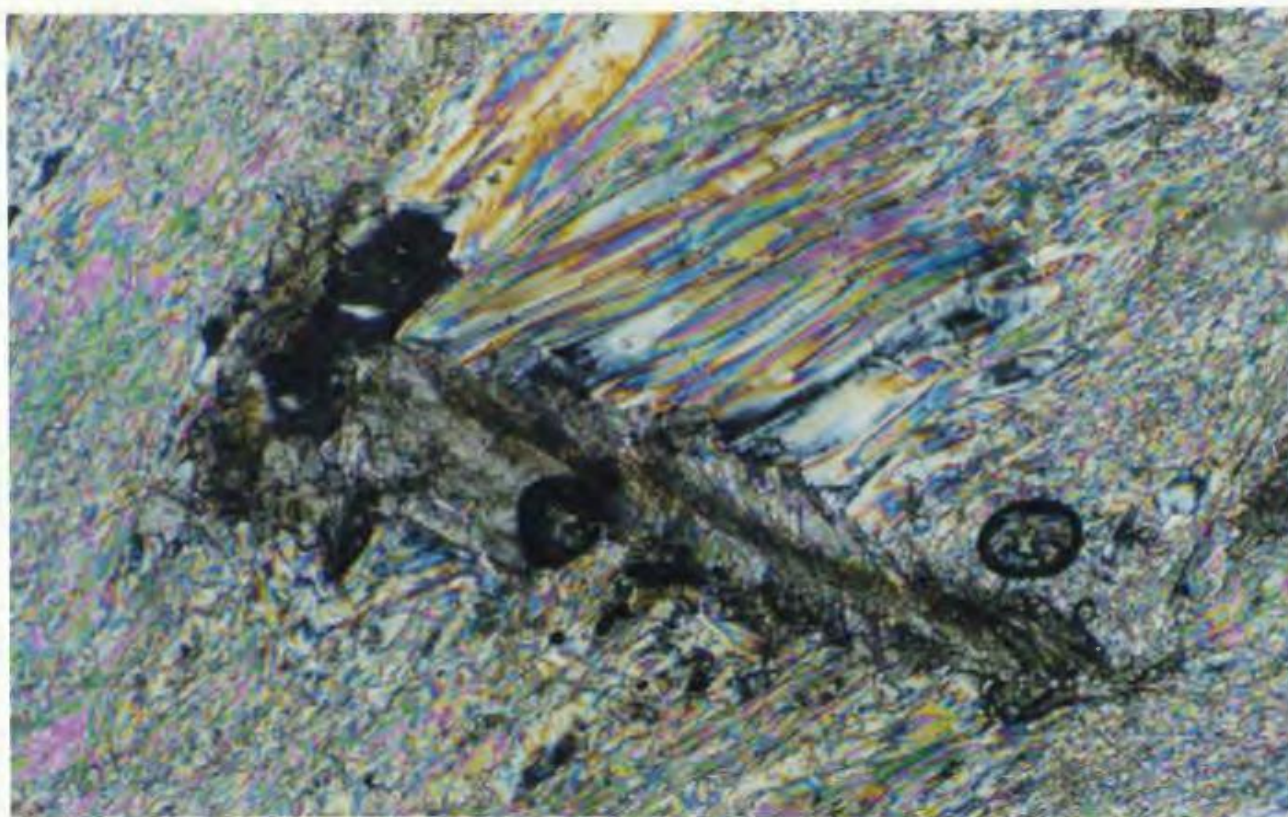


Fig 6.40 Detail of talc-magnesite matrix of tectonic mélange showing evidence for rotational strain. Elongate cryptocrystalline magnesite (brownish) set in fine-grained talc matrix with weak preferred orientation. Asymmetric pressure fringes composed of large late grains of talc and subordinate spathic magnesite (black at right hand end) indicate an apparent counterclockwise sense of movement in this photomicrograph. The vague sigmoidal pattern in the cryptocrystalline magnesite implies syntectonic growth of magnesite in a periodically open fracture. Specimen 343-C; X 10; crossed polars; bar represents 0.2 mm.

Fig 6.41 General view of chlorite blackwall matrix. Green and blue birefringent material is clinocllore, pink highly birefringent grains with high relief are sphene. Foliation (from upper right, to lower left) is defined by chlorite. Specimen 197; X 20; crossed polars; bar represents 0.1 mm.







texture (Fig 6.39).

Spathic magnesite forms coarse elongate grains (Fig 6.39) or grain aggregates which typically show preferred dimensional orientation in the foliation plane (Fig 6.38). Undulose extinction, polygonization into subgrains and recrystallization adjacent to old grains are common. These features suggest syntectonic growth. Another characteristic feature of spathic magnesite is the presence of small syntectonic grains ( $< 0,5$  mm in length) in pressure shadows adjacent to the larger grains (Fig 6.40).

Talc occurs in narrow lenses and layers  $< 2$  mm in width that pinch and swell, and also in irregularly-shaped crystal aggregates. In layers or lenses, minute talc flakes define a strong foliation with S and C components which may be deformed into microfolds and microfaults produced by shortening subparallel to the foliation. Talc also occurs in scaly aggregates of minute flakes, without any preferred orientation, typically at the margins of the talc layers, within some lenses, and in talc aggregates.

Cr-spinels are commonly pulled apart and extended over several mm in the talc-magnesite matrix, and chlorite occurs in trace amounts adjacent to and replacing Cr-spinel grains.

Very fine magnetite layers less than 0.02 mm in width and several mm in length commonly occur within talc layers and along and along schistosity (S) planes.

#### 6.3.4. Chlorite blackwall rocks

Chlorite-rich rocks occur locally in the outer parts of the tectonic mélanges as narrow zones at contacts between ultramafic and metasedimentary rocks. They are dark green to black, several cm to several tens of cm thick, strongly foliated and have sharp contacts with both serpentinite and metasediments. The blackwall rocks, which are composed almost entirely of chlorite, were formed probably at low-T (based on lack of amphibole). X-ray powder diffraction analyses have identified magnesium-rich chlorite (clinochlore) as the main component. In thin section extremely fine-grained chlorite forms an homogeneous mat, nearly isotropic under crossed polarizers (Fig 6.41). Larger chlorite grains are rare. Relict serpentine occurs in trace amounts as veins and in bastites. Small corroded spinel grains occur locally. Some specimens contain small epidote and sphene grains, the latter comprising up to 15% of the rock volume (Fig 6.41).

## 6.4 QUARTZ-MAGNESITE ROCK

### 6.4.1. Introduction

In the Coy Pond tectonic mélanges, quartz-magnesite rocks were produced by pervasive carbonatization of talc-magnesite or serpentinite assemblages. Commonly the process affected both the fragments and the matrix, so that large portions of the mélanges were transformed to quartz-magnesite assemblages. Locally the carbonatization affected only the matrix, which in this case generally encloses talc-magnesite fragments. Serpentinite relics were not found in quartz-magnesite assemblages.

Quartz-magnesite assemblages outcrop as prominent elongated knobs, covered with ochrous gossan and laced with a quartz stockwork. Weathering produces a very rough surface, a result of surficial leaching of magnesite leaving a framework of quartz and hobnails of Cr-spinel (Fig 6.42). The lenticular shapes of the fragments enclosed in the matrix (Figs 6.42 and 6.43), a feature inherited from the sheared ultramafic precursor, are still visible. The fragments are medium to light brown, and mottled due to the presence of Cr-spinel grains or finely disseminated magnetite (Fig 6.45). The matrix is lighter colored, buff to pale brown and characterized by a weak foliation, and is outlined by the elongate shape of the fragments and the

**Fig 6.42** Photograph of quartz-magnesite outcrop in the western tectonic mélange showing subround quartz-magnesite fragments enclosed in quartz-magnesite matrix. White "dust" on the outcrop is a lacy network of quartz veinlets. Larger quartz veins cutting the foliation at high angle (top of the photograph) are typical of this part of the mélange.

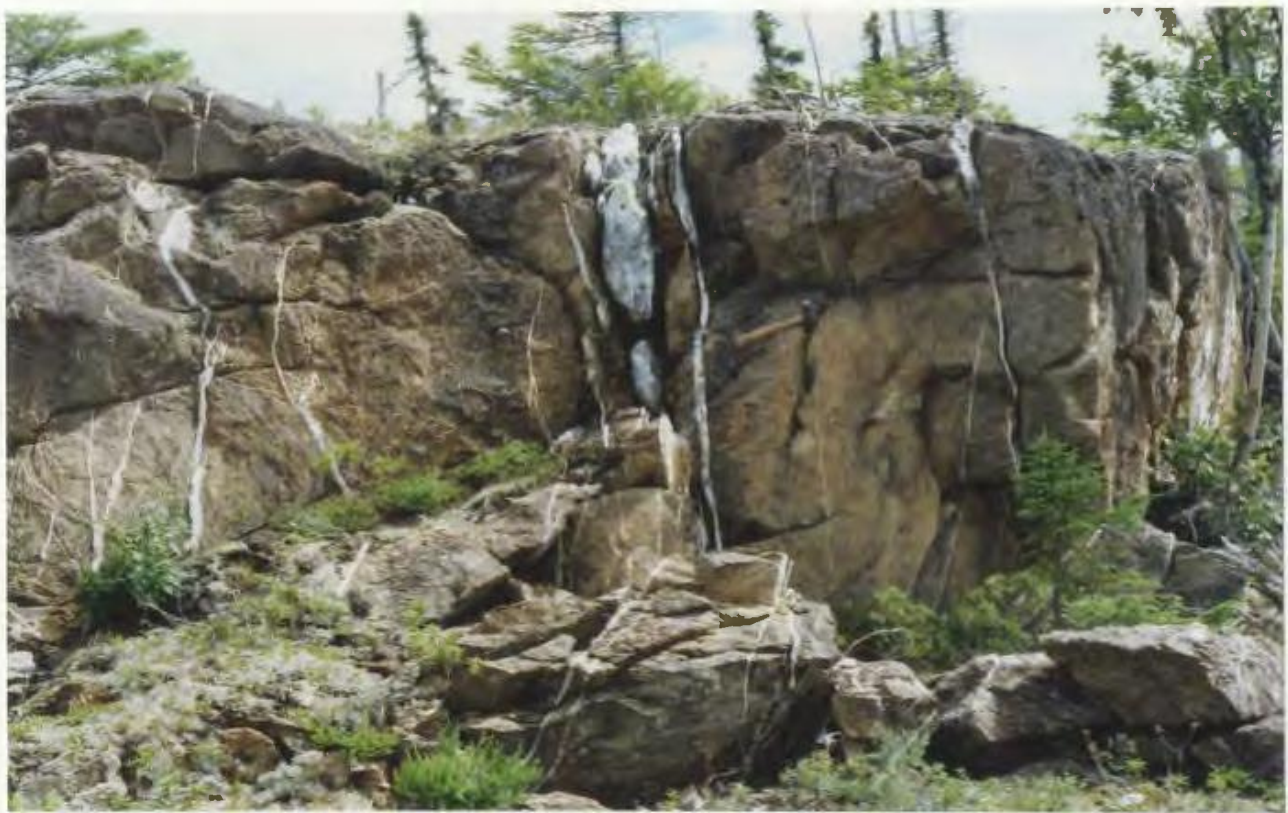
**Fig 6.43** Photograph of quartz-magnesite matrix with a few small quartz-magnesite fragments (reddish colored patches). The schistosity is oriented horizontal in the figure. White quartz patches are remnants of quartz veins parallel to foliation. Outcrop situated in the southern extremity of the western tectonic mélange.



**Fig 6.44** Quartz-magnesite outcrop situated in the southern extremity the eastern tectonic mélange cut by numerous quartz veins. Note that in this example quartz veins are subparallel to foliation and have variable widths over short distances, and some pinch out.

**Fig 6.45** Fragment (left hand side of the figure) composed of quartz-magnesite cut by a quartz vein (white). Quartz-magnesite matrix at right hand side of the figure has a vertical foliation outlined by Fe oxides (brown to black) quartz and magnesite veins.  
Scale in cm.





subparallel distribution of grey magnetite stringers. Commonly the quartz-magnesite rocks are cut by veins of white quartz (Figs 6.42 to 6.45) and buff magnesite (Fig 6.45). These veins may be subparallel to the foliation (Fig 6.44), situated on C planes (Fig 6.46), or may be cross-cutting (Fig 6.42). They are commonly undeformed and suggest that the quartz-magnesite assemblage developed late, after the bulk of deformation in the tectonic mélange.

#### 6.4.2 Petrographic description

Quartz-magnesite rocks have a relatively simple mineralogy being composed almost entirely of magnesite + quartz  $\pm$  talc + opaque phases (Cr-spinel, Fe-oxides). All quartz-magnesite specimens indicate that carbonatization of serpentinite was pervasive. Relict serpentine does not occur, but talc is commonly found (Fig. 6.47) in the eastern tectonic mélange and occurs locally at the southern end of the western tectonic mélange.

Textures are commonly granular, the rock has a massive appearance and does not show a tendency to fracture parallel to foliation planes inherited from serpentinite. In some specimens, a weak foliation (S) is defined largely by the crude mineralogical banding due to segregation among quartz, magnesite and talc. The width of the bands is variable from

a few mm up to several cm, and they commonly pinch and swell. In some samples the foliation is overprinted by shear (C) planes that are commonly outlined by boudins or veins of quartz. Foliation planes are locally pinched-out and sheared into the C planes. In other samples, veins are late and undeformed.

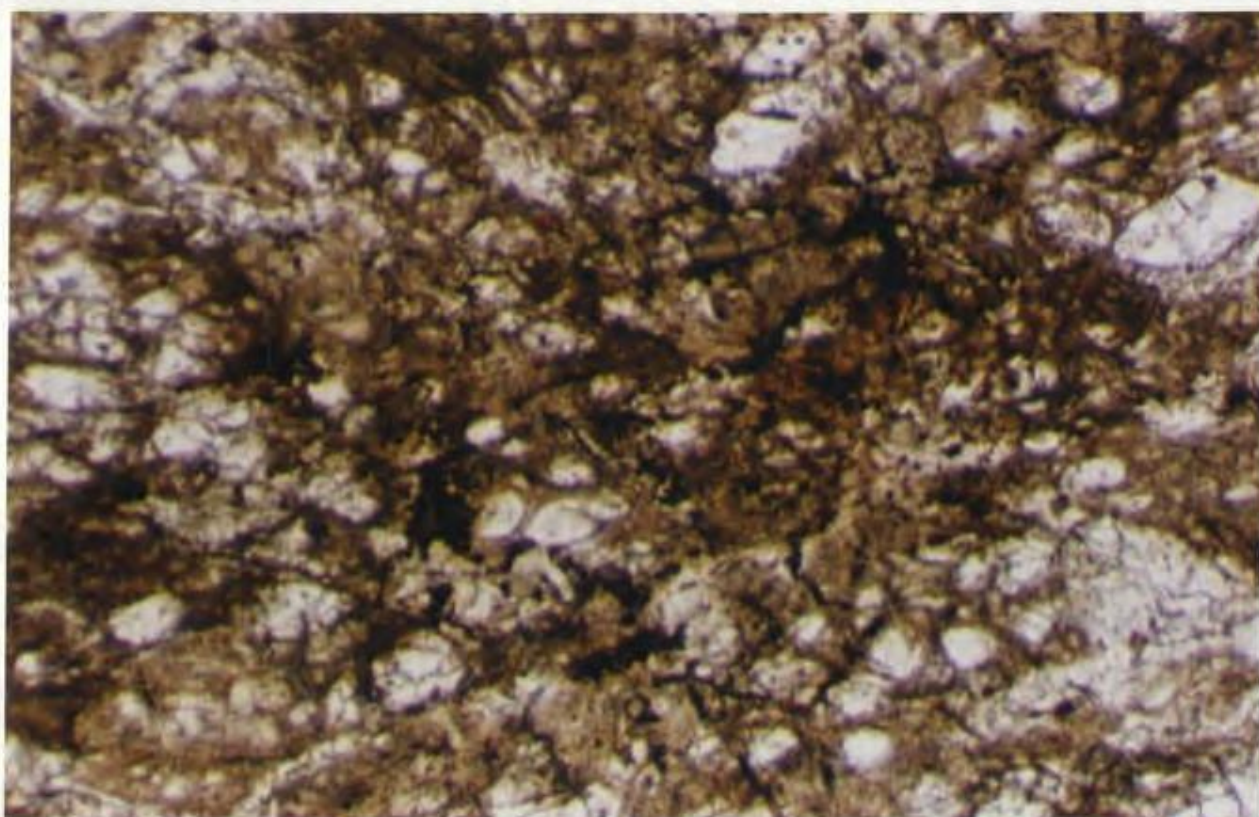
Magnesite in quartz-magnesite rocks forms between 30% and 95% of the rock volume, commonly about 85%-90%. As with its occurrence in serpentinite and talc-magnesite bearing rocks, magnesite occurs in two varieties, microcrystalline and crystalline.

(i) microcrystalline magnesite occurs in both fragments and matrix in quartz-magnesite rocks, forming about half of the total carbonate and composing the groundmass for crystalline magnesite and quartz. It occurs as agglomerates of grains less than 0.1 mm in size with rounded shapes, strong relief and a brown color (Figs 6.48 and 6.51). It always contains impurities such as minute magnetite grains and a brown dust interpreted to be iron oxides. Under crossed polars it can be seen that microcrystalline magnesite has a pale brown birefringence and poor extinction. Commonly the original serpentinite mesh texture is completely obliterated by carbonatization, but in some instances, usually in fragments where the microcrystalline grains are very fine, the relict texture may be vaguely

**Fig 6.46** Example of quartz-magnesite matrix from southern part of the western tectonic mélange. The foliation (S) defined by compositional banding [magnesite (brown), quartz (white), talc (greenish) and Fe oxides (black)] is truncated by a shear plane (C plane) marked by a quartz vein (white), trending from lower left to upper right.

**Fig 6.47** Representative photomicrograph of quartz-magnesite rock. Brown is cryptocrystalline magnesite, pale brown to white is spathic magnesite, black is aggregates of magnetite. Note the lack of quartz in this sample. Specimen 85-A; X 2.5; plane polars; bar represents 0.5 mm.

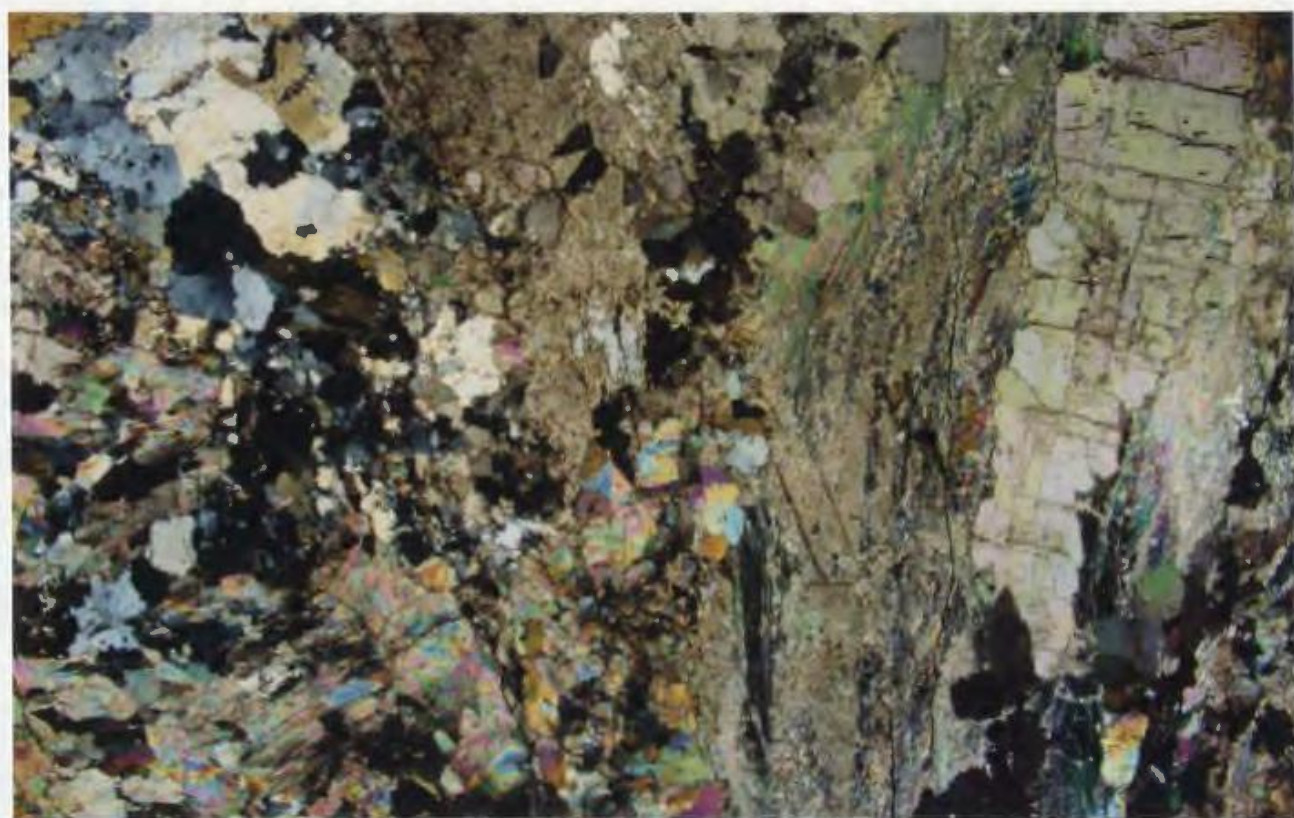
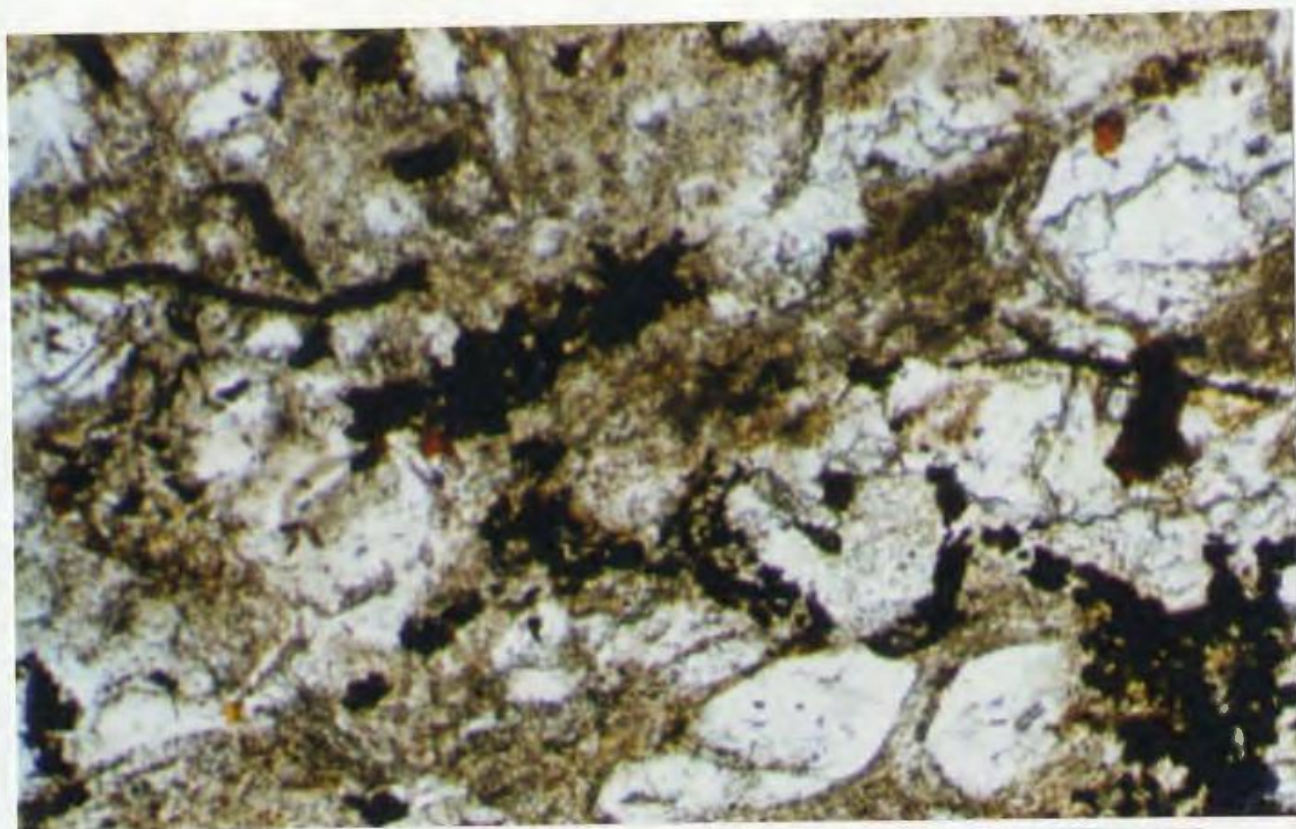




**Fig 6.48** Detail of quartz-magnesite rock. Brownish with dirty appearance is cryptocrystalline magnesite, white inclusion free grains are spathic magnesite, black is aggregates of magnetite grains which are common in cryptocrystalline magnesite. The regular arrangement of magnetite is inherited from mesh textured serpentinite. Note the lack of quartz in this sample. Specimen 85-A; X 10; plane polars; bar represents 0.2 mm.

**Fig 6.49** General view of quartz-magnesite in the matrix of the tectonic mélange. On the right hand side of the figure is a large spathic magnesite grain in a vertical orientation and several smaller grains at extinction. Spathic magnesite shows good cleavage and few inclusions. To the left of the magnesite is a vertical band of strongly foliated talc schist. In the left part of the figure are magnesite grains set in a matrix of talc (green-yellowish) and quartz grains (yellow, bluish and black in the upper left hand corner of the figure). The foliation of the rock (S) is vertical. Specimen 143-A; X 1.5; crossed polars; bar represents 1 mm.

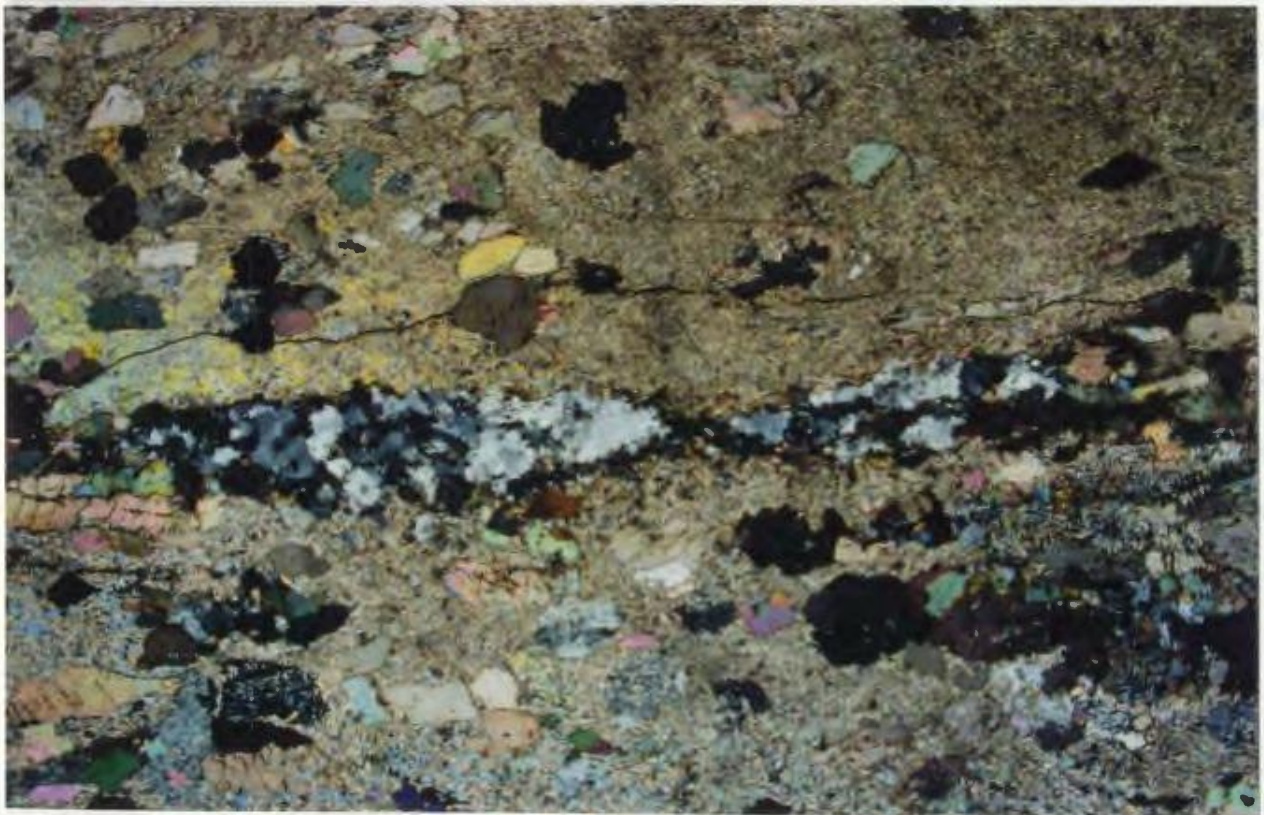
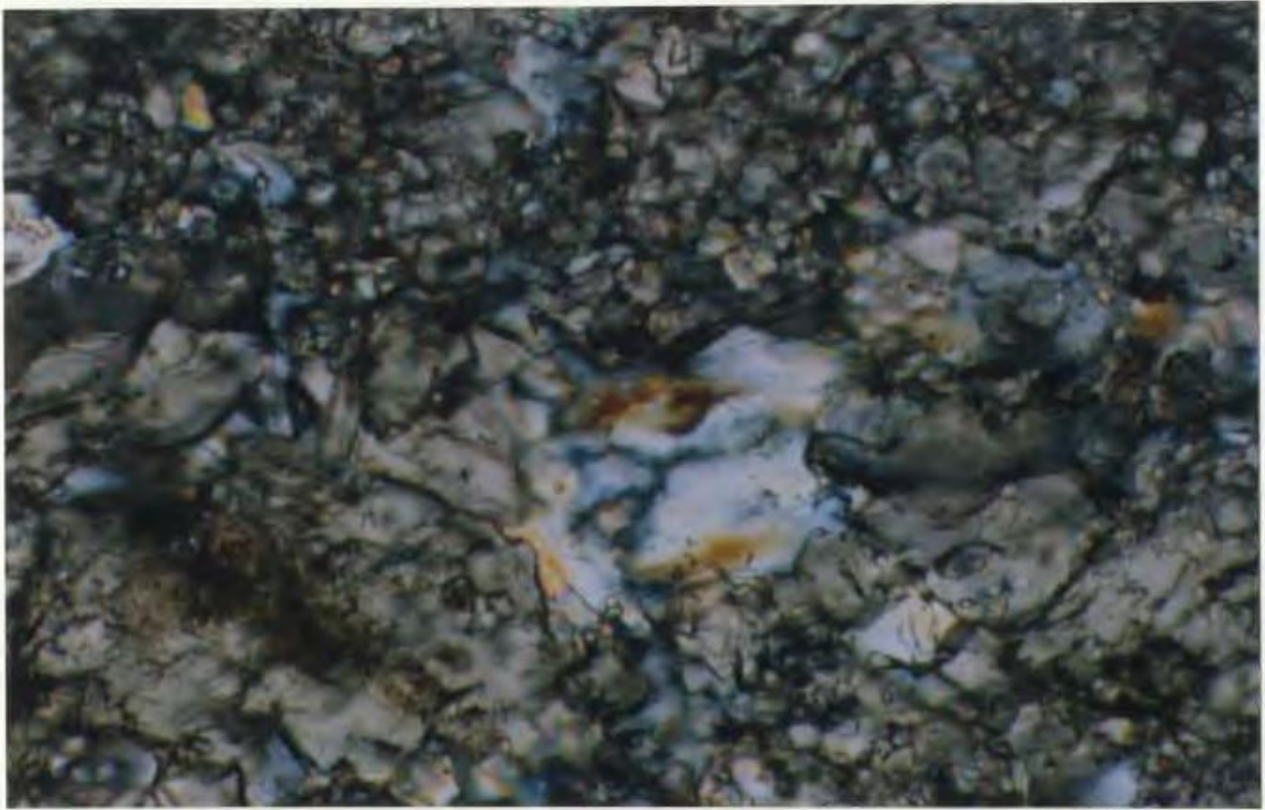




**Fig 6.50** Photomicrograph showing interstitial quartz (central part of figure) between xenoblastic cryptocrystalline magnesite. Specimen 85-F; X 10; crossed polars; bar represents 0.2 mm.

**Fig 6.51** Quartz-magnesite matrix with strong foliation. Quartz vein (horizontal orientation in middle of figure) composed of grains showing undulose extinction and grain boundary recrystallization. Randomly oriented talc flakes (brownish) form the groundmass for larger spathic magnesite grains (high relief and high birefringence colors), and quartz grains (yellow). Specimen 143-A; X 2.5; crossed polars; bar represents 0.5 mm.





distinguished. In such cases, the original partings of the mesh texture can be recognized (Fig 6.48). This feature indicates that quartz-magnesite is chiefly a replacement assemblage in which the larger structure of serpentinite was retained during the conversion of serpentine to magnesite and quartz. However, the process is not entirely a simple replacement as the grains of both magnesite and quartz are generally too coarse to preserve the fine serpentine textures.

(ii) Crystalline or spathic magnesite is more abundant in the matrix than in the fragments. The grain size is variable between 0.15 and 2-3 mm in diameter, the larger grains occurring in the matrix. It is colorless and rarely contains magnetite inclusions. The grains are commonly xenoblastic, granular or lath shaped with good to perfect cleavage in one or two directions (Fig 6.49). Usually the extinction is straight, but undulose extinction is common in the larger grains. Polygonization into subgrains is very common, suggesting the presence of minor strain during or after the carbonatization. Small idioblastic magnesite rhombs commonly occur within talc with their long axes oriented parallel to the foliation. Commonly these magnesite grains are inclusion-free and do not exhibit undulatory extinction. These features suggest a post-tectonic growth.

Quartz in quartz-magnesite assemblages forms between 5%

and 25 % of the rock volume, occurring in larger amounts in fragments than in the matrix. The earliest quartz occurs between cryptocrystalline carbonate as minute ( $<0.1$  mm) interstitial grains (Fig 6.50). With an increasing degree of carbonatization, quartz tends to occur as larger grains, quartz aggregates or veins (Fig 6.51). The veins are variable in size ranging up to several tens of cm in width. In the matrix, quartz and magnesite veins commonly develop in shear (C) planes and are coarser grained than in fragments (Fig 6.46). Quartz, interstitial or veined, commonly exhibits undulose extinction and polygonization into subgrains. Locally quartz may contain minute flakes, rhombs, or irregular grains of magnesite. The replacement of quartz by talc is also common, occurring both marginally and throughout entire quartz grains. Talc appears to preferentially replace poorly crystallized quartz grains with vague extinction and also those grains containing impurities.

Talc occurs commonly in quartz-magnesite of the eastern tectonic mélange in amounts ranging up to 30% of the rock volume. It forms bands a few mm wide (Fig 6.49), or occurs as interstitial material between carbonate and quartz grains (Fig 6.51). Where compact and pure, talc (steatite) bands exhibit a pale green translucent color.

Talc occurs in two situations: most commonly in the

groundmass as small ( $<0.01$  mm) randomly oriented flakes (Fig 6.51), and also as larger grains (up to 0.2 mm) lying in the foliation (Fig 6.49).

Opaque minerals present in quartz-magnesite assemblages occur in amounts less than 1 percent of the rock and are mainly Cr-spinel. The larger (1-2 mm) spinel grains, which commonly exhibit pull-apart structures, are reddish in color and may be bordered by green chlorite. Where present, magnetite generally occurs as fine dust, small grains or grain aggregates that are incorporated in quartz and microcrystalline magnesite; locally it occurs in thin veins (Fig 6.48).

#### 6.4.3 Conclusions on matrix and quartz-magnesite rocks

The examination of the matrix rocks associated with the tectonic mélanges leads to the following conclusions.

(i) The matrix forms up to one quarter of the exposed outcrops of the tectonic mélange, but because of its softness relative to the mélange fragments it is believed to underlie large parts of the unexposed tectonic mélanges.

(ii) The main microstructural characteristic of the matrix rocks is the strong foliation parallel to the boundaries of the unit.

(iii) Formation of the matrix was initiated by a brittle



comminution of serpentinite fragments, followed by ductile deformation and recrystallization into schistose serpentinite matrix.

(iv) Ingress of fluids into the tectonic mélanges provided the appropriate conditions for recrystallization of lizardite into schistose serpentinite and the formation of antigorite; fluids also were the vehicle for transport of CO<sub>2</sub> which controlled the carbonatization processes.

(v) The matrix rocks, because of their foliated nature, were pathways for the passage of the fluids and consequently are the most strained, recrystallized and carbonatized among all mélange assemblages.

(vi) Talc-magnesite assemblages in the western tectonic mélange form characteristic rectiplanar layers (parallel to the mélange boundaries), situated in the zones of high strain and representing major pathways for fluid circulation. However, in the eastern tectonic mélange, because of the pervasive development of quartz-magnesite and its co-mingling with talc-carbonate, this feature is less obvious.

(v) During recrystallization and carbonatization of matrix rocks, some of the phases were mobilized and/or removed. For instance, in schistose serpentinite, magnetite was concentrated along C surfaces, and in talc-magnesite

assemblages, magnesite was concentrated along schistosity planes. This is interpreted to indicate the loci of fluid pathways on a local scale, implying that the planar fabric elements was a major control of fluid infiltration. As a result of remobilization (and partial removal) of magnetite, talc-magnesite and especially quartz-magnesite assemblages become lighter in color compared to their serpentinite parent.

(vi) Narrow planar blackwall rocks, occurring locally at the contacts between serpentinite and metasediments, represent a local metasomatic effect occurring between units of contrasting bulk composition.

(vii) Based on petrographic observations (and stable isotopic compositions (Chapter 10), quartz-magnesite assemblages (listwaenites) are considered to be the latest stage of mineralogical evolution in the rocks of the tectonic mélanges. In contrast to other assemblages, they are at least in part post-tectonic.

(viii) The composition of the quartz-magnesite assemblages is variable with magnesite forming from 30 to 95%, quartz from 70 to 5%, talc from 0 to 30%. The significant local variation in modal abundance of quartz points to the mobility of silica during the formation of the assemblage, a conclusion also supported by the abundance of quartz veins at all scales. More limited mobility of magnesite is

indicated by the presence of rarer magnesite veins.

(ix) Petrographic observations show that quartz-magnesite rocks were formed from two different protoliths: serpentinite in the western tectonic mélange, and talc-magnesite in the eastern tectonic mélange.

(x) The formation of quartz-magnesite assemblages requires the presence of CO<sub>2</sub> bearing fluids. These fluids had no apparent effect on the stability of Cr-spinel, but caused significant breakdown of magnetite (though some still remains), resulting in the light color of the quartz-magnesite rocks.

#### 6.5 MÉLANGE BLOCKS

Blocks (ten to hundred of meters in size) occur in both tectonic mélanges of the Coy Pond ophiolite. They are oriented with their long axes parallel to the foliation and the boundaries of the mélanges, in a manner similar to the smaller fragments.

In the western tectonic mélange, and exclusively in its southern part, four pyroxenite blocks have been mapped (Figs 3.1 and 6.52). They range from 200 to 300 m in length and are about 100 m in width. In the eastern tectonic mélange, there are several blocks of non-ophiolitic origin, including

psammites and volcanogenic metasediments (Fig 3.2). In both tectonic mélanges the blocks form less than 5% of the mélange.

#### 6.5.1 Pyroxenite blocks

Apart from their lensoid shape (3.1) and polished smooth surfaces (Fig 6.52) pyroxenite blocks do not show any effects of shearing or associated metamorphism, and petrographically they are indistinguishable from the layered pyroxenites of the transition zone from which they originated. For this reason, the pyroxenite blocks are not described separately here. Their petrography and mineral chemistry are discussed in Chapters 5 and 8 respectively.

#### 6.5.2 Clastic metasedimentary blocks

Several blocks are composed of fine-grained (0.1 mm) detrital material, consisting principally of quartz and about 10% feldspar grains. The grains are angular and are poorly sorted. The blocks are little deformed internally, but are cut by several generations of late veins composed of prehnite with radiating structure (Fig 6.53).

#### 6.5.3 Volcanogenic metasedimentary blocks

Volcanogenic metasediments have well-defined bedding defined by the alternations of detrital and volcanoclastic

**Fig 6.52** Field photograph showing a massive coarse-grained clinopyroxenite block about 200 m long situated in the western tectonic *mélange*. The block is oriented with its long axis parallel to the boundaries of the tectonic *mélange*.

**Fig 6.53** Photomicrograph showing a metasandstone occurring in a large block in the eastern *mélange*. Fine grained clastic material (right hand side of the figure) comprising principally quartz and subsidiary feldspar is cut by a vein of prehnite (large grains with undulose extinction). Specimen 438; X 2.5; crossed polars; bar represents 0.5 mm.



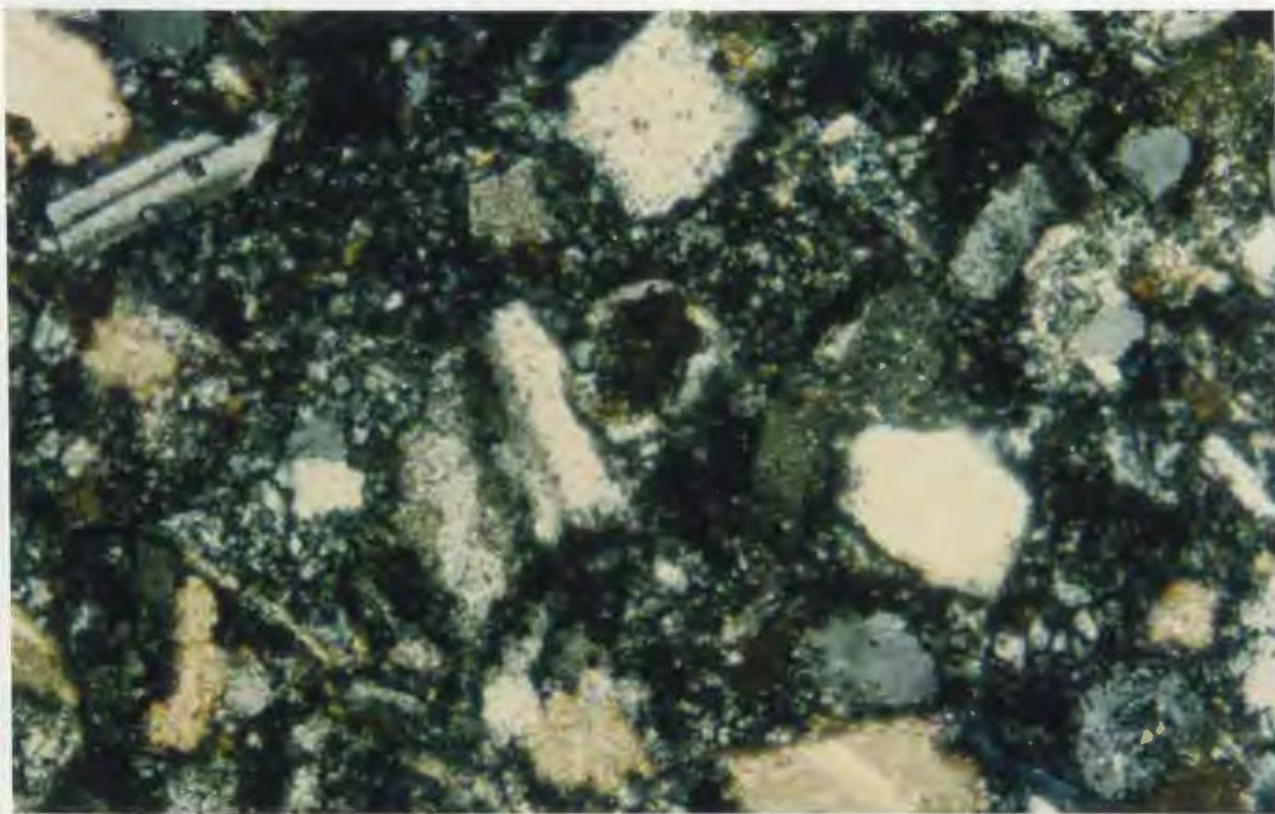
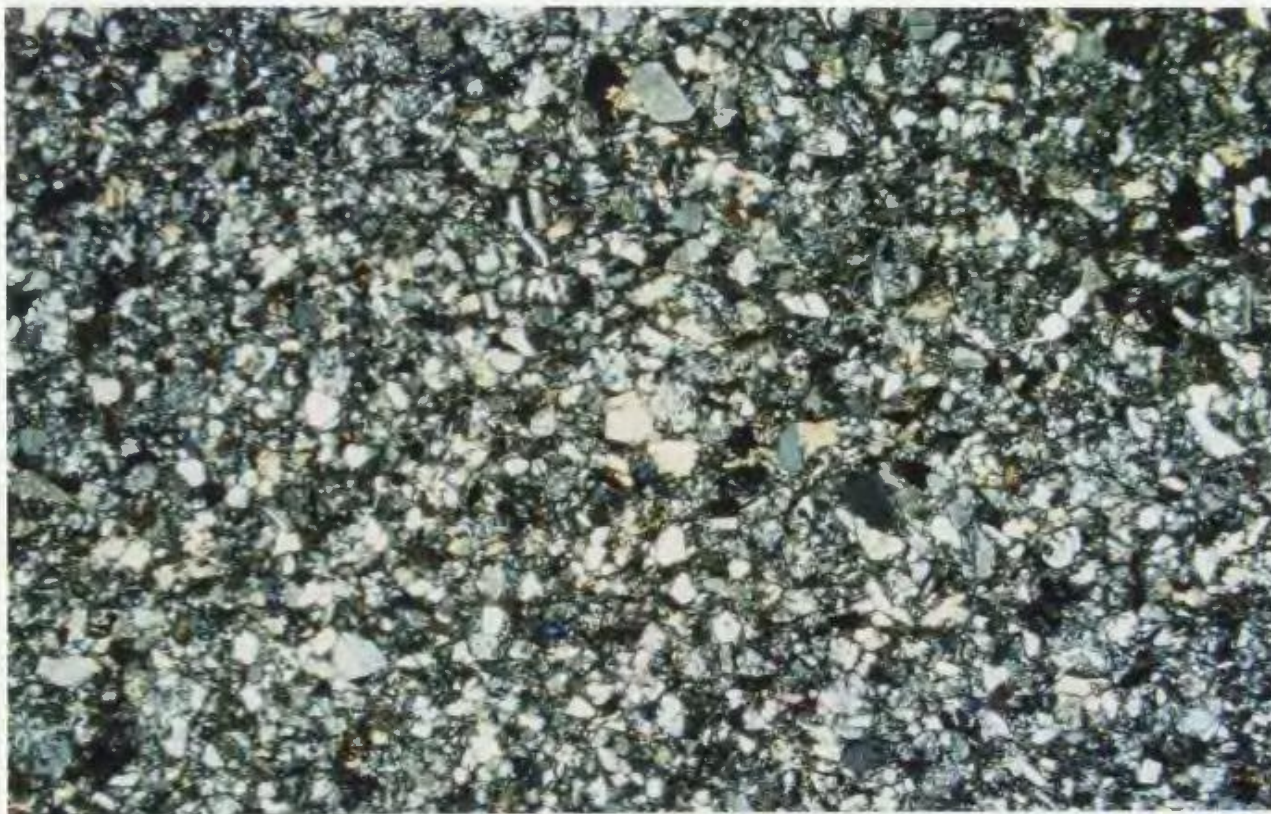


material. Quartz, feldspar and calcite (about 10% of the rock volume), which form the detrital part of the rock are fine grained (< 0.2 mm, most <0.1 mm in size) and have rounded shapes. Volcanogenic input is indicated by vitric pyroclastic fragments (<0.2 mm in size), rare varioles and the fine-grained poorly crystallized and partially chloritized matrix (Figs 6.54 and 6.55). Fe-Ti oxides form <5% of the rock volume.

**Fig 6.54** Photomicrograph showing general view of fine grained volcanogenic metasediment occurring in a block in the eastern tectonic mélange. The rock is a mixture of volcanic and sedimentary clastic material. Specimen 452; X 2.5; crossed polars; bar represents 0.5 mm.

**Fig 6.55** Detail of figure 6.54 showing pyroclastic material. Angular to subrounded quartz grains (colorless) occur in a groundmass of poorly crystallized and chloritized pyroclastic material (dark green). In the central part of the figure is a rounded variole (colorless rim) filled with iron oxides (dark brown). Calcite grains (pale brown), are situated close to the margin of the figure. Relatively fresh plagioclase with polysynthetic twinning is visible locally. Specimen 452; X 20; crossed polars; bar represents 0.1 mm.





## Chapter 7

### MIXED LITHOLOGY SLICE

#### 7.1. Introduction

Throughout most of the Coy Pond Complex, the basal slice of the ophiolite, composed of harzburgite and dunite tectonite, is in thrust contact with, and overlying the autochthonous Spruce Brook Formation. However, in the Chrome Brook-Northwest Gander River confluence area, the basal slice is missing for a distance of about 2 km and its position is taken by the Mixed Lithology Slice composed of slivers of exotic (i.e. non-ophiolitic) material. The Mixed Lithology Slice is at least 2 km long and several hundreds of m wide (Fig 3.1), and consists of imbricate rock slivers of metasedimentary and metavolcanic origin. The lithologies in the Mixed Lithology Slice have been subdivided petrographically on the basis of their original protolith.

#### 7.2 Metabasic and intermediate volcanic/hypabyssal ? rocks

Weakly metamorphosed basic and intermediate volcanic rocks, and relatively little metamorphosed diabase (Figs 7.1) are included under this heading. Characteristically, the rocks show evidence of brecciation, they are weakly foliated



**Fig 7.1** Low grade intermediate volcanic rock composed of quartz-feldspar assemblage partially altered to chlorite and subordinate sericite. Chlorite (blue) in central part of the figure defines a weak foliation. Specimen 118; X 2.5; crossed polars; bar represents 0.5 mm.

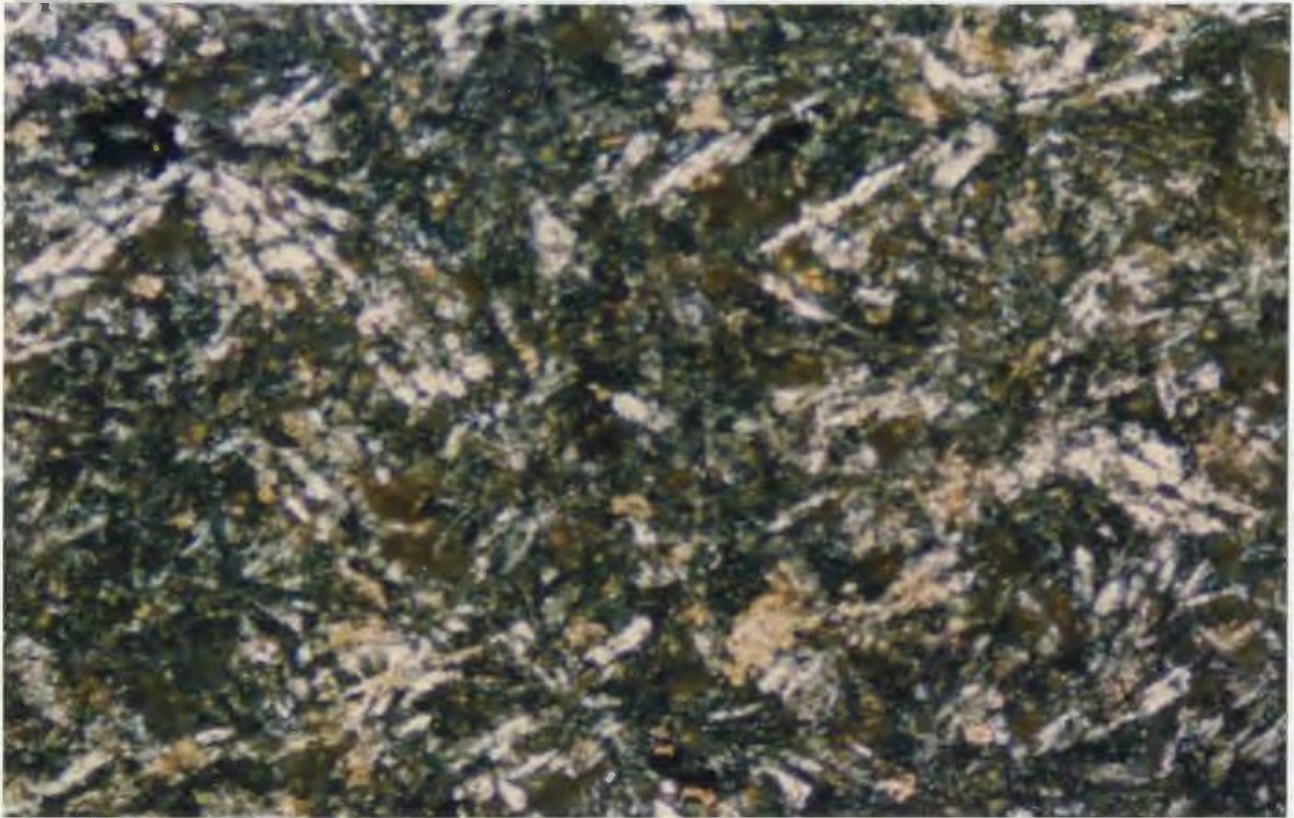
**Fig 7.2** Low grade, fine-grained basic volcanic rock with intersertal texture. Partially altered plagioclase microlites (colorless) are set in a groundmass (brownish) of chlorite with subordinate sericite. Weak foliation (from upper right corner to lower left corner) is outlined by secondary chlorite band (deep blue). Light brown grains and veinlets are calcite. Specimen 453; X 2.5; crossed polars; bar represents 0.5 mm.



**Fig 7.3** Metamorphosed basic or intermediate rock (? pillow lava) with disrupted quartz-feldspar veins (pinkish). Groundmass (greenish color) comprises chlorite-sericite and subordinate calcite. Specimen 505-C; X 2.5; plane polarized light; bar represents 0.5 mm.

**Fig 7.4** Photomicrograph showing weakly metamorphosed basic volcanic rock, probably a pillow lava. Altered plagioclase microlites (white) are set in felted, textured groundmass of chlorite, iron oxides (black) and late carbonate (brown). Specimen 505-A; X 10; crossed polars; bar represents 0.2 mm.





(Figs 7.1 to 7.3) and are partially hydrated to a subassemblage of chlorite-sericite. Commonly the foliation is outlined by chlorite (Figs 7.1 and 7.2) or by disrupted quartz-feldspar veins (Fig 7.3), suggesting that the deformation took place under hydrous low grade metamorphic conditions.

Most commonly the basic rock consists of chlorite, Fe-Ti oxides, carbonate (calcite) and rare altered plagioclase laths (Fig 7.4) occurring in a phacoid-shaped structure that is visible in outcrop. The ellipsoidal-shaped phacoids are less than 10 cm in size and oriented with their long axes in a parallel array. Their shape and arrangement resembles that of the much larger pillow structure in pillow lavas. Their origin is puzzling, however they may result from shearing of original pillow breccia during late (extensional) faulting of the ophiolite.

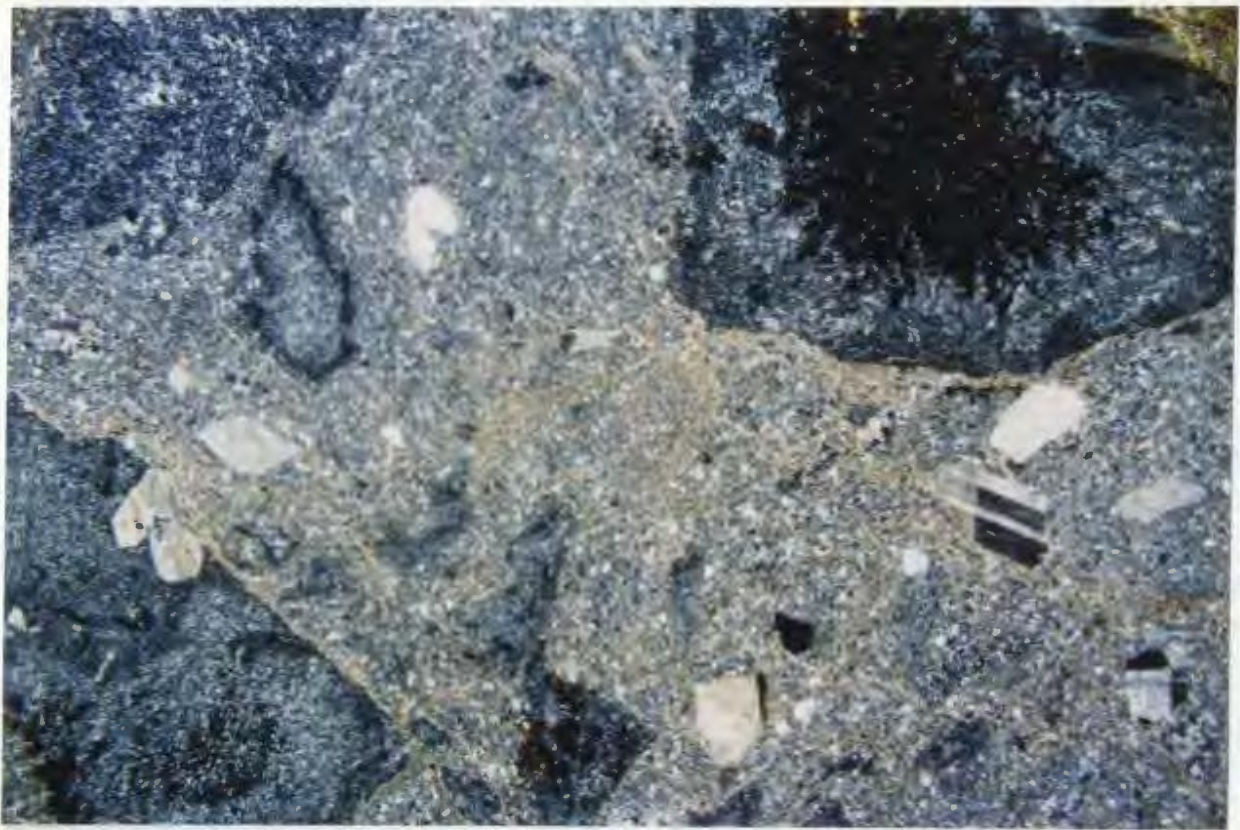
### 7.3 Pyroclastic rocks

Consolidated pyroclastic rocks occur in the Mixed Lithology Slice in two localities. The lithology is composed of lapilli and ash in approximately equal proportions (Fig 7.5). The lapilli are very variable in size, with irregular contours commonly outlined by rounded and concave shapes. Lapilli contain quartz grains in microlitic texture and in



**Fig 7.5** Photomicrograph showing several lapilli (blue) set in microcrystalline groundmass. Large lapilli are situated in the corners of the figure, and the centre of the upper right hand one is filled with iron oxides. Generally the lapilli have vitric rims (dark blue) and devitrified centers which are clearly visible in the small oval lapillus situated to the left of centre of the figure. The lapillus situated in the lower left corner contains several quartz phenocrysts. In the fine grained quartzofeldspathic groundmass (blue-grey), are quartz (colorless) and plagioclase (polysynthetic twinned). The quartz grain situated in central upper left hand side of the figure shows corrosion. Late carbonate alteration occurs, especially in the groundmass (pale brown). Specimen 139; X 1.5; crossed polars; bar represents 1 mm.

**Fig 7.6** Photomicrograph showing shards (dark green) having contours outlined by concave lines. Large elongate shards in the left side of the figure are flattened, the smaller ones in the upper right hand corner still preserve their vesicular form. Small vesicle in the upper left hand side of the figure is filled with quartz grains. The groundmass contains devitrified material, large quartz (grey) and plagioclase (central right hand margin) and calcite (pale brown). Specimen 133; X 2.5; crossed polars; bar represents 0.5 mm.



places quartz and plagioclase phenocrysts.

Characteristically, the grain size in the central part of microlite is larger than that close to the margins (Fig 7.5), showing a difference in the cooling rate. The quartz phenocrysts, where present are commonly corroded. Some lapilli are filled with dark-brown iron oxides.

Elongated and flattened shards of devitrified glass, which are relics of an early spongy texture, occur commonly (Fig 7.6). The matrix of the shards and lapilli is composed of a fine-grained quartz (but coarser grained than in lapilli) and chlorite. Quartz and plagioclase (the latter with polysynthetic twinning) phenocrysts also occur, and are commonly corroded. Late calcite in veins and porphyroblasts forms about 5% of the rock volume.

#### 7.4 Actinolite epidote schist

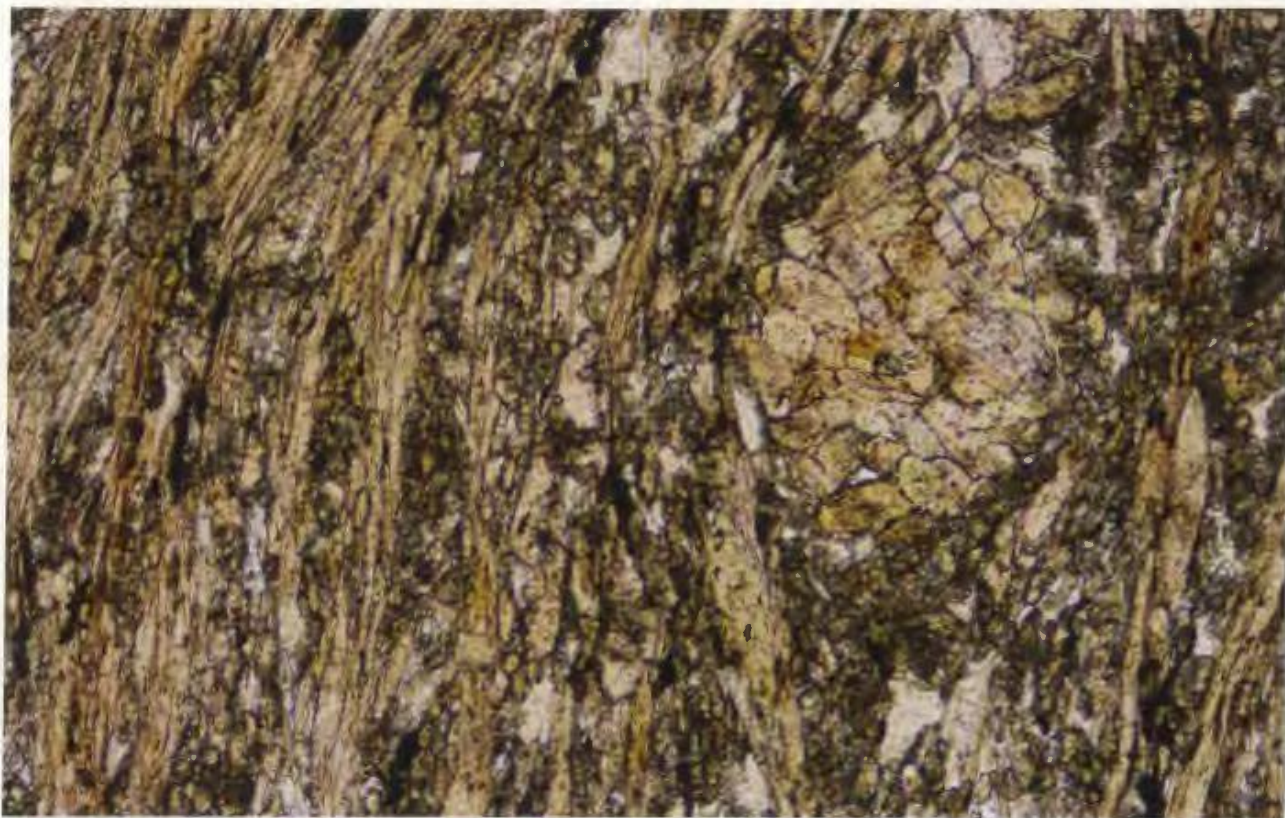
Actinolite epidote schist is composed mainly of actinolite, epidote and subsidiary albite (X-ray powder determination). The rock is composed of fine grained epidote and albite with epidote porphyroblasts set in a nematoblastic schistose matrix (Figs 7.7 and 7.8). Actinolite laths up to 1 mm long in a radial arrangement are also common.

Such rocks were likely produced by hydrothermal

**Fig 7.7** Strongly foliated actinolite-epidote schist with granonematoblastic texture. Elongate actinolite laths (pale green) impart a strong foliation (subvertical) to the rock. Also in the foliation plane are epidote and albite bands. To right of centre is a porphyroblastic aggregate of epidote grains having its long axis parallel to the foliation. Specimen 124; X 10; plane polarized light; bar represents 0.2 mm.

**Fig 7.8** Detail of 7.7. Coarse-grained recrystallized epidote grains set in a finer grained foliated matrix of epidote-feldspar (foliation from upper left to lower right). The larger epidote grain in the left central part of the figure has a fractured core (orange) and an unfractured overgrowth (yellow) on the rim. In the upper left corner of the figure occurs a rare plagioclase grain. Note local absence of actinolite. Specimen 124; X 2.5; crossed polars; bar represents 0.5 mm.







metamorphism of basaltic rocks, and formed under greenschist facies metamorphic (Yardley, 1989).

#### 7.5 Metasedimentary schist

Coarse to fine grained (0.01 to 0.1 mm) metasediments very similar to parts of the Spruce Brook Formation are predominantly composed of quartz, feldspar and chlorite  $\pm$  garnet. In muscovite- chlorite schist, subparallel flakes of muscovite largely replaced by chlorite, form about  $< 5\%$  of the rock volume (Fig 7.9).

Garnet-muscovite schist consists of coarse garnet porphyroclasts up to several mm diameter set in a fine grained retrogressed matrix of sericite and chlorite with relict plagioclase and quartz (Figs 7.10 and 7.11).

Grade of metamorphism in these rocks is not easy to determine due to extensive regression to hydrous greenschist facies assemblages. The assemblage quartz-plagioclase-muscovite is stable over a wide range of metamorphic conditions, the presence of garnet suggests that at least upper greenschist facies conditions were attained, the coarse grain size perhaps being more compatible with an amphibolite facies assemblage.

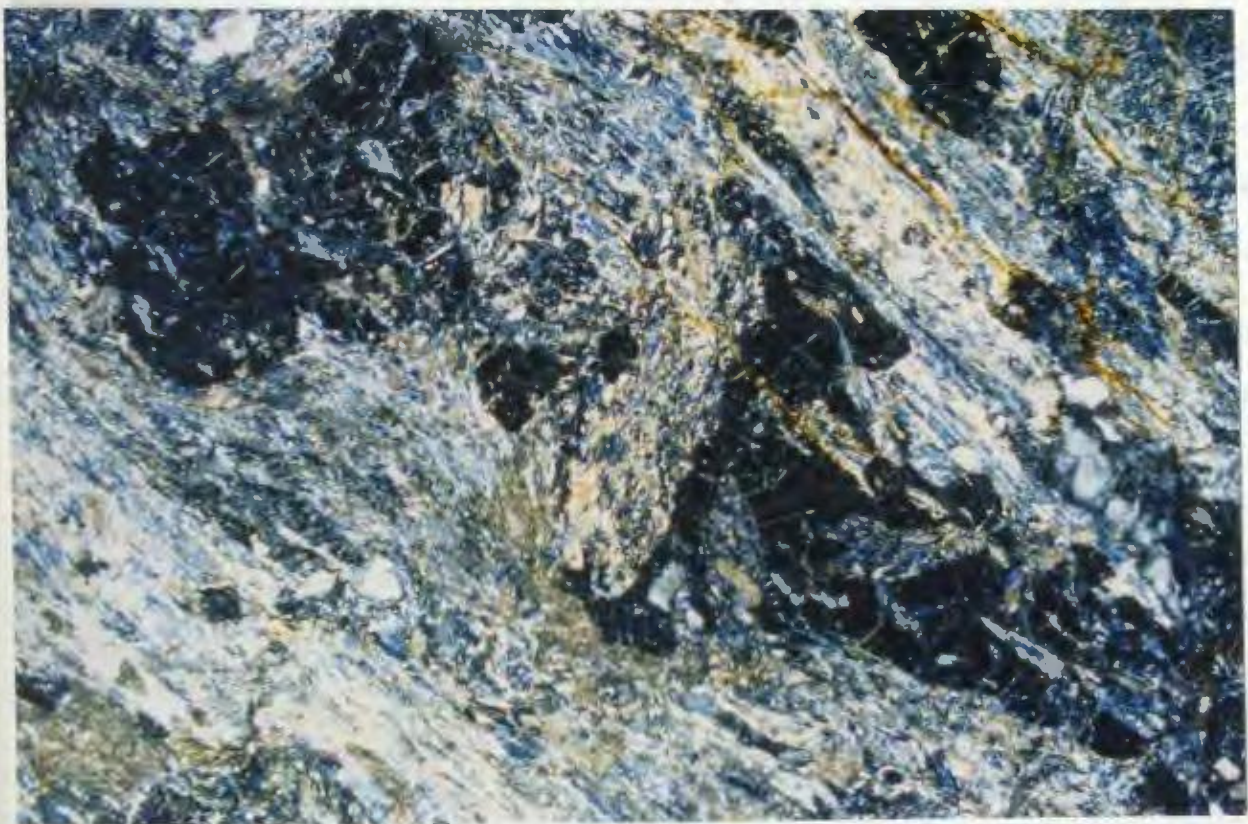
Fig 7.9 Fine grained metasedimentary rock with granolepidoblastic texture originally composed of quartz - albite - muscovite - accessory opaque oxide. Muscovite is largely replaced by a green chlorite which forms weak planar fabric or schistosity. Specimen 134; X 2.5; crossed polars; bar represents 0.5 mm.



**Fig 7.10** Strongly foliated and retrogressed metamorphosed garnetiferous schist. Garnet porphyroblast (strong relief in 7.10 and isotropic in 7.11) is broken and pulled apart in the foliation plane. The lepidoblastic groundmass of chlorite and sericite confer a strong foliation to the rock. Also in foliation plane are aligned elongate quartz-plagioclase veins aggregates (best visible in 7.11 in central right margin). Specimen 505-D; X 2.5; plane polarized light; bar represents 0.5 mm.

**Fig 7.11** Same as 7.10; crossed polars.







## 7.6 Origin of rocks in Mixed Lithology Slice

Clearly, all lithologies in the Mixed Lithology Slice are exotic with respect to the lower part of the ophiolite which surrounds them. The volcanogenic lithologies have no clear correlatives within the immediate vicinity. They are tentatively considered to have been derived from the stratigraphically higher levels of the local Ordovician stratigraphy, namely the Baie d'Espoir Group, on account of the variety of lithologies present and their low grade of metamorphism.

The metasedimentary rocks, on the other hand, are tentatively correlated with the Spruce Brook Formation. These rocks were incorporated into the Mixed Lithology Slice after their peak of metamorphism. The extensive retrogression, which characterizes this lithology, may have occurred during the emplacement of the tectonic slice.

## Chapter 8

### MINERAL CHEMISTRY

#### 8.1. Introduction

Analyses of minerals from the ultramafic part of the Coy Pond Complex were carried out on the electron probe microanalyzer facility in the Department of Earth Sciences, Memorial University. Details of the instrument and operating conditions are described in Appendix 2.A.

Mineral chemistry of the following ultramafic units and their main lithologies were investigated: the mantle tectonite composed of harzburgite and dunite, the tectonic mélanges composed of serpentized and variably carbonatized fragments and matrix, and the transition zone comprising layered clinopyroxenite and dunite.

Chemical data on the primary minerals (olivine, pyroxenes and spinel) can potentially provide information about the P-T conditions of formation, the occurrence of partial melting and the depletion of the ocean crust, and about the environment (mid ocean ridge or island arc) in which the ophiolite formed. Secondary minerals generated during widespread serpentization (lizardite, brucite and magnetite), serpentine recrystallization (antigorite and chrysotile) and during carbonatization (magnesite, talc, quartz) furnish additional information about temperature,

redox conditions and the fluid composition during these processes.

This chapter has been divided into two parts on the basis of the primary or secondary origin of the minerals.

## 8.2 Primary minerals

Hydration and carbonatization processes have affected all of the lithologies to varying degrees, but some primary minerals have survived in the basal tectonite and pyroxenite cumulates. In contrast, in the tectonic mélanges, shearing and extensive fluid circulation have resulted in complete replacement of all primary minerals, with the exception of Cr-spinel, which is apparently exceptionally resistant to a variety of hydration and carbonatization processes, even in the most sheared rocks.

### 8.2.1 Olivine

Twenty three microprobe analyses of olivine from various lithologies have been performed: twelve are from harzburgite, seven from dunite and four from the dunitic wall of an orthopyroxenite dike in harzburgite. The analyses are listed in Table 8.1 and Appendix 3.

The forsterite content of olivines from the mantle

Table 8.1. Electron microprobe analyses of olivine  
from Coy Pond ultramafics

specimen	333	156	184		175
rock	Hz	Hz	Hz		Hz**
mean of	3	3	3	9	2
	1	2	3	4	5
SiO <sub>2</sub>	40.52	37.30	40.30	39.31	40.63
MgO	50.45	49.44	50.30	50.23	51.14
Al <sub>2</sub> O <sub>3</sub>	0.01	0.01	nd	0.01	nd
FeO*	8.61	11.78	8.70	9.69	8.71
Na <sub>2</sub> O	0.02	0.02	nd	0.02	nd
CeO	0.01	0.00	nd	0.00	nd
TiO <sub>2</sub>	0.01	0.16	nd	0.08	nd
Cr <sub>2</sub> O <sub>3</sub>	0.00	0.01	nd	nd	0.04
MnO	0.13	0.16	0.13	0.14	0.12
NiO	0.35	0.52	nd	0.43	nd
Total	100.11	99.26	99.44	99.60	100.66
tetrahedral	formulae based on 4 oxygens				
Si 4+	0.988	0.939	0.982	0.970	0.985
Al 3+	nd	nd	nd	nd	nd
sum	0.988	0.939	0.982	0.970	0.985
octahedral					
Mg 2+	1.835	1.855	1.853	1.848	1.849
Fe 2+	0.175	0.247	0.177	0.200	0.176
Mn 2+	0.002	0.003	0.002	0.002	0.002
sum	2.012	2.105	2.032	2.050	2.026
$X_{Mg} = 100Mg^{2+} / (Mg^{2+} + (Fe^{2+}) + (Mn^{2+}))$					
Fo	91.2	88.1	91.2	90.1	91.2

\* FeO as Fe total

Hz = harzburgite

Hz\*\* = harzburgite fragment in mélange

column 4 = average of columns 1-3

T.8.1 p.2

specimen	299	103	mean	108
rock	Dun+	Dun+		Dun++
mean of	3	4	7	4
	6	7	8	9
SiO <sub>2</sub>	40.39	40.83	40.64	40.43
MgO	50.08	52.47	51.44	50.56
Al <sub>2</sub> O <sub>3</sub>	nd	nd	nd	nd
FeO*	9.00	7.22	7.98	9.32
Na <sub>2</sub> O	nd	nd	nd	nd
CaO	0.02	nd	nd	nd
TiO <sub>2</sub>	nd	nd	nd	nd
Cr <sub>2</sub> O <sub>3</sub>	0.03	0.00	nd	0.03
MnO	nd	0.10	nd	0.14
NiO	0.18	nd	nd	nd
Total	99.70	100.63	100.23	100.48
tetrahedral	formulae based on 4 oxygens			
Si 4+	0.989	0.983	0.986	0.984
Al 3+	0.000	0.000	0.000	0.000
sum	0.989	0.983	0.986	0.984
octahedral				
Mg 2+	1.650	1.884	1.784	1.835
Fe 2+	0.183	0.145	0.161	0.189
Mn 2+	0.000	0.001	0.001	0.002
sum	1.833	2.030	1.946	2.026
Fo	90.9	92.8	91.9	90.8

\* FeO as Fe total

column 8 = average of columns 6-7

Dun+ = dunite in harzburgite

Dun++ = dunitic wall in  
pyroxenite dike



tectonite varies from 88.1% to 92.8%. In detail, the range of forsterite content in harzburgite is larger and slightly lower, from 88.1% to 91.3%, compared to that in dunite, where the range is between 90.9% and 92.8%. Four microprobe analyses (Table 8.1.) from the dunitic wall rock to a pyroxenite dike in harzburgite (the orthopyroxenite dike is separated from its host harzburgite by a dunite layer several cm thick) has a forsterite content of 90.6%. In general, higher forsterite contents in olivine occur in more strongly depleted peridotites, and forsterite content shows an inverse relationship with NiO content (NiO varies from 0.52% in harzburgite olivine to 0.18% in dunite olivine).

There are no significant differences in the MnO content of olivine from harzburgite (0.14%) and dunite (0.10 %).

Cr<sub>2</sub>O<sub>3</sub> in olivine from both dunite and harzburgite is below the limit of detection.

#### 8.2.2 Orthopyroxene

Of a total of thirteen microprobe analyses of orthopyroxenes, seven are from harzburgite and six are from an enstatite dike. The orthopyroxene and clinopyroxene microprobe analyses are listed in Table 8.2 and Appendix 4.

Orthopyroxene from harzburgite and from enstatite dikes

Table 8.2 Electron microprobe analyses and calculated formulae  
of pyroxenes from Coy Pond ultramafics

specimen	333	156	184		175	108
rock	Hz	Hz	Hz	Hz	Hz	dike
mean of	2	3	2	7	3	3
analysis	1	2	3	4	5	6
SiO <sub>2</sub>	56.79	53.97	57.12	55.96	57.13	57.62
MgO	35.03	35.34	34.80	35.06	35.14	35.07
Al <sub>2</sub> O <sub>3</sub>	0.42	0.79	0.63	0.61	0.50	0.33
FeO*	5.45	7.10	5.81	6.12	5.69	6.14
Na <sub>2</sub> O	0.02	0.06	nd	0.03	0.05	0.02
K <sub>2</sub> O	0.00	0.00	0.00	0.00	0.00	0.00
CaO	0.78	1.13	0.94	0.95	0.78	0.57
TiO <sub>2</sub>	0.02	0.02	0.00	0.01	0.00	nd
Cr <sub>2</sub> O <sub>3</sub>	0.26	0.51	0.33	0.37	0.31	0.02
MnO	0.10	0.14	0.11	0.12	0.14	0.13
NiO	nd	0.13	nd	0.04	nd	nd
Total	98.97	99.20	99.55	99.24	99.76	100.20
tetrahedral	formulae based on 6 oxygens					
Si <sup>4+</sup>	1.978	1.904	1.973	1.951	1.972	1.961
Al <sup>3+</sup>	0.016	0.032	0.025	0.024	0.025	0.013
sum	1.992	1.936	1.998	1.975	1.997	1.994
octahedral						
Mg <sup>2+</sup>	1.616	1.858	1.791	1.822	1.791	1.798
Fe <sup>2+</sup>	0.157	0.208	0.167	0.177	0.167	0.176
Ca <sup>2+</sup>	0.029	0.041	0.033	0.034	0.033	0.020
sum	2.002	2.107	1.991	2.033	1.991	1.994
$XMg = 100Mg^{2+} / (Mg^{2+} + (Fe^{2+}) + (Ca^{2+}))$						
Mg	90.7	88.2	90.0	89.6	90.0	90.2
Fe	7.8	9.9	8.4	8.7	8.4	8.8
Ca	1.4	1.9	1.7	1.7	1.7	1.0

\* FeO as Fe total

Hz = harzburgite

1-5 = orthopyroxene in harzburgite

6 = orthopyroxene in orthopyroxenite dike

## T.8.2 p.2

specimen	108	94-C	94-C	404-B	304	304
rock			clinopyroxenite cumulate			
mean of	1	3	3	3	3	3
analysis	7	8	9	10	11	12
Na <sub>2</sub> O	58.16	0.06	0.04	0.11	0.06	0.03
MgO	22.16	16.17	16.47	16.40	16.97	17.24
Al <sub>2</sub> O <sub>3</sub>	1.92	1.97	2.04	2.56	1.10	1.02
SiO	2.57	54.09	53.56	52.85	53.96	52.16
K <sub>2</sub> O	0.93	0.00	0.00	0.01	0.01	0.01
CaO	0.08	23.02	22.86	24.17	24.11	24.77
TiO <sub>2</sub>	11.59	0.14	0.11	0.17	0.01	0.08
Cr <sub>2</sub> O <sub>3</sub>	0.05	0.51	0.56	0.43	0.48	0.32
MnO	0.44	0.11	0.11	0.11	0.09	0.09
FeO*	0.13	3.43	3.86	3.88	2.89	2.82
NiO	0.11	0.06	0.00	0.00	0.02	0.03
total	96.14	99.56	99.61	100.71	99.69	98.57
tetrahedral	formulae based on 6 oxygens					
Si <sup>4+</sup>	2.040	1.973	1.959	1.924	1.969	1.939
Al <sup>3+</sup> + iv	0.000	0.084	0.088	0.109	0.047	0.044
sum	2.040	2.057	2.047	2.033	2.016	1.983
octahedral						
Mg <sup>2+</sup>	1.200	0.878	0.897	0.889	0.924	0.955
Fe <sup>2+</sup>	0.078	0.104	0.118	0.117	0.087	0.087
Ca <sup>2+</sup>	0.451	0.899	0.895	0.942	0.944	0.986
sum	1.729	1.881	1.910	1.948	1.955	2.028
XMg = 100Mg <sup>2+</sup> / (Mg <sup>2+</sup> + (Fe <sup>2+</sup> ) + (Ca <sup>2+</sup> ))						
Mg	69.4	46.7	45.5	44.6	48.6	46.9
Fe	4.51	5.5	6.2	6.0	4.5	4.3
Ca	26.1	47.8	46.9	48.4	48.3	48.8

\*FeO as Fe total

specimen 7 = clinopyroxene in orthopyroxenite dike

304 = clinopyroxenite block in mélange

9, 11 and 12 = porphyroclast in clinopyroxenite

10 and 13 = neoblast in clinopyroxenite

which cut the harzburgite, is unzoned, Mg-rich with an enstatite component from En 87.1 % to En 89.8% in harzburgite, and from En 89.2% to 89.9% in orthopyroxenite dikes. They have similar contents of other elements except for  $\text{Al}_2\text{O}_3$  and CaO which are slightly higher in harzburgite (0.59% and 0.92% respectively) than in enstatite dikes (0.33% and 0.57% respectively).

#### 8.2.3 Clinopyroxene

A total of sixteen analyses of clinopyroxene were performed, one from an enstatite dike in harzburgite and fifteen from layered pyroxenite cumulate of the transition zone.

In rocks of the transition zone (mantle-crust transition), clinopyroxene is the main component in layered clinopyroxenite and olivine pyroxenite. Characteristically it shows a remarkably uniform composition across the entire zone, with minor chemical variations in the proportions of Ca:Mg:Fe. Mineralogically is an augitic diopside. No chemical variations between core and rim have been observed. Aluminum, chromium and titanium contents are very low (<2.5 <0.56 and <0.14% respectively).

Analyses of granular and recrystallized clinopyroxene

(free of exsolution lamellae) from two clinopyroxenite specimens, one in situ (94-C) and another as a block in mélange (304), show no notable differences in chemical composition (analyses 8 and 10 in Table 8.2, and Appendix 4).

In harzburgite, clinopyroxene occurs as thin exsolution lamellae in enstatite grains and could not be resolved adequately with the electron microprobe. In orthopyroxenite dikes, clinopyroxene occurs as small interstitial anhedral grains (<0.5 mm) forming less than one per cent modal of the rock. Overall, clinopyroxene in harzburgite is generally replaced by lizardite-bastite which rendered probe analyses difficult.

#### 8.2.4 Spinel

Accessory spinel occurs in ultramafic assemblages in small amounts, about 1% in harzburgite, 2% in dunite and in trace amounts (<1%) in pyroxenite cumulate. Because of its exceptional resistance to secondary chemical and mechanical processes, the spinel is present even in the tectonic mélanges and can be utilized to determine the nature of the ultramafic protolith. Characteristically, Cr-spinels in all assemblages possess a magnetite rim a few microns wide.

Electron microprobe analyses of Cr-spinels are given in



Table 8.3 : Calculated compositions (mol %) of Cr-spinel  
in Coy Pond ultramafics

specimen		79-A	144-A	175	175**	184
rock		Hz	Hz	Hz	Hz	Hz
analysis*		1	2	3	4	5
Sp	MgAl <sub>2</sub> O <sub>4</sub>	23.45	13.17	7.07	6.85	8.64
MgChr	MgCr <sub>2</sub> O <sub>4</sub>	30.72	32.19	34.09	31.25	34.82
Mgf	MgFe <sub>2</sub> O <sub>4</sub>	1.57	0.65	1.28	1.51	0.95
Usp	FeTi <sub>2</sub> O <sub>4</sub>	0.00	0.00	0.03	0.00	0.00
Her	FeAl <sub>2</sub> O <sub>4</sub>	18.38	15.26	9.50	10.34	10.70
Chr	FeCr <sub>2</sub> O <sub>4</sub>	24.08	37.31	45.80	47.19	43.14
Mt	FeFe <sub>2</sub> O <sub>4</sub>	1.23	0.75	1.72	2.28	1.17
chrome #		56.71	70.97	82.82	82.02	80.13
magn #		56.06	46.32	42.67	39.84	44.67
ferric #		11.45	5.03	9.57	11.30	7.19

specimen		94-B	251-A	251-B	305	389
rock		Dun	Dun	Dun	Dun	Dun
analysis		6	7	8	9	10
Sp	MgAl <sub>2</sub> O <sub>4</sub>	2.26	3.15	2.20	1.09	9.61
MgChr	MgCr <sub>2</sub> O <sub>4</sub>	8.61	29.09	19.28	20.30	20.43
Mgf	MgFe <sub>2</sub> O <sub>4</sub>	4.50	3.04	2.72	3.15	6.05
Usp	FeTi <sub>2</sub> O <sub>4</sub>	0.35	0.07	0.10	0.04	0.25
Her	FeAl <sub>2</sub> O <sub>4</sub>	12.14	5.69	6.77	3.29	16.76
Chr	FeCr <sub>2</sub> O <sub>4</sub>	46.18	52.57	59.30	61.30	35.63
Mt	FeFe <sub>2</sub> O <sub>4</sub>	24.12	5.50	8.38	9.52	10.55
chrome #		79.18	90.23	69.76	94.90	68.01
magn #		15.72	35.62	24.54	24.88	36.44
ferric #		20.60	8.61	11.26	12.85	16.76

Dun = dunite

\* each analysis represents an average of three measurements

\*\* margin (all others are core analyses)

Hz = harzburgite

Sch Sp = schistose serpentinite

T-M = talc magnesite

Q-M = quartz-magnesite

Sp = spinel

MgChr = magnesiochromite

Mgf = magnesioferrite

Usp = ulvöspinel

Her = hercynite

Chr = chromite

Mt = magnetite

Table 8.3 continued

specimen		94-C	251-D	289-A
rock		Pyrox	Pyrox	Pyrox
analysis		11	12	13
Sp	MgAl <sub>2</sub> O <sub>4</sub>	20.12	10.01	4.21
MgChr	MgCr <sub>2</sub> O <sub>4</sub>	13.34	15.80	9.16
Mgf	MgFe <sub>2</sub> O <sub>4</sub>	4.35	3.66	4.66
Usp	FeTi <sub>2</sub> O <sub>4</sub>	0.24	0.17	0.20
Her	FeAl <sub>2</sub> O <sub>4</sub>	32.14	23.58	18.84
Chr	FeCr <sub>2</sub> O <sub>4</sub>	21.31	37.22	40.99
Mt	FeFe <sub>2</sub> O <sub>4</sub>	6.94	8.62	20.86
chrome #		39.87	61.21	68.51
magn #		38.50	29.81	18.26
ferric #		11.49	12.42	25.86

Pyrox = pyroxenite

specimen		255-B	177-C	160	142-A	85-B
rock		Sch Sp	T-M	T-M	Q-M	Q-M
analysis		14	15	16	17	18
Sp	MgAl <sub>2</sub> O <sub>4</sub>	2.81	1.73	14.09	9.38	4.41
MgChr	MgCr <sub>2</sub> O <sub>4</sub>	19.48	18.43	28.80	34.17	38.11
Mgf	MgFe <sub>2</sub> O <sub>4</sub>	3.24	4.14	0.54	1.53	1.84
Usp	FeTi <sub>2</sub> O <sub>4</sub>	0.04	0.28	0.00	0.03	0.03
Her	FeAl <sub>2</sub> O <sub>4</sub>	8.04	5.29	18.13	11.28	5.46
Chr	FeCr <sub>2</sub> O <sub>4</sub>	55.82	56.43	37.08	41.10	47.19
Mt	FeFe <sub>2</sub> O <sub>4</sub>	9.30	12.67	0.70	1.84	2.28
chrome #		87.41	91.44	67.15	78.46	89.64
magn #		25.87	24.62	43.72	45.40	44.68
ferric #		12.70	17.01	1.25	3.81	4.15

Sch Sp = schistose serpentinite

T-M = talc magnesite

Q-M = quartz-magnesite

Sp = spinel

MgChr = magnesiochromite

Mgf = magnesioferrite

Usp = ulvospinel

Her = hercynite

Chr = chromite

Mt = magnetite

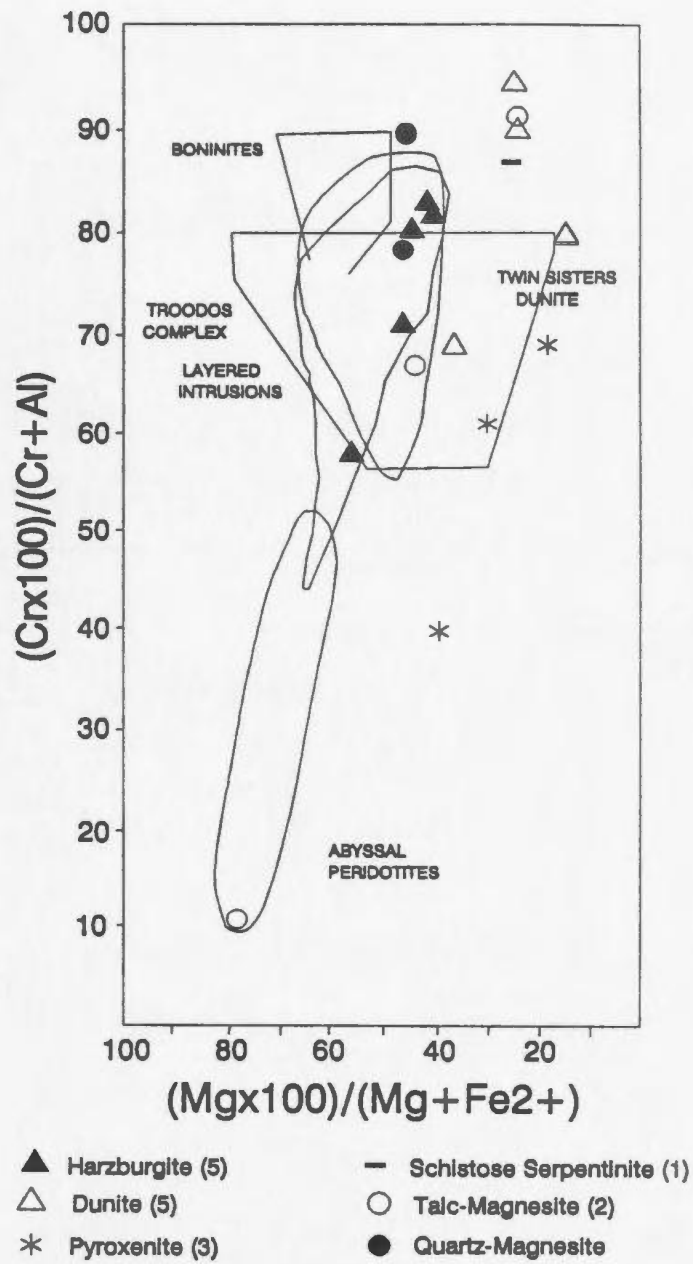
Appendices 5,6,7 and 8, and calculated end-member proportions from different ultramafic assemblages are given in Table 8.3. The total iron (as FeO) determined by electron microprobe analysis has been assigned to the octahedral and tetrahedral sites in accordance with the "ideal" formula. The amount of FeO and Fe<sub>2</sub>O<sub>3</sub> was calculated (using a Newpet program) by assuming that the RO/R<sub>2</sub>O<sub>3</sub> ratio in the chromian spinel is 1/1 (Irvine 1965). Several features are characteristic:

(i) In contrast to the silicate minerals in the ophiolite, the chromian spinels show a considerable range in chemical composition. Small compositional variations are detectable between grains in the same mineral assemblage, and between core and margin of the individual grains (Appendix 8).

(ii) The compositional plots of Cr# ( $\text{Cr} \cdot 100 / (\text{Cr} + \text{Al})$ ) against Mg# ( $\text{Mg} \cdot 100 / (\text{Mg} + \text{Fe}^{2+})$ ) of chromian spinel in Coy Pond ultramafics are shown in Figure 8.1, together with various compositional fields of chromites derived from different geological environments (from Irvine and Findlay, 1972 and Dick and Bullen, 1984). With the exception of one harzburgite having the Cr# close to 60 (Cr# = 56.71) and one pyroxenite from the upper levels of the transition zone (Cr = 39.87), all Coy Pond spinels have the Cr# > 60.

(iii) The richest spinels in Cr are those from dunite with

**Fig 8.1** Compositions of Cr-spinel from Coy Pond Complex plotted as Mg# versus Cr#. Also represented are composition fields for spinels from abyssal peridotites and layered intrusions (Irvine, 1967), boninites (Cameron et al., 1970), Troodos Complex and Twin Sisters Dunite (Dick and Bullen, 1984). Cr# = 60 separates Type I peridotites formed at a mid-ocean ridge (Cr#<60) from Type III peridotites (Cr#>60) formed in an island-arc environment (Dick and Bullen, 1984).





the highest Cr# (68-94.0), followed by those in harzburgite (56.7 to 82.8), and layered pyroxenite (39.8 to 68.5).

(iv) Cr-spinel in harzburgite is characterized by higher  $Al_2O_3$  contents reflected in higher mol percent of calculated "true" spinel ( $MgAl_2O_4$ ) (6.85 to 23.45) compared with spinel from dunite cumulate which yields less spinel (1.09 to 9.61 mol per cent).

(v)  $TiO_2$  contents in Cr-spinels are very low, (<0.20%) a feature typical for alpine-type peridotites, and there is a smaller than expected increase towards higher stratigraphic levels (Pallister and Hopson, 1981).

#### Conclusions on spinel chemistry

With minor exceptions, the Cr# of chromian spinel for the Coy Pond ultramafics is higher than 60, the lower limit for Type III alpine-peridotite of Dick and Bullen (1984), having an arc-related petrogenesis. Only spinels from the Troodos Complex and the Twin Sisters Dunite have similar compositions, which in modern analogs occurs in arc-related volcanics and intrusive rocks, oceanic plateau basalts and continental intrusive assemblages. The absence of diopside in the Coy Pond melting residue of peridotites, which consist of harzburgite and dunite, is typical for Type III

peridotites showing a high degree of depletion that was strongly influenced by the presence of water (Dick and Bullen, 1984).

This situation is opposite to that of the Bay of Islands ophiolite where clinopyroxene is present, the spinel in harzburgite is richer in Cr than spinel in dunite (Malpas and Strong, 1975) and the Cr# is variable (>60 but also <60). All these latter features are typical for Type I peridotites formed at mid-ocean ridges, of which Bay of Islands ophiolite is a classic example.

#### 8.2.5 Conclusions

(i) Olivine is unzoned and shows systematic variations in Fo-content ( $100\text{Mg}/\text{Mg}+\text{Fe}^{2+}$ ), which increases from an average of 90.1 in harzburgite to an average of 91.1 in dunite, confirming that the dunites are the most refractory residue produced by partial melting of the harzburgitic upper mantle.

(ii) The extremely low clinopyroxene content (<1%) in harzburgite (it occurs entirely as exsolution lamellae in orthopyroxene) also shows the extreme depletion of harzburgite;

(iii) Clinopyroxene in pyroxenite and olivine pyroxenite

is unzoned and chemically homogeneous across the entire sampled section of the transition zone.

(iv) With minor exceptions, the Cr# of chromian spinel for the Coy Pond ultramafics is higher than 60, the lower limit for Type III alpine-type peridotites of Dick and Bullen (1984), having an arc-related petrogenesis.

(v) The absence of diopside is typical for Type III peridotites showing a high degree of depletion as a result of partial melting in the presence of water (Dick and Bullen, 1984).

(vi) Cr-spinels in harzburgite are characterized by high  $\text{Al}_2\text{O}_3$  contents reflected in higher mol percent of calculated "true" spinel ( $\text{MgAl}_2\text{O}_4$ ) (from 6.85 to 23.45) compared with dunite cumulate which yields less  $\text{MgAl}_2\text{O}_4$  spinel (from 1.09 to 9.61 mol per cent).

(vi)  $\text{TiO}_2$  content in Cr-spinels is very low, (<0.20%) a feature typical for alpine-type peridotites and shows a smaller increase than expected towards higher stratigraphic levels of the ophiolite (Pallister and Hopson, 1981).

### 8.3 Secondary minerals

Secondary minerals include the three serpentine minerals (lizardite, chrysotile and antigorite), magnetite, brucite

Table 6.4 : Electron microprobe analyses for serpentine  
brucite and talc in mélange assemblages

specimen	432-D	432-D	450-C	450-C	203-B	203-B
serp.type	L	L	L	L	L	L
mean of	3	3	2	2	3	3
	rim	core	rim	core		rim
analysis	1	2	3	4	5	6
Na <sub>2</sub> O	0.01	0.03	0.00	0.02	0.05	0.04
MgO	39.54	40.02	40.10	39.32	38.65	38.81
Al <sub>2</sub> O <sub>3</sub>	0.14	0.02	0.14	0.23	0.05	0.11
SiO	41.21	41.70	40.72	42.25	43.36	44.29
K <sub>2</sub> O	0.00	0.00	0.01	0.00	0.01	0.00
CaO	0.01	0.01	0.03	0.04	0.02	0.02
TiO	0.01	0.01	0.02	0.01	0.01	0.00
Cr <sub>2</sub> O <sub>3</sub>	0.02	0.02	0.01	0.12	0.03	0.03
MnO	0.03	0.03	0.02	0.03	0.07	0.09
FeO*	5.06	3.56	5.68	4.89	4.60	4.47
NiO	0.33	0.30	0.17	0.14	0.14	0.23
total	86.23	85.97	86.88	87.08	87.06	86.11
H <sub>2</sub> O + **	13.77	14.03	13.13	12.92	12.94	11.89
number of ions on the basis of 14 oxygens						
Si	3.810	3.852	3.752	3.852	3.936	3.964
Al	0.000	0.000	0.000	0.026	0.004	0.008
total	3.810	3.852	3.752	3.878	3.940	3.972
Fe	0.148	0.274	0.436	0.369	0.246	0.332
Cr	0.000	0.000	0.000	0.008	0.000	0.000
Mn	0.000	0.000	0.000	0.000	0.108	0.004
Mg	5.448	5.480	5.512	5.346	5.232	5.178
Ca	0.000	0.000	0.000	0.000	0.000	0.000
total	5.596	5.754	5.948	5.723	5.586	5.514

L = lizardite

\* FeO as Fe total

\*\* calculated by difference

analysis 1-4 = lizardite, mesh textures

analysis 5 = lizardite, banded growth textures

analysis 6-7 = lizardite, gamma mesh textures

T 8.4 continued

specimen	203-B	196-C	196-C	450-C	196-C	450-C
serp.type	L	L	L	C	C	L
mean of	3	2	2	3	3	3
analysis	core 7	rim 8	core 9	10	11	12
Na <sub>2</sub> O	0.04	0.05	0.02	0.03	0.01	0.02
MgO	38.35	40.54	39.75	40.17	41.04	38.75
Al <sub>2</sub> O <sub>3</sub>	0.09	0.02	0.01	0.24	0.01	0.50
SiO	44.23	42.51	41.20	44.77	42.61	42.08
K <sub>2</sub> O	0.01	0.00	0.01	0.01	0.01	0.01
CaO	0.01	0.02	0.02	0.01	0.00	0.03
TiO	0.00	0.00	0.04	0.03	0.00	0.00
Cr <sub>2</sub> O <sub>3</sub>	0.04	0.01	0.01	0.05	0.02	0.52
MnO	0.12	0.05	0.11	0.01	0.04	0.03
FeO*	4.53	1.95	2.31	2.47	1.68	4.03
NiO	0.26	0.08	0.29	0.15	0.04	0.08
total	87.71	85.20	83.74	87.94	85.45	86.10
..2O+**	12.29	14.81	16.27	12.06	14.55	13.90
number of ions on the basis of 14 oxygens						
Si	3.978	nd	nd	3.968	4.224	3.860
Al	0.008	nd	nd	0.022	0.000	0.048
total	3.986	nd	nd	3.990	4.224	3.908
Fe	0.234	nd	nd	0.184	0.134	0.306
Cr	0.000	nd	nd	0.000	0.000	0.038
Mn	0.030	nd	nd	0.000	0.000	0.000
Mg	5.142	nd	nd	5.310	5.512	5.220
Ca	0.000	nd	nd	0.000	0.000	0.000
total	5.406	nd	nd	5.494	5.646	1.112

L = lizardite

C = chrysotile

\* FeO as Fe total

\*\* calculated by difference

analysis 8-9 = lizardite, hourglass texture

analysis 10-11 = chrysotile, veined crossfibre



T 8.4 continued

specimen	313	203-B	450-C	313	196-C	256-A
serp.type	L	A	A	B	B	T
mean of	3	3	3	1	1	1
analysis	13	14	15	16	17	18
Na <sub>2</sub> O	0.03	0.01	0.00	0.09	0.00	0.00
MgO	40.42	39.53	38.68	66.63	57.86	30.88
Al <sub>2</sub> O <sub>3</sub>	0.10	0.20	0.98	0.01	0.00	0.02
SiO	41.43	45.73	44.62	3.68	6.69	62.13
K <sub>2</sub> O	0.01	0.01	0.00	0.05	0.00	0.00
CaO	0.02	0.01	0.04	0.02	0.00	0.00
TiO	0.00	0.01	0.01	0.00	0.20	0.00
Cr <sub>2</sub> O <sub>3</sub>	0.47	0.00	0.22	0.00	0.00	0.04
MnO	0.12	0.05	0.05	0.56	0.52	0.00
FeO*	1.12	2.85	3.40	3.05	10.90	1.84
NiO	0.05	0.14	0.17	0.08	0.10	0.06
total	83.78	88.56	88.15	74.15	76.09	94.97
H <sub>2</sub> O+**	16.22	11.44	11.85	25.85	23.91	5.03

number of ions on the basis of 14 oxygens for serpentine,  
1 oxygen for brucite, 24 oxygens for talc

Si	3.428	4.026	3.964	0.033	0.245	8.064
Al	0.008	0.018	0.102	0.000	0.000	0.000
total	3.436	4.044	4.066			
Fe	0.078	0.206	0.252	0.023	0.083	0.128
Cr	0.090	0.000	0.012	0.000	0.000	0.000
Mn	0.004	0.012	0.000	0.004	0.015	0.000
Mg	4.986	5.188	5.120	0.904	0.790	5.990
Ca	0.000	0.000	0.000	0.000	0.000	0.000
total	1.031	1.081	1.077			
X Mg				97.5	90.5	-
X Fe				2.5	9.5	-

L = lizardite

A = antigorite

B = brucite

T = talc

\* FeO as Fe total

\*\* calculated by difference

analysis 12-13 = lizardite, orthopyroxene bastites

analysis 14-15 = antigorite, interpenetrating textures

analysis 16 = brucite, fine grained in vein

analysis 17 = brucite, large grains

analysis 18 = talc large grains, veined

and talc. These minerals occur in subordinate amounts in harzburgite and pyroxenite and as the main phases in the assemblages of the tectonic mélanges.

#### 8.3.1 Serpentine minerals

Forty one microprobe analyses carried out on serpentine minerals are reported in Tables 8.4. and Appendix 9. Most of the analyzed serpentines are from the tectonic mélange units (fragments and matrix), and a few are from serpentized dunite of the transition zone.

During hydration of peridotite, olivine is initially replaced commonly by lizardite with pseudomorphic textures (mesh,  $\gamma$ -mesh, hourglass or banded-growth). During recrystallization, the pseudomorphic textures are replaced by non-pseudomorphic textures such as interpenetrating (composed of antigorite) or interlocking (composed of antigorite  $\pm$  lizardite) textures. The less common chrysotile has a fibrous habit and occurs in late veins associated with both lizardite and antigorite varieties. Similarly, pyroxenes are hydrated (to a lesser degree than olivine) to bastite, which most commonly is lizardite.

The main chemical differences determined in serpentinite among various pseudomorphic varieties of lizardite and between lizardite and recrystallized antigorite or

chrysotile of the Coy Pond Complex are the silica, magnesia, water and iron contents:

(i) Antigorite has a higher  $\text{SiO}_2$  content (42.93% to 46.32%) than lizardite (40.02 to 43.61%) and slightly higher than chrysotile (42.34 to 45.41%). Pseudomorphic lizardite in hourglass textures ( $\text{SiO}_2$  41.07 to 42.69%) and  $\gamma$ -mesh textures (44.01 to 44.48%) have chemical compositions intermediate between those of antigorite and pseudomorphic mesh textures.

(ii) Antigorite has lower  $\text{MgO}$  contents relative to lizardite and chrysotile: 37.79% to 39.80% compared to 39.23% to 40.64% and 39.63% to 41.15 % respectively. Again, the recrystallized  $\gamma$ -mesh textured lizardite has  $\text{MgO}$  close to antigorite values of 37.88% to 38.89%.

(iii) The water content (determined by difference) of antigorite is less than that of lizardite and chrysotile: 9.99% to 13.64 % compared to 12.56% to 14.79 % and 12.62 to 15.96 %, respectively.

(iv) The iron content is higher in lizardite mesh textures (3.56% to 5.68%), than in lizardite hourglass textures (1.94% to 2.31%) and is lowest in antigorite interpenetrating textures (2.85% to 3.40%).

(v) In mesh textures, the iron content in mesh rims (4.48% to 5.98%) is higher than in mesh centers (2.32% to 4.98%).

(vi) Lizardite bastites show a relatively large variation in iron content (average from 1.12% to 4.03%).

(vii) The iron content of chrysotile is the lowest amongst all serpentine minerals (1.55% to 2.52%).

(viii) The average NiO values decrease from mesh-textured lizardite (0.25%) to antigorite (0.15%) and chrysotile (0.09%).

(ix) The  $Al_2O_3$  content, which is about 0.1% in dunite serpentinite (pyroxene free), increases to about 0.23% in serpentinite of harzburgitic origin;

#### 8.3.2 Brucite

In the tectonic mélanges, brucite was found only in a few serpentinite fragments. Elsewhere it has been destabilized by widespread carbonatization. In two hopefully representative brucite analyses (Table 8.4), FeO content (as Fe total) varies widely from 3.05 to 10.90% yielding chemical formulae of  $Mg_{97.5}, Fe_{2.5}(OH)_2$  and  $Mg_{90.5}, Fe_{9.5}(OH)_2$ . Brucite is more common in serpentinitized dunite within the tectonites, where it occurs in intergrowths with lizardite.

### 8.3.3 Talc

Talc in association with magnesite is the product of carbonatization of serpentine and occurs widely in the tectonic mélanges (both fragments and matrix), and less commonly is formed during pyroxene alteration.

For reasons unknown, all attempts to probe talc were unsuccessful, yielding unreasonably low oxide totals. For this reason only one chemical analysis of talc is listed in Table 8.4; it is from a coarse-grained vein. However all analyses have shown that talc is a ferroan variety with FeO between 1.5 and 2 weight %.

### 8.3.4 Magnesite

Magnesite is found chiefly in the tectonic mélanges, forming assemblages with lizardite, antigorite, talc, quartz, and in subordinate amounts with serpentinite in layered pyroxenite.

A total of forty one microprobe analyses of magnesite in diverre assemblages have been carried out: eight magnesites associated with lizardite (three of them are schistose serpentinite), six with antigorite, ten with talc and seventeen are of magnesite associated with quartz.

Almost all magnesite contains very fine inclusions of

serpentinite which could not be avoided during analyses. As a result, the measured Fe/Mg ratio of the magnesite must be corrected for inclusions of serpentine. The correction scheme adopted utilizes the SiO<sub>2</sub> content, which varies from more than 5% in some analyses of magnesite coexisting with lizardite, to about 0.7% in quartz-magnesite assemblages. After complete removal of the SiO<sub>2</sub> content, the excess iron (serpentine related) is also removed (Appendix 2.B and Table A.8.1 for details). The corrected microprobe analyses are listed in Table 8.6 and Appendices 10, 11 and 12.

In Table 8.5 are presented average analyses of magnesite (in weight percent oxides) associated with lizardite, talc, antigorite and quartz. Measured values are given at the top of the table, corrected values are given at the bottom.



Table 8.5

	<u>lizardite</u>	<u>talc</u>	<u>antigorite</u>	<u>quartz</u>
measured oxide values				
SiO <sub>2</sub>	2.73	0.72	1.73	0.68
MgO	40.22	38.6	36.04	38.51
CaO	0.12	0.06	0.23	0.14
FeO	1.11	7.79	12.26	5.51
corrected and calculated values				
MgCO <sub>3</sub>	97.6	89.7	83.4	92.4
CaCO <sub>3</sub>	1.1	0.1	0.3	0.5
FeCO <sub>3</sub>	1.3	10.2	16.4	7.0

**Table 8.5** Microprobe analyses of magnesite in association with lizardite, talc, antigorite and quartz. Measured values are given at the top, corrected values at the bottom. For details of the correction procedure, see Appendix 2B.

SiO<sub>2</sub> (as silicate impurities) in magnesite (Table 8.5 and Table 8.6) is larger in serpentinite assemblages (in lizardite from 2.33 to 5.22%; in antigorite average 1.73%) than in talc (average 0.72%) or quartz-magnesite (average of 0.68%) assemblages. An exception is pseudofibrous magnesite

Table 8.5 Electron microprobe analyses for magnesite  
in mélange assemblages

specimen	343-B	432-D		255-A	94-B	343-D
rock type	L	L	L	L	A	A
mean of	3	2	5	3	3	3
	1	2		3	4	5
SiO <sub>2</sub>	5.22	2.33	4.06	0.51	1.42	2.03
MgO	39.54	41.85	40.46	39.81	35.04	37.03
CaO	0.03	0.06	0.04	0.26	0.27	0.18
FeO*	1.38	0.96	1.21	0.95	14.27	10.25
total	46.16	45.48	45.89	41.55	51.00	49.49
Si	0.102	0.035	0.075	0.010	0.021	0.030
Mg	0.878	0.951	0.907	0.971	0.776	0.830
Ca	0.014	0.016	0.015	0.004	0.004	0.002
Fe	0.020	0.012	0.017	0.015	0.177	0.128
total	1.102	1.035	1.075	1.010	0.978	1.014
Mg**	0.972	0.974	0.973	0.982	0.806	0.861
Ca	0.014	0.016	0.015	0.004	0.004	0.002
Fe	0.014	0.010	0.012	0.014	0.190	0.137
total	1.000	1.000	1.000	1.000	1.000	1.000
MgCO <sub>3</sub>	97.2	97.4	97.3	98.2	80.6	86.1
CaCO <sub>3</sub>	1.4	1.6	1.5	0.4	0.4	0.2
FeCO <sub>3</sub>	1.4	1.0	1.2	1.4	19.0	13.7

\* FeO as Fe total

\*\* column of normalized mole fractions after removal of serpentine

L = lizardite

A = antigorite

analysis 1;2;4;5 = massive fragments

analysis 3 = schistose matrix

Table 8.6 continued

specimen		177-D	270	252	
rock type	A	T-M	T-M	T-M	T-M
mean of	6	4	3	3	10
analysis		6	7	8	
SiO <sub>2</sub>	1.73	0.11	0.80	1.24	0.72
MgO	36.04	38.62	40.68	36.51	38.60
CaO	0.23	0.03	0.00	0.15	0.06
FeO*	12.26	8.89	6.31	10.16	7.79
total	50.25	45.65	47.80	48.06	47.17
Si	0.026	0.001	0.012	0.019	0.011
Mg	0.803	0.908	0.910	0.847	0.888
Ca	0.003	0.000	0.000	0.002	0.001
Fe	0.153	0.311	0.078	0.131	0.173
total	0.996	1.002	1.012	1.019	1.011
Mg**	0.834	0.908	0.921	0.862	0.897
Ca	0.003	0.000	0.000	0.002	0.001
Fe	0.164	0.091	0.079	0.136	0.102
total	1.000	1.000	1.000	1.000	1.000
MgCO <sub>3</sub>	83.4	90.8	92.1	86.2	89.7
CaCO <sub>3</sub>	0.3	0.0	0.0	0.2	0.1
FeCO <sub>3</sub>	16.4	9.1	7.9	13.5	10.2

\* FeO as Fe total

\*\* column of normalized mole fractions after removal of serpentine

T-M = talc-magnesite

analysis 6;8 = schistose matrix

analysis 7 = massive fragment

Table 8.8 continued

specimen	342	85-F	142-C	
rock type	Q-M	Q-M	Q-M	Q-M
mean of	9	5	3	17
analysis	9	10	11	
SiO <sub>2</sub>	1.07	0.34	0.09	0.68
MgO	38.25	38.63	39.08	38.51
CaO	0.17	0.08	0.13	0.14
FeO*	6.06	5.28	4.26	5.51
total	45.57	44.33	43.55	44.85
Si	0.017	0.005	0.000	0.010
Mg	0.900	0.923	0.940	0.914
Ca	0.002	0.000	0.001	0.001
Fe	0.079	0.070	0.056	0.072
total	1.017	1.005	1.001	1.011
Mg**	0.917	0.928	0.941	0.924
Ca	0.002	0.012	0.001	0.005
Fe	0.080	0.059	0.056	0.070
total	1.000	1.000	1.000	1.000
MgCO <sub>3</sub>	91.7	92.8	94.1	92.4
CaCO <sub>3</sub>	0.2	1.2	0.1	0.5
FeCO <sub>3</sub>	8.0	5.9	5.8	7.0

\* FeO as Fe total

\*\* column of renormalized mole fractions after removal of serpentine

Q-M = quartz-magnesite

analysis 9;10 = massive fragments

analysis 11 = schistose matrix

in schistose serpentinite which contains the smallest amount of serpentinite inclusions (specimen 255-B with 0.51% SiO<sub>2</sub> in Table 8.6).

Because of variable amounts of siderite (FeCO<sub>3</sub>) in solid solution, the magnesite is a ferroan variety (bruennerite).

The amount of siderite solid solution in magnesite is dependent on the redox conditions and the resultant degree of reduction of coexisting magnetite. In an evolutionary path the siderite content in magnesite is as follows: magnesite in lizardite-magnesite assemblages is poorest in siderite [Mg<sub>.976</sub>, Fe<sub>.013</sub>, Ca<sub>.011</sub>(CO<sub>3</sub>)]; siderite contents are higher in talc-magnesite assemblages [Mg<sub>.897</sub>, Fe<sub>.102</sub>, Ca<sub>.001</sub>(CO<sub>3</sub>)], and reach a maximum in antigorite-magnesite assemblages [Mg<sub>.834</sub>, Fe<sub>.164</sub>, Ca<sub>.002</sub>(CO<sub>3</sub>)], and decrease in quartz-magnesite [Mg<sub>.924</sub>, Fe<sub>.07</sub>, Ca<sub>.005</sub>(CO<sub>3</sub>)] (Table 8.6).

The amount of the calcite component in magnesite is about 1.5% in pseudomorphic lizardite but is negligible in all other rock types.

Discrete dolomite grains have not been observed in serpentinites, but dolomite occurs locally as late veins associated with magnesite. Analysis of a single grain (Appendix 9) yielded the chemical formula (Mg<sub>.516</sub>, Fe<sub>.033</sub>, Ca<sub>.451</sub>) CO<sub>3</sub>.

#### 8.3.5 Opaque phases

Opaque minerals, ubiquitous in all serpentized peridotites, are represented mainly by magnetite which occurs in amounts less than 5% of the rock volume. SEM investigations have also shown the presence in brucite-bearing serpentinite of trace amounts of awaruite (Fe,Ni alloy) and pentlandite (Fe,Ni)<sub>9</sub>S<sub>8</sub>, and in talc-magnesite the presence of pentlandite and linnaeite (Co,Ni)<sub>3</sub>S<sub>4</sub>.

#### 8.3.6 Conclusions

(i) Secondary minerals, represented by lizardite ± brucite + magnetite have replaced the original assemblages completely in dunite and partially in harzburgite.

(ii) The iron originally present in olivine was redistributed during serpentization, entering into solid solution in lizardite and brucite and also forming opaque phases such as magnetite, awaruite and pentlandite.

(iii) The relatively low iron content in brucite may indicate a high temperature of serpentization (Moody, 1976).

(iv) The presence of trace amounts of awaruite (Ni<sub>3</sub>Fe) and pentlandite (Fe,Ni)<sub>9</sub>S<sub>8</sub> in parageneses with brucite suggests a



reducing environment during serpentinization.

(v) The ubiquitous presence of serpentine inclusions in magnesite associated with all assemblages (2.73% SiO<sub>2</sub> in lizardite-magnesite, 1.73% SiO<sub>2</sub> in antigorite-magnesite, 0.72% SiO<sub>2</sub> in talc-magnesite and 0.68% SiO<sub>2</sub> in quartz-magnesite) shows that carbonatization occurred rather slow and was incomplete.

(vi) The carbonatization process, which produced talc-magnesite (especially in matrix rocks) and quartz-magnesite, occurred by introduction of CO<sub>2</sub> and removal of H<sub>2</sub>O.

(vii) Several authors have noted that carbonatization takes place under relatively oxidizing conditions compared to serpentinization (Ekstrand, 1975). Evidence presented in the next chapter is in accord with this interpretation.

(viii) Recrystallization of lizardite to antigorite could be explained by a progressive metamorphic event (Evans, 1976; Evans et al., 1977; Moody, 1977), but also by stabilization of Fe<sup>2+</sup> in the octahedral sheet, which stabilizes antigorite, a mechanism that is dependent on pH (O'Hanley and Dyar, in press).

## Chapter 9

### PHASE EQUILIBRIA AND METAMORPHISM OF THE TECTONIC MÉLANGE

#### 9.1 Introduction

The presence of relict minerals (e.g. Cr-spinel in the lower sections of the ophiolite) and the serpentine ( $\pm$  magnesite) mineralogy with relict pseudomorphitic serpentinization textures demonstrates that both the western and eastern tectonic mélanges have an ultramafic origin.

During shearing and low grade metamorphism, rocks of dunitic-harzburgitic composition were converted to a large variety of metamorphic assemblages containing not only serpentine minerals (lizardite, antigorite and chrysotile) but also brucite, magnesite, talc and quartz.

Three low P-T metamorphic events can be distinguished which have profoundly affected the tectonic mélanges, but had only a limited effect on the rest of the ophiolitic complex.

(1) The first event was the hydration of the peridotite, which resulted in pervasive and complete serpentinization of the dunitic-harzburgitic component of the tectonic mélanges, complete serpentinization of dunite in both the mantle tectonite and the pyroxenite, and partial serpentinization of the harzburgite tectonite.

(2) The second event involved the partial carbonatization of serpentinite in the tectonic mélanges with both fragments

and matrix being affected to some degree. Carbonatization was in part pervasive, in part related to fractures, and it affected the serpentinites very inhomogeneously.

(3) The third major metamorphic event was the partial recrystallization of serpentine: pseudomorphic lizardite was locally replaced by non-pseudomorphic antigorite ( $\pm$  lizardite).

These three metamorphic events are discussed in more detail below, utilizing petrographic evidence and relevant petrologic information from the literature.

## 9.2 Serpentinization of peridotite

Serpentinization of peridotite resulted in the formation of lizardite-bearing assemblages from olivine. It took place as a result of pervasive hydration of the parental ultramafic assemblage (olivine  $\pm$  pyroxene) both within the tectonic mélanges and elsewhere in the ophiolite. Two pseudomorphic mineral assemblages developed: (i) lizardite + brucite, which is the main assemblage in serpentinized dunite within the tectonite, but is rare (relics) in mélange fragments; and (ii) a secondary assemblage, lizardite  $\pm$  magnesite, which is widespread in the tectonic mélanges (in both fragments and matrix), but does not occur in the peridotite tectonites.

Before discussing possible reactions applicable to the Coy Pond Complex, two observations are pertinent. Firstly, the rate of serpentinization of minerals in peridotite is olivine > orthopyroxene > clinopyroxene (Coleman 1971), the rates being controlled by diffusion and being geologically fast (Martin and Fyfe 1970). Secondly, the presence of iron-bearing olivine (Moody 1976) lowers the reaction temperature and increases the rate at which serpentinization takes place.

Temperature of serpentinization is dependent upon the serpentine mineral species produced. There are few experimental and no thermodynamic data on lizardite, the species formed initially (from petrographic evidence) in the Coy Pond serpentinites. O'Hanley et al. (1989) has recently produced some information on Al-rich lizardite, but this is not very relevant to the Al-free lizardite in this study. The temperature of lizardite formation is therefore only broadly constrained in this study by the data for antigorite, computed by Berman (1988) to be less than 380°C at 2 kbars (Fig 9.1).

In the absence of petrographic observations that indicate specific reaction paths, the serpentine-bearing mineral assemblages noted above could in principle have been generated by any of the following idealized serpentinization reactions:

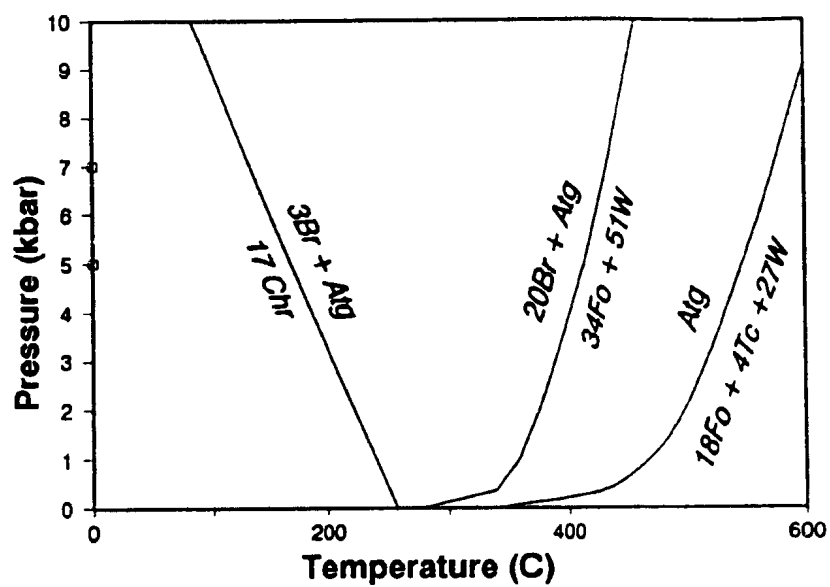
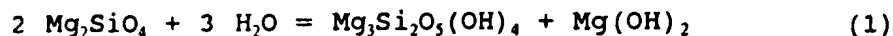


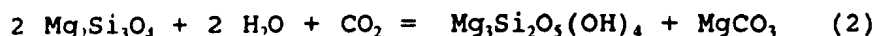
Figure 9.1 Equilibria in the system MgO-SiO<sub>2</sub>-H<sub>2</sub>O-CO<sub>2</sub> computed for  $a(\text{H}_2\text{O}) = 1$ . After Bern:an (1988).

Abbreviations: Fo=forsterite; Tc=taic; Br=brucite;

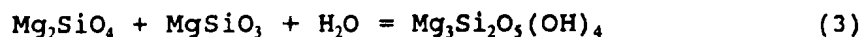
Atg=antigorite; Chr=chrysotile; W=water;



forsterite                      serpentine              brucite

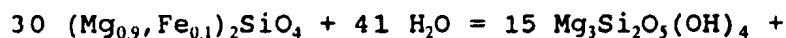


forsterite                      antig/chrys      magnesite



forsterite      enstatite              serpentine

For olivines of the composition occurring in the Coy Pond Complex, and noting the presence of abundant magnetite in the product assemblage, reaction (1) would be modified to:

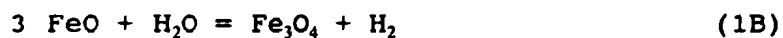


olivine                                      serpentine



brucite      magnetite

As written, this reaction ignores the measured small amounts of iron present in both serpentine and brucite. Of particular importance is the partial reaction:





which implies that the oxygen required to produce magnetite was derived from the decomposition of water ( $\text{H}_2\text{O} = 1/2\text{O}_2 + \text{H}_2$ ). This reaction enriches the fluid phase in  $\text{H}_2$ , generating a strongly reducing environment which is characteristic of serpentinization reactions (Thayer 1966; 1977; Barnes and O'Neil 1969; Frost 1985; Abrajano et al., 1988; Stevens, 1992). Petrographic observations, SEM and microprobe data (not listed) on minor phases occurring in brucite-bearing serpentinite in the Coy Pond Complex, have confirmed the existence of minerals such as awaruite ( $\text{Ni}_3\text{Fe}$ ) and pentlandite ( $\text{Fe,Ni}_9\text{S}_8$ ), indicative of an environment of very low oxygen fugacity at this time.

Reaction (2) has been modelled in the  $\text{MgO-SiO}_2\text{-H}_2\text{O-CO}_2$  system and occurs at extremely small values of  $X\text{CO}_2$  ( $< 0.5$  mole percent) for reasonable estimates of P and T (Greenwood 1967; Johannes, 1969) as shown in Figure 9.2. Reaction (3) represents serpentinization of a harzburgitic rock (Martin and Fyfe, 1970).

Several lines of observation lead us to conclude that serpentinization in the Coy Pond Complex took place through reactions (1) and (3), but not through reaction (2).

(i) The presence in dunite tectonites of only lizardite  $\pm$  brucite assemblages.

(ii) Where mesh-textured lizardite occurs with magnesite,

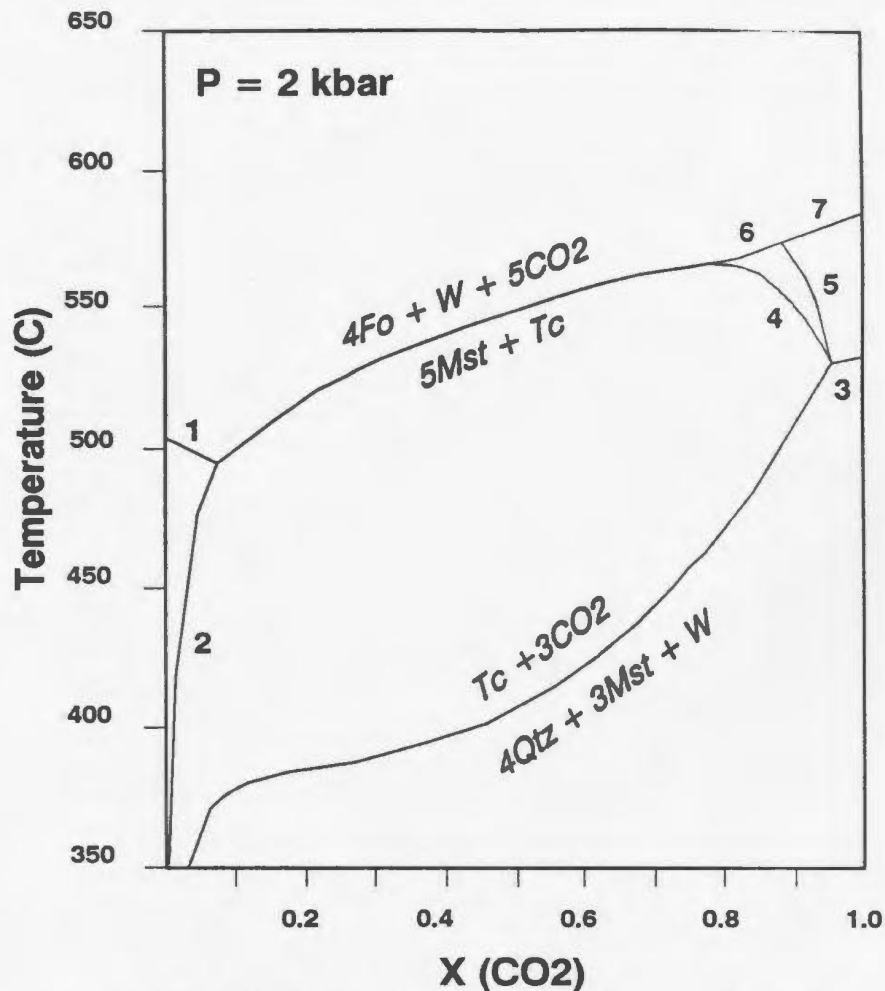


Fig 9.2 (a). Phase diagram showing the isobaric equilibrium curves in the model system

MgO-SiO<sub>2</sub>-H<sub>2</sub>O-CO<sub>2</sub> calculated from thermodynamic data. After Berman (1988). Reactions:

- 1:  $\text{Atg} = 4\text{Tc} + 18\text{Fo} + 27\text{H}_2\text{O}$ ; 2:  $\text{Atg} + 45\text{CO}_2 = 17\text{Tc} + 45\text{Mst} + 45\text{H}_2\text{O}$ ; 3:  $\text{Mst} + \text{Qtz} = \text{En} + \text{CO}_2$ ; 4:  $\text{Mst} + \text{Tc} = 4\text{En} + \text{H}_2\text{O} + \text{CO}_2$ ; 5:  $\text{Tc} = 3\text{En} + \text{Qtz} + \text{H}_2\text{O}$ ; 6:  $\text{Anth} + 9\text{Mst} = 8\text{Fo} + \text{H}_2\text{O} + 9\text{CO}_2$ ; 7:  $\text{En} + 2\text{Mst} = 2\text{Fo} + 2\text{CO}_2$ . Abbreviations as in Fig 9.1; Mst=magnesite; Qtz=quartz; Anth=anthophyllite; En=enstatite.

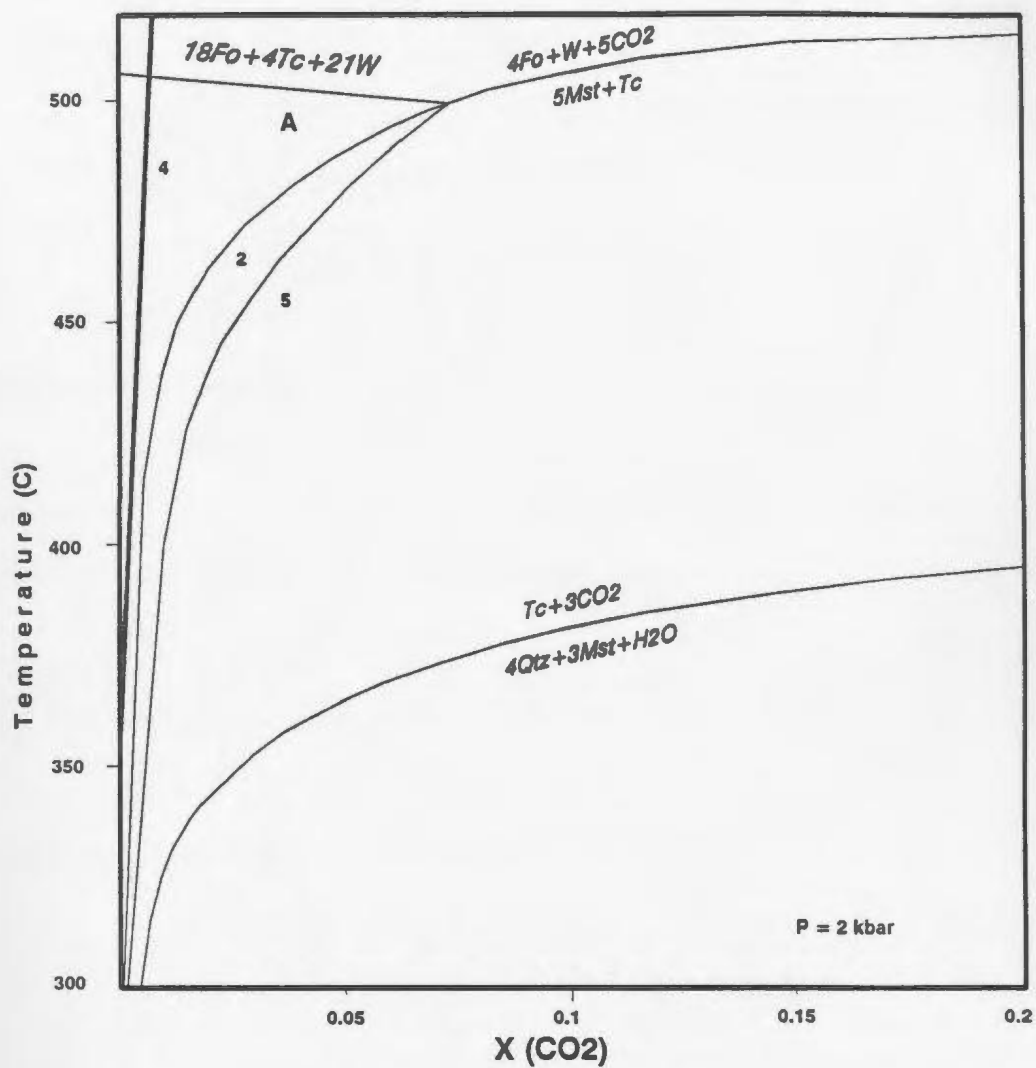


Fig 9.2.B: Diagram representing the water rich part of Fig 9.2.A

Abbreviations and reactions number as in text and in Fig.9.1.A; 2:  $34\text{Fo} + 31\text{W} + 20\text{CO}_2 = \text{A} + 20\text{Ms}$ ; 4:  $\text{Br} + \text{CO}_2 = \text{Mst} + \text{W}$ ; 5:  $2\text{A} + 45\text{CO}_2 = 45\text{Mst} + 17\text{Tc} + 45\text{W}$ ;

the latter phase commonly also preserves details of the mesh texture implying that magnesite formed later, pseudomorphing lizardite.

(iii) Magnesite grains associated with lizardite always contain abundant minute lizardite inclusions, indicating that lizardite was replaced by magnesite.

(iv) Brucite is known to be a very common phase during the early phases of serpentinization of dunite and high-olivine peridotite (Hostetler et al., 1966, Wicks and Whittaker, 1977). In the Coy Pond Complex, brucite is very common in serpentinized dunite, but occurs only rarely in dunite fragments in the tectonic mélanges, where it is a relict phase. It is therefore inferred that carbonatization reactions in the tectonic mélanges destabilized pre-existing brucite, implying that the formation of the brucite-serpentinite assemblage predated carbonatization.

The P-T coordinates of reaction (1) in the model  $\text{MgO-SiO}_2\text{-H}_2\text{O}$  system have been determined experimentally for pure forsterite as the reactant and chrysotile as the serpentine product by Johannes (1968), and Moody (1976) repeated the experiments for iron-bearing olivine ( $\text{Fo}_{93}$ ). These experimental investigations on reaction (1) with chrysotile as the product have shown that serpentinization in the presence of pure water can occur below  $380^\circ\text{C}$  (Johannes,

1968), or 365°C (Moody, 1976 for Fo93) at 2 kbars, results that are generally concordant with phase equilibria computed by Berman (1988) for chrysotile and antigorite (Fig 9.1). The reaction is not very pressure sensitive (it takes place at 500°C at 15 kbars) and so can occur at considerable depth if water is available (Coleman and Keith 1971). Taking into account that natural brucite can accommodate a large amount of ferrous iron, (between 6 and 72 mole percent  $\text{Fe}(\text{OH})_2$  or 15 mole percent on average (Hostetler et al., 1966), and following the conclusion of Moody (1976) that the iron content of brucite is inversely related to the temperature of serpentinization, it may be tentatively concluded from the low iron contents of two relict brucites in mélange fragments of the Coy Pond Complex [ $\text{Mg}_{97.5}\text{Fe}_{2.5}(\text{OH})_2$  and  $\text{Mg}_{90.5}\text{Fe}_{9.5}(\text{OH})_2$ ], that the temperature of serpentinization was probably elevated, close to its upper limit.

There are many estimates of the temperature of serpentinization in the geologic literature. Coleman (1966; 1967) concluded that serpentinization occurred at temperatures as low as 240°C and Bonatti (1983) proposed temperatures <250°C. Temperature estimates obtained using the serpentine-magnetite geothermometer (Wenner and Taylor, 1969; 1972) suggest that serpentinization occurs at lower temperature for continental lizardite (about 85-115°C), than

for oceanic lizardite (about 130-185°C).

### 9.3 Carbonatization of the serpentinite

Carbonatization characterizes the second metamorphic event, which started when  $\text{CO}_2$  became available, most likely during the obduction of the ophiolitic slab onto the continental margin (see Chapter 11). Carbonatization affected only serpentinite assemblages in the tectonic mélanges and in the adjoining pyroxenite, but serpentinitized dunite within harzburgite tectonites is unaffected. Serpentinite lenses (former dunite) in layered pyroxenite are carbonatized only locally and to a lesser degree than serpentinite in the tectonic mélanges. From examination of mineral assemblages, several carbonatization reactions are inferred to have occurred in the tectonic mélanges.

Brucite is virtually absent from the tectonic mélanges, which in contrast contain abundant magnesite. In Figure 9.2, it can be seen that at a given P and T a higher  $\text{XH}_2\text{O}$  is required to stabilize brucite than serpentine, so brucite is the first candidate to react as  $\text{XCO}_2$  increases in the fluid. The formation of magnesite from brucite occurs at extremely low values of  $\text{XCO}_2$  ( $< 0.5 \text{ mol\% CO}_2$  at  $P = 2 \text{ kbar}$  (Johannes, 1967) according to reaction:





Based on the location of reaction (4) on the T-XCO<sub>2</sub> plane, brucite likely decomposed at the first appearance of CO<sub>2</sub> in fluids passing through the tectonic mélanges. The widespread presence of the assemblage lizardite + brucite in dunite tectonite and its absence in the tectonic mélange (which is situated on the fringe of the tectonite unit), is explained by several arguments.

(i) The serpentization process in general and the production of brucite in particular produces a large increase in volume (up to 40%, Hostetler et al. 1966), which in the case of dunite at the base of the transition zone of the Coy Pond Complex, apparently resulted in intense fracturing (see Fig 11.1) which was a precursor to the formation of the fragments in the future mélange.

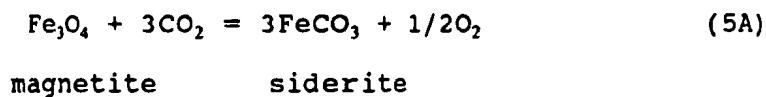
(ii) On the other hand, in the tectonic mélanges, which by definition are extensively sheared, fluid ingress was possible and most brucite was destabilized by the CO<sub>2</sub>-bearing fluids. Local occurrences over a small distance of "incompatible" minerals such as brucite and magnesite may indicate that the rate of diffusion of fluids, rather than availability of fluids, was locally the rate-limiting factor at the reaction site.

(iii) The occurrence in the tectonic mélanges, of predominantly serpentine in the mélange fragments and magnesite in the matrix can be explained in terms of variable infiltration and buffering potential. It is inferred that infiltration of CO<sub>2</sub> bearing fluid in the matrix of the mélanges resulted in the formation of magnesite bearing assemblages, whereas rock-dominated processes occurred in the less permeable fragments and consequently serpentine remained stable.

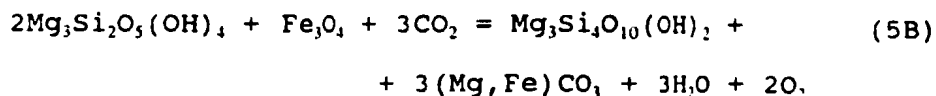
Following the destruction of brucite, the CO<sub>2</sub> concentration of the fluid could increase until it reached the equilibrium curve for the stability of serpentine in the presence of CO<sub>2</sub> (Fig 9.2.B). The idealized reaction is:



However in the presence of magnetite, a second reaction also occurs:



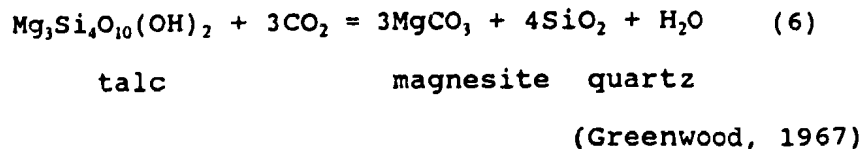
leading to the combined reaction:



(ignoring the small amounts of  $\text{Fe}^{+2}$  in serpentine and talc). The change of oxidation state of iron from  $\text{Fe}^{3+}$  to  $\text{Fe}^{2+}$  releases some oxygen into the fluid simultaneously with the formation of siderite, the latter forming a solid solution with magnesite (breunnerite). Also present in talc-magnesite assemblages are pentlandite  $(\text{Fe,Ni})_9\text{S}_8$  and linnaeite  $(\text{Co,Ni})_3\text{S}_4$ , which reflect an environment with generally low  $\text{fO}_2$  values but higher than that of the serpentinization environment (Eckstrand, 1975).

At 2 kbars (Fig 9.2 B), the equilibrium  $\text{CO}_2$  content of the fluid for the serpentine breakdown [reaction (5)] is about 0.5 mole percent at temperature of  $350^\circ\text{C}$  and about 1 mole percent at about  $450^\circ\text{C}$ .

The formation of quartz and magnesite from talc may have occurred either as a result of a decrease in temperature (and) or due to an increase in the mole fraction of  $\text{CO}_2$  in the fluid (Fig 9.2). In either case, talc became unstable and was replaced by quartz and magnesite, according to reaction (6):



As can be seen in Figure 9.2, at 2 kbar fluid pressure reaction (6) at 3 mole percent  $\text{CO}_2$  occurs at 350°C, and at about 30 mole percent it occurs at about 400°C.

#### 9.4 Recrystallization of serpentine

During serpentinite metamorphism, above about 200°C, chrysotile (or lizardite) react with talc to yield antigorite or, at about 300°C they react on their own to produce antigorite + brucite (Evans et al. 1976, Evans 1977, and Fig 9.1).

It is widely accepted (Evans et al. 1976, Wicks and Whittaker 1977, Moody 1977, Caruso and Chernosky 1979, O'Hanley et al. 1989) that antigorite is a product of prograde metamorphism (primarily due to temperature increase, and to a lesser extent to pressure increase), which develops as non-pseudomorphic replacement of lizardite and chrysotile.

In the western tectonic mélanges, about 75% of the serpentinite fragments are composed of non-pseudomorphic

(interpenetrating or less commonly interlocking textured) antigorite ± recrystallized lizardite. The frequent coexistence in same thin sections of recrystallized antigorite ± lizardite with the original mesh-textured lizardite is very difficult to explain if antigorite was formed as a product of progressive metamorphism. Several observations suggest that the assumption of progressive metamorphism for the formation of the antigorite is not correct.

(i) In the western tectonic mélange, serpentinites still containing relict lizardite are not confined to specific areas, but on the contrary are widespread without any discernible pattern. Taking into consideration the rather small thickness of the mélange (about 1 km), it is hard to imagine large P-T variations during the prograde metamorphism on a such small scale.

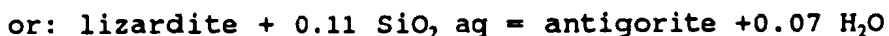
(ii) Petrographic details (Figure 6.17) show antigorite coexisting with undisturbed mesh-textured lizardite on a microscopic scale; the antigorite-lizardite boundary is commonly sharp, with only a few mm of lizardite-antigorite mixture separating the two zones. Again, this is hard to explain by T or P induced recrystallization unless there is extensive metastability.

(iii) The sheared serpentinite matrix, which displays the highest strain among all tectonic mélange assemblages, is

composed almost entirely of lizardite, and thus does not support the concept of antigorite production during shearing conditions (Francis 1956) or even simple lithostatic pressure (Moody 1976).

It is concluded that the observations do not fit an origin of antigorite by progressive metamorphism and that another explanation must be sought. In a recent Mössbauer investigation of the  $\text{Fe}^{3+}$  distribution between octahedral and tetrahedral sites of serpentine minerals, O'Hanley and Dyar (in press) enumerated several observations which are relevant to the assemblage at Coy Pond.

(i) Serpentine recrystallization (via solid-solid reaction) can be an  $\text{H}_2\text{O}$ -conservative, heat-consuming reaction (where lizardite mesh texture recrystallizes to lizardite hourglass or lizardite  $\pm$  chrysotile  $\pm$  antigorite interlocking texture), or can be caused by infiltration metasomatism in which silica was added, stabilizing antigorite at the expense of lizardite according to the reactions:



In the Coy Pond tectonic mélanges,  $\text{CO}_2$ -rich solutions responsible for carbonatization could also have been silica-



rich. Silica could have originated in the underlying metasediments and have been mobilized during the regional metamorphism, or could have been released during partial serpentinization of pyroxene in harzburgite and pyroxenite, a process which most likely occurred after olivine was completely serpentinized.

(ii) O'Hanley and Dyar (1992) also suggested that oxygen fugacity, which played an important role during serpentinization, loses some of its importance during recrystallization in favour of pH, which controls the  $\text{Fe}^{3+}/\text{Fe}^{2+}$  ratio in the octahedral sites in the serpentine polymorphs. High pH stabilizes high  $\text{Fe}^{3+}$ , and consequently enhances the stability of lizardite.

Petrographic details such as the coexistence of lizardite-antigorite coexistence on a small scale and the sharp boundaries between these two minerals are much more easily explained by the presence of a low pH front causing stabilization of antigorite and recrystallization of lizardite, rather than a pressure-temperature related recrystallization.

Using the serpentine-magnetite geothermometer of Wenner and Taylor (1969), O'Hanley and Dyar (1992) determined temperatures between 350 and 220°C for the serpentine recrystallization process, and mentioned that during the

process temperature was dropping. These determinations are in reasonable agreement with the relatively high temperatures ( $>300^{\circ}\text{C}$ ) proposed for contemporaneous carbonatization reactions based on the idealized equilibrium phase diagram (Berman 1988).

#### 9.5 Conclusions

(i) Dunites at the base of the Coy Pond Complex (in the harzburgite and also in the transition zone) were initially pervasively serpentinized to the assemblage lizardite + brucite.

(ii) The waters involved in serpentinization were  $\text{CO}_2$ -poor, most likely ocean waters.

(iii) Based on information in the geologic literature, temperature below  $250^{\circ}\text{C}$  is inferred for the serpentinization event.

(iv) The restriction of carbonatization mainly to the tectonic mélange assemblages demonstrates that  $\text{CO}_2$ -bearing fluids were present after serpentinization ended, during and after the formation of the tectonic mélanges, and that the tectonic mélanges were more permeable than the rest of the ophiolite.

(v) The first formation of magnesite in the tectonic

mélanges occurred when brucite was destabilized in the presence of  $\text{CO}_2$ -bearing fluids at  $X_{\text{CO}_2} > 0.005$  at 2 kbar (Fig 9.2; Johannes 1969).

(vi) The formation of talc-magnesite from serpentinite in the presence of  $\text{CO}_2$ -rich fluids (at 2 kbar fluid pressure) could have occurred at temperatures above  $350^\circ\text{C}$  if  $X_{\text{CO}_2} > 0.005$ , or at temperatures  $< 350^\circ\text{C}$  if  $X_{\text{CO}_2} < 0.005$  (Fig 9.2).

(vii) Partial recrystallization of lizardite to antigorite was chemically driven, probably by lowering of the pH which stabilized antigorite [the cause of the low(er) pH is not known]. Based on the carbon isotopic composition to be presented in Chapter 10, it is concluded that the serpentine recrystallization process occurred late, after the talc-magnesite assemblages formed, at temperatures between 200 and  $350^\circ\text{C}$ .

(viii) Formation of quartz-magnesite in the tectonic mélanges occurred by the action of  $\text{CO}_2$ -rich fluids on serpentinite and talc-magnesite. To produce quartz-magnesite at temperatures  $> 350^\circ\text{C}$  (at 2 kbar), the fluid would have to have had  $X_{\text{CO}_2} > 0.03$ ; at temperatures  $< 350^\circ\text{C}$  the fluid would have to have had  $X_{\text{CO}_2} < 0.03$ . From the available evidence, quartz-magnesite could have formed at any temperature below  $450^\circ\text{C}$  (Fig 9.2), and petrographic or isotopic information do not provide any temperature constraints other than that

assemblage formed last, at the end of carbonatization process.

(ix) Quartz-magnesite specimens (especially those in the western tectonic mélange) containing between 5 and 20 % quartz demonstrate that at least in its latest stages carbonatization was metasomatic and large amounts of  $\text{SiO}_2$  were removed in solution.

Chapter 10  
Carbon isotope geochemistry of magnesite  
in the tectonic mélanges

10.1 Purpose and theoretical considerations

Carbon and oxygen isotopic analyses were employed in this study in order to: (1) assess the sources of oxygen and carbon in the fluids that contributed to the carbonatization process and (2) place constraints on the tectonic setting of the ophiolite during the different stages of metamorphism. The majority of analyses were of magnesite, but a few samples of graphite, dolomite, calcite, aragonite and hydromagnesite were also analyzed.

The isotopic composition of oxygen and carbon in a mineral is a function of temperature and the isotopic composition of the fluid from which it formed. If the temperature of formation can be determined either by isotopic thermometers or by other means, the oxygen isotopic composition of fluids can be calculated. O'Neil (1977) determined empirically that oxygen isotope fractionation factors between minerals and water vary according to the relationship:

$$1000 \ln \alpha_{\text{min-H}_2\text{O}} = A(10^6/T^2) + B \quad (1)$$

where  $\alpha$  is the fractionation factor (equilibrium constant) between the mineral and water in units of per mil, T is the absolute temperature, and A and B are constants.

For kinetic reasons, the fractionation factors for the magnesite-water system have not been determined experimentally. An attempt to resolve this problem was made by Aharon (1988). Due to the fact that the per mil fractionation factors for alkali-earth carbonates are inversely related to the ionic radius of the cation (Golyshev et al., 1981), he proposed that fractionation factors for magnesite can be extrapolated from the known fractionation factors for other alkali earths (Fig 10.1). The oxygen isotope fractionation factor between magnesite and water has been determined by Aharon (1988) in this way to be:

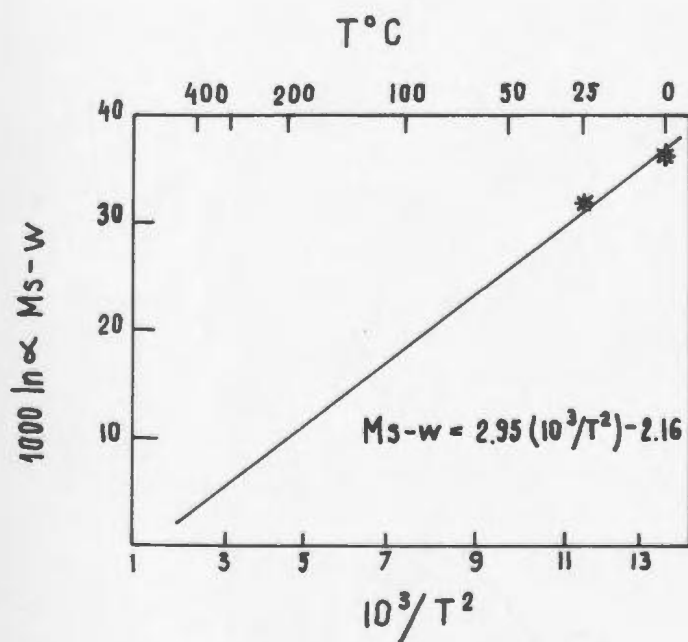
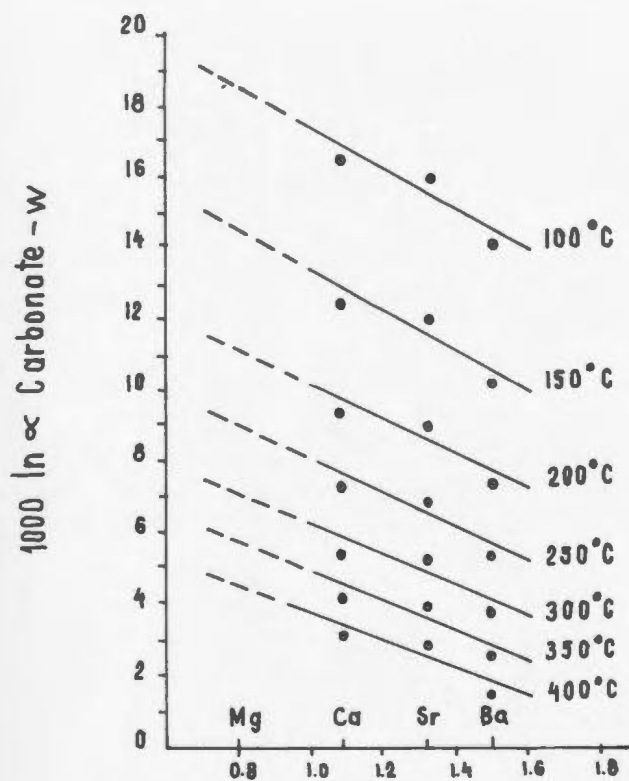
$$1000 \ln \alpha = 2.95(10^6/T^2) - 2.16$$

This result (plotted in Fig 10.2) is in good agreement with two experimentally determined oxygen isotope fractionation factors between hydromagnesite and water measured at 0° and 25°C by O'Neil and Barnes (1971) which also are plotted on Fig 10.2. The effect of crystal structure on the fractionation factors must also be considered, as magnesite



**Fig 10.1** The variation of the equilibrium fractionation factor ( $\alpha$ ) with ionic radius of alkali-earth carbonates at temperatures from 100 to 400°C (data from O'Neil et al., 1969; Whittaker and Muntus, 1970). Magnesite-water fractionation factors for this study were obtained by extrapolation of the data points to the Mg endmember (after Aharon 1988).

**Fig 10.2** Isotopic fractionation curve for magnesite-water, constructed from Fig 10.1. Note the close agreement with hydromagnesite-water fractionation factors (stars) from O'Neil and Barnes (1971).



is trigonal and  $\text{BaCO}_3$  and  $\text{SrCO}_3$  are both orthorhombic. However the  $^{18}\text{O}$  per mil fractionation between aragonite and calcite at  $25^\circ\text{C}$  is 0.5-0.7 (Tarutani et al., 1969; Golyshev et al., 1981), which are rather small values that become even less at higher temperatures. This suggests that the extrapolation of the fractionation factors for magnesite are not critically dependent on the crystal systems.

**Table 10.1** Fractionation factors between alkali-earth carbonates and water at various temperatures (O'Neil et al., 1969; ionic radii are from Whittaker and Muntus, 1970). Data for hydromagnesite (asterisks) at 0 and 25°C are from O'Neil and Barnes (1971), and are plotted on Fig 10.2.

Temperature	Mg	Ca	Sr	Ba
°C	0.80 Å	1.08 Å	1.33 Å	1.50 Å
0	37.8*			
25	31.7*			
100		17.09	16.09	14.24
150		12.65	11.79	10.13
200		9.54	8.78	7.26
250		7.27	6.59	5.17
300		5.58	4.95	3.60
350		4.27	3.69	2.39
400		3.25	2.70	1.44

## 10.2 Carbonate and graphite-bearing lithologies

Magnesite is by far the most abundant carbonate species in the Coy Pond mélange, but hydromagnesite  $[\text{Mg}(\text{OH})_2(\text{CO}_3)]$ , calcite and dolomite also occur locally. Aragonite occurs in several outcrops in sheared serpentized harzburgite, but not in the tectonic mélanges. Calcite occurs commonly outside the tectonic mélanges, in rodingitized pyroxenite and in gabbro and basalt in the upper levels of the ophiolite.

As discussed in detail in Chapter 6, magnesite occurs as a stable phase in assemblages with lizardite, talc, antigorite and quartz in both fragments and matrix of the tectonic mélanges. These assemblages formed as a result of different metamorphic reactions (chapter 9) that occurred under different temperature and/or  $\text{XCO}_2$  conditions. In order to investigate the sources of  $\text{CO}_2$  in the different carbonatization reactions, magnesite was separated from each of the assemblages noted above, and analyzed to determine its O and C isotopic composition. Microstructural details of the magnesite (cryptocrystalline or spathic) in the main assemblages are given in Table 10.2.

Minor amounts of other carbonates occur locally in the tectonic mélanges and in other units of the ophiolite, as

previously stated. However these are not products of carbonatization *sensu stricto* (i.e. produced by the action of CO<sub>2</sub>-bearing fluids on ultramafic silicate assemblages) but are seafloor or late alteration products.

Isotopic measurements were made on a total of twenty-nine magnesite-bearing samples. Fourteen were from serpentinite (five from lizardite, four from antigorite and five from lizardite-antigorite mixtures), nine from talc-rich assemblages and six from quartz-rich assemblages.

To facilitate comparison of the results from the Coy Pond Complex with other isotopic studies of seafloor altered basalts and ophiolites, the isotopic compositions of thirteen samples of carbonates other than magnesite were also measured. These samples were: three graphitic metasedimentary blocks, seven calcite-bearing samples (three from gabbro, two from rodingite, one from a blackwall rock in the eastern tectonic *mélange* and one from a metasedimentary block in the eastern tectonic *mélange*), and one aragonite-bearing sample (in harzburgite), one dolomite-bearing sample (vein in antigorite fragment in the western tectonic *mélange*) and a hydromagnesite-bearing sample (crust and vein in a brucite-bearing lizardite fragment in the western tectonic *mélange*).



### 10.3 Previous isotopic studies of magnesite

Magnesite occurrences in nature have been grouped into four major categories by Pohl and Siegl (1986):

- (i) strata-bound massive, crystalline magnesite commonly associated with Proterozoic and Palaeozoic sedimentary deposits;
- (ii) cryptocrystalline magnesite associated with ultramafic rocks, mostly serpentinite;
- (iii) fine-grained magnesite associated with modern hypersaline environments;
- (iv) magnesite associated with lacustrine environments.

The isotopic composition of magnesite was measured for the first time by Perry and Tan (1972) on early Precambrian (sedimentary or metasomatic origin) massive crystalline magnesite from South Africa. Based on  $\delta^{13}\text{C}$  (between -1.0 and -9.6) and  $\delta^{18}\text{O}$  (maximum 28.8) values of magnesite and other carbonates (calcite, dolomite and siderite), the authors remarked that "the extremely limited isotope exchange between vein carbonate and matrix suggests that magnesite may be an unusually suitable mineral for the preservation of primary ratios".

Strata-bound magnesites from the Lower Proterozoic Rum Jungle Uranium Field, Australia, yielded  $\delta^{13}\text{C}$  and  $\delta^{18}\text{O}$  values of 1.0 to 5.8 and 11.2 to 14.6, respectively (Aharon, 1988).

These were interpreted to have formed at 100-200°C from an epigenetic-metasomatic replacement of dolomite by magnesite due to interaction with Mg-rich basinal fluids.

The isotopic composition of magnesite associated with serpentinite was first reported by Barnes et al. (1973) who studied the Red Mountain Deposit, California. Magnesite there has  $\delta^{13}\text{C}$  and  $\delta^{18}\text{O}$  values from -11.4 to -14.1 and 27.7 to 28.2 respectively, which were similar to nearby hydromagnesite weathering crusts (O'Neil and Barnes, 1971), suggesting that it formed at about 10°C from locally derived meteoric waters that mixed with some metamorphic  $\text{CO}_2$ .

Strata-bound magnesite deposits associated with ophiolitic serpentinite in the Dinarides have  $\delta^{13}\text{C}$  values between -15 and 5 and  $\delta^{18}\text{O}$  values between 24 to 36 (Fallick et al. 1991). These were interpreted to have formed from  $\text{CO}_2$  produced during decarboxilation of organic material ( $\delta^{13}\text{C} < -10$ ) that mixed with carbonated meteoric waters ( $\delta^{13}\text{C} > -10$ ) at temperatures between 20 and 105°C.

Carbon and oxygen isotopic compositions of magnesite associated with serpentinite in Western Tauern, Austria (Schoell et al., 1975) show a very narrow range of  $\delta^{13}\text{C}$  and  $\delta^{18}\text{O}$  values from -3.7 to -4.1 and 7.8 to 8.6, respectively. These isotopic compositions are identical to those of carbonate in the metamorphic country rocks, leading the

authors to conclude that all of the carbonates formed at high temperatures (between 450 and 600°C) from metamorphic fluids.

In two recent studies of carbonate metasomatism in the Archean Abitibi greenstone belt (Ontario), several isotopic compositions of magnesite are presented. At the asbestos Munro mine (Schandl and Wicks 1991), magnesite in serpentinite formed from evolved meteoric water at 250°C (fluid-inclusion data) and has a narrow range  $\delta^{18}\text{O}$  and  $\delta^{13}\text{C}$  values (11.72 to 16.47 and -7.54 to -7.88 respectively). The carbon is considered to be organic in origin. Magnesite from the Slade-Forbes asbestos deposit has  $\delta^{18}\text{O}$  values from 10.1 to 14.1 and  $\delta^{13}\text{C}$  values from -0.7 to -4.7 suggesting sea water as a possible source (Schandl and Naldrett 1992).

In general, studies concerning the isotopic composition of magnesite are few in number and suggest that magnesite can form over a wide range of temperatures from meteoric, basinal or metamorphic fluids. Furthermore, the work of Perry and Tan (1972) suggests that magnesite is resistant to isotopic resetting, and so might retain a considerable memory of the fluid-dominated metamorphic event in which it formed. In the case of the Coy Pond tectonic mélanges, with petrographic evidence of four distinct magnesite-bearing assemblages, the aim was to fingerprint each metamorphic

event. As the results below indicate, this was indeed possible, and the isotopic compositions of magnesite produce a very specific array compared to the previous studies cited above.

#### 10.4 Analytical techniques

For all of the specimens involved in this isotopic investigation, the serpentine minerals and other silicate phases were first identified by petrographic and microprobe methods, and subsequently characterized by XRD analysis.

Most samples contained fine-grained cryptocrystalline magnesite and therefore whole-rock powders were used for isotopic analysis; however spathic magnesite from several coarser grained samples was hand-picked from the 75-100 micron size fraction.

All samples reported in this study were reacted with anhydrous phosphoric acid (McCrea, 1950) in sealed pyrex tubes for 72 hours at 100°C which produced a 100% yield of CO<sub>2</sub> gas. During evacuation of the sample tube, the acid was isolated in a smaller pyrex tube contained inside the larger sample tube.

Seven repeat analyses of an internal magnesite standard (specimen 142-C), reacted between 72 and 156 hours, yielded

a  $\delta^{13}\text{C}$  value of  $-11.1 \pm 0.1$  and  $\delta^{18}\text{O}$  value of  $13.4 \pm 0.3$ . Calcite and aragonite in this study were reacted at  $25^\circ\text{C}$  for 24 hours, dolomite and hydromagnesite at  $25^\circ\text{C}$  for 48 hours. Graphitic samples were pre-treated with HCl to remove carbonate, then mixed with a ten times excess of CuO, and combusted at  $900^\circ\text{C}$  to produce  $\text{CO}_2$  gas for isotopic analysis.

Isotopic measurements were made on a MAT 252 mass spectrometer in the Department of Earth Sciences, Memorial University and are reported using the conventional  $\delta$  notation in units of per mil relative to SMOW for oxygen and PDB for carbon (Craig, 1957). The stable isotope facility at Memorial University reports a  $\delta^{13}\text{C}$  value of 1.99 and a  $\delta^{18}\text{O}$  value of 28.60 for the NBS-19 carbonate standard, and  $\delta^{13}\text{C}$  values of -28.30 for NBS-21 graphite. The oxygen isotope fractionation factor between magnesite and that of the acid-extracted  $\text{CO}_2$ , at  $100^\circ\text{C}$  was 1.00929 (Rosenbaum and Sheppard, 1986).

#### 10.5 Results, interpretation and discussion

Isotopic composition of analysed samples are given in Tables 10.2 and 10.3, together with information on the microstructural setting of the magnesite (Table 10.2).

Magnesite from different lithologies in the tectonic

Table 10.2: Isotopic compositions and microstructural details of magnesite in different assemblages from the Coy Pond tectonic mélanges

Sample no.	d13 PDB	d18O SMOW	Description of magnesite and host rock
..... lizardite - antigorite rock.....			
250-C	-4.2	13.6	10% Ms(cr); L mesh texture
252-A	-7.8	13.6	5-10% Ms(cr) pseudofibrous; schistose L matrix
255-A	-6.0	14.2	10% Ms(cr) pseudofibrous; schistose L matrix
432-E	-6.1	15.2	15% Ms(cr); L mesh texture
343-B	-6.9	15.0	25% Ms(cr); L mesh texture
..... talc - magnesite rocks .....			
351	-5.4	12.3	25% Ms(cr); recrystallized L + A
350	-6.7	13.4	30% Ms(cr); recrystallized L + A
251-A	-6.1	14.2	20% Ms(cr > sp); L = mesh; A = interpenetrating
450-C	-8.8	14.3	10% Ms(cr); recrystallized L + A
256-A	-9.1	13.9	40% Ms(cr > sp); L + A interpenetr. + interlocking
..... quartz - magnesite rocks.....			
94-B	-10.8	12.5	10% Ms(sp > cr); A = interpenetrating texture
343-D	-12.0	15.5	40% Ms(cr = sp); A = interpenetrating texture
160-C	-12.0	17.2	25% Ms(cr = sp); A = interpenetrating texture
337-A	-13.6	14.2	10% Ms(cr = sp); A = interpenetrating texture
272	-1.6	13.9	60% Ms(cr = sp); 40% T;
270	-3.3	14.3	75% Ms(sp > cr); 15% T; abundant magnetite
372	-4.1	13.5	50% Ms(sp = cr); 25% T; relict Sp;
432-A	-6.7	15.0	60% Ms(sp > cr); 25% T; 15% relict A;
378	-7.4	12.0	30% Ms(sp > cr); 70% T; no Sp;
450-A	-7.8	13.9	65% Ms(sp > cr); 35% T;
252-D	-6.0	14.6	20-30% Ms(sp = cr); 70-80% T;
343-C*	-11.3	16.2	50% Ms(sp > cr); 50% T; schistose matrix
177-D*	-11.4	16.8	50% Ms(sp = cr); 50% T; schistose matrix
470	-5.9	16.5	60-70% Ms(sp > cr); 25% Q; 10% T;
447-C	-7.3	14.0	85-95% Ms(sp > cr); 5% Q; 5% Cc; no T;
142-C	-11.9	13.5	90% Ms(cr > sp); 10% Q; no T;
342	-17.6	17.5	75% Ms(sp = cr); 25% Q; 2% T;
85-A	-18.2	17.2	80% Ms(sp = cr); 20% Q; no T;
85-F	-20.4	17.2	90-95% Ms(sp = cr); 5-10% Q; no T;

A = antigorite  
Cc = calcite  
cr = cryptocrystalline  
L = lizardite

Ms = magnesite  
Q = quartz  
sp = spathic  
T = talc



Table 10.3: Isotopic composition of O and C in carbonates other than magnesite and in organic carbon from the Coy Pond Ophiolite Complex

Sample no:	d13 vs PDB	d18 vs SMOW	Description of occurrence
438*	-0.1	15.8	calcite vein in metasediments
453	-1.4	13.5	calcite in gabbro
457	-12.9	8.8	calcite in gabbro
379	9.6	11.2	calcite in rodingite
396	-10.5	11.1	calcite in rodingite
467	-10.3	14.1	calcite in blackwall
505-A	-5.3	7.6	calcite vein in volcanics
68	-16.5	23.4	aragonite in harzburgite
305*	-4.3	10.0	dolomite vein in serpentinite
196-A*	0.2	28.2	hydromagnesite in serpentinite
471*	-20.6		graphite in metasediments
121-A	-23.3		graphite in metasediments
201-B	-25.9		graphite in metasediments

\* specimens in mélange

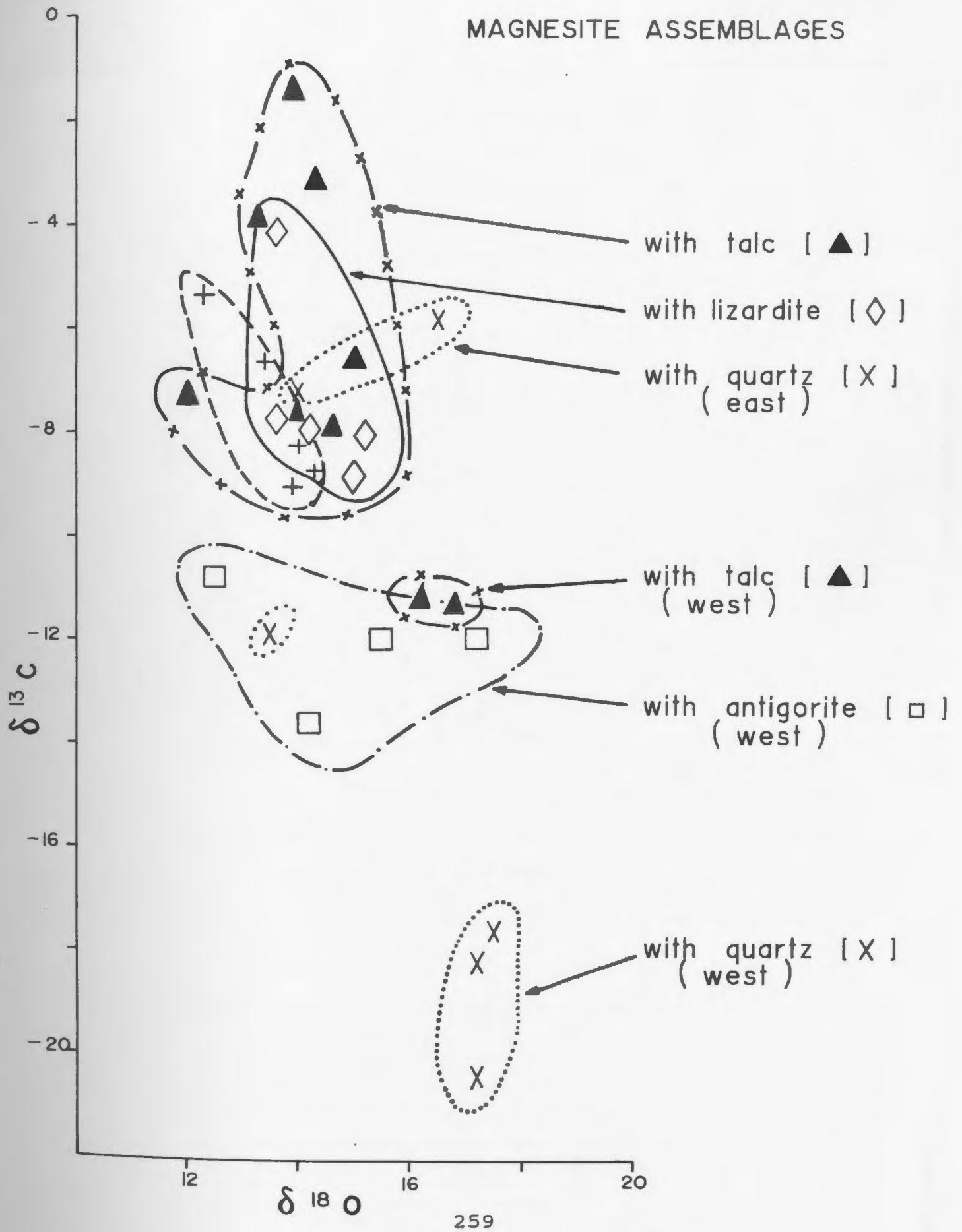
mélanges has a narrow range of  $\delta^{18}\text{O}$  values (from 12.0 to 17.5), and a wide range of  $\delta^{13}\text{C}$  values (from -1.6 to -20.4). The isotopic compositions are related to the mineralogy of the metamorphic assemblage and, in some cases, to whether the sample is from the eastern or western tectonic mélange (Fig. 10.3). The isotopic results define a weak trend with lower  $\delta^{13}\text{C}$  values corresponding to slightly higher  $\delta^{18}\text{O}$  values (Fig. 10.3). Lizardite-bearing serpentinite with pseudomorphic mesh textures contains magnesite with  $\delta^{13}\text{C}$  values from -4.2 to -8.9, and in two samples of highly sheared and recrystallized lizardite serpentinite, magnesite has  $\delta^{13}\text{C}$  values of -7.8 and -8.0. In antigorite-bearing serpentinite, the  $\delta^{13}\text{C}$  values of magnesite vary between -10.8 and -13.6, and in serpentinite with lizardite-antigorite mixtures, the  $\delta^{13}\text{C}$  values are from -5.4 to -9.1.  $\delta^{18}\text{O}$  values of magnesite from these different types of serpentinite broadly overlap from 12.3 to 17.2 (Fig 10.3).

Magnesite from talc-magnesite assemblages has  $\delta^{13}\text{C}$  values from -1.6 to -8.0, and  $\delta^{18}\text{O}$  values between 12.0 and 15.0. Two samples of highly sheared talc-magnesite from the matrix of the mélange have distinctly lower  $\delta^{13}\text{C}$  values (-11.3 and -11.4) and higher  $\delta^{18}\text{O}$  values (16.2 and 16.8) compared to unsheared assemblages.

The quartz-magnesite rocks have the widest range of

Fig 10.3  $\delta^{18}\text{O}$  vs  $\delta^{13}\text{C}$  of magnesite in different mineral assemblages from the Coy Pond tectonic mélanges. Fields of magnesite co-existing with lizardite, talc, antigorite and quartz are shown. Samples from the western and eastern tectonic mélange are identified for reference.

# MAGNESITE ASSEMBLAGES



isotopic compositions compared to all other lithologies, and this is the only assemblage whose isotopic composition shows a geographic dependence. Quartz-magnesite in the eastern tectonic mélange has  $\delta^{13}\text{C}$  values between -5.9 and -7.3, and  $\delta^{18}\text{O}$  values between 14.0 and 16.5, which are similar to those of magnesite from lizardite and talc assemblages. In the western tectonic mélange, most of the magnesite has much lower  $\delta^{13}\text{C}$  values (-17.6 to -20.4) and higher  $\delta^{18}\text{O}$  values (17.2 to 17.5) that are distinct from all other magnesite-bearing assemblages. One exception is a sheared, coarse-grained sample from the matrix of the western tectonic mélange, which has a  $\delta^{13}\text{C}$  value of -11.9 and a  $\delta^{18}\text{O}$  value of 13.5.

Isotopic results for other carbonates are given in Table 10.3. Two calcite samples from gabbros have  $\delta^{13}\text{C}$  values close to zero (-0.1 and -1.4) and  $\delta^{18}\text{O}$  values of 15.8 and 13.5, respectively, and a third calcite sample has lower  $\delta^{13}\text{C}$  (-12.9) and  $\delta^{18}\text{O}$  (8.8) values. Two disseminated calcites from rodingitized pyroxenite have similar  $\delta^{13}\text{C}$  (-9.6 and -10.5) and  $\delta^{18}\text{O}$  (11.2 and 11.1) values to calcite from a vein hosted by chloritic blackwall rocks in the eastern tectonic mélange. A calcite sample from a vein cutting a metasedimentary block in the mélange has  $\delta^{13}\text{C}$  and  $\delta^{18}\text{O}$  values of -5.3 and 7.6, respectively. Aragonite from harzburgite

and dolomite and hydromagnesite from the mélange have  $\delta^{13}\text{C}$  values of -16.5, -4.3 and 0.2, and  $\delta^{18}\text{O}$  values of 23.4, 10.0 and 28.2, respectively. Finally,  $\delta^{13}\text{C}$  values of the three graphitic samples are -20.6, -23.3 and -25.9 (Table 10.2).

#### 10.5.1 Temperature constraints

In order to calculate the oxygen isotopic composition of fluids that produced magnesite in the different mineral assemblages, their formation temperatures must be known or estimated.

It is evident from Figure 9.2 B that at constant pressure, reactions in the  $\text{MgO-SiO}_2\text{-H}_2\text{O-CO}_2$  system depend on temperature and the  $\text{CO}_2$ -content of the fluid. Based on experimental, field and thermodynamic data the following temperature constraints are available:

(1) The serpentinization reaction: **forsterite + water = chrysotile + brucite** ( has been experimentally determined to take place at temperatures  $< 380^\circ\text{C}$  (Johannes 1969) in the end-member (pure forsterite) model  $\text{MgO-SiO}_2\text{-H}_2\text{O-CO}_2$  system, and at  $< 365^\circ\text{C}$  for olivine of composition  $\text{Fo}_{93}$  (Moody 1976). This reaction is metastable; thermodynamic data of Berman (1988) show that at 2 kbar fluid pressure (Fig. 10.4 A), antigorite can be stable up to  $500^\circ\text{C}$ . Field observations



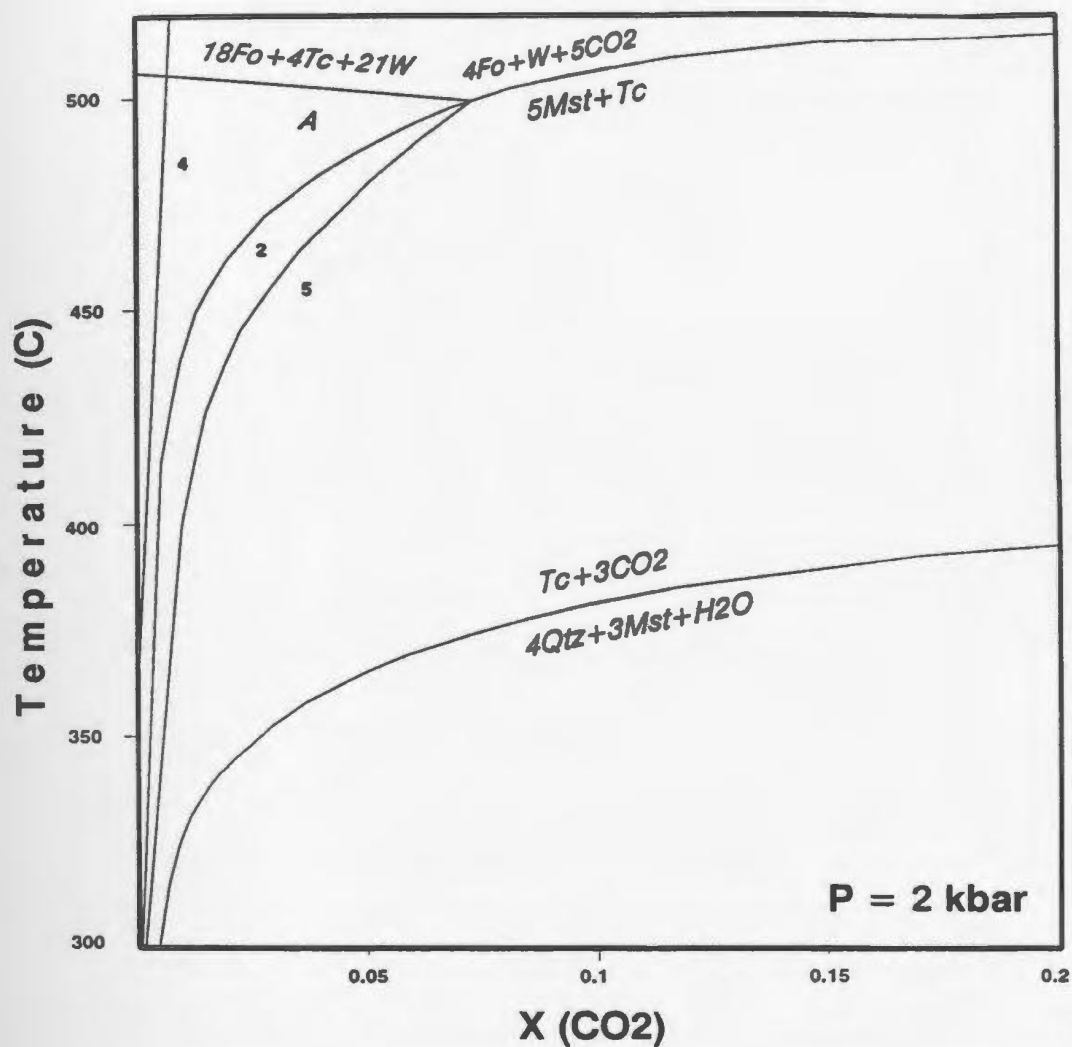


Fig. 10.4a. Phase diagram showing the isobaric equilibrium curves at low temperatures and low values of X(CO<sub>2</sub>) in the model system MgO-SiO<sub>2</sub>-H<sub>2</sub>O-CO<sub>2</sub> (from Berman 1988).

Abbreviations: Atg=antigorite; Br=brucite; Mst=magnesite; Qtz=quartz; Fo=forsterite; Tc=talc; W=water. Reactions as in text; 2:  $34\text{Fo} + 31\text{W} + 20\text{CO}_2 = \text{A} + 20\text{Mst}$ ; 4:  $\text{Br} + \text{CO}_2 = \text{Mst} + \text{W}$ ; 5:  $2\text{Atg} + 45\text{CO}_2 = 45\text{Mst} + 17\text{Tc} + 45\text{W}$ .

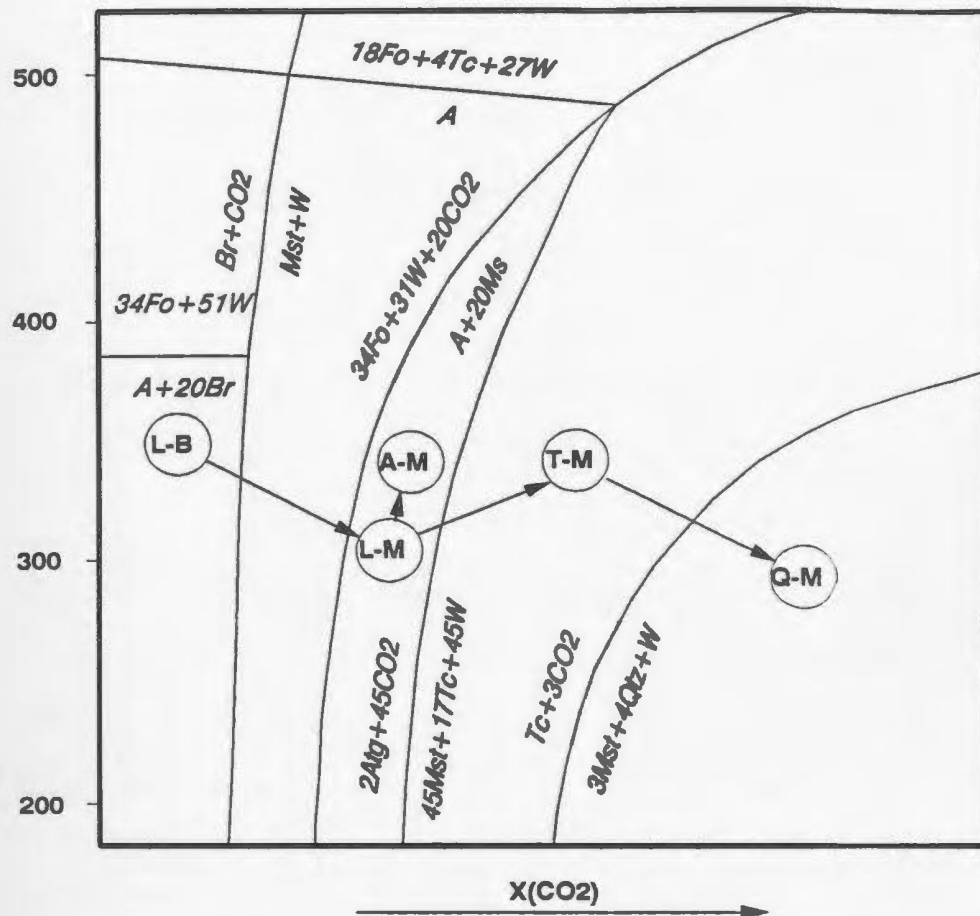


Fig 10.4b Schematic T-X(CO<sub>2</sub>) diagram for relevant phases in the MgO-SiO<sub>2</sub>-H<sub>2</sub>O-CO<sub>2</sub> system for P=2kbar. X(CO<sub>2</sub>) scale is schematic and non-linear for clarity. Circles represent the estimated T-X conditions for mineral assemblages in the Coy Pond tectonic melanges (L-B: lizardite-brucite; L-M:lizardite-magnesite; A-M:antigorite-magnesite; T-M:talca-magnesite; Q-M:quartz-magnesite) Arrows indicate the direction of change of metamorphic conditions as inferred from microstructures petrography and isotopic data. Petrogenetic grid information from Berman (1988). Abbreviations as in Fig. 10.4a.

show that at 2 kbar, the antigorite stability field is up to 480°C at  $X_{CO_2} < 0.02$ , both the temperature and  $X_{CO_2}$  being greater than for lizardite or chrysotile stability (Trommsdorf and Evans 1977). For this reason, an upper temperature limit of 450°C was considered for the stability of lizardite and chrysotile in the Coy Pond tectonic mélanges.

(2) The carbonatization reaction: **serpentine + CO<sub>2</sub>**  
**= talc + magnesite + water** (at P fluid = 2 kbar) occurs at 350°C for  $X_{CO_2} = 0.005$ , at 400°C for  $X_{CO_2} = 0.01$  and at 500°C for  $X_{CO_2} = 0.07$  (Berman 1988 in Fig 10.4). Taking into account the fact that the talc-magnesite assemblage comprises a substantial volume of the tectonic mélanges (it forms the bulk of the matrix and part of the fragments in the western tectonic mélange, and about half of the entire eastern tectonic mélange), it is reasonable to assume that the metasomatic fluid had a somewhat higher  $X_{CO_2}$  value, probably  $\gg 0.005$ . This higher  $X_{CO_2}$  value yields a formation temperature for the talc-magnesite assemblage between 350 and 450°C. However, as seen in Fig 10.4.A it is possible (but less probable) that carbonatization of serpentine to talc-magnesite could have occurred at temperatures  $< 350^\circ\text{C}$ , if there was an influx of very large amounts of fluid having  $X_{CO_2}$  values  $< 0.005$ . At such low temperatures ( $< 350^\circ\text{C}$ ), the

CO<sub>2</sub>-poor fluid would have to maintain its XCO<sub>2</sub> between narrow limits ( $0.005 > XCO_2 < 0.03$  for  $T=350^{\circ}C$ , see Fig. 10.4.A) otherwise a quartz-magnesite assemblage would be produced (Fig 10.4).

(3) Based on metamorphic constraints (Evans et al., 1976; Evans 1977), the temperature of recrystallization of lizardite to antigorite is about 300°C or greater (see Chapter 9 for details). O'Hanley and Offler (1992) using the magnetite-serpentine thermometer of Wenner and Taylor (1969), determined the temperatures between 350 and 220°C for serpentine recrystallization at Woodsreef (New South Wales, Australia). Using the same method, O'Hanley et al. (in press) have determined temperature of serpentine recrystallization at Cassiar, British Columbia to have been  $300 \pm 36^{\circ}C$  at  $P(H_2O) < 800$  bars. In the Coy Pond tectonic mélanges, the constraints described above suggest that the partial recrystallization of serpentine likely occurred in a similar temperature interval between 220 and 350°C. Petrographic information and also carbon isotopic composition (Figs 10.3 and 10.7) suggest that the recrystallization of serpentine occurred later following the formation of the talc-magnesite assemblage.

(4) The reaction: **talc + CO<sub>2</sub> = quartz + magnesite + H<sub>2</sub>O** at constant fluid pressure (2 kbar) depends on XCO<sub>2</sub>-fluid and

temperature as follows: at  $X_{CO_2} < 0.02$  it occurs anywhere below 350°C and is strongly temperature dependent; at  $X_{CO_2} > 0.02$  the reaction depends strongly on  $X_{CO_2}$  and less on temperature (Fig 10.4).

In the eastern tectonic mélange, the quartz-magnesite and talc-magnesite assemblages are closely intermingled and both contain magnesite with similar carbon isotopic compositions to that of magnesite in the serpentinites. The common  $\delta^{13}C$  values suggest that formation of magnesite associated with lizardite, talc and quartz occurred as a result of a single fluid having a constant isotopic composition over time. Furthermore, the temperature and  $X_{CO_2}$  of the fluid was probably close to the talc-quartz phase boundary (Fig 10.4) which would explain the intermixed nature of the talc-magnesite and quartz-magnesite assemblages. The preservation of some serpentinite fragments unaffected by carbonate metasomatism could imply that the carbonatization process, in the eastern tectonic mélange, took place in the  $X_{CO_2}$ -poor region of the phase diagram close to the talc-quartz phase boundary (Fig 10.4). As such, a fluid having a temperature  $< 350^\circ C$  and  $X_{CO_2} < 0.02$  is inferred for the formation of the quartz-magnesite in the eastern tectonic mélange. In contrast, the quartz-magnesite assemblage in the western tectonic mélange has distinctive petrographic and isotopic

features that suggest it formed late in the paragenesis from isotopically distinct waters (Fig 10.3) having  $X_{CO_2}$  values  $> 0.02$  (quartz-magnesite assemblage is very poor in talc) at temperatures  $< 350^{\circ}C$ .

(5) The Spruce Brook Formation which underlies the ophiolite consists of metasediments in the sub-biotite to biotite zones, regionally metamorphosed under greenschist facies conditions, with temperatures qualitatively estimated at about  $400^{\circ}C$  (Deveau 1992).

(6) Within the tectonic mélanges, and at the contacts with the country rocks, occurrences of narrow chloritic blackwall assemblages imply that these rocks (which typically form during serpentinization of ultramafics) formed at temperatures  $< 400^{\circ}C$ , otherwise at higher temperatures the chlorite would have been replaced by amphibole.

Based on mineral equilibria and the regional geological context, temperatures less than  $400^{\circ}C$  down to ambient values, are reasonable for the formation of the metamorphic assemblages (carbonate metasomatism) in the tectonic mélanges of the Coy Pond ophiolite. Elevated temperatures at the higher end of the range could have been achieved via several different mechanisms: (i) the obducted ophiolite complex was still hot; (ii) the ophiolite was originally cold but hydrothermal fluids from below were hot; or (iii)



the heat was induced during regional metamorphism. Although no metamorphic sole was found at the faulted contact between the metasediments and the Coy Pond Complex, there are several arguments that suggest the Coy Pond ophiolite was hot during emplacement: (1) the igneous age of the ophiolite complex is 494 Ma (Dunning and Krogh, 1985), and it was emplaced prior to  $474 \pm 6/-3$  Ma, which is the age of a stitching pluton, the Partridgeberry Hills granite (Colman-Sadd et al., 1992). This allows less than 20 M.y. between formation, detachment, obduction and emplacement of the ophiolite, time most likely insufficient for cooling prior to emplacement on the continental margin; (2) the recent description of a metamorphic sole of amphibolite schist beneath the nearby (and contiguous) Great Bend ophiolite has been reported by Dickson (1992), suggesting it was emplaced while hot.

In summary, the ophiolite was probably still hot during emplacement, after which it became involved in regional metamorphism, which reached at least greenschist facies conditions (about 400°C and muscovite-chlorite stable in pelites) in the underlying Spruce Brook Formation.

#### 10.5.2 Constraints on fluid compositions

Direct measurements of the fluid composition, such as from the study of fluid inclusions, are not available, and so the source of the solutes and the waters can only be constrained indirectly using the isotopic compositions of magnesite.

The isotopic compositions of magnesite in the Coy Pond tectonic mélanges clearly comprise three separate populations indicating that the formation of magnesite was a result of at least three fluids with different compositions, each possibly representing a distinct event (Figs 10.3 and 10.6).

##### (i) Type 1 fluid - marine/crustal source

Type 1 fluids include those that formed magnesite in both the lizardite and talc assemblages (Fig 10.5). The oxygen isotopic composition of waters calculated to be in equilibrium with magnesite in lizardite and talc assemblages (assuming formation temperatures between 300 and 450°C) is between 5.2 and 11.7 (Table 10.4). This is in the general range of metamorphic waters (Taylor, 1974), more specifically, those derived via sea floor metamorphism of the oceanic crust which have  $\delta^{18}\text{O}$  values between 4 and 12 (Muehlenbachs et al., 1974; Sheppard, 1977; Heaton and Sheppard, 1977). The oxygen isotopic composition of the

Table 10.4: Oxygen isotopic compositions of waters calculated to be in equilibrium with magnesite from different assemblages at specified temperatures

magnesite in:	formation temperature	magnesite-water fract. factor	$^{18}$ O water
lizardite	450	3.5	10.1 to 11.7
	400	4.4	9.2 to 10.8
	350	5.4	8.2 to 9.8
	300	6.8	6.8 to 8.4
talc	450	3.5	8.5 to 11.5
	400	4.4	7.6 to 10.8
	350	5.4	6.6 to 9.6
	300	6.8	5.2 to 8.2
talc (schistose matrix)	450	3.5	12.7 to 13.3
	400	4.4	11.8 to 12.4
	350	5.4	10.8 to 11.4
	300	6.8	9.4 to 10.0
antigorite	350	5.4	7.1 to 11.8
	300	6.8	5.7 to 10.4
	250	8.8	3.9 to 8.8
	200	11.0	1.5 to 6.2
qtz - magnesite (east)	350	5.4	11.8 to 12.1
	300	6.8	10.4 to 10.7
	250	8.8	8.6 to 8.9
	200	11.0	6.2 to 6.5
	150	14.3	2.9 to 3.2
	100	19.0	-1.8 to -1.5
qtz - magnesite (west)	50	26.1	-8.9 to -8.8
	350	5.4	8.6 to 11.1
	300	6.8	7.2 to 9.7
	250	8.8	5.4 to 7.9
	200	11.0	3.0 to 5.5
	150	14.3	-0.3 to 2.2
	100	19.0	-5.0 to -2.5
	50	26.1	-12.1 to -9.6

fluids varied about 6.5 per mil, and the carbon isotopic composition varied from about -1 to -9. This relatively large range of  $\delta^{13}\text{C}$  values (Table 10.2; Figs 10.3 and 10.5) suggests that the carbon was derived from different sources. The high  $\delta^{13}\text{C}$  values (ca. -1) are consistent with marine carbon (Keith and Weber, 1964; Schidlowsky et al., 1974), whereas the  $\delta^{13}\text{C}$  values from -4 to -9 probably reflect average oceanic, crustal or magmatic sources, although the lowest values might reflect a very small component of organic carbon (Fig 10.5).

Hoefs (1965) has shown that, in small amounts, carbon exists in all igneous rocks in both reduced (about 200 ppm) and oxidized form (<100 to several thousand ppm), and he also demonstrated that the average carbon isotopic composition in the Earth's crust and upper mantle is about -7. However, the measurements of deep seated carbon in carbonatites and kimberlites are in the range of -2 to -8 (Deines and Gold, 1973).  $\text{CO}_2$  vesicles in ocean floor basalts have average  $\delta^{13}\text{C}$  values of -7.6 (Pineau et al., 1976), -6.2 (Sakai et al., 1984) or range between -4 to -9 (Pineau and Javoy, 1983) or -5 to -7 (Des Marais and Moore, 1984). Submarine hot springs and hydrothermal vents have similar  $\delta^{13}\text{C}$  values of -5 to -8 (Craig et al. 1980), and reported  $\delta^{13}\text{C}$  values from Hawaiian fumaroles are in the range of -7 to

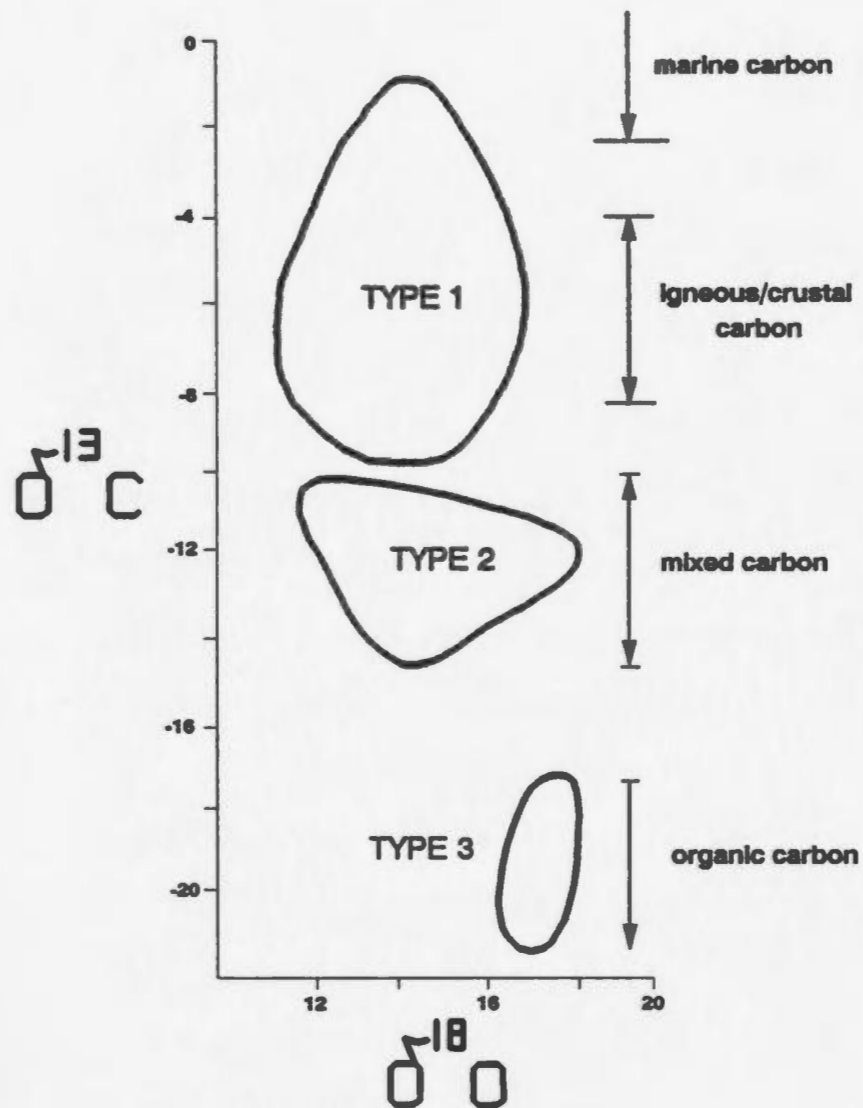


Fig 10.5  $\delta^{18}\text{O}$  vs  $\delta^{13}\text{C}$  diagram showing the 3 fields of magnesite composition in Coy Pond tectonic melanges, and the  $\delta^{13}\text{C}$  ranges of possible carbon sources.

-9 (Gerlach and Thomas, 1986). Finally, the peculiar methane gas seeps in the Zambales ophiolite, considered to be of an abiogenic origin, have  $\delta^{13}\text{C}$  values of about -7 (Abrajo et al., 1986).

Regardless of the precise  $\delta^{13}\text{C}$  value of average oceanic crustal carbon, the  $\delta^{13}\text{C}$  values of magnesite in the lizardite and talc assemblages of the Coy Pond Complex are consistent with their formation while the ophiolite was in an oceanic environment.

Magnesite associated with quartz in the eastern tectonic mélange has  $\delta^{13}\text{C}$  and  $\delta^{18}\text{O}$  values that are similar to those that occur with lizardite and talc, yet differ substantially from those of quartz-magnesite from the western tectonic mélange (Fig 10.3). If quartz-magnesite formed at  $T > 200^\circ$ , the oxygen isotopic composition of fluids would have been between 6.2 and about 12; however, if it formed at  $T < 200^\circ\text{C}$ , the oxygen isotopic composition of fluids would have been between about -9 and 6.5 (Table 10.4). In the former case, the calculated fluid is consistent with metamorphic fluids (Sheppard, 1977), in the latter case, with meteoric-hydrothermal fluids (Sheppard, 1987). However, in the absence of reliable temperature data, the role of ground water in the eastern tectonic mélange cannot be ruled out.

The  $\delta^{13}\text{C}$  values of magnesite associated with quartz in the



eastern tectonic mélange are -5.9 and -7.3 (samples 470 and 447-C in Table 10.2). This contrasts with much lower values for magnesite in the western tectonic mélange (between -11.9 and -20.4), indicating that carbon in each tectonic mélange was derived from different sources (Figs 10.3 and 10.5). Because the quartz-magnesite event is petrographically late in both tectonic mélanges, the  $\delta^{13}\text{C}$  values probably reflect differences in the nature of the fault systems that served as conduits for the  $\text{CO}_2$ -rich fluids. The eastern tectonic mélange contains no magnesite with low  $\delta^{13}\text{C}$  values suggesting that the carbon was locally derived from within the ophiolite, whereas the magnesite in the western tectonic mélange was formed from carbon derived in part from the metamorphic basement (discussed below).

**(ii) Type 3 fluid - organic source**

Type 3 fluids are those that formed magnesite associated with quartz in the western tectonic mélange, and they are a component of the Type 2 fluids that formed antigorite (Fig 10.5). As was discussed previously for quartz-magnesite in the eastern tectonic mélange, if quartz-magnesite assemblage in the western tectonic mélange formed at  $T > 200^\circ\text{C}$ , the calculated oxygen isotopic composition of the fluids would be from 5.4 to 11.1. For temperatures less than  $200^\circ\text{C}$ , the

$\delta^{18}\text{O}$  values of fluids would be between 5.5 and -12.1 (Table 10.4). For reasons discussed earlier, the preferred scenario for the formation of the quartz-magnesite assemblage is that it formed in equilibrium with metamorphic fluids similar to those which produced magnesite with antigorite and schistose talc.

With one exception (sample 142-C), the carbon isotopic composition of magnesite associated with Type 3 fluids exhibits a narrow range (< 3 per mil) between -17.6 to -20.4 (Table 10.2 and Figs 10.3 and 10.5). These values can only be derived from an organic source, most likely from graphite in the underlying continental sediments (see below).

#### **Organic matter in sediments**

The average amount of reduced carbon in sedimentary rocks is estimated at 0.40 wt %, and for Cambrian and Ordovician sediments from North America, the amount is estimated to be 0.68 wt % (Zemann, 1972). The transformation and evolution of organic matter starts with diagenesis and catagenesis when petroleum, coal, methane and  $\text{CO}_2$  are formed (Tissot and Welte 1984). Under metamorphic conditions, the organic matter is commonly converted to  $\text{CO}_2$ ,  $\text{CH}_4$  and graphitic carbon. Three  $\delta^{13}\text{C}$  analyses of graphitic material from sediments of the Spruce Brook Formation yield values between

-20.6 and -25.9. These are within the range of  $\delta^{13}\text{C}$  values of organic materials preserved in sedimentary rocks (-20 to -40; Degens, 1969) and are close to the  $\delta^{13}\text{C}$  values of magnesite in the quartz-magnesite assemblage. Calculations have shown that at 500°C and 5 kbars an average pelitic rock undergoing devolatilization during regional metamorphism will produce a volume of fluid equal to about 12% of the rock volume, or 2 moles of fluid per kg of rock with about 72 mol %  $\text{H}_2\text{O}$  and 28 mol %  $\text{CO}_2$  (Walther and Orville, 1982; Wilkinson, 1991).

The metamorphic grade in the Mount Cormack Terrane underlying the Coy Pond ophiolite ranges from greenschist to upper amphibolite and in places partial melting has occurred. Metamorphism of these continental sediments is considered to be the source of  $\text{CO}_2$ -rich fluid. The fluid circulation was focused along the western tectonic mélange where it produced magnesite with characteristically low  $\delta^{13}\text{C}$  values.

### **(iii) Type 2 fluid - mixed sources**

Type 2 fluids are those that were in equilibrium with magnesite in antigorite assemblages and in the schistose talc matrix (Fig 10.3). As discussed previously, the recrystallization of lizardite to antigorite probably

occurred in a temperature interval between 200 and 350°C. The oxygen isotopic composition of fluids calculated to be in equilibrium with this magnesite is between 1.5 and 11.8 (Table 10.4.A). These isotopic compositions are at the upper limit of metamorphic waters produced during sea floor hydrothermal metamorphism, but they are in the general compositional range of metamorphic waters produced during metamorphism of sedimentary and igneous rocks (which can be as high as 25 per mil; Sheppard, 1987). Metamorphic waters are those released during metamorphic dehydration reactions in equilibrium with metamorphic minerals (Sheppard, 1984).

The carbon isotopic compositions of magnesite associated with antigorite and schistose talc matrix are between -10.8 and -13.6 (Table 10.2 and Fig 10.3). These values are lower than those associated with carbon from magmatic or average oceanic crustal sources, but they are higher than those associated with organic sources (Fig 10.5). The  $\delta^{13}\text{C}$  values can best be interpreted as a mixture of these two distinct sources.

Petrography and phase relations (Fig 10.4.B) suggest that magnesite in the antigorite assemblage formed later than that in the lizardite and talc assemblages, but earlier than that in the quartz assemblage. From the perspective of carbon isotopic arguments, it is reasonable that the

progressive lowering of  $\delta^{13}\text{C}$  values in magnesite from lizardite to antigorite to quartz assemblages represents the influx of  $^{13}\text{C}$ -depleted  $\text{CO}_2$  from the metasedimentary basement. In this scenario, both the antigorite and the quartz assemblages formed after emplacement of the ophiolite on the continental margin, with antigorite forming before oceanic crustal  $\text{CO}_2$  in the mélange had been completely flushed from the system.

#### 10.5.3 Differences between the eastern and western tectonic mélanges

There are significant lithologic and isotopic differences between the western and eastern tectonic mélanges.

##### **Eastern tectonic mélange:**

(i) generally, the eastern tectonic mélange exhibits a pervasive carbonatization; most of the original lithologies (serpentinite) have been replaced by talc-magnesite and quartz-magnesite assemblages;

(ii) relict assemblages such as serpentinite (lizardite) are still preserved in fragments, but the matrix is entirely replaced by quartz-magnesite;

(iii) petrographic evidence shows that the predominant quartz-magnesite assemblage formed by carbonatization of

talc-magnesite, with which it is intimately associated;

(iv) isotopically, magnesite associated with all mineral assemblages (with lizardite, talc and quartz) is very homogeneous, with  $\delta^{13}\text{C}$  and  $\delta^{18}\text{O}$  values between -5.9 and -8.8, and 13.9 and 16.5 respectively.

**Western tectonic mélange:**

(i) carbonatization of the western tectonic mélange was less pervasive, leaving some fragments unaffected (i.e. brucite-bearing);

(ii) fragments in the mélange are less carbonatized than the matrix, which largely is composed of the talc-magnesite assemblage;

(iii) the  $\delta^{13}\text{C}$  values of magnesite associated with antigorite and with schistose talc matrix are much lower ( $< -11$ ) than any magnesite in the eastern mélange;

(iv) magnesite associated with quartz has the lowest  $\delta^{13}\text{C}$  values (-11.9 to -20.4), lower than any magnesite in either the eastern or western tectonic mélanges.

These observations suggest that in the eastern tectonic mélange, all of the carbonate metasomatism resulted from a relatively homogeneous fluid at around 300 - 350°C with the  $\text{XCO}_2$  near the talc-quartz and serpentine-talc phase boundary. In the western tectonic mélange up to a point, the carbonate metasomatism occurred under similar conditions

being caused by similar fluid. However in the final stage of carbonatization, fluids with unusually low  $\delta^{13}\text{C}$  values formed the quartz-magnesite assemblage in the western tectonic mélange.

#### 10.5.4 Other carbonates

The isotopic compositions of other carbonates are quite variable (Table 10.3) further suggesting that, like magnesite, different fluids have affected the Coy Pond ophiolite at different times. The carbon and oxygen isotopic compositions of hydromagnesite, dolomite, calcite and aragonite reflect formation from low to high temperatures from fluids that derived their carbon from marine, crustal and organic sources. For example, hydromagnesite which occurs as white crumbling crusts associated with brucite-bearing lizardite fragments, has a  $\delta^{13}\text{C}$  value of 0.2 and  $\delta^{18}\text{O}$  value of 28.2, consistent with formation as a low-temperature weathering product of brucite (e.g. O'Neil and Barnes, 1971) with a marine source for the carbon.

Two calcite veins, one in metasediments and the other in a gabbro, have  $\delta^{13}\text{C}$  values of -0.1 and -1.4, and  $\delta^{18}\text{O}$  values of 15.8 and 13.5 respectively. Though a marine source of carbon is likely, the  $\delta^{18}\text{O}$  values suggest the calcites formed from



metamorphic fluids at elevated temperatures.

Two disseminated calcite samples of rodingite and a calcite vein in a blackwall chloritic rock have similar  $\delta^{13}\text{C}$  and  $\delta^{18}\text{O}$  values (-9.6, -10.5, -10.3 and 11.2, 11.1 and 14.1 respectively). The fluids were most likely metamorphic in origin, but the low  $\delta^{13}\text{C}$  values suggest that a small component of organic carbon was present.

The wide variation of isotopic compositions of carbonates from throughout the ophiolite indicate that further work, beyond the scope of this study, will yield significant information regarding the complexity of carbonatization of oceanic crust.

#### 10.6 Conclusions

A comparison between the published studies and the results of this work shows that in terms of oxygen isotopic compositions, magnesite from the Coy Pond mélanges is within the range of other magnesites reported previously (Barnes et al., 1973; Schoell et al., 1975; Schandl and Wicks 1991; Schandl and Naldrett 1992). In terms of carbon isotopic compositions, the Coy Pond magnesite specimens cover the entire range of values previously reported (reflecting its complex geologic history) with magnesite associated with

quartz (in the western tectonic mélange) having values lower than any magnesite previously reported (Fig 10.6).

Magnesite associated with different mineral assemblages records the complete history of the Coy Pond tectonic mélange (Fig 10.7). The earliest carbonatization events produced magnesite-lizardite and magnesite-talc assemblages having  $\delta^{13}\text{C}$  values of -1.6 to -8.9, the carbon being derived from oceanic/crustal sources (Fig 10.5). This event can best be related to the transport of the ophiolite nappe in an oceanic environment, though the lowest  $\delta^{13}\text{C}$  values may reflect the first phase of its interaction with the continental margin (Fig 10.7).

The next phase of carbonatization was associated with metamorphism of the underlying Spruce Brook Formation, and the generation of large amounts of  $\text{CO}_2$  (low  $\delta^{13}\text{C}$  values) produced by decarboxilation of the organic material in the sediments. This phase of carbonatization, which occurs only in the western tectonic mélange, is associated with the recrystallization of most of the lizardite to antigorite, and with the formation of the schistose talc-magnesite in the matrix of the mélange.

Quartz-magnesite was the last assemblage to form during carbonatization of serpentinite. The large difference in  $\delta^{13}\text{C}$  values for magnesite from both tectonic mélanges reflects

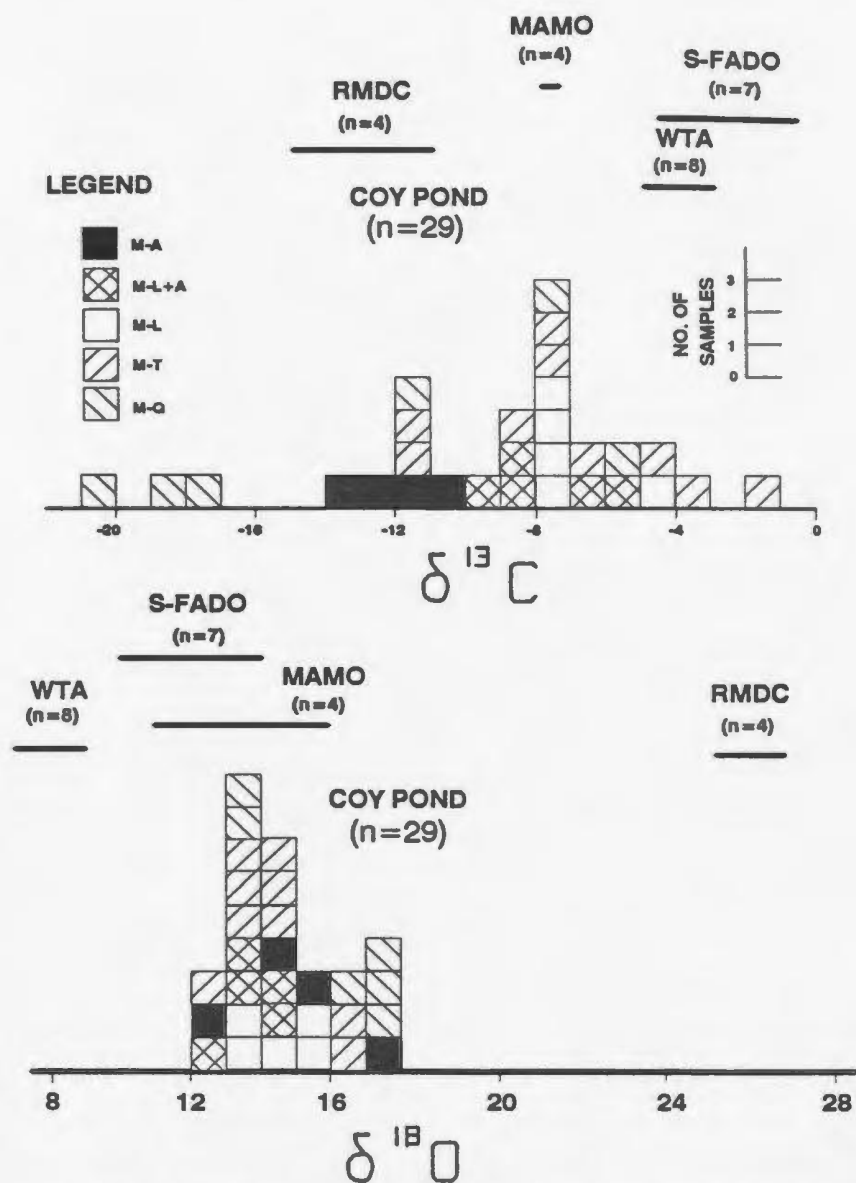
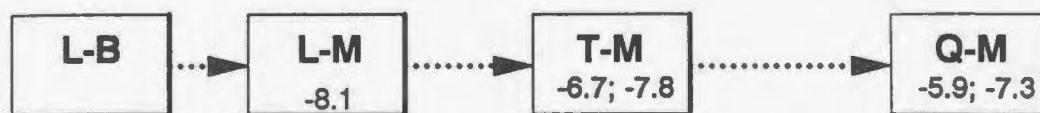


Fig. 10.6 Isotopic distribution of oxygen and carbon in crypto-crystalline and spathic magnesite from principal mineral assemblages in the Coy Pond tectonic melanges. For comparison, data for magnesite from Red Mountain Deposit California (RDMC) (Barnes et al., 1973), Western Tauern Austria (WTA) (Schoell et al., 1975), Munro Asbestos Mine Ontario (MAMO) (Schandl and Wicks 1991), and Slade-Forbes Asbestos Deposit Ontario (S-FADO) are shown. The legend include observations for magnesite (M), lizardite (L), antigorite (A), talc (T) and quartz (Q).

### EASTERN TECTONIC MELANGE



### WESTERN TECTONIC MELANGE

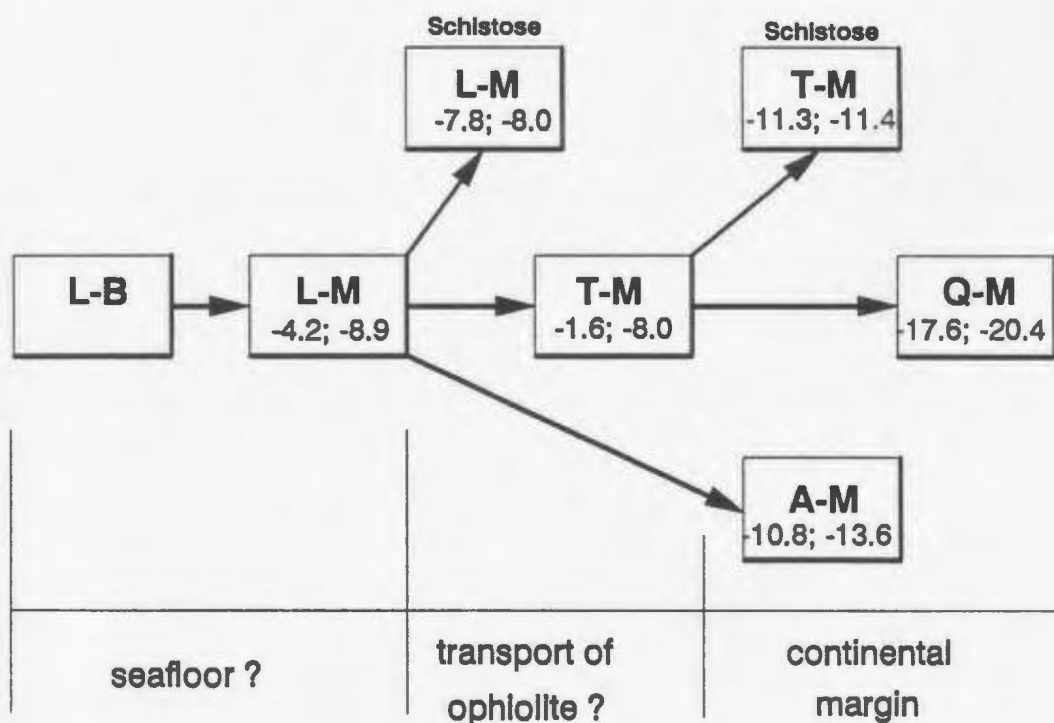


Fig 10.7 The evolution of  $\delta^{13}\text{C}$  values of magnesite and the different mineral assemblages in tectonic melanges of the Coy Pond ophiolite. Time increases to the right. Inferred environments, including metamorphism when the ophiolite was in the seafloor environment. In transport to the continental margin, and emplaced on the continental margin, are indicated below. Abbreviations: A=antigorite; B=brucite; L=lizardite; M=magnesite; Q=quartz; T=taic.

differences in the plumbing system that controlled fluid flow. Only the western mélange was affected by CO<sub>2</sub>-rich fluids from the metasediments (low  $\delta^{13}\text{C}$  values). This assemblage and the antigorite-magnesite assemblage formed after the ophiolite was emplaced onto the continental margin.

Isotopic results for magnesite and other carbonates demonstrate the existence of distinct carbon sources which have had variable contributions to carbonatization throughout the history of the tectonic mélanges. Carbonatization seems to have been related to the position of the ophiolite nappe relative to the continental margin.

## Chapter 11

### GEOTECTONIC MODELS FOR THE FORMATION OF THE TECTONIC MÉLANGES AND EVOLUTION OF THE COY POND OPHIOLITE COMPLEX

The formation of the ophiolitic tectonic mélanges was probably related to tectonic processes that occurred during the transport, emplacement and deformation of the ophiolite sheet. Based on structural, petrographic and geochemical information obtained during this study, an attempt is made to reconstruct the evolution of the tectonic mélanges in this chapter. Three hypotheses are explored: (i) that the formation of the tectonic mélanges occurred relatively early during transport and obduction of the ophiolite nappe onto the continental margin; (ii) that the formation of the tectonic mélanges occurred relatively late, after obduction ceased, mainly during and after emplacement; and (iii) that the formation involved both early and late stages, incorporating parts of both the earlier, and later movements. The hypotheses differ not only in the timing of mélange formation, but also on the principal cause for the mélange formation. However the basic mechanisms required to form the tectonic mélanges are similar in all hypotheses.

Before relating the formation of the tectonic mélanges to one or another major tectonic event, it is important to note

that based on petrographic information, at the time of mélangé formation, olivine in the participating dunite and harzburgite was completely and partially serpentinized respectively, and orthopyroxene was partially serpentinized. Oxygen isotopic compositions of the serpentine minerals are not yet available to specify the nature of the waters involved in the serpentinization process, and thus allow inferences to be made concerning the environment in which the process occurred (ocean floor or continental). It is clear, however that the waters responsible for the serpentinization were chemically different to those fluids ( $\text{CO}_2$ -bearing) which subsequently affected the mélangé assemblages.

Bearing in mind that: (i) once in contact with water, the serpentinization of peridotite proceeds very rapidly (Martin and Fyfe, 1970); and (2) that there is a complete absence of carbonate minerals in the serpentinized mantle tectonite unit underlying the western tectonic mélangé, it appears reasonably safe to affirm that the waters responsible for the serpentinization were effectively  $\text{CO}_2$ -poor. Thus it is most likely that serpentinization of the Coy Pond peridotite (including dunite within the mantle tectonite, those at the base of the transition zone, those interlayered with pyroxenite and partially those within the harzburgite



tectonite) occurred on the ocean floor and was caused by oceanic waters some time before, during or soon after detachment of the ophiolitic slab, but before obduction onto the continental margin.

In contrast, the carbon isotopic compositions of magnesite in assemblages such as schistose talc-magnesite, antigorite-magnesite and especially quartz-magnesite (see Chapter 10), which subsequently replaced the earlier formed serpentinite, strongly point to an organic source for the carbon which could have been available only if the ophiolite sheet was already emplaced onto the continental margin at the time of carbonatization.

**Hypothesis 1.** In this model, the displacement of the Coy Pond ophiolite nappe, about 7 km thick (Fig 11.1.A and B), produced high frictional shear stresses at its base that exceeded the shear strength of the serpentinite and produced shear zones. These shear zones would have developed along the weakest zones, namely the contacts of serpentinitized dunite of the transition zone with the contiguous units (Fig 11.1.C). Both the underlying harzburgite and the overlying pyroxenite were (and still are) barely serpentinitized and were rheologically more competent units. On the other hand, the dunites, already fractured and partially serpentinitized, deformed easily. The increase in volume associated with serpentinitization of dunite produced the typical orthogonal

**Fig 11.1. A - Reconstructed stratigraphic column of the Coy Pond Ophiolite complex. Thickness of the mantle tectonite and also of pillow lava and sediments, is variable from 0 to less than 1 km.**

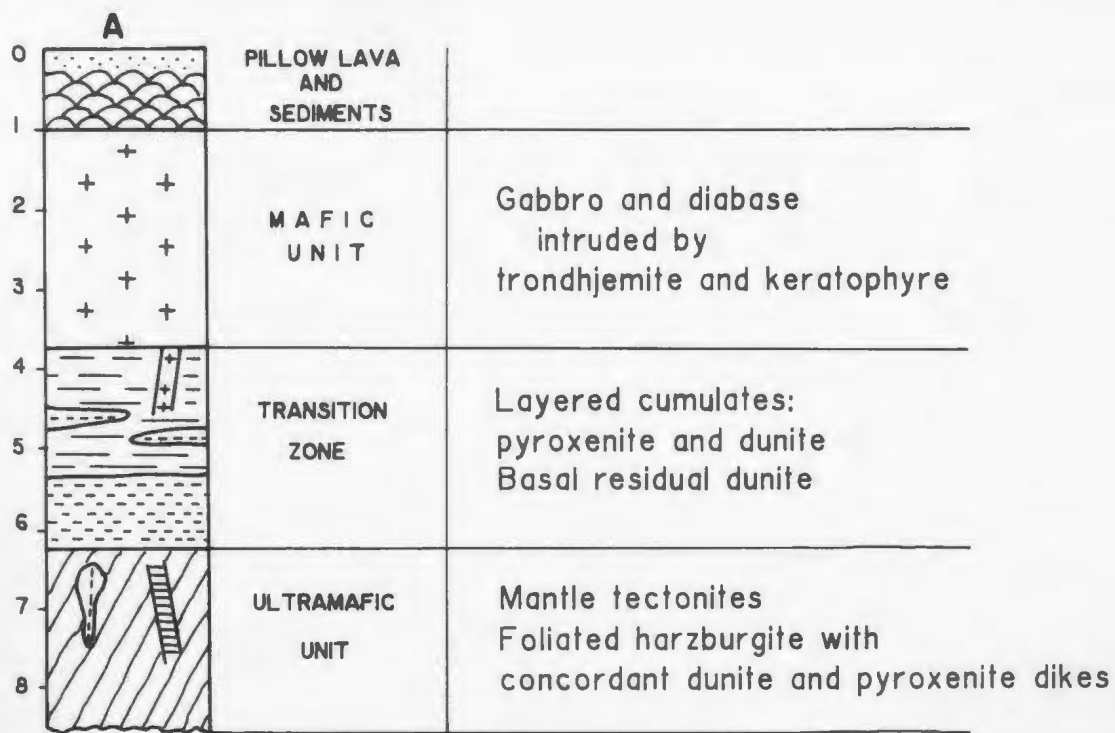
**B to E Model for evolution of tectonic mélanges.**

**B - Initial stage showing the dunite layer at the base of transition zone between layered pyroxenite and harzburgite tectonite.**

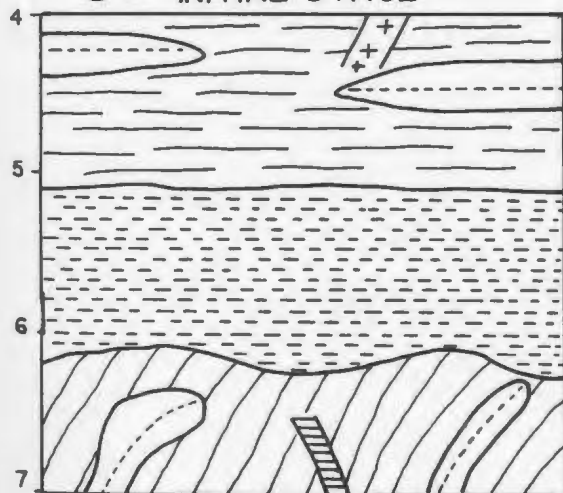
**C - Shear stresses induced during either (i), transport and emplacement of the ophiolite nappe or (ii), late extensional faulting of already emplaced ophiolite. Serpentinization (wavy lines) took place early in this process, possibly on sea floor.**

**D - During the dismemberment stage, part of the dunitic-harzburgitic material was comminuted in the brittle domain to meter-sized fragments. Remaining material underwent grain size reduction in the ductile domain to become the enclosing matrix. Fluid penetration through matrix caused recrystallization to a variety of mineral assemblages.**

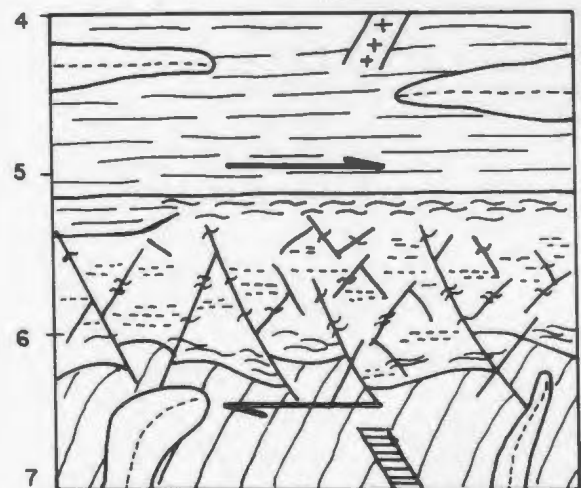
**E - Continued strain resulted in mechanical corrosion of fragments to elliptical shapes enclosed in a variably carbonatized matrix. Rare large blocks of ophiolitic origin (pyroxenite in the western tectonic mélange) or non-ophiolitic origin (metasediments in the eastern tectonic mélange) are also shown.**



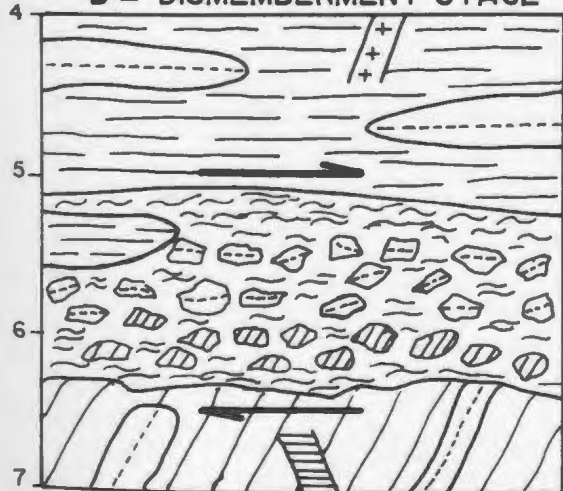
**B = INITIAL STAGE**



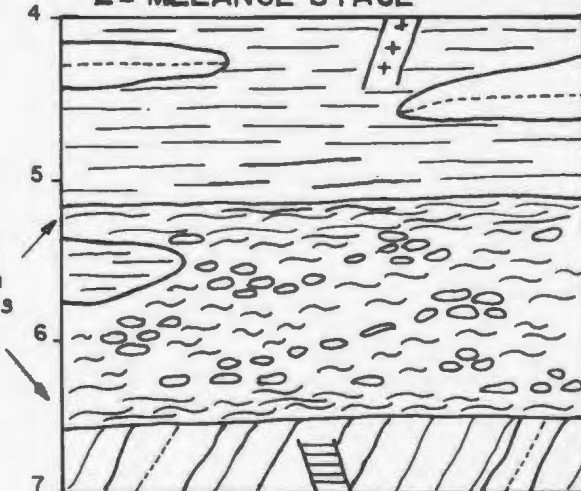
**C = FRACTURING STAGE**



**D = DISMEMBERMENT STAGE**



**E = MÉLANGE STAGE**



fracture pattern in serpentinites (Coleman, 1971; see Fig 11.1.C). The formation of many suitably oriented fractures allowed for additional shear deformations, producing more fractures which led to fragmentation and dismembering of the ultramafic rocks (Fig 11.1.D). Fragmentation and comminution of dunite/peridotite occurred in the brittle domain and resulted mainly in the formation of *mélange* fragments. During shearing, fragments were greatly reduced in size by mechanical comminution and fluid ingress enhanced ductile recrystallization to form the enclosing matrix (Fig 11.1.D and E). This is compatible with experimental results which have shown that brucite-bearing lizardite at 3 kbars confining pressure deforms in the ductile domain below about 300°C, and in the brittle domain above about 300°C (due to dehydration; Scarfe and Wyllie, 1967). Shearing of serpentinite and its concomitant recrystallization occurred in the locus of plastic flow, producing the flaky schistose matrix (Chapter 6). The formation and development of the tectonic *mélanges* was probably a function of the relative shear stresses along the ophiolitic nappe/autochthon boundary and those set up internally in the deforming nappe during tectonic transport.

The ophiolite nappe most probably advanced by gliding partially on the sedimentary substrate, partially on the western tectonic *mélange*. In this way, under modest stress

and at relatively low temperatures, the large imbricated ophiolite nappe could have been tectonically transported a great distance on the upper crust (Fig 11.2). After transport ceased, during doming of the Mount Cormack Terrane, the ophiolite nappe was tilted into a subvertical orientation and emplaced in its present-day position, probably by extensional faulting. In this hypothesis, the tectonic *mélanges* were formed early, during obduction and imbrication, and subsequently acted as passive units during the deformation on the continental margin. This is the model of Rivers et al., (1989).

**Hypothesis 2.** The central idea of the second hypothesis is that the formation of both tectonic *mélanges* occurred late after transport of the ophiolite had terminated, and was related to rotation of the ophiolite from its original subhorizontal to present subvertical orientation. The impetus for this hypothesis comes from the observation that tectonic *mélanges* are unusual features of ophiolites in general, implying that there may be special circumstance behind their formation in the Coy Pond Complex (and also the Pipestone Pond Complex; Swinden, 1988). Inasmuch as all ophiolite complexes are transported, but not all contain tectonic *mélanges*, it would seem possible that the formation of the tectonic *mélanges* may be unrelated to the transport of the ophiolite, and have occurred some time later after

**Fig 11.2** Schematic diagram showing the inferred tectonic setting for the formation and obduction of the Coy Pond Complex onto the Gander Zone continental margin.  
Abbreviations: A = asthenosphere, AW = accreted wedge, CC = continental crust, LM = lithospheric mantle, FA = fore arc, IA = island arc, OC = oceanic crust.

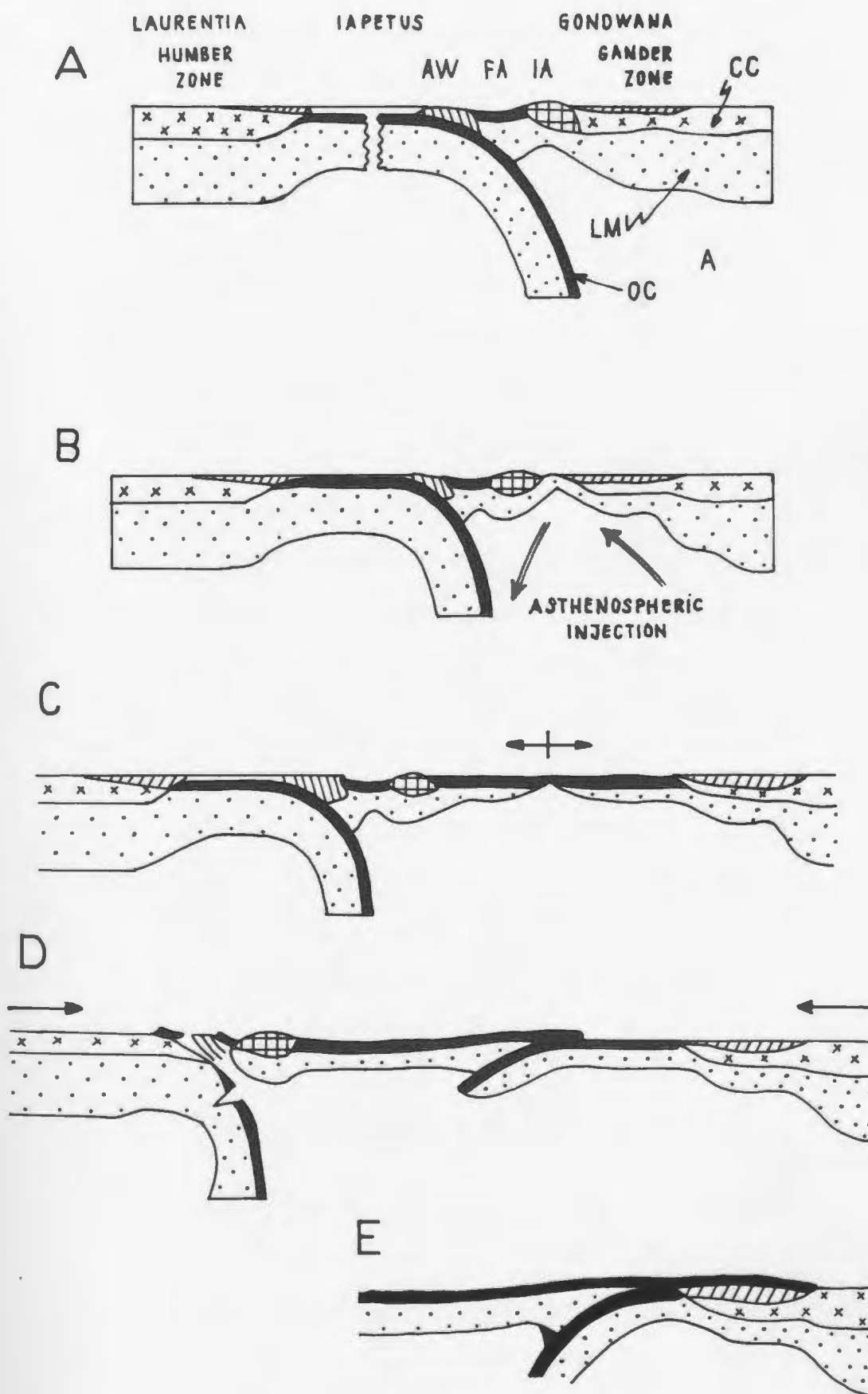
**A** - Idealized plate tectonic section across Iapetus Ocean in Central Newfoundland, in Cambrian (after van Staal et al., 1991).

**B** - Initiation of rifting and formation of a back-arc basin in late Cambrian probably occurred by asthenospheric injection (Tatsumi et al., 1988).

**C** - Formation of the Coy Pond Ophiolite at a young spreading centre in an island arc environment occurred in mid-Tremadocian (Dunning and Krogh, 1985).

**D** - Reversal of polarity from divergent to convergent tectonics occurred during early Arenig, resulting in collision of the western Dunnage Zone with the Laurentian continental margin (Humber Zone) and the eastern Dunnage Zone with the Gondwanan continental margin (Gander Zone).

**E** - Coy Pond Complex was emplaced on the Gondwana continental margin before mid-Arenig when it was intruded by the Partridgeberry Hills granite of  $474 \pm 6/-3$  Ma (Colman-Sadd et al., 1992).





transport ended. In this second model, it is therefore assumed that the Coy Pond ophiolite, although partially serpentized along shear zones, was emplaced onto the continental margin without significant internal deformation. The recent discovery of an amphibolite sole in the contiguous Great Bend Complex suggests that gabbros may have formed the glide horizon for the emplacement of the ophiolite, at least locally.

After emplacement, a period of extensional tectonism on the Gondwana continental margin with its ophiolitic cover is envisaged (Fig 11.3). The evidence for this is circumstantial and comes principally from the low-P metamorphic field gradient in the underlying Spruce Brook Formation. Thompson and England (1984) and Thompson and Ridley (1987) have pointed out that low-P metamorphic sequences are related to thinning of the upper crust by extension, allowing the isotherms to move towards the surface, creating a high geothermal gradient. Such a scenario is compatible with the situation in the Mount Cormack Terrane in which early subhorizontal structures in the Spruce Brook Formation, interpreted to be associated with ophiolite obduction, pre-date the metamorphic peak and the establishment of the isograds (Deveau, 1992).

The low-P metamorphism caused upper amphibolite facies metamorphism and migmatization at shallow crustal levels (3-

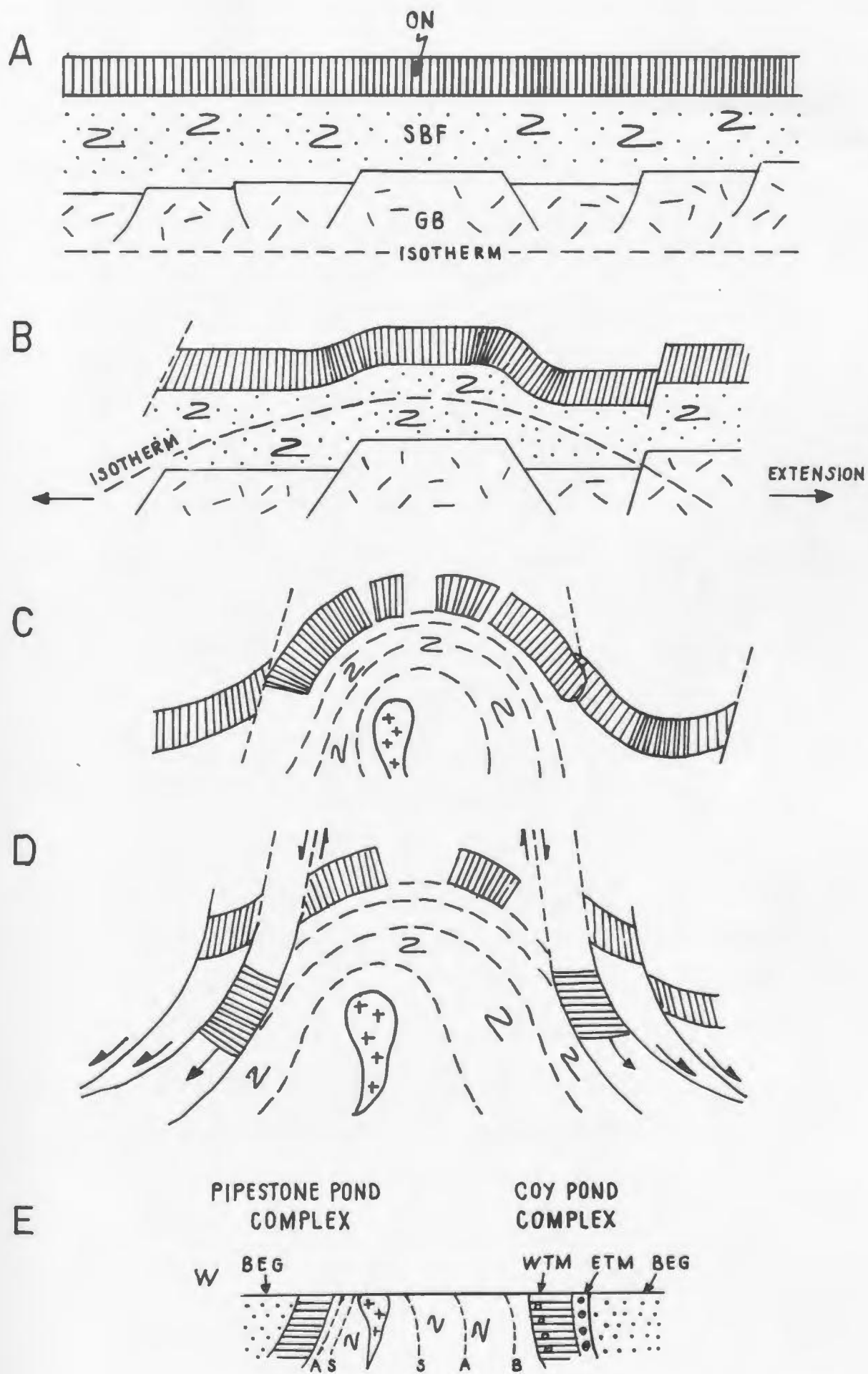
**Fig 11.3** The evolution of the Mount Cormack Terrane and Coy Pond Complex after obduction of ophiolite nappe onto the continental margin. Abbreviations:

ON = ophiolitic nappe, SBF = Spruce Brook Formation, GB = Gander basement, BEG = Baie d'Espoir Group, WTM = western tectonic mélange, ETM = eastern tectonic mélange, A = andalusite, B = biotite, S = sillimanite.

**A** - Collision tectonics ceased about mid-Arenigian when the large ophiolite nappe (comprising the actual Coy Pond, Pipestone Pond, Great Bend Complexes and other ophiolitic remnants surrounding the Mount Cormack Terrane) was emplaced onto the Gondwana continental margin. Note that the continental margin comprises a weakened basement (due to extensional faulting during earlier rifting and back-arc formation) and a craton-related sedimentary wedge (Spruce Brook Formation).

**B** - The Dunnage-Gander collision is inferred to have been followed by a period of extension, when the basement was stretched and thinned by newly formed faults, or reactivated listric extensional faults (Jackson, 1980; Wernicke and Burchfield, 1982). Thinning of the lithosphere produced upwelling of the asthenosphere and heating of the continental margin to give rise to a low-P, high-T geothermal gradient. Vertical movements along extensional faults separating basement blocks may have resulted in fragmentation of the initially continuous ophiolite nappe.

**C** - During Llanvirn-Llandeilo time, the thermal and mechanical doming resulted in intrusions of granite, migmatization and metamorphism of the metasediments in andalusite-sillimanite facies, all features typical of low-P metamorphism (Myashiro, 1972; 1980; Thompson and Ridley, 1987). On account of its high-temperature and low-density, the Spruce Brook Formation and associated S-type granitoids are inferred to have acted as a diapir, uplifting the ophiolite and rotating it into a subvertical orientation at the margins of Mount Cormack Terrane. The development of western tectonic mélange started by extensional faulting (or continued if started earlier) during tilting of the ophiolite by ductile flow along weak dunite zone located at the base of transition zone.



4 kbars, about 10-12 km, Deveau, 1992) and melt formation at slightly greater depth (e.g. Through Hill Granite). The melts were buoyant, moved upwards in the crust, and were emplaced in the upper amphibolite facies metamorphic rocks.

It is postulated that the high geothermal gradient resulted in gravitational instability of the crust locally, as follows. The pelitic and semipelitic rocks have a density in the range 2.63-2.70 g/cm<sup>3</sup>, whereas the density of ultramafic rocks is about 2.68-2.86 g/cm<sup>3</sup> (based on measurements of samples from the Spruce Brook Formation, Through Hill Granite and Coy Pond and Pipestone Pond Complexes, by Deveau, 1992). Densities >3 gm/cm<sup>3</sup> are likely for unserpentinized samples. These values indicate the presence of a significant density contrast, that would have been enhanced by the temperature contrast between the Spruce Brook Formation (400-700°C) and the Coy Pond Complex (<350°C) during metamorphism. Diapiric emplacement of the metamorphic rocks into the overlying ophiolitic carapace is suggested from the dome shape of Mount Cormack Terrane (and also Meelpaeg Terrane to the south-west) and by the observation that there is no tectonic fabric associated to the dome itself (Deveau, 1992). Earlier fabrics (S1 and S2, Deveau, 1992) form a concentric pattern, subparallel to the margins of the Mount Cormack Terrane, but there is no

evidence for a superimposed fabric associated with the dome itself. This lack of superimposed fabric is difficult to explain in a fold superposition model considering the very steep dips of the surrounding ophiolitic rocks ( $>80^\circ$ ), but is compatible with a diapiric origin (Fig 11.3).

The final stage of the model involves extensional faulting of the ophiolite off the flanks of the diapir. Extensional faults initiated in zones of weakness in the ophiolite (i.e. dunite contacts in the transition zone), and the tectonic mélanges developed as a result of gravitational sliding off the margins of the dome (Fig 11.3). Some of the extensional faults must have cut down to the underlying Spruce Brook Formation, and transported these and low grade rocks (Baie d'Espoir Group ?) in the Mixed Lithology Slice, which was emplaced against the higher grade metamorphic rocks of the Spruce Brook Formation. The emplacement of low grade rocks over those of higher grade is consistent with extensional faulting, and evidence of the cataclastic/brittle nature of the deformation in the pelitic /semipelitic units is compatible with the high level process envisaged. Fluid invasion in the extensional shear zones was important, and resulted in the formation of hydrous sericite-chlorite assemblages in the Mixed Lithology Slice and in the extensive carbonatization of the tectonic mélanges.

**Hypothesis 3.** Without the benefit of stable isotopic

analyses, it would not be possible with the available data to choose between the two hypotheses. However, based on stable isotopic data, which show involvement of average crustal and/or marine carbon in magnesite associated with early lizardite and talc, and of organic (continental) carbon in magnesite associated with antigorite and quartz, a third hypothesis for the origin of the tectonic mélanges is envisaged. In this scenario, development of the tectonic mélanges was initiated during transport of the ophiolite thrust sheet on the ocean floor, and was completed during later phases of extensional faulting after the ophiolite was emplaced on the continental margin. At this time, CO<sub>2</sub>-bearing fluids reacted with early formed lizardite and talc, resulting in antigorite-magnesite and finally quartz-magnesite assemblages.

Based on age constraints (Dunning and Krogh, 1985; Colman-Sadd et al., 1992), a time span of about 20 Ma elapsed between the formation of the Coy Pond Complex at a spreading center and its emplacement on the continental margin.

After emplacement, low-P metamorphism produced a doming and diapiric uplifting of the Mount Cormack Terrane, emplacing the Coy Pond Complex in a subvertical orientation by extensional faulting. During extensional faulting, the formation of tectonic mélanges was completed and most of the

lizardite recrystallized to antigorite or was replaced by quartz-magnesite.

The history of development of the tectonic mélanges is constrained by carbonatization events that occurred while the ophiolite was in an oceanic realm and after its emplacement on the continental margin.



## REFERENCES

Abrajano, T.A., Sturchino, N.C., Bohlke, J.K., Lyon, G.L., Poreda, R.J., and Stevens, C.M., 1988. Methane-hydrogen gas seeps, Zambales Ophiolite, Philippines: deep or shallow origin? 1988. *Chemical Geology*, v 71, p. 211-222.

Aharon, P., 1988. A stable-isotope study of magnesite from the Rum Jungle uranium field, Australia: implications for the origin of strata-bound massive magnesites. *Chemical Geology*, v.69; p.127-145.

Allerton, S., and Vine, F.J., 1987. Spreading structure of the Troodos ophiolite, Cyprus: Some palaeomagnetic constraints. *Geology*, v.15 p.593-597.

Backer, D.R., and Claypool, G.E., 1970. Effects of incipient metamorphism on organic matter in mudrock. *American Association of Petroleum Geologists Bulletin*, v.54; p.456-468.

Barnes, I., O'Neil J.R., Rapp, J.B., and White, D.E., 1973. Silica-carbonate alteration of serpentine: wall rock alteration in mercury deposits of the California Coast Ranges. *Economic Geology* v.68, p.388-398.

Barnes, I. and O'Neil J.R., 1969. The relationship between fluids in some fresh Alpine-type ultramafics and possible modern serpentinization, Western U.S. *Geological Society of America Bulletin*, v.80, p.1947-1960.

Berman, R.G., 1988. Internally-consistent thermodynamic data for minerals in the system  $\text{Na}_2\text{O}-\text{K}_2\text{O}-\text{CaO}-\text{MgO}-\text{FeO}-\text{Fe}_2\text{O}_3-\text{Al}_2\text{O}_3-\text{SiO}_2-\text{TiO}_2-\text{H}_2\text{O}-\text{CO}_2$ . *Journal of petrology* V.29, p.445-453.

Blackwood, R.F., 1983. Notes on the geology of the Great Gull Lake map area (2D/6) Newfoundland: Newfoundland Department of Mines and Energy, Mineral Development Division.

Boudier, F. and Coleman, R.G., 1981. Cross section through the peridotite in the Samail ophiolite, Southeastern Oman Mountains. *Journal of Geophysical Research*, v.86, B4, Special Issue, p.2573-2592.

- Cameron, W.E., Nisbet E.G. and Dietrich, V.J. 1980. Petrographic dissimilarities between ophiolitic and ocean floor basalts: In: Panayiotou A (ed) Ophiolites, Proceedings International Ophiolite Symposium, Cyprus, 1979. p.182-193.
- Caruso, L.J., and Chernosky, J.V., 1979. The stability of lizardite. The Canadian Mineralogist, v.17, p.757-771.
- Coleman, R.G., 1967. Glaucophane schists from California and New Caledonia: Tectonophysics, v.4, p.479-498.
- Coleman, R.G. and Keith, T.E., 1971. A chemical study of serpentinization-Burro Mountain, California. Journal of Petrology, v.12, p.311-328.
- Coleman, R.G., 1971. Petrologic and geophysical nature of serpentinite. Bulletin Geological Society of America v.82, p.897-918.
- Coleman, R.G., 1977. Ophiolites; Berlin, Springer-Verlag, 229p.
- Colman-Sadd, S.P. and Swinden, H.S., 1984. A tectonic window in central Newfoundland? Geological evidence that the Appalachian Dunnage Zone may be allochthonous. Canadian Journal of Science 21, p.1349-1367.
- Colman-Sadd, S.P., 1985. Geology of the Burnt Hill map area (2D/5) Newfoundland. Newfoundland Department of Mines and Energy. Mineral Development Division. Report 85-3.
- Colman-Sadd, S.P., Dunning, G R. and Dec, T., 1992. Dunnage-Gander relationship and Ordovician orogeny in Central Newfoundland: a sediment provenance and U/Pb age study. American Journal of Science, v.292; p.317-355.
- Coombs, D.S., Landis, C.A., Norris, R.J., and Craw, D., 1976. The Dunn Mountain ophiolite Belt, New Zealand, its tectonic setting, constitution and origin with special reference to the southern portion. American Journal of Sciences; v.276, p.561-603.
- Cowan, D.S., and Mansfield, C.F., 1970. Serpentinite flows on Joaquin Ridge, southern Coast Ranges, California. Geological Society of America Bulletin. v.81, p.2615-2628.

Dec, T. and Colman-Sadd, S., 1990. Timing of ophiolite emplacement onto the Gander Zone: evidence from provenance studies in the Mount Cormack Subzone. Current Research. Newfoundland Department of Mines and Energy, Geological Survey Branch, Report 90-1, p.289-303.

Deines, P. and Gold, D.P., 1973. The isotopic composition of carbonatite and kimberlite carbonates and their bearing on the isotopic composition of deep-seated carbon. *Geochimica et Cosmochimica Acta*, v.37,p.1709-1733.

Degens, E.T., 1969. Biogeochemistry of stable carbon isotopes, In: Eglinton, G., and Murphy, M.T.J., (eds.) *Organic geochemistry; methods and results*; p.304-329.

Des Marais, D.J., and Moore, J.G., 1984. Carbon and its isotopes in Mid Oceanic glasses. *Earth and Planetary Science Letters*, v.69, p.43-57.

Deveau, S.W., 1992. A metamorphic, structural and geophysical investigation of the Mount Cormack Terrane, Central Newfoundland (M.Sc. thesis, Memorial University of Newfoundland)

Dewey, J.F. and Bird, J.M., 1970. Mountain belts and the new global tectonics. *Journal of Geophysical Research*, v.75, p.2625-2647.

Dick, H.J.B. and Sinton, J.M., 1979. Compositional layering in ophiolite peridotites: evidence for pressure solution creep in the mantle. *Journal of Geology* v.87, p.403-416.

Dick, H.J.B. and Bullen, T., 1984. Chromian spinel as a petrogenetic indicator in abyssal and alpine-type peridotites and spatially associated lavas. *Contributions to Mineralogy and Petrology*, v.86,p.54-76.

Dickson, W.L., 1992. Ophiolites, sedimentary rocks, posttectonic intrusions and mineralization in the Eastern Pond (NTS 2D/11W) map area, Central Newfoundland. Current Research, 1992. Newfoundland Department of Mines and Energy, geological Survey Branch, Report 92-1, p.97-118.

Donath, F.A., 1961. Experimental study of shear failure in anisotropic rocks. *Bulletin of Geological Society of America*, v.72,p.985-990.

Dunning G.R. and Krogh, T.E., 1985. Geochronology of ophiolites of the Newfoundland Appalachians. Canadian Journal of Sciences, v. 22, p.1659-1670.

Elias, P., 1981. Geochemistry and petrology of granitoid rocks of the Gander Zone, Bay d'Espoir area, Newfoundland. M.Sc. thesis, Memorial University of Newfoundland.

Elias, P., and Strong, D.F., 1982. Palaeozoic granitoid plutonism of southern Newfoundland: contrasts in timing, tectonic setting and level of emplacement. Transactions of the Royal Society of Edinburgh: Earth Sciences, v.73, p.43-57.

Eckstrand, O.R., 1975. The Dumont serpentinite: a model for control of nickeliferous opaque mineral assemblage by alteration reactions in ultramafic rocks. Economic geology v.70, 183-201.

Evans, B.W., Johannes, J., Otterdoorn, H., Trommsdorff, V., 1976. Stability of chrysotile and the antigorite in the serpentinite multisystem. Schweizer Mineralogische Petrologische Mitteilungen v.56 p.79-93.

Evans, B.W., 1977. Metamorphism of alpine peridotite and serpentinite. Annual Reviews Earth and Planetary Sciences, v.5, p.397-447.

Fallick, A.E., Ilich, M. and Russel, M., 1991. A stable isotope study of the magnesite deposits associated with the alpine-type ultramafic rocks of Yugoslavia. Economic Geology v.86 p.847-861.

Fitch, T.J., 1972. Plate convergence, transcurrent faults, and internal deformation adjacent to southeast Asia and the western Pacific. Journal of geophysical research, v.77, no.23, p. 4432-4450.

Francis, G.H., 1956. The serpentinite mass in Glen Urquhart, Inverness-Shire, Scotland. American Journal of Science, v.254, p.201-226.

Friedman, I. and O'Neil, J.R. 1977. Compilation of stable isotope fractionation factors of geochemical interest. U.S. Survey Professional Paper 440-KK.

Frost, B.R., 1985. On the stability of sulfides, oxides and native metals in serpentinite. Journal of petrology v.26, p.31-63.

Gansser, A., 1974. The ophiolitic mélange, a World-wide Problem on Tethian Examples. *Eclogae Geologicae Helveticae* v.67 p.479-507.

Gerlach, T.M., and Thomas, D.M., 1986. Carbon and sulphur isotopic composition of Kilauea parental magma. *Nature*, v.319;p.480-483.

Cirardeau, J. and Nicolas, A., 1981. Structures in two of the bay of Islands (Newfoundland) ophiolite massifs: a model of oceanic crust and upper mantle. *Tectonophysics*, v.77; p.1-34.

Golyshev, S.I., Padalko, N.L. and Pechenkin, S.A., 1981. Fractionation of stable oxygen and carbon isotopes in carbonate systems. *Geochemica International*, v.10,p.85-99.

Green, D.H., and Ringwood, A.E., 1967. An experimental investigation of the gabbro to eclogite transformation and its petrographical applications. *Geochemica and Cosmochimica Acta*, v.31,p.767-833.

Greenwood, H.G., 1967. Mineral equilibria in the system  $MgO-SiO_2-H_2O-CO_2$ . *Researches in Geochemistry*, ed. P.H. Abelson,p.542-567.New York, London, Sydney.

Griffis, R. 1972. Genesis of a magnesite deposit, Deloro Twp., Ontario. *Economic Geology*, v.67,p.63-71.

Harland, W.B. and Gayer, R.A., 1972. The Arctic Caledonides and earlier oceans. *Geological Magazine*.109.p.289-314.

Harte, B., 1977. Rock nomenclature with particular relation to deformation and recrystallization textures in olivine-bearing xenoliths. *Journal of Geology*, v.85,p.279-288.

Hibbard, J. and Williams, H., 1979. Regional setting of the Dunnage mélange in the Newfoundland Appalachians. *American Journal of Science*; p. 993-1031.

Hoefs, J., 1973. A contribution on the isotope geochemistry of carbon in igneous rocks. *Contribution to mineralogy and petrology*, v.41,p.277-300.

Hopson, C.A., Coleman, R.G., Gregory, R.T., Pallister J.S. and Bailey E.H., Geologic section through the Samail ophiolite and associated rocks along a Muscat-Ibra transect, southeastern Oman Mountains, *J,Geoph.Res.*,v.86,2527-2544.

Hostetler, P.B, Coleman, R.G., Mumpton, F.A., and Evans, B.W., 1966. Brucite in alpine serpentinites. The American Mineralogist, v.51, p.75-98.

Hsü., K.J., 1968. Principles of Mélanges and their bearing on the Franciscan-Knoxville paradox. Geological Society of America, v.79, p.1063-1074.

Hsü, K.J., 1983. Geosynclines in plate-tectonics settings: sediments in mountains. Mountain building processes, K.J.Hsü, ed. p.3-12.

Irvine, T.N., 1965. Chromian spinel as an petrogenetic indicator, Part 1. Theory. Canadian Journal of Earth Sciences, v.2, p.648-672.

Irvine, T.N., 1967. Chromian spinel as an petrogenetic indicator, Part 2. Petrologic applications. Canadian Journal of Earth Sciences, v.4, p.71-103.

Irvine, T.N. and Findlay, T.C. 1972. Alpine-type peridotite with particular reference to Bay of Islands igneous complex. In: The Ancient Ocean Lithosphere, Publications of the Earth Physics Branch, Dept Energy Mines and Resources Ottawa Canada 43 no 3, p.97-126.

Irvine, T.N., 1974. Petrology of the Duke Island ultramafic complex, southeastern Alaska. Geological Society of America Memoir 138.

Jackson, J.A., 1980. Reactivation of basement faults and crustal shortening in orogenic belts. Nature, v.283, p.343-346.

Johannes, W., 1968. Experimental investigation in the reaction forsterite + H<sub>2</sub>O = serpentine + brucite. Contribution to Mineralogy and Petrology, v.19, p.309-315.

Johannes, W., 1969. An experimental investigation of the system MgO-SiO<sub>2</sub>-H<sub>2</sub>O-CO<sub>2</sub>. American Journal of Sciences, v.267, p.1083-1104.

Malpas, J. and Strong, D.F., 1974. A comparison of chrome-spinels in ophiolite and mantle diapirs of Newfoundland: Geochimica and Cosmochemica Acta, v.39 p.1045-1060.

Malpas, J. and Strong, D.F., 1975. A comparison of chrome-spinel in ophiolites and mantle diapirs of Newfoundland. *Geochimica and Cosmochimica Acta*, v.39, p.1045-1060.

Martin, B. and Fyfe, W.S., 1970. Some experimental and theoretical observations on the kinetics of the hydration reactions with particular reference to serpentinization. *Chemical Geology*, v.6 p.185-202.

Mc Crea, J.M., 1950. The isotope chemistry of carbonates and a paleotemperature scale. *Journal of Chemistry and Physics*, v.18; p.849-857.

McKirdy, D.M., and Powell, T.G., 1974. Metamorphic alteration of carbon isotopic composition in ancient sedimentary organic matter: new evidence from Australia and South Africa. *Geology*, 1974, p.561-595.

Mercier, J.C., and Nicolas, A., 1975. Textures and fabrics of upper mantle peridotites as illustrated by xenoliths from basalts. *Journal of Petrology*, v.16, p.454-487.

Miyashiro, A., 1973. *Metamorphism and metamorphic belts*. Allen and Undwin. New York, 492 p.

Moody, J.B., 1976. An experimental study of the serpentinization of iron-bearing olivines. *Canadian mineralogist* v.14, p.462-478.

Moody, J.B., 1976. Serpentinization: a review. *Lithos* v.9, p.125-138.

Nicolas, A., Boudier, F., and Bouchez, J.L., 1980. Interpretation of peridotite structures from ophiolitic and oceanic environments. *American Journal of Science* v.280(A) p.192-210.

Nicolas, A., 1986. A melt extraction model based on structural studies in mantle peridotites. *Journal of Petrology*, v.27, p. 999-1022.

Nicolas, A. and Prinzhofer, A., 1982. Cumulative or residual origin of the transition zone in ophiolites: structural evidence. *Journal of petrology*, v.24; p.188-206.

Norell, G.T., Harper, G.D., 1988. Detachment faulting and amagmatic extension at mid-ocean ridges: The Josephine ophiolite as an example. *Geology*, v.16, p.827-830.



O'Brien, S.J., Wardle, R.J., and King, A.F., 1983. The Avalon Zone: a Pan-African terrane in the Appalachian orogen of Canada. *Geological Journal*, v.18, p.195-122.

O'Hanley, D.S., 1991. Fault-related phenomena associated with hydration and serpentine recrystallization during serpentization. *Canadian mineralogist* v.29, p.21-35.

O'Hanley, D.S., Chernosky, J.V., Jr. and Wicks, F.J., 1989. The stability of lizardite and chrysotile. *Canadian Mineralogist*, v.27, p.483-494.

O'Hanley, D.S., and Dyar, M.D., (in press). The crystal chemistry of lizardite and the formation of magnetite.

O'Hanley, D.S. and Offler, R., (in press). Characterization of multiple serpentization, Woodsreef, New South Wales.

O'Hanley, D.S., Shandl, E.S., and Whicks, F.J., in press. Pressure and temperature estimates for serpentine recrystallization at Cassiar, British Columbia, based on  $^{18}\text{O}/^{16}\text{O}$  serpentine-magnetite thermometry and fluid inclusions in rodingite minerals.

Ohmoto, H., 1972. Systematics of sulphur and carbon isotopes in hydrothermal ore deposits. *Economic Geology*, v.67, p.551-558.

O'Neil, J.R., Clayton, R.N. and Mayeda, T.K., 1969. Oxygen isotope fractionation in divalent metal carbonates. *Journal of Chemistry and Physics*, v.51; p.5547-5558.

O'Neil, J.R. and Barnes, I., 1971.  $^{13}\text{C}$  and  $^{18}\text{O}$  compositions in some fresh water carbonates associated with ultramafic rocks and serpentinites: western United States. *Geochemica and Cosmochemica Acta*, v.35; p.687-697.

O'Neil, J.R., 1977. Stable isotope in mineralogy. *Physics and Chemistry of Minerals*. v.2; p.105-123.

Pallister, J.S. and Hopson, C.A. 1981. Samail Ophiolite Suite: Field relations, phase variation, cryptic variation and layering, and a model of a spreading ridge magma chamber. *Journal of Geophysical Research*, v.86, no.B4, p.2593-2644.

Peacock, S.M., 1987. Serpentinization and infiltration metasomatism in the Trinity peridotite, Klamath province, northern California: implications for subduction zones. *Contributions to mineralogy and petrology*, v.95,p.55-70.

Perry, E.C. and Tan, F.C., 1972. Significance of oxygen and carbon isotope determinations in early Precambrian cherts and carbonate rocks of southern Africa. *Bulletin of Geological Society of America* v. 83;p.647-664.

Pike, J.E.N. and Schwarzman, E.C., 1976. Classification of textures in ultramafic xenoliths. *Journal of Geology*, v.85, p.49-61.

Pineau, F., Javoy, M. and Bottinga, Y., 1976.  $^{13}\text{C}/^{12}\text{C}$  ratios of rocks and inclusions of popping rocks of the Mid-Atlantic Ridge and their bearing on the problem of the isotopic composition of deep-seated carbon. *Earth and Planetary Science Letters*, v.29,p.413-421.

Pineau, F., and Javoy, M. 1983. Carbon isotope and concentrations in mid-ocean ridge basalts. *Earth and Planetary Science Letters*, v.62,p.239-257.

Pohl, W. and Siegl, W., 1986. Sediment hosted magnesite deposits. In: K.H. Wolf (editor), *Handbook of stratabound and stratiform ore deposits*; v.14;p.223-310.

Prichard, H.M., 1979. A petrographic study of the process of serpentinization in ophiolite and the ocean crust. *Contributions to mineralogy and Petrology*, v.68,p.231-241.

Raleigh, C.B., and Patterson, M.S., 1965. Experimental deformations of serpentinite and its tectonic implications. *Journal of Geophysical Research*, v.70, p.3965-3985.

Rosenbaum, J. and Sheppard, S.M.F., 1986. An isotopic study of siderites, dolomites and ankerites at high temperatures. *Geochimica et Cosmochimica Acta*, v.50, p.1147-1150.

Rucklidge, J.C. and Patterson, G.C., 1977. The role of chlorine in serpentinization. *Contributions to Mineralogy and Petrology*, v.65,p.39-44.

Sakai, H., Des Marais, D.J., Ueda, A. and Moore, J.G., 1984. Concentrations and isotope ratios of carbon, nitrogen and sulphur in ocean-floor basalts. *Geochemica et Cosmochemica Acta*, v.48, p.2433-2441.

Sanford, R.F., 1981. Mineralogical and chemical effects of hydration reactions and applications to serpentinization. *American Mineralogist*, v.66, p.290-297.

Scarfe, C.M., and Wyllie, P.J., 1967. Serpentine dehydration curves and their bearing on serpentinite deformation in orogenesis. *Nature*, v.215, p.945-946.

Schidlowsky, M., Eichmann, R. and Junge, C.E., 1975. Precambrian sedimentary carbonates: carbon and oxygen isotope geochemistry and implications for the terrestrial oxygen budget. *Precambrian Research*, v.2, p.1-69.

Sheppard, S.M.F., 1977. Identification of the origin of ore forming solutions by the use of stable isotopes. In *Volcanic processes in ore genesis*. London: Institution of Mining and Metallurgy and Geological Society, 1977, p.25-41.

Sheppard, S.M.F., 1984. Stable isotope studies of formation waters and associated Pb-Zn hydrothermal ore deposits. In: *Thermal phenomena in sedimentary basins*; B. Durhand (ed.) Paris, 1984; p.301-317.

Shoell, M., Morteani, G. and Hormann, P.K. 1975.  $^{18}\text{O}/^{16}\text{O}$  and  $^{13}\text{C}/^{12}\text{C}$  ratios of carbonates from gneisses, serpentinites and marbles of the Zillertaler Alpen, Western Tauern area (Austria). *Neues Jahrbuch Min.*, 1975, v.10, p.444-459.

Stevens, R.K., 1970. Cambro-Ordovician flysh sedimentation and tectonics in west Newfoundland and their possible bearing on a proto-Atlantic ocean. In: *Flysh sedimentology in North America*. Ed. by J.Lajoie. Geological Association of Canada. Special Paper 7, p.165-177.

Stevens, R.K., Strong, D.F. and Kean, B.F., 1974. Do some eastern Appalachian ultramafic rocks represent mantle diapirs produced above a subduction zone?: *Geology* 2, p.175-178.

Stevens, R.K., 1992. Have the remnants of the proto Atlantic any use as fuel? some implications for the early history of the earth, early life and other things, personal communication. The Tuzo Wilson cycle: GAC-MAC Program with Abstracts. A 25th anniversary symposium, February 1992, St. John's Newfoundland.

Swinden, H.S., 1988. Geology and economic potential of the Pipestone Pond area (12A/1NE;12A/8E), Central Newfoundland. Newfoundland Department of Mines and Energy. Mineral Development Division. Report 88-2.

Tarutani, T., Clayton, R.N. and Mayeda, T.K., 1969. The effect of polymorphism and magnesium substitution on oxygen isotope fractionation between calcium carbonates and water. *Geochemica et Cosmochimica Acta*, v.33, p.987-996.

Tatsumi, Y., Otofujii, Y., Matsuda, T., and Nohda, S., 1988. Opening of the Sea of Japan back-arc basin by asthenospheric injection. *Tectonophysics*, v.166; p.317-329.

Taylor, H.P., 1968. The oxygen isotope geochemistry of igneous rocks. *Contrib. Mineral. Petrol.* v.19, p.1-71.

Taylor, H.P.Jr., French, J. and Degens, E.T., 1967. Oxygen and carbon isotope studies of carbonatites from the Laacher See district, West Germany, and the Alno district, Sweden. *Geochemica et Cosmochimica Acta*; v.31; p.407-430.

Taylor, H.P., 1974. The application of oxygen and hydrogen isotope studies to problems of hydrothermal alteration and ore deposition. *Economic geology* v.69 p.843-883.

Taylor, H.P.Jr., 1977. Water/rock interaction and the origin of H<sub>2</sub>O in granitic batholiths. *Journal of Geological Society London*, v.133; p.509-558.

Thayer, T., 1966. Serpentinization considered as a constant volume metasomatic process. *American Mineralogist* v.51, p.685-710.

Thayer, T., 1967. Serpentinization considered as a constant volume metasomatic process: a reply. *American Mineralogist* v.52, p.549-553.

Tissot, B.P., and Welte, D.H., 1984. Petroleum formation and occurrence; p.69-73.

Walter, J.V., and Orville, P.M., 1982. Volatile production and transport in regional metamorphism. Contribution to Mineralogy and Petrology, v.79;p.252-257.

Weir, R. H., and Kerrick, D.M., 1987. Mineralogic, fluid inclusion, and stable isotope studies of several gold mines in the Mother Lode, Toulumne and Mariposa Counties, California. Economic Geology v. 82, p.328-344.

Wenner, D.B. and Taylor Jr.H.P., 1971. Oxygen and hydrogen isotope studies of the serpentinization of ultramafic rocks in oceanic environments and continental ophiolite complexes. American Journal of Sciences, v.272, p.207-239.

Wenner, D.B. and Taylor Jr.H.P., 1973. Oxygen and hydrogen isotope studies of the serpentinization of ultramafic rocks in oceanic environments and continental ophiolite complexes. American Journal of Sciences, v.273, p.207-239.

Whittaker, E.J.W. and Muntus, R., 1970. Ionic radii for use in geochemistry. Geochemica and Cosmochimica Acta v.34;p.945-956.

Wicks, F.J., and Whittaker, E.J.W., 1977. Serpentine textures and serpentinization. Canadian Mineralogist v.15, p.459-488.

Wicks, F.J., 1984. Deformation histories as recorded by serpentinites. III, Fracture patterns developed prior to serpentinization. Canadian Mineralogist, v.22, p.205-209.

Wilkinson, J.J., 1991. Volatile production during contact metamorphism: the role of organic matter in pelites. Journal of the Geological Society, London, v.148; p.731-736.

Williams, H., 1964. The Appalachians in northeastern Newfoundland-a two-sided symmetrical system. American Journal of Science, 262, p.1173-1158.

Williams, H., Colman-Sadd, S.P., and Swinden, H.S., 1988. Tectonic-stratigraphic subdivisions of central Newfoundland. Current Research, part B: Geological Survey of Canada, Paper 88-1B, p.91-98.

Wilson, J.T., 1966. Did the Atlantic close and then re-open?. Nature 211, 676-681.

Windley B.F., 1977. Island arcs. In: The evolving continents. Windley B.F., (ed.) p.241-257.

Winkler, H.G.F., 1974. Petrogenesis of metamorphic rocks.

Yardley, W.D.B., 1989. An introduction to metamorphic petrology.

Zemann, J., 1972. Carbon. In: Wederpohl, K.H., (ed.) Handbook of geochemistry, II-1, Springer-Verlag, Berlin, Chapter 6A.

Zwicker, E.J. and Strong, D.F., 1974. The Great Bend ophiolite, eastern Newfoundland: field investigations; Current Research, Part A, Geological Survey of Canada, Paper 86-1A, p.393-397, 1986.

## Appendix 1

### Serpentine pseudomorphic textures

**Pseudomorphic textures** (Fig 6.1) are produced during initial serpentinization, whereas **nonpseudomorphic textures** are produced during serpentine recrystallization. Providing that the state of strain is low, pseudomorphic textures are produced during the serpentinization of almost all minerals in ultramafic rocks. According to Wicks (1984), such textures may form during either retrograde or mild prograde metamorphism. Pseudomorphic textures are commonly valuable for the determination of the nature of the protolith and for the interpretation of the history of the ultramafic rocks as the pseudomorphs may preserve the outline and some details of the solid-state deformation textures of olivine and pyroxene. In case of perfect pseudomorphism, it is not difficult to recognize kink bands and undulatory extinction in olivine and elongation of pyroxenes.

However deformation events during or after serpentinization may disturb or replace pseudomorphic textures with non-pseudomorphic textures such as interpenetrating and interlocking. Non-pseudomorphic textures are produced by recrystallization of lizardite to antigorite (interpenetrating texture) or to lizardite  $\pm$  chrysotile  $\pm$  antigorite (interlocking texture).

#### **Mesh texture**

The regular, polyhedral or irregular central areas enclosed by the meshwork have been called **cores** (Francis, 1956; Deer et al. 1962, Grub 1962) or **mesh centers** (Wicks and Whittaker 1977). The outer zones surrounding the mesh centers are composed of pseudofibrous serpentine that has been referred to as a **collar** (Francis 1956), **veinlet** (Coats 1967), **cord** (Maltman 1978; Lauder, 1965) or **mesh rim** (Wicks et al., 1977).

#### **Mesh texture - development and nomenclature**

The process of serpentinization suggested by Wicks and Whittaker (1977) firstly involves the formation of well-crystallized and well-oriented lizardite mesh rims, followed by the production of fine grained, randomly oriented serpentine within mesh centers (Fig 6.1). However Cressey (1979), proposed another process based on electron microscopy observations of the products of the experimental hydration of olivine to serpentine and brucite performed by Martin and Fyfe (1970). In this model the mesh rim, with its well-crystallized serpentine was formed by recrystallization of the first-formed, poorly crystalline serpentine. According to this mechanism, serpentine recrystallization



started virtually simultaneously with serpentinization. If the serpentinization front advanced more rapidly than the recrystallization front, one may expect to find mesh centers with poorly crystallized serpentine remaining (Fig 6.4). A pure hour-glass texture is to be expected when suitable conditions were maintained and the whole serpentine had recrystallized (Fig 6.7 and 6.8). If for some reason the recrystallization stopped before reaching the cell center, an incomplete hourglass texture will be produced (Fig 6.9).

In optical descriptions of serpentine minerals and textures, the terms  $\alpha$ - and  $\gamma$ -serpentine (Francis 1956) are commonly used.  $\alpha$ -serpentine is length-fast, with apparent fibers having negative elongation, and  $\gamma$ -serpentine length-slow, with apparent fibers having positive elongation. It was determined (Wicks and Zussman, 1975) that  $\alpha$ -serpentine is pseudofibrous lizardite, and that  $\gamma$ -serpentine can be chrysotile, lizardite or antigorite. For this reason the authors recommend the use of  $\alpha$ - and  $\gamma$ -serpentine only as petrographic terms, and conventionally the elongation of the mesh rims gives the character of the entire mesh texture regardless of the optical orientation of the serpentine in the mesh centers. Electron microscopy of ion-thinned samples (Cressey, 1979) has shown that the mesh rim consists of parallel stacks of lizardite plates.

#### **Banded growth texture**

Banded growth (Figs 6.1 and 6.4) textures were first described by Francis (1956) and attributed to the effect of local shearing on regular mesh textures. The same texture was referred to as "ribbon" by Maltman (1978) who considered it to be derived from mesh texture during regional shear-stress. Wicks et al. (1977) considered banded growth texture to be a variant mesh texture which reflects the fracture pattern of the olivine rather than the shear stress during or after the serpentinization.

#### **Bastite texture**

The serpentinization process of pyroxenes appears to proceed similarly to that of olivine, beginning at grain boundaries and fractures and following cleavages and fractures (Figs 6.1; 6.10 and 6.11). This phenomenon may be seen in partially serpentinized specimens. A close topotactic relationship between lizardite bastite and its parent silicates has been found to exist (Wicks and Zussman 1975; Dungan 1979).

## APPENDIX 2

### (A) MICROANALYSER CHARACTERISTICS

Electron microprobe analyses were done with a JEOL JXA 50-A Electron Probe Microanalyzer with 3 wavelength dispersive crystal spectrometers situated at the Department of Earth Sciences, Memorial University of Newfoundland. The instrument is operated through a PDP-11 computer. Counts were collected for 30 seconds, or up to 30 000 counts were recorded. Operating conditions were: accelerating voltage 15 kv, beam current 22 nA and a size beam size 10 microns was used for silicates, and a 30 microns beam for carbonate (magnesite). The total iron was expressed in FeO.

In order to evaluate analytical errors, at the beginning and also during each microprobe session, natural olivine, orthopyroxene, clinopyroxene or Cr-spinel standards were analyzed. All the analytical errors associated with repeated microprobe analysis of the olivine, orthopyroxene and clinopyroxene standards were <3% and for Cr-spinel <4%.

### (B) CORRECTION FOR MAGNESITE ANALYSES CONTAINING SERPENTINE INCLUSIONS

Electron microprobe analyses of carbonates were done with a 30 micron diameter beam and 10 nA current. Magnesite, especially in serpentinite rocks contains minute serpentine inclusions (often visible under crossed polars) indicated by SiO<sub>2</sub> in the analytical results.

Corrected magnesite compositions have been calculated by removal of silicate (serpentine) component from the magnesite analysis in the following manner:

(i) Specimen 432-D was chosen as an average lizardite composition to be subtracted from all magnesite analyses containing silicate inclusions.

NA	Mg	Al	Si	Ca	Ti	Cr	Mn	Fe*	Ni	Total
.02	40.0	.02	41.02	.01	.00	.03	.04	4.71	.40	86.24
FM*	2.857		1.966					0.188	5.027	

Si/Mg = 0.688; Si/Fe = 10.407;

Fe\* = FeO as Fe total

FM\* = number of ions based on 7 oxygens (calculated)

**Table A.8.1** Composition of average lizardite from sample 432-D used to correct magnesite analyses with lizardite inclusions.

(ii) Si/Mg and Si/Fe cation ratios (as ions) were calculated from average lizardite (Table A.9.1).

(iii) For each magnesite analysis which contained Si (serpentine impurities), Si was subtracted entirely, and Mg and Fe reduced accordingly to the Si/Mg and Si/Fe ratios determined in average lizardite.

(iv) After subtraction, the sum of Ca and the remaining Mg and Fe in magnesite were normalized to 1 cation.

### (C) X-RAY POWDER DIFFRACTION PROCEDURE

In thin sections, the nature of serpentine polymorphs was determined petrographically using criteria described by Wicks and Whittaker (1977), and afterwards verified and confirmed by X-ray means.

Representative samples of all observed serpentine textures were ground to a fine powder, and any magnetite present, was removed magnetically. The powder was mixed with acetone and the slurry spread on glass slides which, after drying, were placed in a standard X-ray diffraction unit (Rigaku CN 4148 C1 R-RU 200) employing  $\text{CuK}\alpha$  radiation. A scan rate of  $1^\circ 2\theta/\text{minute}$  generate satisfactory patterns.

The specific serpentine minerals were determined using criteria suggested by Whittaker and Zussman (1956), and by comparison with JCPDS (Joint Committee on Powder Diffraction Standards) standard patterns.

Antigorite is distinguishable from lizardite and chrysotile by:

- (i) the absence of a major peak at  $2\theta = 19.2 - 19.4^\circ$
- (ii) a major peak at  $2\theta = 35.5^\circ$
- (iii) a moderate peak at  $2\theta = 59.0 - 59.1^\circ$

In contrast, lizardite and chrysotile have:

- (i) a moderate asymmetric peak at  $2\theta = 19.2 - 19.4^\circ$
- (ii) a major peak at  $2\theta = 35.9 - 36^\circ$
- (iii) a moderate single peak at  $2\theta = 60.2^\circ$

Chrysotile and lizardite were distinguished by their (204) and (208) peaks. The lizardite (204) peak occurs at  $2\theta=42.07^\circ$  and (208) peak occurs at  $2\theta=61.74^\circ$ . The chrysotile (204) peak occurs at  $2\theta=43.16^\circ$ , and no peak is present in the region  $2\theta=61.7^\circ$ .

Appendix 3: Microprobe analyses of olivine

specimen	333	333	333	156	156	156
rock	H <sub>z</sub>	H <sub>z</sub>	H <sub>z</sub>	H <sub>z</sub>	H <sub>z</sub>	H <sub>z</sub>
analysis	1	2	3	4	5	6
Na <sub>2</sub> O	0.02	0.02	0.30	0.01	0.01	0.05
MgO	49.76	51.21	50.38	49.46	49.90	48.96
Al <sub>2</sub> O <sub>3</sub>	0.00	0.00	0.20	0.00	0.00	0.02
SiO <sub>2</sub>	41.11	40.66	39.79	37.19	37.57	0.14
CaO	0.02	0.00	0.00	0.02	0.00	0.01
TiO <sub>2</sub>	0.00	0.20	0.00	0.00	0.00	0.00
Cr <sub>2</sub> O <sub>3</sub>	0.00	0.00	0.00	0.00	0.00	0.02
MnO	0.15	0.11	0.14	0.18	0.21	0.11
FeO*	8.52	8.86	8.47	12.25	11.93	11.18
NiO	0.34	0.39	0.32	0.49	0.56	0.51
Total	99.91	101.27	99.15	99.61	100.19	98.00
number of ions on the basis of 4 oxygens						
Na	0.000	0.000	0.000	0.000	0.000	0.002
Mg	1.800	1.844	1.852	1.854	1.857	1.856
Al	0.000	0.000	0.000	0.000	0.000	0.000
Si	1.002	0.982	0.981	0.935	0.938	0.945
Ca	0.000	0.000	0.000	0.000	0.000	0.000
Ti	0.000	0.000	0.000	0.000	0.000	0.000
Cr	0.000	0.000	0.000	0.000	0.000	0.000
Mn	0.020	0.020	0.002	0.003	0.003	0.002
Fe	0.173	0.178	0.174	0.257	0.249	0.237
Ni	0.006	0.070	0.050	0.009	0.011	0.010
Total	2.994	3.014	3.015	3.059	3.059	3.053
Fo	91.0	88.1	89.2	87.5	87.7	88.3

\*FeO as Fe total

H<sub>z</sub> = harzburgite

continued

appendix 3 (continued)

specimen	184	184	184	175	175
rock	Hz	Hz	Hz	Hz	Hz
analysis	7	8	9	10**	11**
Na2O	nd	nd	nd	nd	nd
MgO	51.39	50.44	50.58	51.43	50.86
Al2O3	nd	nd	nd	nd	nd
SiO2	39.90	40.41	40.08	40.32	40.94
CaO	nd	nd	nd	nd	nd
TiO2	nd	nd	nd	nd	nd
Cr2O3	0.00	0.00	0.02	0.00	0.09
MnO	0.14	0.11	0.14	0.15	0.09
FeO*	8.72	8.84	8.55	8.75	8.68
NiO	nd	nd	nd	nd	nd
Total	100.16	99.80	99.36	100.66	100.66
Na	-	-	-	-	-
Mg	1.870	1.838	1.851	1.861	1.835
Al	-	-	-	-	-
Si	0.974	0.988	0.984	0.979	0.991
Ca	-	-	-	-	-
Ti	-	-	-	-	-
Cr	0.000	0.000	0.000	0.000	0.001
Mn	0.002	0.002	0.002	0.002	0.001
Fe	0.177	0.180	0.175	0.177	0.175
Ni	-	-	-	-	-
Total	3.024	3.008	3.013	3.019	3.004
Fo	91.4	91.1	91.4	91.3	91.3

continued

\* FeO as Fe total

\*\* fragment in mélange

Appendix 3 (continued)

specimen	299	299	299	103	103	103
rock	Dun*	Dun*	Dun*	Dun**	Dun**	Dun**
analysis	13	14	15	16	17	18
Na2O	nd	nd	nd	nd	nd	nd
MgO	49.71	49.74	50.80	52.21	52.44	52.59
Al2O3	nd	nd	nd	nd	nd	nd
SiO2	40.63	40.14	40.39	40.63	41.03	40.89
CaO	nd	nd	nd	nd	nd	nd
TiO2	nd	nd	nd	nd	nd	nd
Cr2O3	0.02	0.00	0.04	0.00	0.00	0.02
MnO	0.02	0.08	0.00	0.07	0.09	0.09
FeO*	8.46	10.27	8.27	7.23	7.14	7.42
NiO	0.11	0.24	0.19	nd	nd	nd
Total	98.95	100.48	99.69	100.13	100.70	101.00
Na	—	—	—	—	—	—
Mg	1.284	1.816	1.851	1.885	1.880	1.883
Al	—	—	—	—	—	—
Si	1.000	0.983	0.986	0.983	0.987	0.982
Ca	—	—	—	—	—	—
Ti	—	—	—	—	—	—
Cr	0.000	0.000	0.000	0.000	0.000	0.000
Mn	0.000	0.010	0.000	0.001	0.001	0.001
Fe	0.174	0.209	0.168	0.146	0.143	0.148
Ni	0.001	0.004	0.003	—	—	—
Total	2.998	3.014	3.009	3.015	3.011	3.015
Fe	88.0	89.5	91.5	92.8	92.9	92.7

\* FeO as Fe total

continued

Dun\* = dunite in pyroxenite

Dun\*\* = dunite in harzburgite



Appendix 3 (continued)

specimen	103	108	108	108	108
rock	Dun**	Dun	Dun	Dun	Dun
analysis	19	20	21	22	23
Na2O	nd	nd	nd	nd	nd
MgO	52.65	50.15	50.57	50.69	50.84
Al2O3	nd	nd	nd	nd	nd
SiO2	40.79	40.54	40.30	40.56	40.34
CaO	nd	nd	nd	nd	nd
TiO2	nd	nd	nd	nd	nd
Cr2O3	0.00	0.03	0.02	0.03	0.02
MnO	0.16	0.11	0.16	0.16	0.13
FeO*	7.09	9.03	9.21	9.37	9.69
NiO	nd	nd	nd	nd	nd
Total	100.69	99.86	100.25	100.81	101.02
Na	—	—	—	—	—
Mg	1.890	1.828	1.840	1.835	1.839
Al	—	—	—	—	—
Si	0.982	0.991	0.983	0.985	0.979
Ca	—	—	—	—	—
Ti	—	—	—	—	—
Cr	0.000	0.000	0.000	0.000	0.000
Mn	0.002	0.002	0.002	0.002	0.002
Fe	0.143	0.184	0.188	0.190	0.196
Ni	—	—	—	—	—
Total	3.017	3.004	3.013	3.012	3.017
Fo	93.0	90.9	90.7	90.6	90.4

\*FeO as Fe total

analysis 20–23 (specimen 108) = olivine from  
dunitic wall of a pyroxenite dike

Appendix 4: Microprobe analyses of pyroxenes

analysis	1	2	3	4	5	6
Na <sub>2</sub> O	0.00	0.04	0.07	0.04	0.06	0.00
MgO	34.62	35.45	35.55	35.26	35.21	34.67
Al <sub>2</sub> O <sub>3</sub>	0.36	0.48	0.77	0.74	0.86	0.59
SiO <sub>2</sub>	56.14	57.44	53.82	54.33	53.78	57.05
CaO	0.93	0.64	1.08	1.25	1.07	0.73
TiO <sub>2</sub>	0.03	0.01	0.03	0.02	0.02	0.03
Cr <sub>2</sub> O <sub>3</sub>	0.27	0.26	0.41	0.63	0.51	0.30
MnO	0.07	0.14	0.16	0.12	0.16	0.11
FeO*	5.33	5.57	7.23	7.11	6.97	5.72
NiO	0.04	0.11	0.11	0.16	0.12	nd
Total	97.80	100.15	99.22	99.65	98.75	99.20
tetrahedral	formulae based on 6 oxygens					
Aliv	0.014	0.019	0.031	0.030	0.035	0.023
Si	1.976	1.975	1.901	1.907	1.904	1.979
Total	1.990	1.994	1.932	1.937	1.939	2.000
octahedral						
AlM	0.000	0.000	0.000	0.000	0.000	0.002
Na	0.000	0.002	0.004	0.002	0.003	0.000
Mg	1.815	1.817	1.872	1.846	1.858	1.793
Ca	0.035	0.023	0.040	0.046	0.039	0.026
Ti	0.000	0.000	0.000	0.000	0.000	0.000
Cr	0.007	0.006	0.010	0.016	0.013	0.008
Mn	0.020	0.004	0.004	0.003	0.004	0.003
Fe	0.156	0.159	0.212	0.208	0.206	0.166
Ni	0.001	0.002	0.002	0.004	0.003	0.000
Total	2.034	2.013	2.144	2.125	2.126	1.998
Enstatite	89.2	90.3	87.3	86.9	87.4	89.7

\*FeO as Fe total

continued

analyses 1 - 2 (specimen 333) = orthopyroxene in harzburgite  
analyses 3 - 5 (specimen 156) = orthopyroxene in harzburgite  
analyses 6 - 7 (specimen 184) = orthopyroxene in harzburgite

App.4 continued

analysis	7	8	9	10	11	12
Na2O	0.00	0.04	0.04	0.09	0.00	0.00
MgO	34.94	35.43	34.54	35.46	34.39	35.16
Al2O3	0.88	0.40	0.58	0.53	0.39	0.28
SiO2	57.20	56.45	57.54	57.40	57.79	57.43
CaO	1.15	0.43	1.01	0.91	0.48	0.64
TiO2	0.00	0.00	0.03	0.00	0.00	0.00
Cr2O3	0.35	0.32	0.30	0.30	0.30	0.27
MnO	0.11	0.15	0.15	0.13	0.14	0.16
FeO*	5.91	5.67	5.76	5.64	6.25	6.43
NiO	nd	nd	nd	nd	nd	nd
Total	100.35	98.89	99.95	100.45	100.27	100.38
tetrahedral	formulae based on 6 oxygens					
Aliv	0.027	0.016	0.023	0.021	0.015	0.011
Si	1.967	1.967	1.983	1.969	1.985	1.975
Total	1.994	1.983	2.000	1.990	2.000	1.986
octahedral						
Alvi	0.000	0.000	0.006	0.000	0.000	0.000
Na	0.000	0.002	0.002	0.005	0.000	0.000
Mg	1.790	1.839	1.774	1.813	1.790	1.803
Ca	0.041	0.015	0.036	0.033	0.016	0.023
Ti	0.000	0.000	0.000	0.000	0.000	0.000
Cr	0.009	0.008	0.008	0.008	0.008	0.007
Mn	0.003	0.004	0.004	0.003	0.004	0.004
Fe	0.169	0.165	0.166	0.161	0.179	0.185
Ni	0.000					
Total	2.012	2.033	1.996	2.023	1.997	2.022
Enstatite	89.6	90.5	88.9	89.6	89.6	89.2

\* FeO as Fe total

continued

analyses 8 - 10 (specimen 175) = orthopyroxene in harzburgite  
fragment in mélange  
analyses 11 - 13 (specimen 108) = orthopyroxene in pyroxenite dike

App.4 continued

analysis	13	14	15	16	17	18
Na <sub>2</sub> O	0.06	0.93	0.00	0.11	0.10	0.00
MgO	35.12	22.16	15.67	16.23	16.63	16.73
Al <sub>2</sub> O <sub>3</sub>	0.33	1.92	2.11	2.03	1.77	2.05
SiO	57.65	56.16	53.81	54.06	54.42	53.54
K <sub>2</sub> O	0.00	0.00	0.01	0.00	0.00	0.00
CaO	0.62	11.59	23.19	22.72	23.15	22.39
TiO <sub>2</sub>	0.00	0.05	0.10	0.25	0.09	0.14
Cr <sub>2</sub> O <sub>3</sub>	0.31	0.44	0.56	0.45	0.52	0.62
MnO	0.11	0.13	0.11	0.16	0.06	0.09
FeO*	5.76	2.57	3.56	3.40	3.34	4.04
NiO	nd	0.11	0.09	0.04	0.05	0.00
total	99.96	96.14	99.23	99.45	100.11	99.61
formulae based on 6 oxygens						
Na	0.004	0.065	0.000	0.007	0.006	0.000
Mg	1.801	0.122	0.857	0.883	0.898	0.912
Al	0.000	1.200	0.090	0.086	0.075	0.088
Si	1.984	2.040	1.975	1.975	1.974	1.958
K	0.000	0.000	0.000	0.000	0.000	0.000
Ca	0.022	0.451	0.911	0.889	0.899	0.877
Ti	0.000	0.001	0.002	0.006	0.002	0.003
Cr	0.008	0.012	0.016	0.013	0.014	0.017
Mn	0.003	0.003	0.003	0.004	0.001	0.002
Fe	0.166	0.078	0.108	0.103	0.101	0.123
Ni	nd	0.002	0.002	0.001	0.001	0.000
total	2.004	1.934	3.964	3.967	3.972	3.980

\*FeO as Fe total

continued

analysis 14 (specimen 108) = clinopyroxene

analysis 15-17 (specimen 94-C) = clinopyroxene porphyroblast

analysis 18-20 (specimen 94-C) = clinopyroxene neoblast

App.4 (4) continued

analysis	19	20	21	22	23
Na <sub>2</sub> O	0.14	0.02	0.08	0.13	0.11
MgO	16.48	16.21	16.58	15.93	16.68
Al <sub>2</sub> O <sub>3</sub>	1.98	2.11	2.58	2.51	2.58
SiO	53.86	53.31	54.35	51.77	52.43
K <sub>2</sub> O	0.00	0.00	0.00	0.03	0.01
CaO	23.02	23.18	23.86	24.23	24.43
TiO <sub>2</sub>	0.13	0.09	0.16	0.11	0.23
Cr <sub>2</sub> O <sub>3</sub>	0.53	0.53	0.46	0.40	0.43
MnO	0.09	0.14	0.22	0.09	0.03
FeO*	3.83	3.72	4.04	4.00	3.61
NiO	0.00	0.00	0.00	0.00	0.00
total	100.05	99.30	102.33	99.18	100.62
formulae based on 6 oxygens					
Na	0.009	0.001	0.005	0.008	0.007
Mg	0.894	0.887	0.882	0.880	0.906
Al	0.084	0.090	0.108	0.108	0.110
Si	1.960	1.958	1.941	1.920	1.911
K	0.000	0.000	0.000	0.001	0.000
Ca	0.897	0.912	0.913	0.962	0.954
Ti	0.003	0.002	0.004	0.002	0.006
Cr	0.015	0.015	0.012	0.011	0.012
Mn	0.002	0.003	0.006	0.002	0.000
Fe	0.116	0.113	0.120	0.123	0.109
Ni	0.000	0.000	0.000	0.000	0.002
total	3.980	3.979	3.991	4.017	4.017

\*FeO as Fe total

continued

analysis 21 - 23 (specimen 404) = clinopyroxene porphyroclast  
in pyroxenite

App.4 continued

analysis	24	25	26	27	28	29
Na <sub>2</sub> O	0.14	0.00	0.03	0.00	0.02	0.08
MgO	16.86	17.03	17.02	16.92	17.46	17.35
Al <sub>2</sub> O <sub>3</sub>	1.05	1.38	0.88	1.04	0.96	1.07
SiO	53.93	53.43	54.21	52.49	51.66	52.34
K <sub>2</sub> O	0.00	0.02	0.00	0.00	0.01	0.02
CaO	24.27	23.68	24.37	25.10	24.91	24.29
TiO <sub>2</sub>	0.10	0.14	0.05	0.05	0.07	0.11
Cr <sub>2</sub> O <sub>3</sub>	0.55	0.43	0.46	0.32	0.27	0.37
MnO	0.04	0.13	0.10	0.11	0.07	0.09
FeO*	2.87	3.04	2.76	2.95	2.70	2.82
NiO	0.05	0.00	0.00	0.00	0.04	0.04
total	99.89	99.28	99.89	98.97	98.18	98.57
formulae based on 6 oxygens						
Na	0.009	0.000	0.002	0.000	0.001	0.005
Mg	0.917	0.931	0.924	0.933	0.972	0.960
Al	0.045	0.059	0.037	0.044	0.042	0.045
Si	1.970	1.960	1.976	1.943	1.929	1.944
K	0.000	0.000	0.000	0.000	0.000	0.000
Ca	0.950	0.930	0.952	0.995	0.996	0.966
Ti	0.002	0.003	0.001	0.001	0.001	0.002
Cr	0.015	0.012	0.013	0.008	0.007	0.011
Mn	0.001	0.003	0.002	0.003	0.001	0.002
Fe	0.086	0.092	0.083	0.091	0.083	0.087
Ni	0.001	0.000	0.000	0.000	0.001	0.000
total	3.997	3.989	3.990	4.019	4.032	4.023

\*FeO as Fe total

24-26 = (specimen 304) clinopyroxene porphyroclast  
in pyroxenite

27-29 = (specimen 304) clinopyroxene neoblast  
in pyroxenite

Appendix 5: Microprobe analyses of Cr-spinel in harzburgite

specimen	79-A core			144-A core		
analysis	wt %	corrected	cations	wt %	corrected	cations
		1			2	
MgO	12.06	12.06	0.557	9.52	9.52	0.460
Al <sub>2</sub> O <sub>3</sub>	23.02	23.02	0.841	14.98	14.98	0.572
TiO <sub>2</sub>	0.00	0.00	0.000	0.00	0.00	0.000
VO <sub>2</sub>	0.16			0.25		
Cr <sub>2</sub> O <sub>3</sub>	44.96	44.96	1.102	54.59	54.59	1.399
MnO	0.21	0.21	0.006	0.24	0.24	0.007
FeO*	19.03			20.71		
NiO	0.05			0.02		
Sum	99.50			100.32		
Fe <sub>2</sub> O <sub>3</sub>	0.00	2.42	0.056	0.00	1.16	0.028
FeO	19.03	16.85	0.437	20.71	19.67	0.533
Sum	99.28	99.52	3.000	100.04	100.16	3.000
endmember		mol %			mol %	
Sp	MgAl <sub>2</sub> O <sub>4</sub>	23.45			13.17	
MgChr	MgCr <sub>2</sub> O <sub>4</sub>	30.72			2.19	
Mgf	MgFe <sub>2</sub> O <sub>4</sub>	1.57			0.65	
Usp	FeTi <sub>2</sub> O <sub>4</sub>	0.00			0.00	
Her	FeAl <sub>2</sub> O <sub>4</sub>	18.38			15.26	
Chr	FeCr <sub>2</sub> O <sub>4</sub>	24.08			37.31	
Mt	FeFe <sub>2</sub> O <sub>4</sub>	1.23			0.75	
Cr100/ Cr + Al			56.71			70.97
Mg100/ Mg + Fe <sup>2+</sup>			56.06			46.32
Fe <sup>3+</sup> +100/Fe <sup>3+</sup> + Cr + Al			11.45			5.03

\*FeO as Fe total

continued

FeO as Fe<sub>2</sub>O<sub>3</sub> obtained assuming RO/R<sub>2</sub>O<sub>3</sub> ratio in chromian spinel is 1/1 (Irvine 19)

wt% = analyses with electron microprobe

corrected = calculated (Newpet program)

Sp = spinel

MgChr = magnesiochromite

Mgf = magnesioferrite

Usp = ulvospinel

Her = hercinite

Chr = chromite

Mt = magnetite



App.5 continued

=====						
specimen	175 core			175 margin		
	wt %	corrected	cations	wt %	corrected	cations
analysis	3			4		
-----						
MgO	8.40	8.40	0.425	7.85	7.85	0.396
Al2O3	8.33	8.33	0.333	8.67	8.67	0.346
TiO2	0.02	0.02	0.001	0.00	0.00	0.000
VO2	0.29			0.17		
Cr2O3	59.86	59.86	1.606	58.96	58.96	1.578
MnO	0.17	0.17	0.005	0.20	0.20	0.396
FeO*	22.24			23.82		
NiO	0.03			0.02		
Sum	99.36			99.70		
Fe2O3	0.00	2.36	0.060	0.00	2.99	0.076
FeO	22.24	22.12	0.571	23.82	21.13	0.598
Sum	99.02	99.26	3.000		99.80	3.000
endmember	mol %			mol %		
Sp	MgAl2O4	7.07			6.85	
MgChr	MgCr2O4	34.09			31.25	
Mgf	MgFe2O4	1.28			1.51	
Usp	FeTi2O4	0.03			0.00	
Her	FeAl2O4	9.50			10.34	
Chr	FeCr2O4	45.80			47.19	
Mt	FeFe2O4	1.72			2.28	
Cr100/						
Cr + Al			82.82			82.02
Mg100/						
Mg+Fe2+			42.67			39.84
Fe3+100/Fe3+						
Cr + Al			9.57			11.30

continued

App.5 continued

specimen	184		
	core		
	wt %	corrected	cations
analysis	5		
MgO	9.07	9.07	0.444
Al <sub>2</sub> O <sub>3</sub>	10.05	10.05	0.389
TiO <sub>2</sub>	0.00	0.00	0.000
VO <sub>2</sub>	0.24		
Cr <sub>2</sub> O <sub>3</sub>	60.40	60.40	1.568
MnO	0.21	0.21	0.008
FeO*	21.58		
NiO	0.04		
Sum	101.59		
Fe <sub>2</sub> O <sub>3</sub>	0.00	1.72	0.043
FeO	21.58	20.03	0.550
Sum	101.31	101.48	3.000

	mol %	
Sp	MgAl <sub>2</sub> O <sub>4</sub>	8.64
MgChr	MgCr <sub>2</sub> O <sub>4</sub>	34.82
Mgf	MgFe <sub>2</sub> O <sub>4</sub>	0.95
Usp	FeTi <sub>2</sub> O <sub>4</sub>	0.00
Her	FeAl <sub>2</sub> O <sub>4</sub>	10.70
Chr	FeCr <sub>2</sub> O <sub>4</sub>	43.14
Mt	FeFe <sub>2</sub> O <sub>4</sub>	1.17
Cr100/ Cr + Al		80.13
Mg100/ Mg + Fe <sup>2+</sup>		44.67
Fe <sup>3+</sup> 100/Fe <sup>3+</sup> + Cr + Al		7.19

Sp = spinel	Her = hercinite
MgChr = magnesiochromite	Chr = chromite
Mgf = magnesioferite	Mt = magnetite
Usp = ulvospinel	

Appendix 6: Microprobe analyses of Cr-spinel in dunite

specimen	94-B			251-A		
	wt %	corrected	cations	ox wt%	corrected	cations
analyses		1			2	
MgO	2.98	2.98	0.155	6.88	6.88	0.354
Al <sub>2</sub> O <sub>3</sub>	7.13	7.13	0.293	4.39	4.39	0.178
TiO <sub>2</sub>	0.16	0.16	0.004	0.04	0.00	0.001
VO <sub>2</sub>	0.30			0.11		
Cr <sub>2</sub> O <sub>3</sub>	40.43	40.43	1.116	60.43	60.43	1.647
MnO	0.60	0.60	0.018	0.29	0.29	0.008
FeO*	48.45			28.14		
NiO	0.60			0.03		
Sum	100.11			100.30		
Fe <sub>2</sub> O <sub>3</sub>	0.00	0.58	0.583	0.00	6.64	0.172
FeO	48.45	0.83	0.831	28.14	22.16	0.639
Sum		101.97	3.000		100.84	3.000
		mol %			mol %	
Sp	MgAl <sub>2</sub> O <sub>4</sub>	2.26			3.15	
MgChr	MgCr <sub>2</sub> O <sub>4</sub>	8.61			29.09	
Mgf	MgFe <sub>2</sub> O <sub>4</sub>	4.50			3.04	
Usp	FeTi <sub>2</sub> O <sub>4</sub>	0.35			0.07	
Her	FeAl <sub>2</sub> O <sub>4</sub>	12.14			5.69	
Chr	FeCr <sub>2</sub> O <sub>4</sub>	45.18			52.57	
Mt	FeFe <sub>2</sub> O <sub>4</sub>	24.12			5.50	

Cr100/(Cr+Al)	79.18	90.23
Mg100/(Mg+Fe <sup>2+</sup> )	15.72	35.62
Fe <sup>3+</sup> 100/(Fe <sup>3+</sup> +Cr+Al)	20.60	8.61

\*FeO as Fe total

continued

FeO and Fe<sub>2</sub>O<sub>3</sub> obtained assuming RO/R<sub>2</sub>O<sub>3</sub> ratio in spinel  
is 1/1 (Irvine, 1965)

wt % = analyzed with electron microprobe

corrected = recalculated by Newpet program

Sp = spinel

MgChr = magnesiochromite

Mgf = magnesianferite

Usp = ulvospinel

Her = hercynite

Chr = chromite

Mt = magnetite

App. 6 continued

specimen		251-B	
	wt %	corrected	cations
analysis	3		
MgO	4.63	4.63	0.243
Al2O3	4.38	4.38	0.182
TiO2	0.05	0.05	0.001
VO2	0.19		
Cr2O3	57.22	57.22	1.591
MnO	0.41	4.63	0.012
FeO*	33.02		
NiO	0.03		
Sum	99.93		
Fe2O3	0.00	8.49	0.225
FeO	33.02	25.38	0.746
Sum		100.56	3.000
		mol %	
Sp	MgAl2O4	2.20	
MgChr	MgCr2O4	19.28	
Mgf	MgFe2O4	2.72	
Usp	FeTi2O4	0.10	
Her	FeAl2O4	6.77	
Chr	FeCr2O4	59.30	
Mt	FeFe2O4	8.38	
Cr100/(Cr + Al)			89.76
Mg100/(Mg + Fe2+)			24.54
Fe3+100/(Fe3+ + Cr + Al)			11.28

\*FeO as Fe total

continued

App.6 continued

specimen	305			389		
analysis	wt %	corrected 4	cations	wt %	corrected 5	cations
MgO	4.68	4.68	0.246	7.33	7.33	0.364
Al <sub>2</sub> O <sub>3</sub>	2.14	2.14	0.089	13.52	13.52	0.530
TiO <sub>2</sub>	0.02	0.02	0.001	0.16	0.16	0.004
VO <sub>2</sub>	0.18			0.27		
Cr <sub>2</sub> O <sub>3</sub>	59.37	59.37	1.653	42.85	42.85	1.128
MnO	0.43	0.43	0.013	0.21	0.21	0.006
FeO*	33.91			34.78		
NiO	0.07			0.07		
Sum	100.79			99.20		
Fe <sub>2</sub> O <sub>3</sub>	0.00	9.69	0.257	0.00	13.33	0.334
FeO	33.91	25.19	0.742	34.78	22.79	0.634
Sum		101.52	3.000			

		mol %	mol %
Sp	MgAl <sub>2</sub> O <sub>4</sub>	1.09	9.61
MgChr	MgCr <sub>2</sub> O <sub>4</sub>	20.30	20.43
Mgf	MgFe <sub>2</sub> O <sub>4</sub>	3.15	6.05
Usp	FeTi <sub>2</sub> O <sub>4</sub>	0.04	0.25
Her	FeAl <sub>2</sub> O <sub>4</sub>	3.29	16.76
Chr	FeCr <sub>2</sub> O <sub>4</sub>	61.30	35.63
Mt	FeFe <sub>2</sub> O <sub>4</sub>	9.52	10.55

Cr100/(Cr+Al)	94.90	68.01
Mg100/(Mg+Fe <sup>2+</sup> )	24.88	36.44
Fe <sup>3+</sup> +100/(Fe <sup>3+</sup> +Cr+Al)	12.85	16.76

\*FeO as Fe total

FeO and Fe<sub>2</sub>O<sub>3</sub> obtained assuming RO/R<sub>2</sub>O<sub>3</sub> ratio in spinel

wt % = analyzed with electron microprobe

corrected = recalculated by Newpet program

Sp = spinel

MgChr = magnesiochromite

Mgf = magnesioferite

Usp = ulvospinel

Her = hercinite

Chr = chromite

Mt = magnetite

Appendix 7: Microprobe analysis of Cr-spinel in pyroxenite

specimen	94-C			251-D		
	corrected	cations	wt %	corrected	cations	
analysis	1			2		
MgO	8.22	8.22	0.381	5.98	5.98	0.296
Al <sub>2</sub> O <sub>3</sub>	28.93	28.93	1.060	17.30	17.30	0.678
TiO <sub>2</sub>	0.17	0.17	0.004	0.10	0.10	0.002
VO <sub>2</sub>	0.32			0.40		
Cr <sub>2</sub> O <sub>3</sub>	28.59	28.59	0.703	40.70	40.70	1.070
MnO	0.54	0.54	0.381	0.30	0.30	0.008
FeO*	32.22			34.02		
NiO	0.05			0.04		
Sum	99.04			98.84		
Fe <sub>2</sub> O <sub>3</sub>	0.00	9.79	0.229	0.00	9.91	0.248
FeO	32.22	23.41	0.609	34.02	25.10	0.698
Sum		99.65	3.000		99.39	3.000

spinel		mol %	mol %
Sp	MgAl <sub>2</sub> O <sub>4</sub>	20.12	10.01
MgChr	MgCr <sub>2</sub> O <sub>4</sub>	13.34	15.80
Mgf	MgFe <sub>2</sub> O <sub>4</sub>	4.35	3.66
Usp	FeTi <sub>2</sub> O <sub>4</sub>	0.24	0.17
Her	FeAl <sub>2</sub> O <sub>4</sub>	32.14	23.58
Chr	FeCr <sub>2</sub> O <sub>4</sub>	21.31	37.22
Mt	FeFe <sub>2</sub> O <sub>4</sub>	6.94	8.62

Cr <sub>100</sub> /(Cr + Al)	39.87	61.21
Mg <sub>100</sub> /(Mg + Fe <sub>2</sub> +)	38.50	29.81
Fe <sub>3</sub> +100/(Fe <sub>3</sub> + + Cr + Al)	11.49	12.42

\*FeO as Fe total

FeO and Fe<sub>2</sub>O<sub>3</sub> obtained assuming RO/R<sub>2</sub>O<sub>3</sub> ratio in spinel is 1/1 (Irvine, 1965)

continued

wt % = analyses with electron microprobe

corrected = recalculated with Newpet program

Sp = spinel

MgChr = magnesiochromite

Mgf = magnesioferrite

Usp = ulvo-spinel

Her = hercynite

Chr = Chromite

Mt = magnetite

App. 7 continued

specimen	289-A		
	wt %	corrected	cations
analysis	3		
-----			
MgO	3.61	3.61	0.181
Al2O3	11.74	11.74	0.466
TiO2	0.10	0.10	0.003
VO2	0.56		
Cr2O3	38.07	38.07	1.013
MnO	0.36	0.36	0.010
FeO*	47.12		
NiO	0.03		
Sum	101.59		
Fe2O3	0.00	20.35	0.516
FeO	47.12	28.81	0.811
Sum		103.84	3.000
spinel	mol %		
Sp	MgAl2O4	4.21	
MgChr	MgCr2O4	9.16	
Mgf	MgFe2O4	4.66	
Usp	FeTi2O4	0.20	
Her	FeAl2O4	18.84	
Chr	FeCr2O4	40.99	
Mt	FeFe2O4	20.88	

Cr100/(Cr+Al) 68.51

Mg100/(Mg+Fe<sup>2+</sup>) 16.26

Fe<sup>3+</sup>100/(Fe<sup>3+</sup>+Cr+Al) 25.86

Cr+Al

-----

\*FeO as Fe total

FeO and Fe<sub>2</sub>O<sub>3</sub> obtained assuming RO/R<sub>2</sub>O<sub>3</sub> ratio in spinel  
is 1/1 (Irvine, 1965)

wt % = analyses with electron microprobe

corrected = recalculated with Newpet program

Sp = spinel

MgChr = magnesiochromite

Mgf = magnesioferrite

Usp = ulvöspinel

Her = hercynite

Chr = chromite

Mt = magnetite



Appendix 8: Microprobe analysis of Cr-spinel  
in mélange assemblages

specimen rock	wt %	255-B Sch Sp corrected	cations
analysis		1	
MgO	4.95	4.95	0.256
Al <sub>2</sub> O <sub>3</sub>	5.38	5.38	0.220
TiO <sub>2</sub>	0.02	0.02	0.001
VO <sub>2</sub>	0.23		
Cr <sub>2</sub> O <sub>3</sub>	55.70	55.70	1.525
MnO	0.43	0.43	0.430
FeO*	34.05		
NiO	0.04		
Sum	100.79		
Fe <sub>2</sub> O <sub>3</sub>	0.00	9.74	0.254
FeO	34.05	25.28	0.732
Sum		101.51	3.000

		mol %
Sp	MgAl <sub>2</sub> O <sub>4</sub>	2.81
MgChr	MgCr <sub>2</sub> O <sub>4</sub>	19.48
Mgf	MgFe <sub>2</sub> O <sub>4</sub>	3.24
Usp	FeTi <sub>2</sub> O <sub>4</sub>	0.04
Her	FeAl <sub>2</sub> O <sub>4</sub>	8.04
Chr	FeCr <sub>2</sub> O <sub>4</sub>	55.82
Mt	FeFe <sub>2</sub> O <sub>4</sub>	9.30

Cr100/(Cr+Al) 87.41

Mg100/(Mg+Fe<sup>2+</sup>) 25.87

Fe<sup>3+</sup>100/(Fe<sup>3+</sup>+Cr+Al) 12.70

Sch Sp = schistose serpentinite

continued

\*FeO as Fe total

FeO and Fe<sub>2</sub>O<sub>3</sub> obtained assuming RO/R<sub>2</sub>O<sub>3</sub> ratio  
in spinel is 1/1 (Irvine, 1985)

wt % = analysed by electron microprobe

corrected = recalculated by Newpet program

T-M = talc-magnesite

Q-M = quartz-magnesite

Sp = spinel

MgChr = magnesiochromite

Mgf = magnesioferrite

Usp = ulvospinel

Her = hercinite

Chr = chromite

Mt = magnetite

App.8 continued

specimen rock	177-C T-M			160 T-M		
	wt %	corrected 2	cations	wt %	corrected 3	cations
analysis						
MgO	4.66	4.66	0.245	9.00	9.00	0.434
Al <sub>2</sub> O <sub>3</sub>	3.41	3.41	0.142	17.01	17.01	0.649
TiO <sub>2</sub>	0.14	0.14	0.004	0.00	0.00	0.000
VO <sub>2</sub>	0.20			0.20		
Cr <sub>2</sub> O <sub>3</sub>	54.27	54.27	1.512	51.83	51.83	1.326
MnO	0.32	0.32	0.010	0.25	0.25	0.007
FeO*	36.95			21.57		
NiO	0.03			0.04		
Sum	99.98			99.92		
Fe <sub>2</sub> O <sub>3</sub>	0.00	12.80	0.339	0.00	1.02	0.025
FeO	36.95	25.43	0.749	21.57	20.65	0.559
Sum		101.03	3.000		99.76	3.000

		mol %	mol %
Sp	MgAl <sub>2</sub> O <sub>4</sub>	1.73	14.09
MgChr	MgCr <sub>2</sub> O <sub>4</sub>	18.43	28.80
Mgf	MiFe <sub>2</sub> O <sub>4</sub>	4.14	0.54
Usp	FeTi <sub>2</sub> O <sub>4</sub>	0.28	0.00
Her	FeAl <sub>2</sub> O <sub>4</sub>	5.29	18.13
Chr	FeCr <sub>2</sub> O <sub>4</sub>	56.43	37.06
Mt	FeFe <sub>2</sub> O <sub>4</sub>	12.67	0.70

Cr <sub>100</sub> /(Cr+Al)	91.44	67.15
Mg <sub>100</sub> /(Mg+Fe <sub>2</sub> +) )	24.62	43.72
Fe <sub>3</sub> +100/(Fe <sub>3</sub> + +Cr+Al)	17.01	1.25

Sch Sp = schistose serpentinite

continued

App. 8 continued

specimen rock	142-A			85-B		
	Q-M			Q-M		
analyses	wt %	corrected 5	cations	wt %	corrected 6	cations
MgO	9.02	9.02	0.451	8.57	8.57	0.444
Al <sub>2</sub> O <sub>3</sub>	10.52	10.52	0.416	4.96	4.96	0.199
TiO <sub>2</sub>	0.02	0.02	0.001	0.02	0.02	0.001
VO <sub>2</sub>	0.20			0.15		
Cr <sub>2</sub> O <sub>3</sub>	57.11	57.11	1.515	63.96	63.96	1.717
MnO	0.23	0.23	0.007	0.23	0.23	0.007
FeO*	21.75			22.28		
NiO	0.03			0.03		
Sum	98.87			100.18		
Fe <sub>2</sub> O <sub>3</sub>	0.00	2.68	0.068	0.00	3.25	0.083
FeO	21.75	19.34	0.543	22.28	19.36	0.550
Sum		98.92	3.000		100.55	3.000
			mol %			
Sp	MgAl <sub>2</sub> O <sub>4</sub>	9.38			4.41	
MgChr	MgCr <sub>2</sub> O <sub>4</sub>	34.17			38.11	
Mgf	MfFe <sub>2</sub> O <sub>4</sub>	1.53			1.84	
Usp	FeTi <sub>2</sub> O <sub>4</sub>	0.03			0.03	
Her	FeAl <sub>2</sub> O <sub>4</sub>	11.28			5.46	
Chr	FeCr <sub>2</sub> O <sub>4</sub>	41.10			47.19	
Mt	FeFe <sub>2</sub> O <sub>4</sub>	1.84			2.28	
Cr100/(Cr+Al)			78.46	89.84		
Mg100/(Mg+Fe <sup>2+</sup> )			45.40	44.68		
Fe <sup>3+</sup> +100/(Fe <sup>3+</sup> +Cr+Al)			3.81	4.15		

Appendix 8: Microprobe analyses of serpentine

analysis	1	2	3	4	5	6	7
	rim	rim	rim	core	core	core	rim
Na <sub>2</sub> O	0.00	0.02	0.00	0.00	0.04	0.05	0.00
MgO	39.23	40.00	39.38	39.52	40.64	39.91	40.45
Al <sub>2</sub> O <sub>3</sub>	0.20	0.20	0.02	0.00	0.05	0.00	0.14
SiO	40.76	41.02	41.85	41.48	43.81	40.02	40.91
K <sub>2</sub> O	0.00	0.01	0.00	0.00	0.00	0.01	0.01
CaO	0.02	0.01	0.01	0.02	0.02	0.00	0.04
TiO	0.00	0.00	0.04	0.00	0.00	0.03	0.03
Cr <sub>2</sub> O <sub>3</sub>	0.02	0.03	0.00	0.03	0.04	0.00	0.00
MnO	0.01	0.04	0.04	0.00	0.08	0.04	0.02
FeO*	5.98	4.71	4.46	4.37	2.32	4.00	5.46
NiO	0.24	0.40	0.35	0.29	0.27	0.35	0.16
total	86.29	86.24	86.16	85.68	87.03	85.21	87.21
H <sub>2</sub> O+**	13.71	13.76	13.84	14.32	12.97	14.79	12.79
number of ions on the basis of 14 oxygens							
Na	0.000	0.000	0.000	0.000	0.005	0.005	0.000
Mg	5.637	5.717	5.805	5.656	5.647	5.745	5.735
Al	0.000	0.000	0.000	0.000	0.005	0.000	0.014
Si	3.929	3.934	3.995	3.981	4.065	3.943	3.892
K	0.000	0.000	0.000	0.000	0.000	0.000	0.000
Ca	0.000	0.000	0.000	0.000	0.000	0.000	0.000
Ti	0.000	0.000	0.000	0.000	0.000	0.000	0.000
Cr	0.000	0.000	0.000	0.000	0.000	0.000	0.000
Mn	0.000	0.000	0.000	0.000	0.000	0.000	0.000
Fe	0.481	3.780	0.355	0.350	0.182	0.317	0.429
Ni	0.014	0.028	0.023	0.187	0.019	0.023	0.009
total	10.061	10.057	9.982	9.982	9.921	10.038	10.085

\* FeO as Fe total

continued

\*\*H<sub>2</sub>O+ calculated by difference

analysis 1 - 3 (specimen 432-D) = lizardite mesh rim  
 analysis 4 - 6 (specimen 432-D) = lizardite mesh center  
 analysis 7 - 8 (specimen 450-C) = lizardite mesh rim

App. 9 continued

	8	9	10	11	12	13	14
	rim	core	core				rim
Na <sub>2</sub> O	0.00	0.04	0.00	0.07	0.00	0.08	0.02
MgO	39.74	39.05	39.58	38.94	37.88	39.14	38.46
Al <sub>2</sub> O <sub>3</sub>	0.14	0.46	0.01	0.02	0.05	0.07	0.12
SiO	40.52	41.71	42.79	43.77	43.14	43.16	44.33
K <sub>2</sub> O	0.01	0.00	0.00	0.01	0.02	0.00	0.00
CaO	0.02	0.04	0.04	0.04	0.00	0.02	0.01
TiO	0.01	0.02	0.00	0.00	0.01	0.02	0.00
Cr <sub>2</sub> O <sub>3</sub>	0.02	0.23	0.01	0.02	0.05	0.03	0.04
MnO	0.02	0.05	0.00	0.01	0.14	0.06	0.14
FeO*	5.90	4.98	7.79	4.98	4.70	4.13	4.54
NiO	0.17	0.14	0.14	0.02	0.19	0.21	0.31
total	86.54	86.72	87.44	88.09	86.18	86.92	87.96
H <sub>2</sub> O+ **	13.46	13.28	12.56	11.91	13.82	13.08	12.04
number of ions on the basis of 14 oxygens							
Na	0.000	0.005	0.000	0.010	0.000	0.014	0.002
Mg	5.893	5.539	5.544	5.412	5.372	5.496	5.338
Al	0.014	0.051	0.005	0.000	0.004	0.004	0.010
Si	3.892	3.967	4.023	4.082	4.104	4.086	4.126
K	0.000	0.000	0.000	0.000	0.000	0.000	0.000
Ca	0.000	0.000	0.000	0.002	0.000	0.000	0.000
Ti	0.000	0.000	0.000	0.000	0.000	0.000	0.000
Cr	0.000	0.014	0.000	0.000	0.002	0.002	0.000
Mn	0.000	0.000	0.000	0.008	0.010	0.024	0.008
Fe	0.471	0.392	0.573	0.386	0.372	0.314	0.352
Ni	0.009	0.005	0.005	0.010	0.014	0.006	0.003
total	10.080	9.977	9.954	9.912	9.878	9.918	9.856

\*FeO as Fe total

\*\*H<sub>2</sub>O+ calculated by difference

continued

analysis 9 - 10 (specimen 450-C) = lizardite mesh center

analysis 11-13(specimen 203-B) = lizardite;banded growth texture

analysis 14-16(specimen 203-B) = rim,lizardite;gamma mesh texture

App. 9 continued

	15	16	17	18	19	20	21
	rim	rim	core	core	core	rim	rim
Na <sub>2</sub> O	0.06	0.03	0.01	0.07	0.05	0.00	0.09
MgO	39.49	38.47	38.89	37.88	38.28	40.54	40.53
Al <sub>2</sub> O <sub>3</sub>	0.08	0.13	0.12	0.08	0.07	0.02	0.02
SiO	44.06	44.48	44.37	44.32	44.01	42.69	42.32
K <sub>2</sub> O	0.00	0.01	0.00	0.01	0.01	0.00	0.00
CaO	0.04	0.00	0.00	0.00	0.04	0.02	0.02
TiO	0.00	0.00	0.00	0.00	0.00	0.00	0.00
Cr <sub>2</sub> O <sub>3</sub>	0.01	0.04	0.02	0.05	0.05	0.00	0.01
MnO	0.11	0.01	0.11	0.11	0.13	0.02	0.08
FeO*	4.69	4.19	4.84	4.30	4.56	1.92	1.97
NiO	0.12	0.26	0.43	0.19	0.15	0.03	0.12
total	88.66	87.71	88.70	87.10	87.34	85.23	85.16
H <sub>2</sub> O+**	11.34	12.29	11.30	12.90	12.68	14.77	14.84
number of ions on the basis of 14 oxygens							
Na	0.008	0.002	0.016	0.010	0.080	nd	nd
Mg	5.440	5.334	5.384	5.292	5.344	nd	nd
Al	0.008	0.012	0.010	0.008	0.004	nd	nd
Si	4.070	4.138	4.104	4.154	4.124	nd	nd
K	0.000	0.000	0.000	0.000	0.000	nd	nd
Ca	0.002	0.000	0.000	0.000	0.002	nd	nd
Ti	0.000	0.000	0.000	0.000	0.000	nd	nd
Cr	0.000	0.002	0.000	0.002	0.002	nd	nd
Mn	0.008	0.004	0.080	0.008	0.008	nd	nd
Fe	0.360	0.324	0.358	0.340	0.035	nd	nd
Ni	0.008	0.018	0.030	0.014	0.010	nd	nd
total	9.904	9.834	9.890	9.828	9.858	nd	nd

\* FeO as Fe total

continued

\*\*H<sub>2</sub>O+ calculated by difference

analysis 17-19(specimen 203-B) = center, liz. gamma mesh texture

analysis 20-21 (specimen 196-C) = rim, liz. hourglass texture

App.9 (4) continued

	22	23	24	25	26	27	28
	core	core					
Na2O	0.00	0.03	0.00	0.05	0.03	0.00	0.00
MgO	39.74	39.76	40.33	40.54	39.63	41.06	41.15
Al2O3	0.00	0.02	0.26	0.29	0.17	0.00	0.00
SiO	41.32	41.07	44.45	45.41	44.45	42.87	42.34
K2O	0.00	0.01	0.01	0.01	0.01		0.02
CaO	0.00	0.04	0.00	0.32	0.00		0.00
TiO	0.04	0.03	0.04	0.01	0.03		0.00
Cr2O3	0.00	0.02	0.05	0.05	0.04	0.00	0.02
MnO	0.11	0.10	0.00	0.00	0.04	0.08	0.02
FeO*	2.15	2.47	2.52	2.49	2.41	1.55	1.64
NiO	0.04	0.54	0.08	0.18	0.20	0.02	0.03
total	83.39	84.08	87.74	89.05	87.02	85.59	85.22
H2O+ **	16.61	15.92	12.26	10.95	12.98	11.41	14.78
number of ions on the basis of 14 oxygens							
Na	nd	nd	0.000	0.005	0.005	0.000	0.000
Mg	nd	nd	5.544	5.483	5.493	7.695	7.765
Al	nd	nd	0.023	0.028	0.014	0.000	0.000
Si	nd	nd	4.097	4.121	4.130	5.395	5.357
K	nd	nd	0.000	0.000	0.000	0.000	0.000
Ca	nd	nd	0.000	0.000	0.000	0.000	0.000
Ti	nd	nd	0.000	0.000	0.000	0.000	0.000
Cr	nd	nd	0.000	0.000	0.000	0.000	0.000
Mn	nd	nd	0.000	0.000	0.000	0.005	0.000
Fe	nd	nd	0.191	0.191	0.187	0.163	0.173
Ni	nd	nd	0.005	0.009	0.009	0.000	0.000
total	nd	nd	9.865	9.837	9.842	13.258	13.295

\* FeO as Fe total

\*\*H2O+ calculated by difference

continued

analysis 22-23 (specimen 196-C) = center, lizardite hourglass

analysis 24-26 (specimen 450-C) = fibrous chrysotile

analysis 27-29 (specimen 196-C) = fibrous chrysotile



App. 9 continued

	29	30	31	32	33	34	35
Na <sub>2</sub> O	0.02	0.00	0.05	0.00	0.05	0.00	0.04
MgO	40.91	37.93	39.39	38.94	40.52	40.20	40.54
Al <sub>2</sub> O <sub>3</sub>	0.04	0.51	0.45	0.55	0.07	0.10	0.12
SiO	42.62	41.32	43.17	41.74	41.17	41.57	41.54
K <sub>2</sub> O	0.00	0.02	0.00	0.01	0.01	0.02	0.00
CaO	0.00	0.02	0.02	0.04	0.02	0.00	0.05
TiO	0.01	0.00	0.00	0.00	0.00	0.00	0.00
Cr <sub>2</sub> O <sub>3</sub>	0.04	0.43	0.57	0.56	0.43	0.46	0.46
MnO	0.03	0.00	0.00	0.09	0.16	0.09	0.10
FeO*	1.80	4.43	3.58	4.07	1.00	1.17	1.20
NiO	0.06	0.01	0.15	0.07	0.08	0.07	0.00
total	85.53	84.83	87.38	86.08	83.59	83.70	84.04
H <sub>2</sub> O+**	14.470	15.170	12.620	13.920	16.410	16.300	15.960

number of ions on the basis of 14 oxygens

Na	0.000	0.000	0.005	0.000	0.000	0.000	0.004
Mg	5.772	5.215	5.488	5.539	5.772	5.786	5.817
Al	0.000	0.056	0.047	0.058	0.000	0.011	0.011
Si	4.032	4.004	4.032	3.981	4.032	4.015	3.997
K	0.000	0.000	0.000	0.000	0.000	0.000	0.000
Ca	0.000	0.000	0.000	0.000	0.000	0.000	0.000
Ti	0.000	0.000	0.000	0.000	0.000	0.000	0.000
Cr	0.000	0.028	0.042	0.042	0.000	0.032	0.000
Mn	0.000	0.000	0.000	0.005	0.000	0.004	0.004
Fe	0.140	0.359	0.275	0.322	0.140	0.091	0.095
Ni	0.000	0.009	0.009	0.000	0.000	0.004	0.000
total	9.951	9.935	9.898	9.945	9.951	9.947	9.965

analysis 30-32 (specimen 450-C) = lizardite, orthopyroxene bastite

analysis 33-35 (specimen 313) = lizardite, orthopyroxene bastite

continued

App. 9 continued

	36	37	38	39	40	41
Na <sub>2</sub> O	0.02	0.00	0.00	0.00	0.00	0.00
MgO	39.77	39.46	39.36	38.46	37.79	39.80
Al <sub>2</sub> O <sub>3</sub>	0.12	0.26	0.21	0.77	1.68	0.50
SiO	45.83	45.93	45.44	42.93	41.60	46.32
K <sub>2</sub> O	0.02	0.00	0.00	0.00	0.00	0.00
CaO	0.01	0.01	0.00	0.02	0.01	0.10
TiO	0.03	0.00	0.00	0.02	0.02	0.00
Cr <sub>2</sub> O <sub>3</sub>	0.00	0.00	0.00	0.22	0.44	0.00
MnO	0.05	0.09	0.00	0.00	0.09	0.05
FeO*	3.30	3.03	2.22	3.76	3.31	3.13
NiO	0.10	0.21	0.11	0.18	0.14	0.19
total	89.25	89.00	87.43	86.36	88.07	90.01
H <sub>2</sub> O + **	10.75	11.00	12.57	13.64	11.93	9.99

number of ions on the basis of 14 oxygens

Na	0.020	0.000	0.002	0.000	0.000	0.000
Mg	5.386	5.348	5.408	5.418	5.186	5.332
Al	0.010	0.026	0.022	0.084	0.180	0.052
Si	4.166	4.176	4.188	4.055	4.108	4.164
K	0.000	0.000	0.000	0.000	0.000	0.000
Ca	0.000	0.000	0.000	0.000	0.000	0.000
Ti	0.000	0.000	0.000	0.000	0.000	0.000
Cr	0.000	0.000	0.000	0.014	0.030	0.000
Mn	0.002	0.040	0.000	0.000	0.004	0.002
Fe	0.250	0.230	0.170	0.294	0.254	0.234
Ni	0.004	0.012	0.004	0.009	0.008	0.012
total	9.822	9.798	9.792	9.875	9.770	9.796

analysis 36-38 (specimen 203-B) = interpenetrating antigorite

analysis 39-41 (specimen 450-C) = interpenetrating antigorite  
continued

App. 9 continued

	42	43	44	45	46
Na2O	0.09	0.04	0.07	0.00	0.07
MgO	66.63	69.90	29.46	30.88	29.82
Al2O3	0.01	0.00	0.07	0.02	0.02
SiO	3.68	0.05	62.54	62.13	62.31
K2O	0.05	0.00	0.00	0.00	0.01
CaO	0.02	0.02	0.02	0.00	0.00
TiO	0.00	0.00	0.01	0.00	0.02
Cr2O3	0.00	0.00	0.01	0.04	0.04
MnO	0.56	0.69	0.00	0.00	0.00
FeO*	3.05	2.66	1.66	1.84	1.64
NiO	0.08	0.06	0.03	0.06	0.06
total	74.15	73.42	93.88	94.97	93.99

42 and 43 = ions based on 1 oxygen

44 to 46 = ions based on 22 oxygens

Na	0.002	0.001	0.011	0.000	0.011
Mg	1.205	1.295	5.660	5.885	5.731
Al	0.000	0.000	0.006	0.000	0.000
Si	0.044	0.000	8.063	7.942	8.030
K	0.001	0.000	0.000	0.000	0.000
Ca	0.000	0.000	0.000	0.000	0.000
Ti	0.000	0.000	0.000	0.000	0.000
Cr	0.000	0.000	0.000	0.000	0.000
Mn	0.006	0.007	0.000	0.000	0.000
Fe	0.031	0.027	0.176	0.193	0.171
Ni	0.001	0.000	0.000	0.000	0.000
total	1.288	1.331	13.921	14.025	13.954

analysis 42-43 (specimen 313) = brucite

analysis 44-46 (specimen 256-A) = talc

Appendix 10: Microprobe analyses of magnesite  
from serpentinite

specimen	94-B	94-B	94-B	94-B	343-D	343-D	343-D
serp.host	A	A	A	A	A	A	A
mean of analysis	1	2	3	3	4	5	6
SiO <sub>2</sub>	1.14	1.35	1.77	1.42	2.16	2.21	1.72
MgO	35.66	34.45	35.00	35.04	36.68	38.00	36.41
CaO	0.18	0.30	0.31	0.27	0.18	0.17	0.18
FeO*	13.98	14.11	14.74	14.27	9.71	9.17	11.88
total	50.96	50.20	51.82	51.00	48.72	49.55	50.19
Si	0.016	0.020	0.025	0.021	0.033	0.033	0.025
Mg	0.790	0.776	0.763	0.776	0.810	0.849	0.800
Ca	0.002	0.004	0.004	0.004	0.002	0.002	0.002
Fe	0.173	0.178	0.180	0.177	0.124	0.115	0.146
total	0.982	0.978	0.973	0.978	1.033	1.034	0.974
Mg**	0.815	0.805	0.800	0.806	0.866	0.875	0.840
Ca	0.002	0.004	0.004	0.004	0.002	0.002	0.002
Fe	0.183	0.191	0.196	0.190	0.132	0.123	0.158
total	1.000	1.000	1.000	1.000	1.000	1.000	1.000
MgCO <sub>3</sub>	81.5	80.5	80.0	80.6	86.6	87.5	84.0
CaCO <sub>3</sub>	0.2	0.4	0.4	0.4	0.2	0.2	0.2
FeCO <sub>3</sub>	18.3	19.1	19.6	19.0	13.2	12.3	15.8

\* FeO as Fe total

continued

\*\* column of normalized mole fractions after removal of serpentine

A = antigorite

analysis 1-3 (specimen 94-B) = magnesite-antigorite assemblage

analysis 4-6 (specimen 343-D) = magnesite-antigorite assemblage

App. 10 continued

specimen	343-D	343-B	343-B	343-B	343-B	432-D	432-D
rock type	L	L	L	L	L	L	L
mean of analysis	4-6	7	8	9	7-9	10	11
SiO <sub>2</sub>	2.03	1.82	4.54	9.29	5.22	1.83	2.83
MgO	37.03	39.50	39.64	39.48	39.54	41.39	42.30
CaO	0.18	0.05	0.04	0.00	0.03	0.07	0.04
FeO*	10.25	0.95	1.92	1.26	1.38	0.89	1.03
total	49.49	42.33	46.14	50.02	46.16	44.46	46.49
Si	0.030	0.030	0.070	0.134	0.102	0.028	0.042
Mg	0.830	0.957	0.905	0.850	0.878	0.959	0.944
Ca	0.002	0.001	0.001	0.000	0.000	0.001	0.001
Fe	0.128	0.013	0.025	0.015	0.020	0.012	0.013
total	1.014	1.030	1.070	1.134	1.102	1.028	1.042
Mg**	0.861	0.972	0.963	0.984	0.972	0.974	0.975
Ca	0.002	0.017	0.015	0.013	0.014	0.016	0.015
Fe	0.137	0.011	0.022	0.003	0.014	0.010	0.010
total	1.000	1.000	1.000	1.000	1.000	1.000	1.000
MgCO <sub>3</sub>	86.1	97.2	96.3	98.4	97.2	97.4	97.5
CaCO <sub>3</sub>	0.2	1.7	1.5	1.3	1.4	1.6	1.5
FeCO <sub>3</sub>	13.7	1.1	2.2	0.3	1.4	1.0	1.0

\* FeO as Fe total

continued

\*\* column of normalized mole fractions after removal of serpentine

L = lizardite

analysis 4-6 (specimen 343-D) = magnesite-antigorite assemblage

analysis 7-9 (specimen 343-B) = magnesite-lizardite assemblage

analysis 10-11 (specimen 432-D) = magnesite-lizardite assemblage

App.10 continued

specimen	432-D	255-A	255-A	255-A	255-A
rock type	L	L	L	L	L
mean of analysis	10-11	12	13	14	12-14
SiO <sub>2</sub>	2.33	0.32	0.02	1.20	0.51
MgO	41.85	40.41	39.53	39.50	39.81
CaO	0.06	0.36	0.30	0.11	0.26
FeO*	0.96	0.66	0.83	1.36	0.95
total	45.48	41.76	40.68	42.20	41.55
Si	0.035	0.005	0.000	0.020	0.010
Mg	0.951	0.980	0.983	0.960	0.971
Ca	0.001	0.006	0.005	0.002	0.004
Fe	0.012	0.009	0.012	0.019	0.015
total	1.035	1.005	1.000	1.020	1.010
Mg**	0.974	0.974	0.983	0.980	0.982
Ca	0.016	0.018	0.005	0.002	0.004
Fe	0.010	0.010	0.012	0.018	0.014
total	1.000	1.000	1.000	1.000	1.000
MgCO <sub>3</sub>	97.4	97.4	98.3	98.0	98.2
CaCO <sub>3</sub>	1.6	1.6	0.5	0.2	0.4
FeCO <sub>3</sub>	1.0	1.0	1.2	1.8	1.4

\* FeO as Fe total

continued

\*\* column of normalized mole fractions after removal of serpentine

L = lizardite

analysis 10-11(specimen 432-D) = magnesite-lizardite assemblage

analysis 12-14(specimen 255-A) = magnesite-lizardite assemblage

App.10 continued

specimen rock type analysis	Do		
	255-A	256-A	450-C
	L	L+A	L+A
	15	16	17
SiO <sub>2</sub>	0.47	4.06	1.71
MgO	21.98	39.78	41.91
CaO	26.31	0.27	0.02
FeO*	1.38	1.37	2.34
total	50.39	45.48	46.43
Si	0.008	0.063	0.025
Mg	0.524	0.916	0.916
Ca	0.451	0.004	0.008
Fe	0.018	0.018	0.028
total	1.008	1.063	0.974
Mg**	0.516	0.982	0.966
Ca	0.451	0.004	0.006
Fe	0.033	0.014	0.028
total	1.000	1.000	1.000
MgCO <sub>3</sub>	51.6	98.2	96.6
CaCO <sub>3</sub>	45.1	0.4	0.6
FeCO <sub>3</sub>	3.3	1.4	2.8

\* FeO as Fe total

\*\* column of normalized mole fractions after removal of serpentine

Do = dolomite

L+A = lizardite + antigorite assemblage

analysis 15(specimen 255-A) = dolomite in liz. serpentinite

analysis 16(specimen 256-A) = magnesite in liz. + antigorite

analysis 17(specimen 450-C) = magnesite in liz. + antigorite

Appendix 11: Microprobe analyses of magnesite  
from talc - magnesite

specimen	177-D	177-D	177-D	177-D	177-D	270	270
mean of							
analysis	1	2	3	4	1-4	5	6
SiO <sub>2</sub>	0.09	0.03	0.00	0.32	0.11	0.83	0.40
MgO	37.90	38.86	38.96	38.76	38.62	41.79	39.77
CaO	0.08	0.02	0.00	0.02	0.03	0.01	0.00
FeO*	7.40	6.85	6.80	6.50	6.89	7.75	5.09
total	45.46	45.75	45.77	45.61	45.65	50.43	45.26
Si	0.000	0.000	0.000	0.005	0.001	0.012	0.008
Mg	0.900	0.910	0.911	0.909	0.908	0.895	0.928
Ca	0.000	0.000	0.000	0.000	0.000	0.000	0.000
Fe	0.098	0.091	0.088	0.085	0.091	0.093	0.066
total	1.002	1.000	1.000	1.005	1.002	1.012	1.006
Mg**	0.900	0.910	0.911	0.914	0.908	0.905	0.934
Ca	0.000	0.000	0.000	0.000	0.000	0.000	0.000
Fe	0.100	0.090	0.089	0.086	0.091	0.095	0.066
total	1.000	1.000	1.000	1.000	1.000	1.000	1.000
MgCO <sub>3</sub>	90.0	91.0	91.1	91.4	90.8	90.5	93.4
CaCO <sub>3</sub>	0.0	0.0	0.0	0.0	0.0	0.0	0.0
FeCO <sub>3</sub>	10.0	9.0	8.9	8.6	9.1	9.5	6.6

\* FeO as Fe total

continued

\*\* column of normalized mole fractions after removal of serpentine  
analysis 1-4 (specimen 177-D) = spathic magnesite  
in foliated matrix  
analysis 5-7 (specimen 270) = spathic magnesite  
in massive fragment



App.11 continued

specimen	270		252-D	252-D	252-D	252-D
mean of		5 - 7				8 - 10
analysis	7		8	9	10	
SiO2	1.17	0.39	0.37	1.48	1.87	1.24
MgO	40.47	13.49	36.09	37.07	36.36	36.51
CaO	0.00	0.00	0.14	0.16	0.16	0.15
FeO*	6.06	2.02	12.76	6.14	11.57	10.16
total	47.70	15.90	49.36	44.85	49.96	48.06
Si	0.017	0.006	0.005	0.023	0.028	0.019
Mg	0.907	0.302	0.828	0.891	0.823	0.847
Ca	0.000	0.000	0.002	0.002	0.002	0.002
Fe	0.076	0.025	0.164	0.082	0.146	0.131
total	1.019	0.340	1.006	1.022	1.028	1.019
Mg**	0.922	0.921	0.832	0.913	0.843	0.862
Ca	0.000	0.000	0.002	0.002	0.002	0.002
Fe	0.076	0.079	0.166	0.085	0.155	0.136
total	1.000	1.000	1.000	1.000	1.000	1.000
MgCO3	92.2	92.1	83.2	91.3	84.3	86.2
CaCO3	0.0	0.0	0.2	0.2	0.2	0.2
FeCO3	7.8	7.9	16.6	8.5	15.5	13.6

\* FeO as Fe total

\*\* column of normalized mole fractions after removal of serpentine  
 analysis 5-7 (specimen 270) = spathic magnesite  
 in massive fragment  
 analysis 8-10 (specimen 252-D) = spathic magnesite  
 in poor foliated matrix

Appendix 12: Microprobe analyses of magnesite  
from quartz-magnesite

specimen mean of analysis	342 1	342 2	342 3	342 1 - 3	342 4	342 5	342 6
SiO <sub>2</sub>	0.00	0.00	0.02	0.00	0.09	0.03	0.04
MgO	38.26	38.47	39.03	38.67	39.13	39.40	39.19
CaO	0.27	0.25	0.08	0.20	0.22	0.36	0.10
FeO*	9.21	8.86	5.18	7.75	7.45	6.55	7.05
total	47.74	47.58	44.30	46.62	46.88	46.34	46.38
Si	0.000	0.000	0.000	0.000	0.001	0.000	0.000
Mg	0.877	0.882	0.930	0.896	0.899	0.909	0.906
Ca	0.004	0.004	0.000	0.003	0.003	0.006	0.001
Fe	0.119	0.113	0.069	0.101	0.096	0.084	0.092
total	1.000	0.999	1.000	0.999	1.001	1.000	0.999
MgO**	0.877	0.882	0.931	0.896	0.900	0.909	0.906
Ca	0.004	0.004	0.000	0.003	0.003	0.006	0.001
Fe	0.119	0.113	0.069	0.101	0.097	0.085	0.092
total	1.000	0.999	1.000	1.000	1.000	1.000	0.999
MgCO <sub>3</sub>	87.7	88.2	93.0	89.6	90.0	90.9	90.6
CaCO <sub>3</sub>	0.4	0.4	0.0	0.3	0.3	0.6	0.1
FeCO <sub>3</sub>	11.9	11.3	6.9	10.1	9.7	8.5	9.2

\* FeO as Fe total

continued

\*\* column of normalized mole fractions after removal of serpentine  
analysis 1 - 3(specimen 342) = spathic magnesite in vein  
analysis 3 - 6(specimen 342) = spathic magnesite

App. 12 continued

specimen	342	342	342	342	342	142-C	142-C
mean of	mean 4-6				mean 7-9		
analysis		7	8	9		10	11
SiO <sub>2</sub>	0.05	3.25	2.68	3.52	3.18	0.03	0.18
MgO	39.24	36.91	36.12	37.49	36.86	38.79	39.22
CaO	0.23	0.09	0.11	0.11	0.10	0.06	0.02
FeO*	7.02	2.34	3.47	4.50	3.43	2.86	2.93
total	46.53	42.58	42.38	45.73	43.58	41.74	42.35
Si	0.000	0.053	0.044	0.057	0.052	0.000	0.002
Mg	0.905	0.913	0.905	0.882	0.900	0.959	0.957
Ca	0.003	0.001	0.001	0.001	0.001	0.000	0.000
Fe	0.090	0.032	0.048	0.059	0.046	0.041	0.040
total	1.000	1.054	1.046	1.057	1.052	1.000	1.003
MgO**	0.905	0.968	0.950	0.936	0.951	0.959	0.960
Ca	0.003	0.001	0.001	0.001	0.001	0.000	0.000
Fe	0.091	0.031	0.049	0.063	0.048	0.041	0.040
total	1.000	1.000	1.000	1.000	1.000	1.000	1.000
MgCO <sub>3</sub>	90.5	96.8	95.0	93.6	95.1	95.9	96.0
CaCO <sub>3</sub>	0.3	0.1	0.1	0.1	0.1	0.0	0.0
FeCO <sub>3</sub>	9.1	3.1	4.9	6.3	4.6	4.1	4.0

\* FeO as Fe total

continued

\*\* column of normalized mole fractions after removal of serpentine

analysis 3 - 6 (specimen 342) = spathic magnesite

analysis 7 - 9 (specimen 342) = cryptocrystalline magnesite

analysis 10 - 12 (specimen 142-C) = spathic magnesite

App.12 continued

specimen	142-C	142-C	85-F	85-F	85-F	85-F
mean of		10 - 12				3 - 15
analysis	12		13	14	15	
SiO <sub>2</sub>	0.05	0.02	0.12	0.08	0.19	0.13
MgO	39.23	39.08	39.17	38.83	39.75	39.25
CaO	0.30	0.12	0.02	0.08	0.07	0.06
FeO*	6.98	4.25	4.50	4.15	4.57	4.40
total	46.55	43.54	43.80	43.14	44.58	43.84
Si	0.000	0.000	0.001	0.000	0.002	0.001
Mg	0.905	0.942	0.938	0.945	0.938	0.938
Ca	0.004	0.001	0.000	0.000	0.000	0.000
Fe	0.090	0.057	0.060	0.056	0.060	0.058
total	1.000	1.001	1.001	1.001	1.003	1.002
MgO**	0.905	0.942	0.940	0.945	0.940	0.941
Ca	0.004	0.001	0.000	0.000	0.000	0.000
Fe	0.090	0.057	0.060	0.055	0.060	0.059
total	1.000	1.000	1.000	1.000	1.000	1.000
MgCO <sub>3</sub>	90.5	94.2	94.0	94.5	94.0	94.1
CaCO <sub>3</sub>	0.4	0.1	0.0	0.0	0.0	0.0
FeCO <sub>3</sub>	9.0	5.7	6.0	5.5	6.0	5.9

\* FeO as Fe total

continued

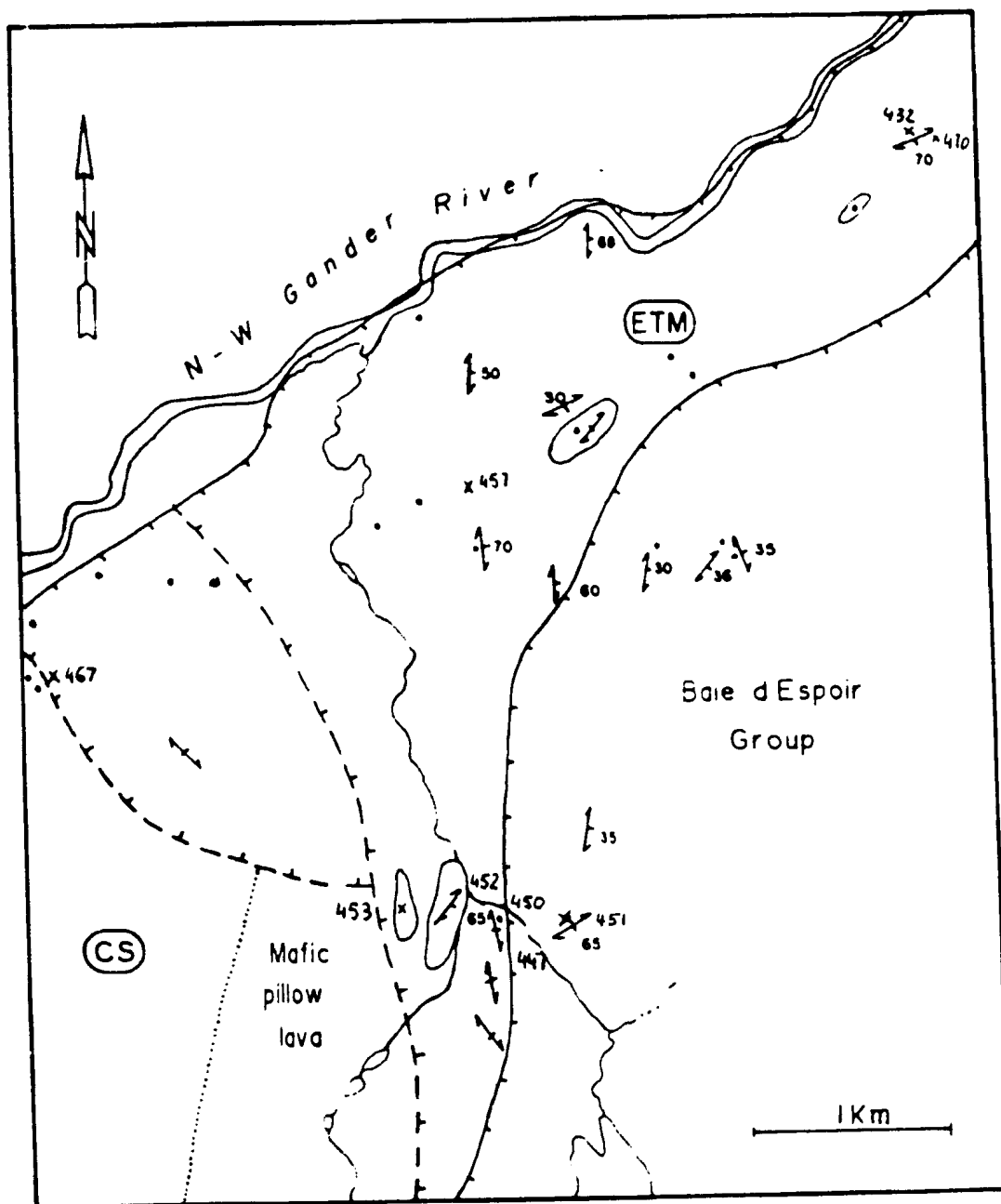
\*\* column of normalized mole fractions after removal of serpentine  
analysis 10-12(specimen 142-C) = spathic magnesite  
analysis 13-15(specimen 85-F) = spathic magnesite

App.12 continued

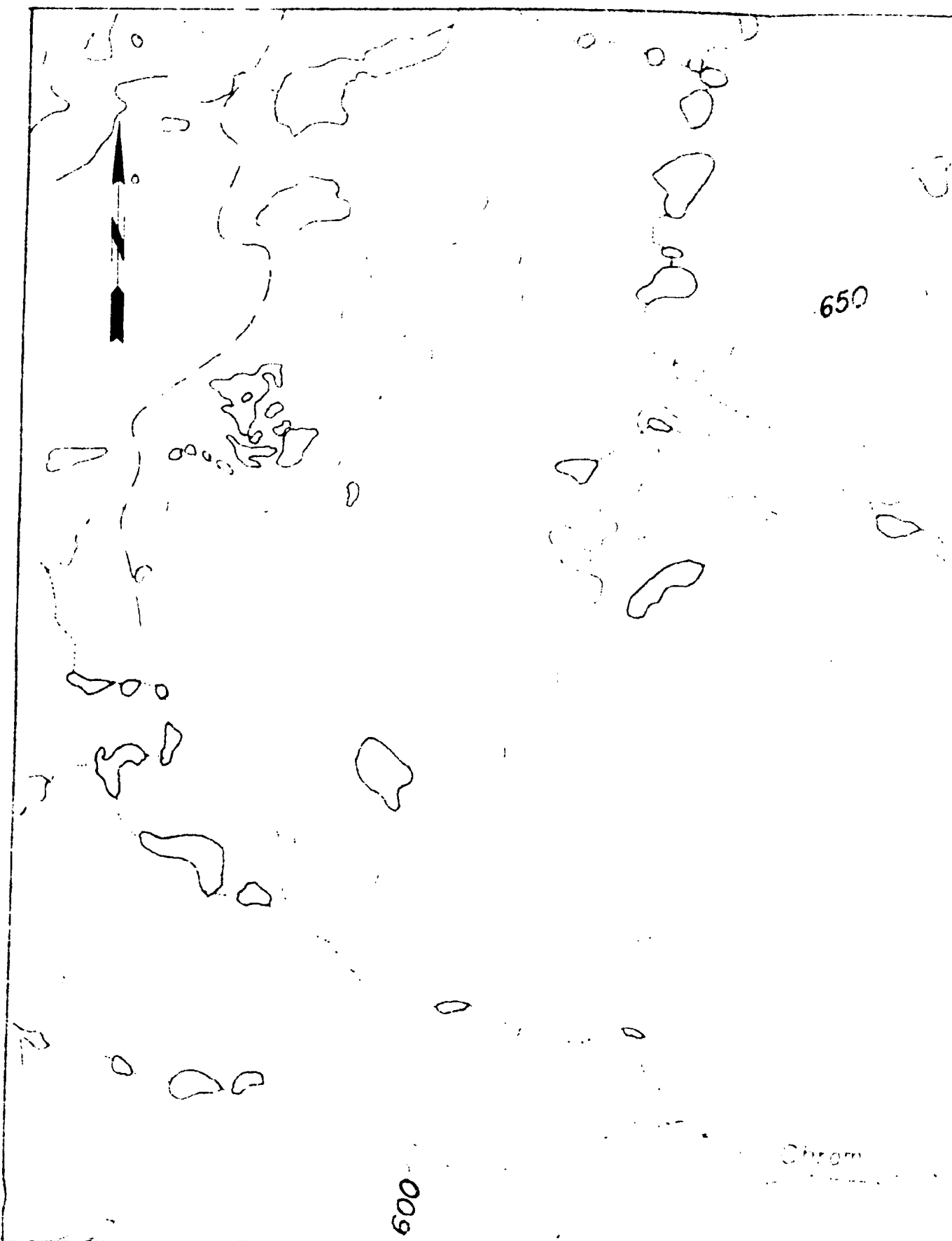
specimen	85-F	85-F	85-F
mean of			16 - 17
analysis	16	17	
SiO <sub>2</sub>	0.57	0.75	0.66
MgO	38.52	36.87	37.69
CaO	0.11	0.14	0.12
FeO*	6.93	6.23	6.58
total	46.13	43.99	45.06
Si	0.008	0.012	0.010
Mg	0.898	0.900	0.899
Ca	0.001	0.002	0.001
Fe	0.090	0.085	0.087
total	1.009	1.011	1.010
MgO**	0.908	0.911	0.910
Ca	0.001	0.002	0.001
Fe	0.091	0.087	0.089
total	1.000	1.000	1.000
MgCO <sub>3</sub>	90.8	91.1	91.0
CaCO <sub>3</sub>	0.1	0.2	0.1
FeCO <sub>3</sub>	9.1	8.7	8.9

\* FeO as Fe total

\*\* column of normalized mole fractions after removal of serpentine  
analysis 16-17(specimen 85-F) = cryptocrystalline magnesite



SAMPLE LOCATION MAP - EASTERN TECTONIC MÉLANGE



650

600

Chrom

500

x 187

205  
203  
201 x 197  
x 196

x 108

103  
x

68

x 30

x 156

x 175

x 160

113  
x

x 179



500

GANDER

205  
2032  
2018 197  
x 196

x  
108

103  
x

x 175

x 160

630



609

X 333

239

119  
x  
124  
x  
121

x 79

177  
x  
343

x 505

133  
x  
134

x 342  
x 85

x 139

x 337

650

142  
143  
144  
274  
270  
402

x 404

350  
x  
351  
356

372  
x  
378  
379  
371  
383

251  
x  
250  
x  
252  
x  
253  
x  
256  
x  
257

289  
x  
305

ORTHWEST

60

λ 342  
λ 85

x 404

402

λ 396

350  
x  
351

389  
x

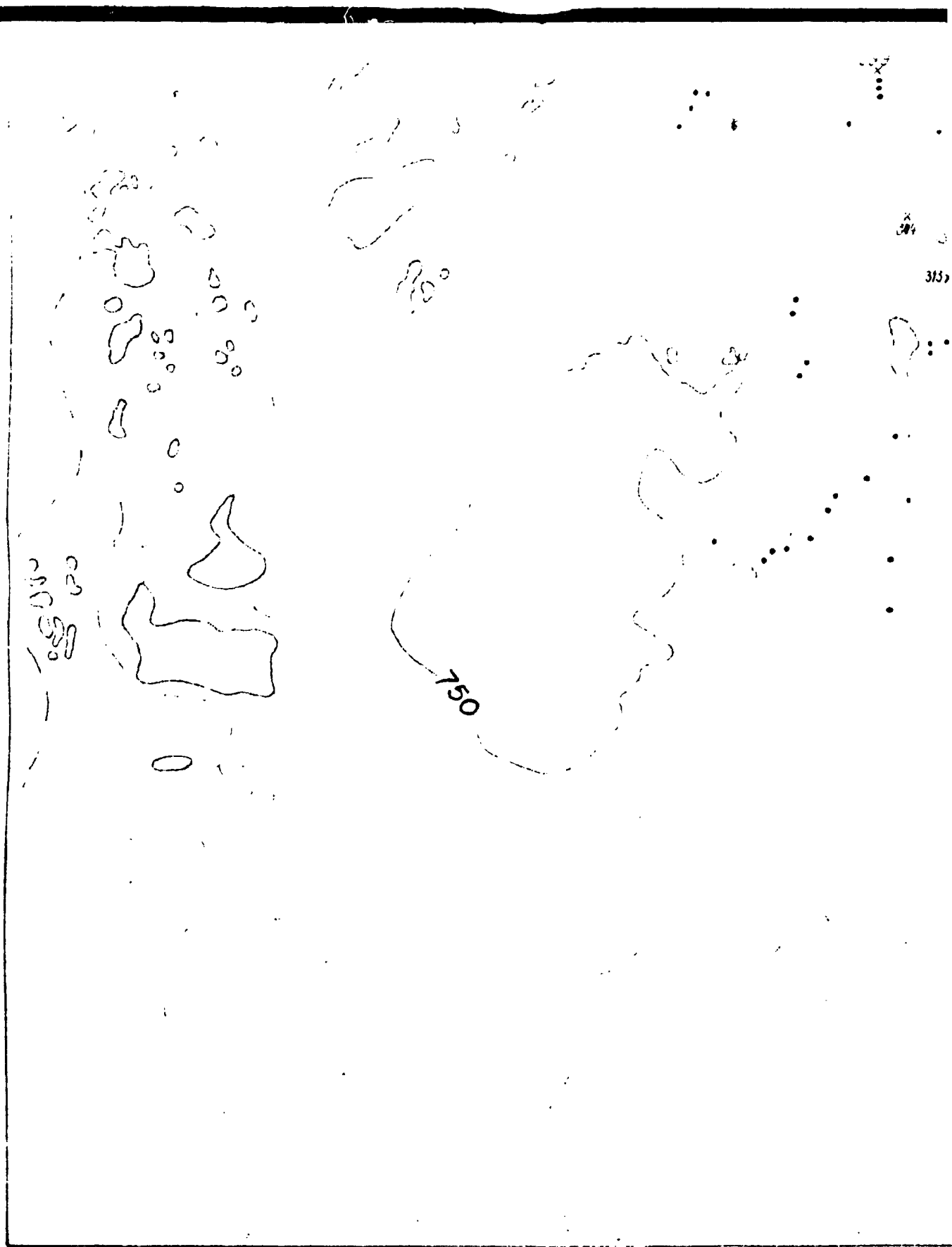
372  
x

373  
x

379

600





289

305

304

313x

550

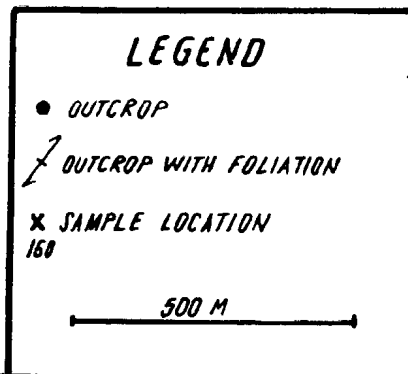
55

Gardner

SAMPLE LOCATION MAP



550  
Gardner



**SAMPLE LOCATION MAP - WESTERN TECTONIC MÉLANGE**



